Andrea Perino

Wave propagation through discontinuous media in rock engineering

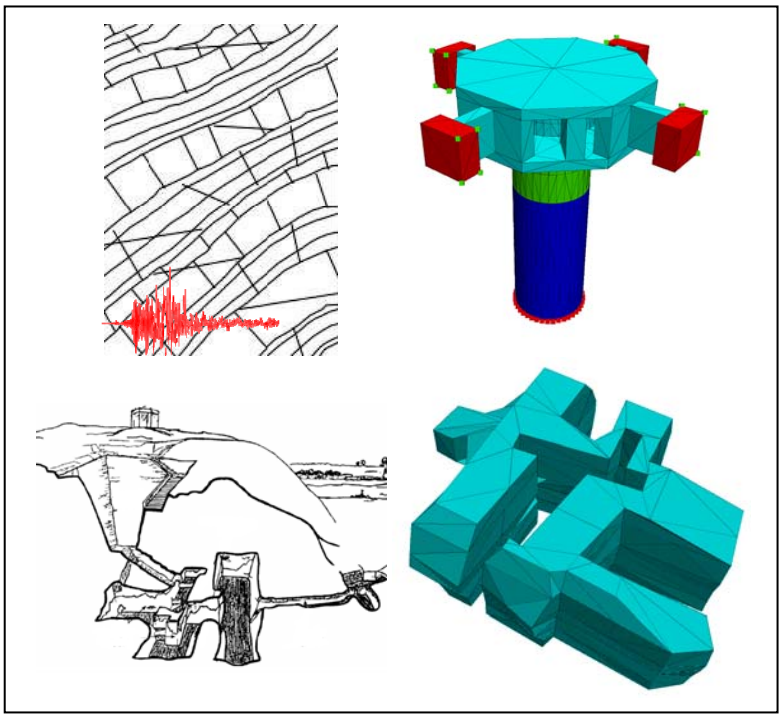

Politecnico di Torino

Dottorato di ricerca in Ingegneria per la
Gestione delle Acque e del Territorio (XXIII° ciclo)

Dottorato di Ricerca in Ingegneria per la Gestione delle Acque e del Territorio (XXIII° ciclo)

Politecnico di Torino

May 2011

Wave propagation through discontinuous media in rock engineering

.....
Andrea Perino
Author

.....
Prof. Giovanni Barla
Adviser

.....
Prof. Renato Orta
Co-adviser

.....
Prof. Claudio Scavia
Head of the Research Doctorate Programme in Geotechnical Engineering

Abstract

The analysis of wave propagation in jointed rock masses is of interest for solving problems in geophysics, rock protective engineering, rock dynamics and earthquake engineering. At present, more than in the past, analyses of underground structures in seismic conditions need be considered.

The aim of the present thesis is to contribute to the understanding of wave propagation in rock masses and of its influence on the stability of underground structures. The research is focused first on the analysis of the phenomenon through analytical, numerical and experimental methods. Then, static and dynamic stability analyses of a real case study such as the water storage cavern of the Tel Beer Sheva archaeological site in Israel (Iron age 1200-1700bc) are carried out.

An analytical method such as the Scattering Matrix Method (SMM) is developed for the study of wave propagation through rock masses. This method (SMM) is based on the scattering matrix and is borrowed from electromagnetic wave propagation theory of transmission lines such as coaxial cables, optical fibres, strip-lines, etc. The scattering matrix is composed of reflection and transmission coefficients of a single joint or a set of parallel joints.

Dry, fluid filled or frictional joints are considered. The computation can also be performed with material damping. Both P, SV or SH-waves can be applied to the model with any oblique angle of incidence. The analytical solution is obtained in the frequency domain and allows one to consider multiple wave reflections between joints. The analytical results obtained with the SMM are compared with other analytical methods and with the Distinct Element Method (DEM) by using the UDEC and 3DEC codes (from Itasca Consulting Group).

The results obtained with the SMM applied to different joint models are compared with those obtained experimentally with the Hopkinson pressure bar (SHPB) tests. Resonant column laboratory tests are also performed to investigate the effects of fractures on wave propagation in a soft rock. A three-dimensional DEM model is implemented to simulate the resonant column test. Numerical and experimental results are compared.

The stability of the water storage cavern of the Tel Beer Sheva archaeological site in Israel, excavated in a jointed chalk is assessed by means of static and dynamic DEM analyses in two and in three dimensional conditions. A back analysis of both the roof collapse during construction and of the cavern in its present configuration with a pillar installed in the centre is also carried out.

Finally dynamic analyses are performed to evaluate the influence of wave propagation on the stability of the cavern with a deconvoluted motion produced by the Nuweiba earthquake (1995) being applied as input. Additional numerical analyses are performed to evaluate the dependence of the damage on the amplitude, duration, frequency and direction of the input wave.

Further developments are needed and some open questions remain to be addressed for the study of wave propagation phenomenon in rock masses and of their effects on the stability of geotechnical structures. In particular, the extension of the SMM to other more complex joint models, additional Resonant Column tests for other geometries of fractures and for a greater number of joints in the rock specimens are of interest.

Acknowledgements

I would like to express my thanks to my adviser, Professor Giovanni Barla for his attention and relentless support of my studies, and his guidance toward a deeper scientific way of thinking. My deepest gratitude is due to my co-adviser, Professor Renato Orta, who introduced and supported me into the analytical analyses of wave propagation.

An important part of my work has been developed in laboratory. Hence, I would like to thank the technicians of the DIPLAB and MASTRLAB laboratories of the department of Structural and Geotechnical Engineering of the Politecnico di Torino and in particular Enzo Pallara for helping me in resonant column tests and Marco Alessio for uniaxial compression strength tests and ultrasonic tests.

I am specially grateful to professor Jian Zhao, head of the Rock Mechanics Laboratory (LMR) of the EPFL of Lausanne, and in particular to PhD student Jianbo Zhu and to researcher Jianchun C. Li for their collaboration in the comparative theoretical study described in my thesis.

I am grateful to my friends and colleagues of the department of structural and geotechnical engineering for their help and their support. My thanks to Elena, Maria Elena, Giovanna, Daniele, Marco, Mariacristina, Michele, Qingrui, Kai and Francesco.

To my parents: thank you for giving me the freedom and opportunity to pursue my own interests. I also thank them for teaching me that there is no substitute for honest hard work.

Table of contents

List of Tables

List of Figures

List of symbols

The derivative of a quantity x over the time t is indicated as $\dot{x}$.
Lowercase letters in bold indicate the vectors while bold capital letters individuate the matrices.
The symbol ^ over a letter indicates the unit vector.

Arabic letters:

$\mathbf{A}$	transmission matrix
A	coefficient of adsorption of a frictional interface
$\mathbf{A}_{ij}$	sub-matrix of the transmission matrix
$\mathbf{A}_{str}$	transmission matrix of a layer
a	rms acceleration amplitude
$a_1,\ a_2$	curve-fitting coefficients
$A_1,\ A_2,\ B_1,\ B_2$	constants function of the boundary conditions and the natural pulsation of the system
ACF	calibration factor of the accelerometer of the RCA
$\mathbf{B}$	matrix of joint compliances
B	amplitude parameter
b	thickness of bond of the interface; parameter function of the joint admittance
c	wave propagation velocity; damping coefficient; coesion
C	capacitance
C^*	constant of proportionality
C_0	original undeformed circumference of the specimen
c_{eq}	equivalent damping
c_i	joint or fracture compliance
C_{ij}	elastic constants
$c^{P\pm},\ c^{SV\pm},\ c^{SH\pm}$	amplitudes of the incident and reflected waves
c_p	dashpot coefficient
C_{plate}	plate velocity of the filling medium in a joint
d	joint spacing; diameter of the bar
D	damping ratio; amplitude parameter
e	Nepero's number
$e^{SH},\ e^{SV},\ e^{P}$	particle motion directions for three polarizations
E	Young's modulus
$E[\cdot]$	logic averaging operator (Iwan, 1973)

E_A	amount of energy absorbed from a frictional interface
E_a	Young's modulus of the intact rock
E_d	Dynamic Young's modulus
E_I, E_R, E_T	energy flux per unit area per cycle of oscillation associated with the incident, transmitted and reflected waves
E_t, E_m, E_s	tangent, average and secant Young's modulus
E_v	stiffness contributed by the joints
F	impedance ratio between the filling material and the rock amplitude of the sinusoidal force
f	sinusoidal force; symbol of function
f_1, f_2	frequencies
f_{kc}	force related to the spring and dashpot connected in series
f_n	resonant frequency
G	shear modulus
G_f	shear modulus of the filling material of the joint
h	joint thickness; height of the specimen
H	normalized joint viscosity
$\mathbf{I}$	identity matrix
I	electric current; wave amplitude
i	cell number
I_S	mass polar moment of inertia of the specimen
I_T	mass polar moment of inertia of the rigid added mass over the specimen
j	imaginary index; non-dimensional time
J	area polar moment of inertia of the cross-section of the specimen
k	dynamic joint or fracture stiffness
K	bulk modulus; normalized dynamic joint stiffness
$\mathbf{k}$	wave vector
$\mathbf{K}$	joint stiffness matrix
K_{nn}, K_{ss}	normalized normal and shear joint stiffness
k_1, k_2	stiffnesses
k_A	stiffness of system specimen A + driving
k_{B1}	stiffness of system specimen B1 + driving
k_e	equivalent propagation constant
k_{eq}	equivalent stiffness
k_P, k_S	propagation constant for P and S-waves
k_{nn}, k_{ss}	normal and shear joint stiffness
k_{zP}, k_{zS}	longitudinal wave vector component for P and S-waves
l	stopband period
$\boldsymbol{l}$	direction of propagation
L	inductance; length normal to the fractures
l_0	original measured axial length

l_i	travelled distance normal to the fractures before the first and after the last fracture from the ends of the specimen of length L
L_1, L_2	distances between the transducer axis and the specimen axis for the transducer n° 1 and n° 2
L_{acc}	accelerometer distance from the vertical axis of the specimen
$\mathbf{M}$	modal matrix
m	mass
M_0	torque applied from the RCA
M_{ij}	components of the modal matrix
$\mathbf{M}_{ij}$	sub-matrix of the modal matrix
m_n, m_t	normal and tangential masses of filling medium of the joint
M_t	torque applied to the head of the specimen
N	number of discontinuities
n	total number of cells, non-dimensional distance
$\mathbf{n}$	normal direction
$N^{P\pm}$, $N^{SV\pm}$, $N^{SH\pm}$	normalization factors for P, SV and SH-waves
Q	quality factor; correction factor for RCA results
q	parameter dependent on the plate velocity of the filling medium in a joint
R	resistance
R_i	reflection coefficient; radius of the specimen
r	radial distance
r_a	radial distance between the axis of rotation and the point in which is located the accelerometer in the laboratory RCA
$\mathbf{s}$	slowness vector
s_x, s_y, s_z	components of the slowness vector
$\mathbf{S}$	scattering matrix
$\mathbf{S_{ij}}$	sub-matrix of the scattering matrix
S	cross-section area of the cylindrical specimen
S_c	contact area of the joint
T_i	transmission coefficient
t	time
$\mathbf{T}$	stress tensor
t_{eff}	effective group travel time
t_{frac}	group time delay due by the fractures
t_{gT}, t_{gR}	time delay for the transmitted and reflected waves
T_{zx}	amplitude of the shear stress τ_{zx}
u	displacement
$\mathbf{u}$	displacement vector
U	amplitude of the incident harmonic displacement wave u.
v	velocity

$\mathbf{V}$	matrix of the eigenvectors of the transmission matrix of the unit cell
V	electric voltage; amplitude of particle velocity
$V_{S,eff}$	effective shear wave velocity
V_g	group velocity of the intact homogeneous isotropic rock
V_n	electric voltages in input in a unit cell n
V_{n+1}	electric voltages in output
$V_{P,S}$	P and S-wave propagation velocity
V_x^{inc}	amplitude of the incident particle velocity
W	peak of energy stored in a single cycle
x	relative displacement
X	amplitude of the steady-state response
$x,\ y,\ z$	spatial coordinates
x_0	displacement representing the limit of the elastic zone
$\ddot{x}_g$	ground surface acceleration
Y	joint or fracture admittance
$\mathbf{Y}$	admittance matrix
Y_S	medium shear admittance
Z	seismic impedance
$\mathbf{Z}$	impedance matrix
$Z_1,\ Z_2$	local impedances
$z_1,\ z_2$	amplitudes of motion
Z_∞	characteristic impedance
$Z_{\infty ND}$	characteristic impedance of the not discretized mechanical system

Greek letters:

α	attenuation coefficient; P-wave propagation velocity; propagation factor
β	variable; S-wave propagation velocity
δ	logarithmic decrement; phase shift of the propagation factor
δ_0	ratio between the joint thickness and the wavelength in the filling material
Δa	displacement of the accelerometer
$\Delta a_1,\ \Delta a_2$	displacements measured by the transducer n° 1 and n° 2
Δa_{acc}	accelerometer tangential displacement
ΔC	change in circumference
Δd	change in diameter
Δl	change in measured axial length
ΔW	elastic energy dissipated in a single cycle

Δx	displacements measured in the laboratory tests in a generic point P
Δz	single element size of the mesh
Δz_{lim}	maximum allowable single element size of the mesh
ε	strain; residue from the equivalent linearization
ε_a, ε_c, ε_d	axial, circumferential and diametric strain
ε_{ij}	strain tensor
ϕ	diameter of the specimen
γ	shear strain
γ_{SA}	single amplitude of the shear strain
η	specific material viscosity
η_f	viscosity of the filling material of the joint
η_v	specific material viscosity
φ	phase angle; friction angle
Θ_T	phase shift of the transmission coefficient
ϑ	variable; rotation; angle of incidence
ϑ_B	Brewster angle
ϑ_c	critical angle
ϑ_i, ϑ_r, ϑ_t	angle of the incident, reflected and transmitted waves
ϑ^{inc}	angle of incidence
ϑ^P, ϑ^{SV}	P and SV-wave angle of incidence
λ	Lamé elastic constants; eigenvalues; wavelength
$\boldsymbol{\lambda}$	diagonal matrix of the eigenvalues
λ_f	wavelength of the medium of filling of the joint
μ	shear modulus
ν	Poisson's ratio
ν_d	Dynamic Poisson's ratio
$\boldsymbol{\Pi}$	matrix of masses of filling medium of the joint
θ	variable
Θ^*	parameter of the equivalent linearization procedure
Θ_R, Θ_T	phase angle of the reflection and transmission coefficients
ρ	mass density
ρ_0	mass density of the medium of filling of the joint
σ_t	joint tensile strength
σ_u	uniaxial compressive strength
τ	stress
τ_F	frictional stress
$\boldsymbol{\tau}_{ij}$	stress tensor
τ_{imax}	maximum stress of the incident wave
τ_S	joint shear strength
τ_{trasm}	maximum amplitude of the transmitted stress wave
ω	angular wave frequency
ω_c	critical circular frequency

ω_n	natural pulsation of a system
ξ	transverse wave-vector component
Ψ	state vector
ψ	variable
ζ	joint spacing ratio

Chapter 1

Introduction

1.1 Framework

Propagation of seismic waves in jointed rock masses can be modelled by assuming the medium to be continuous or discontinuous. A realistic response of the rock mass is however provided when modelling wave propagation through discontinuities. In fact, the understanding of the effects of such features on wave propagation is essential for the solution of problems in geophysics, seismic investigations, rock dynamics, rock protective engineering and earthquake engineering.

Also, the analysis of the dynamic behaviour of rock joints/discontinuities is fundamental to study the stability of tunnels and caverns excavated in fractured rock masses. Generally, it is assumed that underground structures are resistant to earthquakes, nevertheless some underground structures have undergone relevant damages in recent large earthquakes. The level of damage depends on the magnitude of the earthquake, rock mass properties, overburden depth, shape and type of lining of the geotechnical structures.

1.2 Problem statement

Wave propagation in rock masses and its influence on the stability of geotechnical structures are some of the most important topics in rock dynamics and earthquake engineering. Rock joints/discontinuities play an important role on wave propagation: when an elastic wave impinges a joint, part of the energy is transmitted and part is reflected. The amplitude of the transmitted and reflected waves depends on the joint model assumed, on its geometrical properties (spacing, length, thickness) and on the frequency content. These non-welded interfaces can be modelled with a linear elastic behaviour or with more complex models with dissipative behaviour. In this latter case some energy, owned from the incident wave, is dissipated along the interface between the two faces of the joint. The principal effects of rock joints on wave propagation are the attenuation and the slowdown of the incident wave.

The problem of wave propagation in discontinuous media has been studied by many authors but the analysis of the effects of the multiple reflections between the joints has not been widely analysed. Moreover, there is not a unique complete study on this problem for various types of joints. On the other hand, the influence of the dynamic loads on underground structures embedded in rock masses has not been extensively investigated. Given the above, a better understanding of wave propagation in rock masses and of its effects on the stability of the underground structures is needed.

1.3 Scope and objectives

The scope of the present thesis is to contribute to the understanding of wave propagation in rock masses and of its influence on the stability of underground structures. The study encompasses first the use of analytical, numerical and experimental methods. Then, the attention is focussed on a real case study, the water storage system of Tel Beer Sheva, an archaeological site in Israel (Iron age 1200-700bc).

In line with the need to provide a reliable analytical tool, the scattering matrix method (SMM) is developed first. The SMM is implemented to study wave propagation through rock joints represented with different models of behaviour. In addition, laboratory tests are performed in parallel with numerical analyses with the discrete element methods (UDEC and 3DEC codes from Itasca).

Finally, the numerical models developed with the Tel Beer Sheva archaeological site in mind allow one to provide a comprehensive back analysis of the roof collapse of the cavern, occurred during the construction stages, and to verify the stability of the cavern under both gravitational and seismic loadings.

The following main tasks have been undertaken:

- Detailed bibliographic study, in order to identify the theories, the methods and the experimental observations available in the present literature to describe wave propagation in discontinuous media.

- Development of the scattering matrix method (SMM) to evaluate the effects of joints on wave propagation from the analytical point of view.

- Comprehensive analytical study by using the SMM for different joint behaviours, with the interest in either a single joint or a set of joints.

- Comparison and validation of the SMM with theoretical and numerical methods (e.g. the Distinct Element Method, DEM).

- Laboratory resonant column apparatus tests on soft rock for studying the possible use of this apparatus to testing of both intact and jointed rock specimens, with interest in the latter case on the influence of fractures on wave propagation.

- Numerical analysis in both two dimensional and three dimensional conditions of the Tel Beer Sheva water storage system, with the intent to evaluate its stability under both static and dynamic loading.

1.4 Organisation of thesis

This thesis is divided into twelve chapters and two appendices. The present chapter is intended to provide a general introduction to the subject. Chapter 2 presents a review of wave propagation theories with particular attention on discontinuous media. Both analytical and numerical methods are described.

The following two chapters present the fundamentals of the scattering matrix method (SMM). Chapter 3 is devoted to the definition of the SMM in continuous media and the use of some numerical computations to study the influence of welded interfaces on wave propagation. Chapter 4 extends the SMM to discontinuous media with particular emphasis on rock mass response to wave propagation.

The following three chapters are then dedicated to the study of the effects of different models of rock joint behaviours. The transmitted and the reflected waves generated from a joint with linear elastic behaviour are studied in Chapter 5. The SMM is then validated in Chapter 5 by comparing the results with both analytical solutions and numerical methods. In chapter 6 the results of SMM in the study of filled joints are compared with experimental laboratory results obtained with modified split Hopkinson pressure bar (SHPB) tests. Additional comparisons of SMM are performed with theoretical methods. Chapter 7 describes the application of the SMM to study the effects of frictional joints through an equivalent linearization procedure. Some comparative numerical analyses are performed.

Chapter 8 describes the application of DEM to the solution of wave propagation problems by comparing the results obtained with the SMM. The problem of the appropriate mesh element size when using DEM numerical models is also addressed.

Chapter 9 is focussed on the description of the Resonant Column Apparatus tests performed on either intact of jointed rock specimens. The implementation of a three-dimensional numerical DEM model of the resonant column apparatus is performed. Experimental and numerical results are compared.

The final two chapters are devoted to the DEM analyses performed on the Tel Beer Sheva water storage system in both two and in three dimensional conditions.

Chapter 10 describes the static analyses performed in order to reproduce the roof collapse undergone during the excavation as reported through archaeological studies. Chapter 11 presents the corresponding dynamic analyses of the cavern with the Nuweiba earthquake (1995) as input, by underlining the dependence of damage on the amplitude and direction of the input wave.

Finally, some conclusions and suggestions for further works are given in Chapter 12.

Appendix A describes the analytical derivation of the normalization coefficients used in the SMM and Appendix B gives the database of seismic damage to underground structures.

Chapter 2

State of the art

2.1 Introduction

Rock joints represent the main obstacle to stress wave propagation in rock masses. Through several types of interaction, wave peaks are diminished, propagation is delayed and frequencies are selectively filtered. The interaction is two-ways because waves with sufficient amplitude can change the state of the joints. Voids, micro-fractures, beddings and schistosities are also responsible for wave attenuation.

In this chapter, a review of the available studies on the effects of fractures or micro-fractures on wave propagation is reported. We will summarize only the main theoretical developments dealing with the simulation of the influence of fractures on wave propagation and we will discuss the fields of application and the main assumptions introduced. Special consideration will be given to wave propagation across discontinuous media.

The theoretical methods for studying the influence of joints on elastic wave propagation are essentially based on (Cai, 2001; Weidong, 2005):

1. Displacement Discontinuity Method (DDM)
2. Equivalent Medium Method (EMM)
3. Wave Scattering Method (WSM).

2.2 Displacement Discontinuity Method (DDM)

The DDM was originally proposed by Mindlin (1960) and applied to seismic wave propagation by Schoenberg (1980). The basic assumption of this method is that the particle displacements of a seismic wave as this propagates through a joint are discontinuous, while the stresses remain continuous.

The DDM is applicable to macro-fractures that are large in extent, small in thickness and in asperity separation if compared with wave length. Cook (1992) analyzes the effects of the fracture on wave propagation through the rock mass and states that this problem is not studied in detail as is the case of the effects of micro-fractures. In Rock Mechanics and Rock Engineering the effects of fractures in jointed rock masses are generally predominant and several applications of DDM are reported.

In DDM a planar fracture is physically envisioned as a planar collection of collinear micro-voids and asperities in contact. The closure of the voids and the asperities deformation define the global deformation of the fracture. When a wave propagates across a fracture of this type the stress field is continuous while the displacement field is discontinuous, given that the fracture undergoes a deformation.

With these assumptions, a fracture is a non-welded interface if along it the relative displacements between the two sides of the fracture are not zero as for a welded interface. In DDM the discontinuity of displacements is applied as a boundary condition in the wave equations.

The effects of a fracture or a rock joint on an incident wave are evaluated in terms of transmission and reflection coefficients. These coefficients are defined respectively as the ratio between the amplitude of the transmitted or reflected wave and the amplitude of the incident one.

The DDM derives from the traditional theories of wave propagation in stratified media (Zoeppritz et al, 1919; Macelwane & Sohon, 1936; Kolsky, 1952; Cagniard, 1962; Aki & Richards, 2002; and others). In these theories the interfaces are welded and then across the joint or the fracture a continuity of displacements and stresses is assumed to hold true.

When an elastic plane wave impinges a welded interface between two different media a reflected and a transmitted wave are generated. Let us consider, as an example, a P-wave that impinges a flat interface at an angle of incidence ϑ_1. In an elastic medium four waves are generated from the interaction of the incident wave and the interface (Figure 2.1):

- A reflected P-wave at reflection angle ϑ_1;
- A reflected SV-wave at reflection angle ϕ_1;
- A transmitted P-wave at transmission angle ϑ_2;
- A transmitted SV-wave at transmission angle ϕ_2.

It is well known that the angles of reflected and transmitted waves are defined by using Snell's law. In optics and physics, Snell's law (also known as Descartes' law or the law of refraction) is used to describe the relationship between the angles of incidence and refraction, when referring to light or other waves, passing through a boundary between two different isotropic media, such as water and glass. This law says that the ratio of the sine of the angles of incidence and of refraction is a constant that depends on the media.

If we consider a refraction of a wave at the interface between two media of different stiffness, the velocity of wave propagation is lower in the second medium ($V_1 < V_2$), then the angle of transmission ϑ_t is less than the angle of incidence ϑ_i. Therefore, for a wave that impinges an interface the Shell's law is:

$$\frac{\sin \vartheta_i}{V_1} = \frac{\sin \vartheta_r}{V_1} = \frac{\sin \vartheta_t}{V_2} \tag{2.1}$$

where ϑ_r is angle of the reflected wave.

When ϑ_r is 90°, a reflected wave is generated which propagates along the interface between two materials. This situation is called critical refraction.

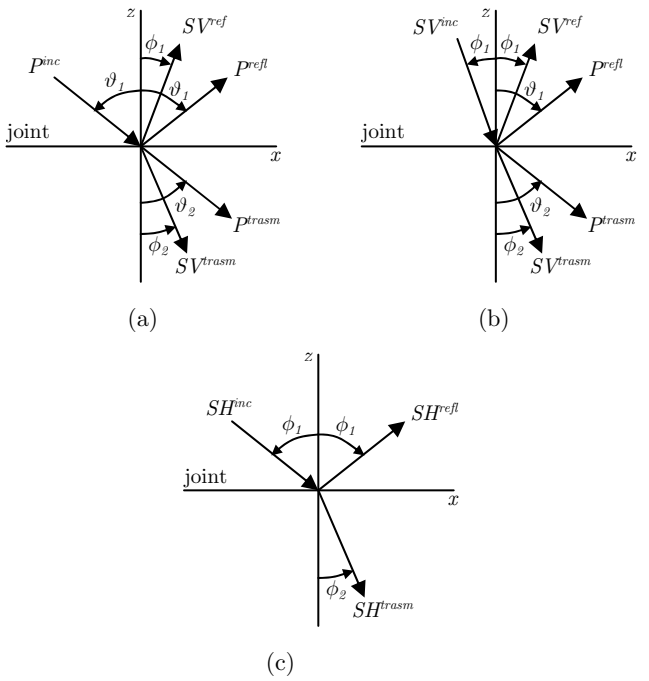

Figure 2.1 - Transmitted and reflected waves at discontinuities: compression wave (a), vertical shear wave (b) and horizontal shear wave (c)

In DDM stress (and therefore velocity) is continuous across the joint, while displacement is proportional to stress since normal and shear stiffness are finite and constant. A fracture or a joint can be treated as an incompletely-welded interface or a non-welded interface. A fracture can undergo a closure, an aperture or a slip under normal or shear stress.

These conditions can be simulated with a discontinuity of displacement in normal or tangential direction across a joint. These assumptions are applied as boundary conditions along a joint or a fracture. DDM provides solutions for three-dimensional shear and normal wave interaction with rock joints and has been

shown to be accurate when compared with the results for normally incident shear and normal waves.

Schoenberg (1980) integrated the wave equation of P and S-waves with arbitrary angles of incidence, expressing the joint dynamic response as a function of joint compliance. When the fracture is dry, the displacement discontinuity at the fracture is linearly related to stresses and fracture compliances. Later, Pyrak-Nolte et al. (1990a) expanded Schoenberg's solution to the case of discontinuities filled with viscous fluids (Kelvin and Maxwell models). In Pyrak-Nolte's formulation, the joint response is expressed by means of the dynamic stiffness, i.e. the inverse of joint compliance.

In addition, DDM has been established by considering a slip rate dependent deformational behaviour (e.g., White, 1965; Miller, 1977, 1978; Chen et al., 1993). In these studies, the shear stress has been assumed to be a nonlinear function of slip rate and frictional slip, which refers to the shear displacement discontinuity across the fracture. Miller (1977, 1978) developed an approximate method to simplify the nonlinear problem into a linear one and accordingly derived a solution for S-wave normal incidence at a slip interface with finite shear strength. He found that transmission and reflection coefficients are dependent on the ratio of the maximum shear stress of incident wave to fracture shear strength. At the same time, a new coefficient, termed absorption coefficient, has been applied to account of energy absorption at the fracture interface due to the fracture slip. For example, Zhao XB et al. (2006b) presented a study on S-wave attenuation across parallel fractures with the Coulomb slip behaviour, where the fracture shear behaviour is directly incorporated into the theoretical formulation and no simplification is involved. The effects of shear stress ratio, fracture spacing and number of fractures on wave attenuation are examined.

Jones & Whitter (1967) considered the effects of a flexible-bonded interface on wave propagation of an elastic plane wave. Two half spaces joined together at a plane interface by an elastic bond are assumed. In this study the displacements across the interface are taken as discontinuous. The relative displacement, between two sides of the interface, is function of the stress through the shear rigidity and the elastic moduli of the bonding material of the interface.

For this formulation the boundary conditions are as follows:

$$\begin{aligned} \tau_{zz}^{(1)} &= \tau_{zz}^{(2)} \\ \tau_{xz}^{(1)} &= \tau_{xz}^{(2)} \end{aligned} \quad \text{➔ continuity of stress}$$

$$\begin{aligned} u_z^{(1)} - u_z^{(2)} &= \frac{\tau_{zz} b}{E} \\ u_x^{(1)} - u_x^{(2)} &= \frac{\tau_{xz} b}{G} \end{aligned} \quad \text{➔ discontinuity of displacement} \qquad (2.2)$$

where:
$\tau_{zz}^{(i)}$ and $\tau_{xz}^{(i)}$ are the normal and the tangential stresses for each side of the interface;
$u_z^{(i)}$ and $u_x^{(i)}$ are the normal and tangential displacement along the interface;
E and G are respectively the Young modulus and the shear modulus of the bonding material of the interface;
b is the thickness of bond of the interface.

Kendall & Tabor (1971) analysed the effects of an incompletely-welded interface on wave propagation. They incorporated the discontinuity of displacements in the boundary conditions for solving the problem of a P-wave that impinges normally an incompletely-welded interface. This problem was also studied experimentally through ultrasonic wave transmission tests.

Schoenberg (1980) used the displacement discontinuity model to simulate the effects of a linear slip interface. The displacements are linearly dependent from the stresses by the fracture compliance that is the inverse of the fracture stiffness. The boundary conditions are:

$$\begin{aligned} \tau_{zz}^{(1)} &= \tau_{zz}^{(2)} \\ \tau_{xz}^{(1)} &= \tau_{xz}^{(2)} \end{aligned} \quad \rightarrow \text{ continuity of stress}$$

$$\begin{aligned} u_z^{(1)} - u_z^{(2)} &= c_y \tau_{zz} \\ u_x^{(1)} - u_x^{(2)} &= c_x \tau_{xz} \end{aligned} \quad \rightarrow \text{ discontinuity of displacement} \tag{2.3}$$

where, after the studies of Pyrak-Nolte (1988) and Pyrak-Nolte et al. (1987 and 1990a), c_x and c_z are the fracture compliances that are defined for a linear elastic fracture as:

$$c_x = \frac{1}{k_{ss}} \qquad c_z = \frac{1}{k_{nn}}$$

where k_{ss} and k_{nn} are the shear and the normal dynamic fracture stiffness.

Analytical expressions of reflection and transmission coefficients were obtained for a linear slip interface. Pyrak-Nolte et al. (1990a) using the same approach analyzed the effects on wave propagation of a linear elastic dry fracture and a fluid filled fracture. In this case the fluid in the fracture is modelled by using the rheological models of Kelvin and Maxwell. In these conditions the displacement-stress relation is given as a function of both the stiffness of the fracture and of the specific viscosity of the infilling fluid.

For each type of body wave interacting with a joint, as illustrated in Figure 2.1, DDM provides the amplitude and phase delay of each of the reflected and transmitted waves. For the general case, a 4x4 system of equations need be solved;

however, for normally incident waves ($\vartheta_1 = 0$ or $\phi_1 = 0$) no wave conversion occurs and the amplitudes of the reflected and transmitted waves on the frequency domain are obtained by:

$$R_1 = \frac{i}{-i + 2\left(\frac{k}{Z\omega}\right)} \qquad \left|R_1\right| = \left[\frac{1}{1 + 4\left(\frac{k}{Z\omega}\right)^2}\right]^{1/2} \tag{2.4}$$

(for compressional wave incidence)

$$R_1 = \frac{-i}{-i + 2\left(\frac{k}{Z\omega}\right)} \qquad \left|R_1\right| = \left[\frac{1}{1 + 4\left(\frac{k}{Z\omega}\right)^2}\right]^{1/2} \tag{2.5}$$

(for shear wave incidence)

$$T_1 = \frac{2\left(\frac{k}{Z\omega}\right)}{-i + 2\left(\frac{k}{Z\omega}\right)} \qquad \left|T_1\right| = \left[\frac{4\left(\frac{k}{Z\omega}\right)^2}{1 + 4\left(\frac{k}{Z\omega}\right)^2}\right]^{1/2} \tag{2.6}$$

(for compressional/shear wave incidence)

where:
R_1 and T_1 are the reflection and transmission coefficients for a single linearly deformable fracture;
ω is the angular wave frequency.

For compressional wave incidence, k denotes the dynamic normal stiffness of the fracture, and Z ($= \rho V_P$) the seismic impedance of the rock for compressional waves. For shear wave incidence, k denotes the dynamic shear stiffness, and Z ($=\rho V_S$) is the seismic impedance for shear waves.

The parameter that controls the amount of transmission and reflection of the compressive wave is the relation between the wave angular frequency and the joint dynamic or seismic specific stiffness K:

$$K = \frac{k}{Z\omega} \tag{2.7}$$

A change in the wave amplitude causes a phase shift that corresponds to a time delay t_g:

$$t_g = \frac{\frac{2k}{Z}}{\left(\frac{2k}{Z}\right)^2 + \omega^2} \tag{2.8}$$

In laboratory tests of joint-wave interaction the frequency content of the incident and transmitted waves and the impedance of the rock material can be measured directly. Therefore the only unknown variable in Equations (2.4) - (2.6), the dynamic stiffness k, can be determined. Finally, and given that the system is elastic, there is no loss of energy associated to the wave reflection and transmission:

$$\left|R_1\right|^2 + \left|T_1\right|^2 = 1 \tag{2.9}$$

Figure 2.2 displays the plots of transmission and reflection coefficients (Equations (2.4)-(2.6)) and the time delay (Equation (2.8)). When frequency is low in comparison to the specific stiffness, the wave is completely transmitted with no time delay, as this corresponds to a wave with zero frequency. On the other hand, when the frequency is high the wave is completely reflected.

Hence the studies of Schoenberg (1980) and Pyrak-Nolte (1988) are dependent on the ratio between the fracture stiffness and the product of the medium impedance and wave frequency. When the frequency is high and the stiffness is low the attenuation of the wave due to the fracture is high. If k approaches to infinity we obtain a reflection coefficient R_1 equal to zero and T_1 equal to 1. This situation represents a welded interface with total wave transmission. On the other hand, if the fracture stiffness approaches to zero, R_1 becomes 1 and T_1 equal to zero. In this case the fracture can be considered as a free boundary with total wave reflection.

The previous analytical solutions for a single fracture are verified with ultrasonic laboratory tests using specimens with artificial or natural fractures. Myer et al. (1985 and 1990) compared the theoretical results obtained with the theory of displacement discontinuity with ultrasonic laboratory tests on a single artificial fracture. In these tests the fracture is modelled as a partial contact with two steel cylinders separated by thin strips of lead. Pyrak-Nolte (1988) and Pyrak-Nolte et al. (1987 e 1990a) performed a large number of ultrasonic tests across a single fracture in dry or wet conditions and with high and low confinement and

temperature. The results of the tests are shown to be in good agreement with the analytical methods.

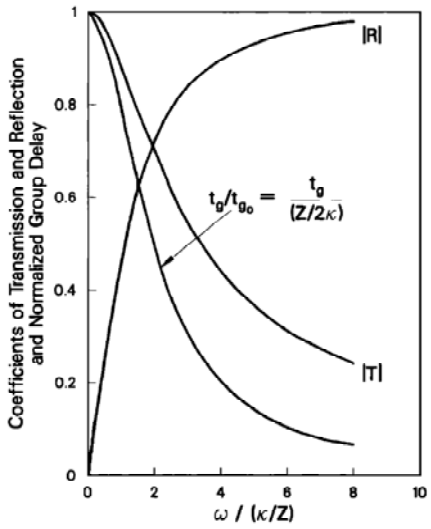

Figure 2.2 - Magnitude of transmission, reflection coefficients and normalized group time delay as functions of nondimensional frequency for P and S-waves normally incident to an elastic discontinuity (Pyrak-Nolte et al. 1990a)

Other experimental studies have been performed by Suarez-Rivera et al. (1992), who also analyzed the effects of clay-coated and fluid-filled fractures from a theoretical point of view. The interaction between various fluids (polar or non-polar) and the coating clay layers were taken into account in the theoretical analyses. The boundary condition introduced across the fracture is the discontinuity of particle velocities. The filling material is assumed to exhibit a viscoelastic behaviour according to the Kelvin and Maxwell models. In these tests the fractures are artificially built with fused silica disks coated with thin layers of sodium montmorillonite and filled with fluid. Also in this case the experimental results compare satisfactorily with the theoretical ones.

Based on the displacement discontinuity theories, Rossmanith et al. (1993) examined the interaction of incident stress waves with a pre-damage fracture. A theoretical solution was obtained for the wave transmission across the fracture by taking into account the pre-damage state of the fracture. Daehnke & Rossmanith (1997a,b) conducted parametric studies of the effects of fractures on wave propagation in terms of a wide variety of measurable fracture properties, such as the Joint Roughness Coefficient (JRC), the Joint Compressive Strength (JCS), stiffness, shear strength, fracture pre-stress and pre-damage.

Watanabe (1995) used Cagniard's technique (1962) to derive the analytical solutions for reflection and transmission of an impulsive elastic wave at a fracture (termed as jointed interface). His findings show that the incident P-wave, the reflected and transmitted amplitudes are affected only by the ratio between the normal and shear joint stiffness; while for the incident SH-wave, the reflected and transmitted amplitudes are not affected by the joint stiffness.

In addition to the above studies on P and S-wave propagation across a fracture, elastic interface wave propagation along a fracture has been examined by other authors from both theoretical and experimental points of view. Earlier studies were conducted by Murty (1975), who examined a loosely-bonded interface with a shear displacement discontinuity. Pyrak-Nolte & Cook (1987), Pyrak-Nolte et al. (1992 and 1996) and Roy & Pyrak-Nolte (1995 and 1997) performed laboratory measurements on the interface waves propagating along the fracture. Gu (1994) and Gu et al. (1995) used the plane wave analytical method to analyse the plane interface wave propagation along a fracture. They also conducted boundary element modelling to simulate the propagation of interface waves along the fracture generated by a line source. Both methods were used in combination with the displacement discontinuity model. Pyrak-Nolte & Nolte (1995) performed the wavelet analysis on seismic waveforms of interface waves propagating along a fracture. The analytical results on wave propagation velocity dispersion were compared satisfactorily with the prediction from the displacement discontinuity theories.

Gu et al. (1996) conducted a complete study on wave reflection and transmission and wave conversion upon plane wave incidence on a single fracture at arbitrary angles. In particular, these Authors studied the conversion between the interface wave, head wave, P-wave, SV-wave and SH-wave. The results obtained show that for some combinations of the fracture stiffness and the Poisson's ratio of the half-space, no reflection or transmission of a P-wave or SV-wave occurs at the fracture. In addition, the P interface wave and head wave are generated when a SV-wave is incident to a fracture, at and beyond a critical angle determined by Snell's law. In a limiting case, when the wave is incident parallel to the single fracture, a generalized Rayleigh wave is produced which propagates along the fracture. Nakagawa et al. (2000a) investigated the phenomenon of wave conversion from P-waves and S-waves to new waves with particle motions that are not present in the incident waves, for the cases of P-waves and S-waves incident normally to a fracture subjected to a shear movement.

Verweij & Chapman (1997) analysed the transmitted and reflected transient elasto-dynamic wave field at a fracture based on the displacement discontinuity theory, where the fracture is termed as linear slip interface. For both the SH and the P/SV wave incidence, the reflection and transmission coefficients of a fracture are solved. Their solution can provide the exact transmitted and reflected waves including the body wave, interface wave and head wave contributions.

Cai and Zhao (2000) and Zhao J. et al. (2006) used the method of characteristics for solving the wave propagation across a set of parallel joints, where multiple wave reflections were considered with an iterative method. Zhao and Cai (2001), Zhao XB et al. (2006a) used the method of characteristics to study P-wave attenuation across a single fracture with nonlinearly deformational behaviour, where the static BB (Barton Bandis) model was adopted. They found that not only initial normal fracture specific stiffness and wave frequency, but also incident wave amplitude and maximum allowable fracture closure have significant effects on wave attenuation. The method of characteristics was also used by Zhao XB et al. (2006b) for studying the effects of fractures with Coulomb slip behaviour on wave propagation.

On the other hand, efforts have been made to establish the displacement discontinuity boundary conditions by considering the slip rate-dependent shear behaviour of a fracture (e.g. White, 1965; Miller, 1977 and 1978; Chen et al., 1993). In these studies, the shear stress was assumed to be a nonlinear function of frictional slip (discontinuity in shear displacement across the fracture) and slip rate of the fracture, which define the displacement discontinuity boundary conditions as:

$$\begin{aligned} \tau_{zz}^{(1)} &= \tau_{zz}^{(2)} \\ \tau_{xz}^{(1)} &= \tau_{xz}^{(2)} \end{aligned} \quad \Rightarrow \text{ continuity of stress}$$

$$\begin{aligned} u_z^{(1)} - u_z^{(2)} &= \frac{1}{k_{nn}} \tau_{zz} \\ \tau_{xz} &= f\left\{\left(u_x^{(1)} - u_x^{(2)}\right), \left(\dot{u}_x^{(1)} - \dot{u}_x^{(2)}\right)\right\} \end{aligned} \quad \Rightarrow \text{ discontinuity of displacement} \tag{2.10}$$

where:
$\dot{u}$ is the slip rate;
f is the nonlinear function of stress-shear deformation relation.

If the form of f is determined, the wave equation can be solved for wave reflection and transmission across the fracture. However, due to the mathematical difficulties in handling the nonlinear governing equation (last of Equations (2.10)), the derivation of analytical solutions for wave reflection and transmission is usually difficult. A simplified method is to consider the fracture deformational behaviour as linear. For example, Miller (1977 and 1978) used an approximate analytical approach to simplify the nonlinearity into linearity and accordingly derived a solution for normally incident harmonic S-wave. In this approach, the nonlinear term in the governing equations is replaced by a combination of linear terms in such a way that the mean square difference between the resulting linear and the original nonlinear systems is minimized for all harmonic solutions. The parameters in the linear terms depend generally on the nature of the solution of the linearized system.

Miller (1977 and 1978) applied three different constitutive relations of shear behaviour, including Loeb friction model (1961), Fortsch friction model (1956) and Coulomb friction model with kinematic locking. These studies showed that the reflection and transmission coefficients are dependent upon the ratio between the amplitude of the incident stress wave and a characteristic frictional stress associated with each model. The high value of this stress ratio results in a small magnitude of the transmission coefficient, and in turn, high wave attenuation. It seems however that very few studies have been conducted to establish the displacement discontinuity boundary conditions by considering the nonlinear normal behaviour (closure) of the fracture.

Compared to wave attenuation across a single fracture, wave attenuation across multiple parallel fractures is more complex due to multiple wave reflections between fractures. Theories of wave propagation in continuous multi-layered media containing welded-interfaces have been well developed (e.g. Rytov, 1956; Brekhovskikh, 1960; Treitel & Robinson, 1966; O'Doherty & Anstey, 1971; Schoenberger & Levin, 1974; Spencer et al., 1977; Kennett, 1983; Banik et al., 1985; Bedford & Drumheller, 1994). In particular, Watanabe & Sassa (1989 and 1995) applied the communication matrix method, originally developed for multi-layered media, to include the effects of internal multiple reflections on wave propagation across fractures assumed as thin low-velocity layers. However, the methods may not be entirely applicable to the multi-fractured rock masses because of the assumed displacement discontinuities across the fractures.

Some researchers represented the fractures with the displacement discontinuity boundary conditions to study the wave propagation through multiple parallel fractures (e.g. Schoenberg, 1983; Pyrak-Nolte et al., 1990b; Coates & Schoenberg, 1995; Yi et al., 1997; Nihei et al., 1999; Nakagawa, 2000b). However, since the displacement discontinuity theory analyses wave attenuation across fractures based on explicit reflections and transmissions at individual fractures, it is often difficult to explicitly determine the complex process of superposition of the multiple reflected and transmitted waves between many fractures. A real case without the presence of multiple reflections is that of incident waves parallel to the fractures, which are captured within the parallel fractures as channelling waves (Nihei et al, 1999).

In the past, for non-parallel incidence, a simplified method for analysing wave attenuation across multiple fractures was to ignore the multiple reflections as short wavelength approximation. By ignoring the multiple reflections, Pyrak-Nolte et al. (1990b) proposed a simple formula for calculating the magnitude of transmission coefficient ($|T_N|$) for wave incidence normal to the multiple parallel fractures with identical stiffness:

$$\left|T_N\right| = \left|T_1\right|^N \tag{2.11}$$

where:
$|T_1|$ is the magnitude of the transmission coefficient for normal incident wave transmission across a single fracture;
N is the number of fractures.

The above method has been shown to predict wave attenuation satisfactorily based on laboratory measurements of ultrasonic wave transmission across multiple parallel fractures by Hopkins et al. (1988), Pyrak-Nolte et al. (1990b) and Myer et al. (1995 and 1997). The same method was also used successfully in field seismic cross-hole tests of wave transmission across parallel vertical joints in a basalt rock mass by King et al. (1986) and Rezowalli et al. (1984). The laboratory measurements by Hopkins et al. (1988) and Myer et al. (1995) indicate that $|T_N|$ increases from $|T_1|^N$, when the fracture spacing is very small relative to the wavelength.

Based on an exact dispersion equation for wave propagation across multiple parallel fractures of equal spacing, Nakagawa et al. (2000b) found that the Equation (2.11) is valid only when the first-arriving pulse is not contaminated by multiple wave reflections. These findings imply that the Equation (2.11) is not entirely applicable, if the effects of multiple reflections are significant due to the close spacing of fractures.

To avoid the difficulty in determining the complex multiple reflections between individual fractures, the equivalent medium theories have been used for analysing wave propagation across multiple parallel fractures in a long wavelength limit (e.g. White, 1983; Schoenberg & Muir, 1989; Schoenberg & Sayers, 1995; and others). Frazer (1995) presented theoretical studies on SH-wave slowness and attenuation across multiple parallel fractures without the assumption of the long wavelength limit.

Schoenberg (1983) and Schoenberg & Douma (1988) combined the equivalent medium method and displacement discontinuity method to analyse the wave reflections from a periodically stratified medium with slip interfaces (displacement discontinuities). The medium containing sets of parallel displacement discontinuities is represented as an equivalent homogeneous transversely isotropic medium functioning as a "group element" of displacement discontinuities. The wave reflection coefficient for this "group element" of displacement discontinuities was then derived by setting the displacement discontinuities boundary conditions in the wave equation.

Coates & Schoenberg (1995) proposed a finite difference scheme to model the discontinuity displacement boundary conditions of planar faults and fractures (termed as slip interface conditions) by setting them parallel to the finite difference grid lines. However, this approach is more difficult for arbitrary non-planar fault surfaces. For this case, the equivalent medium theory is introduced to model the material behaviour in the cells of the finite difference grid intersected by the fault.

Finally, the DDM can be applied to model the effects of plane fractures with large extent, small thickness and small spacing of asperities relative to the

wavelength, on wave propagation across a fractured medium. The fundamental parameter for modelling a fracture is the fracture compliance that is function of the fracture stiffness and/or of the specific viscosity of the infilling material.

2.3 Equivalent Medium Method (EMM)

The EMM has been used to analyze the effects of pores, impurities, inclusions or micro-cracks on stress wave propagation in porous or cracked media. It has also been used to study the effects of the macro-fractures with high density of distribution in rock masses. The intact material (for example rock) including the fractures and pores is modelled as a continuous, homogeneous and isotropic equivalent medium with effective properties. With these assumptions, a stress wave propagates through a cracked and porous medium in the same manner as through an equivalent continuous, homogeneous and isotropic medium.

The effective properties of the equivalent medium are used for evaluating the global effects of pores and cracks on the attenuation of velocity and amplitude of the wave that crosses the medium. An effective elastic modulus E_e is generally introduced to consider the effects of pores and cracks on the velocity of wave propagation. On the other hand the quality factor Q and the attenuation coefficient α are used to represent the attenuation characteristics. Q and α are defined by the appropriate real and imaginary components in the effective elastic moduli or determined directly from the basic wave equation of the equivalent dissipative medium by assuming viscous attenuation mechanisms. The quality factor is inversely proportional to the fractional decrease in wave energy density per cycle of harmonic loading. For $Q > 10$, Q and α are related by $Q = \pi/(\alpha\lambda)$, where λ is the wave length in the medium. The viscosity of a cracked medium is generated by the viscosity of the base material and the filling fluid, the friction between the grain surfaces and the existence of cracks.

The most relevant initial study of the effects of the pores on wave propagation in a fluid saturated porous solid was performed by Biot (1956a, b). Biot introduces a complete theory for evaluating the effects of parallel cylindrical saturated pores with fluid on P-wave propagation in the direction of these pores. Wave attenuation is produced by the viscous dissipation due to the fluid in the pores and the expression of the attenuation coefficient function of the wave frequency is defined. Biot's theory was subsequently modified and extended by many authors. For example, McCann & McCann (1985) extended this theory to the case of pores with a certain size distribution in liquid-saturated porous sediments and derived the attenuation coefficient of linear variation with wave frequency ranging from 10 *kHz* to 2.25 *MHz*.

The evaluation of the stress and strain fields inside and outside an ellipsoidal inclusion embedded in an isotropic solid was performed by Eshelby (1957), who

defined the effective elastic moduli based on energy considerations. His method was extended by Nur & Simmons (1969) and Nur (1971) who evaluated the effective elastic compliance of rocks with an anisotropic distribution of cracks and defined the anisotropy in the wave velocity by assuming a pressure dependence of crack parameters. Using a similar method to that proposed by Eshelby (1957), Kinoshita & Mura (1971) studied the effects of the inclusions on the elastic properties of anisotropic media.

Walsh (1965a, b) developed an Excess Energy Method to compute the effective elastic moduli and the compressibility of cracked materials under the assumption of no stress field interactions between cracks. The solution obtained is accurate only for low crack density. Subsequently, also Walsh (1966) presented a method for defining the quality factor and the attenuation coefficient from effective elastic constants and friction coefficient of crack surfaces in contact. The frictional dissipation at crack faces produces the attenuation mechanism. Toksoz et al. (1979) presented an experimental laboratory method for measuring the attenuation of a seismic wave and for defining the seismic quality factor of cracked materials.

An important contribution on the equivalent medium theories for defining the effective moduli was given by O'Connell & Budianski (1974), who evaluated the interaction between highly-concentrated cracks. These Authors proposed a self-consistent method (SCM) to obtain the elastic moduli of a solid with randomly oriented ellipsoidal cracks and to examine the wave propagation velocities under dry and saturated conditions. This method allows one to predict a faster decrease in the effective moduli with respect to that obtained with the non-iterative method proposed by Walsh (1965a, b).

In the following years, Salganik (1973) presented a modified SCM for estimating the effective elastic moduli from the crack density and O'Connel & Budianski (1977) used the same method to analyse wave attenuation based on the effective viscoelastic properties of a fluid-saturated cracked solid. The wave attenuation was regarded due to liquid squirting in the fully saturated cracks.

Many other authors improved the SCM. For example, Zimmerman (1984a) verified if the method modified by Salganik (1973) can correctly predict the effective elastic moduli of a solid containing pores and spherical inclusions. He also (Zimmerman, 1984b) derived an analytical expression of the effective moduli of a cracked solid versus the crack density. Subsequently, based on the field measurements obtained by King (1966) and Johnston (1978), Zimmerman & King (1985) found that Salganik's method is correct.

Nishizawa (1982) developed a numerical approach applicable for evaluating the seismic velocity anisotropy in transversely isotropic media containing dense aligned cracks. This numerical scheme is based on the SCM. Then, Xu et al. (1990), starting from the numerical scheme of Nishizawa (1982), elaborated a new model for evaluating the effective elastic constants and the cracks closure under pressure in an initially transversely isotropic solid containing aligned cracks. Ultrasonic wave velocities laboratory measurements were used by King & Xu (1989) for the

experimental verification of the previous numerical approach. Smyshlyaev et al. (1993) applied the SCM for studying the wave propagation in a matrix-crack composite.

Many studies are reported in the literature on the determination of the elastic effective moduli from crack shapes, structures and distribution. Chatterjee & Mal (1978) presented a method for computing the elastic moduli of a cracked medium based on the crack shape and distributions. Subsequently Crampin (1984) gave a definition of the effective elastic moduli for rock masses containing preferred oriented cracks. A simple method for defining the effective elastic constants of cracked solids based on arbitrary crack orientation statistics was also introduced by Sayers & Kachanov (1991).

The wave attenuation phenomenon in porous or cracked media is interpreted with different types of physical mechanisms. Normally, the viscous dissipation of the base material and the filling fluid is considered to be the main mechanism of wave attenuation. Mavko & Nur (1975) and O'Connell & Budianski (1977) proposed the mechanism of squirting flow to explain wave attenuation in fully saturated cracked rocks. Mavko & Nur (1979) suggested the mechanism of bubble movement in partially saturated cracks for partially saturated rocks.

Johnston (1978) carried out a comprehensive study on the attenuation of seismic waves in dry and saturated cracked rocks, where the wave attenuation was attributed to frictional sliding at grain boundaries and crack faces. Johnston & Toksoz (1980) carried out laboratory studies on the ultrasonic wave attenuation in dry and saturated cracked rocks subjected to pressure, and the wave attenuation was interpreted in terms of friction at grain boundaries and crack faces.

The same interpretation on wave attenuation was adopted by Murphy (1982a,b and 1984) in the experimental studies of wave attenuation in cracked rocks. The experimental results obtained by him were later compared with the theoretical predictions due to Mochizuki (1982) based on a modified Biot's model (1956a,b). Discrepancies between the experimental results and theoretical predictions were found within the typical range of seismic frequencies. The reason seems that the attenuation mechanism involved in the experiments is different from that assumed in the theoretical predictions. Miksis (1988) investigated the wave attenuation arising from contact line movement between pores and contained fluid, in addition to the fluid viscous dissipation.

Equivalent medium models have also been applied for analyzing the effects of a set of fractures on seismic wave propagation in rock masses. White (1983) studied the effects of a set of parallel fractures on wave propagation by using the effective moduli of the fractured rock mass. This author developed an equivalent medium model for computing the effective moduli of the global multi-fractured rock mass from the stiffness of the single fractures and the fracture spacing. Effective elastic moduli of the rock masses are computed based on different attenuation mechanisms and these moduli are used to relate velocity and attenuation through elastic-dynamic equations.

White (1983) introduced complex moduli for a dissipative medium. Two independent complex moduli are required for isotropic material. The number of complex moduli increases with the degree of anisotropy (e.g. five complex moduli are required for a transversely isotropic medium). A result of this approach is that strain is out of phase with respect to stress by an amount which is determined by the ratio of the real to imaginary parts of the modulus. The inverse of this phase angle is commonly referred to as quality factor (Q) which can be used to characterize the medium anelasticity.

Schoenberg & Muir (1989) incorporated the effects of multiple sets of parallel fractures in finely layered anisotropic media by representing them as group elements. These considerations allow manipulating the fractures and layered anisotropic rocks in a consistent and uniform manner. Schoenberg & Sayers (1995) studied the effects of multiple sets of parallel fractures with spacing smaller than the wave length. A method for including the effects of fractures on seismic wave propagation was proposed by writing the effective compliance tensor of the fractured rock mass as the sum of the compliance tensor of the background rock material and the compliance tensor for each set of parallel fractures.

Recently, Li et al. (2010) proposed an equivalent viscoelastic medium model, which is composed of a viscoelastic medium model and the concept of virtual wave source (VWS). By using continuum mechanics concepts and an equivalent viscoelastic model wave propagation was studied across the rock mass by solving an explicit wave propagation equation, so as to simplify the problem. This method will be analyzed in Chapter 5.

The equivalent medium theories have been applied for studying the effects of pores, cracks and fractures on wave propagation and for defining the effective elastic constants of the porous cracked media. The methods for computing the effective constants are based on the geometry, structures, concentration and distribution of pores and cracks and the fluid filling the pores and cracks.

Many mechanisms have been introduced to simulate the wave attenuation due to the pores and cracks. In this way, many methods have been developed. These methods have been based on different assumptions on the wave attenuation mechanisms and on the viscosity, friction, squiring flow, bubble movement and contact line movement.

These methods can be grouped into the intrinsic mechanisms of attenuation involving internal energy dissipation. A detailed description of these mechanisms has been given by Crampin (1981) and Xu & King (1990). A discussion of the wave attenuation mechanisms in view of wave frequency ranges was presented by Johnston et al. (1979). The conclusions of these studies are that the frictional dissipation is dominant in the range of ultrasonic frequencies and that fluid flow plays a second role in the frictional dissipation while the fluid squirting flow exists for lower frequency ranges.

2.4 Wave Scattering Method (WSM)

The WSM has been used to study the effects of the micro-cracks on wave propagation velocity and amplitude attenuation in cracked media. The stress waves propagating through cracks are considered to be uniformly scattered by the cracks, provided that the crack size is small compared to the wave length and the crack concentration is diluted so that no interactions of wave scattering occur between individual cracks.

Early in 1945, Foldy (1945) developed a multiple scattering theory of waves at cracks in a defective solid. The same theory was also proposed by Lax (1952). Considering the effects of wave scattering at the crack faces, Garbin & Knopoff (1973 and 1975a, b) presented methods for analysing the wave velocity variations with the incident angle and the polarization of the waves in a material permeated by a random distribution of voids (stress-free), circular cracks, and liquid-filled cracks. In these studies, the elastic shear and compression moduli were determined for the cracked material to account for the velocity variations.

Kuster & Toksoz (1974a, b) derived a theoretical solution for wave scattering at inclusions in two-phase media and examined the wave dispersion and attenuation characteristics. The theoretical model was further verified with laboratory tests.

Waterman (1976) presented a matrix theory of elastic wave scattering at cracks for investigating the wave propagation in cracked media. Chatterjee et al. (1980) examined the wave propagation velocity and amplitude attenuation variation at parallel thin penny-shaped cracks filled with a viscoelastic fluid. This study considered both the effects of wave scattering at cracks, with a technique similar to that used by Garbin & Knopoff (1973 and 1975a, b), and the effects of viscous attenuation caused by the filling fluid. It was concluded that the effects of the fluid viscosity is more significant than that of scattering at low frequencies.

Hudson (1980 and 1981) proposed a "method of smoothing" in order to calculate the overall elastic constants and examined the wave velocity and attenuation in cracked materials by taking into account the wave scattering effects. Compared to the study of Chatterjee et al. (1980), Hudson's method (1981) considers only the wave scattering effects, and also predicts the frequency dependence of attenuation caused by wave scattering as derived by Chatterjee et al. (1980). In addition, Hudson showed that the attenuation coefficient due to wave scattering is proportional to the crack density and to the third power of the ratio between the mean crack radius and the wavelength.

Hudson (1986 and 1990), Hudson & Knopoff (1989), Peacock & Hudson (1990), and Hudson et al. (1996) extended the method proposed by Hudson (1980) to the cases of various orders of crack density or multiple sets of cracks aligned in different directions. Furthermore, Hudson (1988) modified the analytical expressions obtained in 1981 to evaluate the wave attenuation across partially

saturated ellipsoidal cracks. The results show that the situation where cracks are partially liquid-filled is different from the limiting cases of either dry or fully liquid-filled cracks, since the liquid is forced to flow laterally inside the cracks.

Laboratory experiments have been carried out by many researchers to measure the wave propagation velocity and amplitude attenuation in the cracked media, where comparisons between the experiments and scattering theory were made. For example, Xu & King (1990) carried out laboratory tests of ultrasonic wave propagation through slate specimens before and after cracking. The testing results of wave attenuation were consistent with the theoretical predictions based on the Hudson's scattering model (1981). In addition, the observations due to Xu & King (1990) indicated that the quality factor (Q), representing wave attenuation characteristics of the cracked materials, is more sensitive to the presence of cracks than the wave propagation velocity.

Ass'ad et al. (1993) conducted a laboratory study of shear wave scattering at randomly distributed cracks, and compared the results obtained with Hudson's theory (1981). It was shown that the experimental results and the theoretical predictions agreed well for the situation of crack density up to 7%. However, discrepancies were observed at relatively higher crack densities (10%). Such discrepancies were explained by the additional energy dissipation due to the absorption of rubber inclusions used in the experiments.

With the development of damage mechanics, some researchers used the damage mechanics-based method to evaluate the scattering effects of aligned cracks on the dynamic behaviours of rock masses and the wave scattering phenomenon in cracked rock masses (e.g. Han et al., 1986; Han, 1995).

The effects of wave scattering at cracks on wave attenuation have been examined in terms of reflection and transmission coefficients of a single or a periodic distribution of cracks over a plane. A relatively simple case of wave scattering by a penny-shaped crack has been analysed by Mal (1970), Martin (1981), Achenbach & Norris (1982) and Martin & Wickham (1983). Furthermore, Bostrom & Eriksson (1993) examined the wave scattering by two penny-shaped cracks.

Baik & Thompson (1984) determined the reflection coefficient of an imperfect bond composed of a planar distribution of cracks. Angel & Achenbach (1985a, b) investigated the elastic wave scattering by a periodic array of cracks for normal an oblique incidence of waves, respectively. In their study, the reflection and transmission coefficients of a planar periodic array of cracks were analytically and numerically solved, and the balance of energy rates was checked.

Further efforts to examine the wave scattering in terms of reflection and transmission coefficients of cracks were made for a periodic array of spherical cavities (Achenbach & Kitahara, 1986), a doubly periodic array of cracks (Angel & Achenbach, 1987), a multiple periodic arrays of cracks (Achenbach & Li, 1986a), a periodic array of inclined screens (Achenbach & Li, 1986b), and a periodic array of inclined cracks (Mikata & Achenbach, 1988).

The complexities of wave scattering by arbitrary distributions of cracks were examined by Piau (1979), Sotiropoulos & Achenbach (1988a, b), Zhang & Gross (1993) and Eriksson et al. (1995). Since analytical solutions for more complicated crack distributions are often difficult to derive, numerical methods such as the boundary element method have been used (e.g. Angel & Achenbach, 1985a, b and 1987; Achenbach & Li, 1986a, b; Sotiropoulos & Achenbach, 1988a, b; Coutant, 1989; Achenbach & Zhang, 1990; Hirose & Kitahara, 1991).

A first attempt to consider the coplanar crack distribution over a bounded region (with a thickness) in space rather than in a plane was made by Achenbach & Zhang (1990). In this study, the reflection and transmission coefficients were expressed in terms of integrals over a number (N) of cracks, and the variation of these coefficients with frequency, relative region thickness and incident angle was examined. Lin & Keer (1987) and Budreck & Achenbach (1988) analysed the wave scattering at three-dimensional planar cracks.

The above studies on wave scattering are based on the linear model of scattering. That is, the wave scattering is modelled based on the spring contact condition of cracks. On the other hand, studies on wave scattering at cracks with nonlinear contact conditions have been conducted (e.g. Morris et al., 1979; Achenbach & Norris, 1982; Hirose & Achenbach, 1993; Smyshlyaev & Willis, 1994; Capuani & Willis, 1997). In these studies, the nonlinear scattering is generally considered to arise from the nonlinear process of interaction of crack faces in contact.

Morris et al. (1979) conducted laboratory measurements of nonlinear scattering by surface ultrasonic waves in an aluminium alloy subjected to fatigue loads. They observed an important phenomenon of higher harmonics of scattered waves at cracks caused by the nonlinear relation between the crack face traction and crack closure. Achenbach & Norris (1982) analytically investigated the wave reflection and transmission by an infinite flaw plane, where the interaction between the crack faces was modelled by a nonlinear relation between the crack-face tractions and the crack-opening displacements.

Hirose & Achenbach (1993) used a time-domain boundary element method to numerically examine the nonlinear scattering problem at a penny-shaped crack subjected to a longitudinal incident wave. In this study, the contact-boundary conditions on the crack faces are of no overlap and no friction, which give rise to a boundary-type nonlinear problem of wave scattering. The higher harmonics phenomenon in the far field due to the nonlinear crack face contacting conditions was also described.

A comparative study of linear and nonlinear scattering at cracks was conducted by Smyshlyaev & Willis (1994), based on the quasi-static approximation for the displacement jump across the crack. In their study, the linear scattering results from the assumption that either the crack faces never come into contact, or they remain in permanent gliding contact; whereas, nonlinear scattering arises when a unilateral constrain is introduced to crack deformation, corresponding to the

opening of the crack under tension, closure under compression and frictionless slip under shear.

Capuani & Willis (1997) presented theoretical formulations for the transient nonlinear response of a flat crack. Explicit formulae were derived for the crack subjected to one-dimensional incident P-waves. In addition, numerical results were obtained for the crack subjected to various incident waves, by introducing a unilateral constrain to describe the nonlinear interaction between frictionless crack faces.

To sum up, the wave scattering theories are suitable for analysing the wave attenuation across the micro-cracks of smaller sizes compared to wave length. The crack shape, crack density and distribution are very important parameters in the wave scattering formulations. Apparent wave attenuation due to the scattering of energy at cracks is considered as the principal attenuation mechanism. The wave attenuation is evaluated in terms of the reflection and transmission coefficients of a distribution of cracks. If cracks are filled with liquid, intrinsic attenuation can be taken into account based on the real energy loss - viscous dissipation by the filling liquid. The quality factor (Q) and wave attenuation coefficient (α) can also be derived to quantify the wave attenuation due to both energy scattering and dissipation.

2.5 Comparison of the above methods

Three different approaches have been analysed for evaluating the effects of micro-fractures or fractures on wave propagation.

The equivalent medium methods have some limitations. The first negative aspect of this approach (White 1983; Schoenberg and Muir 1989; Pyrak-Nolte et al. 1990b; Zhao J. et al. 2006) is due to the simplification of the discontinuous rock mass to an equivalent medium. Moreover the discreteness of wave amplitudes attenuated at individual fractures is lost.

Another limitation is that the frequency-dependent amplitude and velocity variations with respect to fracture orientation is not introduced, due to reflection losses across and wave channelling along fractures. The reason is that the equivalent medium approaches are usually based on static approximation (i.e. zero-frequency). This problem has been addressed by Pyrak-Nolte (1988), Pyrak-Nolte et al. (1990b), Frazer (1990) and Coates & Schoenberg (1995).

In particular, Yi et al. (1997) compared the two approaches by carrying out finite difference modelling of seismic wave propagation across multiple parallel fractures, where the displacement discontinuity model and the equivalent transversely-isotropic model for fracture representation are both incorporated in the numerical code. It is shown that the equivalent medium model underestimates the amplitude anisotropy and never predicts frequency-dependent wave propagation

velocity. By contrast, the displacement discontinuity model considers explicitly the effects of individual fractures by representing them as discontinuity displacement boundary conditions in the wave equation, and takes into account the frequency-dependent amplitude attenuation across the fractures.

The conditions of the applicability of displacement discontinuity theories have been discussed in past studies (e.g. Myer et al., 1985; Pyrak-Nolte, 1988; Pyrak-Nolte et al., 1990a,b; Gu, 1994; and others). Considering a planar fracture as a planar collection of collinear micro-voids and asperities in contact, Nolte et al., (2000) paid attention to the limit of applicability of displacement discontinuity. Their study showed that the displacement discontinuity theories are valid only if the spacing between the asperities is much smaller than wave length, in addition to the conditions that the fracture extent is larger and the thickness is smaller than the wavelength.

If the asperity spacing is comparable to the wave length, resonant scattering may occur at the voids between the asperities, resulting in the invalidity of the displacement discontinuity theories. Moreover, Nolte et al. (2000) found that in case the distribution of finely distributed asperities is strongly inhomogeneous, where the correlation length describing the fluctuation in the fracture stiffness may be comparable to or larger than the average asperities spacing, then even if the individual asperity separations are smaller than the wave length, resonant scattering possibly occurs and the displacement discontinuity theories are not applicable.

The equivalent medium method cannot work well in representing media where the fractures are relatively large and sparsely spaced (with spacing of the order of, or larger than, a seismic wavelength) (Pyrak-Nolte et al. 1990b).

The wave scattering theories are only applicable to micro-cracks. At microscopic scale, a fracture appears as a planar collection of void spaces and asperities (asperities refer to contacts between two fracture surfaces). The effects of micro-cracks are analysed from the uniform wave scattering as a distribution of collinear cracks, and represented by the wave reflection and transmission coefficients in terms of integrals over the N numbers of collinear cracks in a plane.

The point of view taken in these theories can be thought of as a middle ground between the equivalent medium theories and in the displacement discontinuity theories. That is, the scattering theories consider individual cracks and contact characteristics between the crack faces, but derive the wave reflection and transmission coefficients of a collection of cracks (such as a periodic array of cracks distributed over a plane, and a thick region of collinear defects and cracks distributed over a space).

The wave scattering model is established in a long wave length limit, i.e. the crack size is small with respect to the wave length. This assumption is true for micro-cracks contained in rock materials, but may be inappropriate for macro-fractures that are dominant in fractured rock masses, resulting in the limited applicability of the scattering theories to the fractured rock masses. In addition,

solutions to the wave scattering problems are derived usually under the assumption of weak concentration of cracks (no interaction between the adjacent cracks), which also limits the use of these theories for densely-cracked materials.

Finally, the displacement discontinuity theories can be applied for simulating the effects of fractures or rock joints on wave propagation if they are planar, large in extent and small in thickness compared to the wavelength. These are good for obtaining the effects of fractures in the far field.

The equivalent medium theories are particularly suitable for the analyses of the global effects on wave propagation of densely-concentrated micro-cracks or micro-fractures. Moreover these theories are applicable to analyse wave propagation in highly fractured medium.

The previous methods have advantages or disadvantages. Depending on the problem to be solved (e.g. scale, type and extension of fractures, fracture behaviour, type of input signal, etc.), a specific method can be chosen and adopted.

2.6 Numerical Methods

Many numerical methods are today available for studying rock engineering problems. These methods are very useful for solving more complex real problems that with the previous approaches cannot be solved. In this paragraph we will summarize the main numerical methods available:

- Finite Element Method (FEM);
- Boundary Element Method (BEM);
- Discrete Element Method (DEM);

2.6.1 Finite Element Method (FEM)

The Finite Element Method is still one the most popular numerical methods in engineering. It has been applied to the solution of a large number of problems in different fields. Its popularity, particularly for load-deformation problems, largely depends on the fact that it is very appealing to engineers. They are able to relate it to a large extent to the background of structural mechanics as the physical meaning of the steps of calculations is relatively transparent. FEM is extremely popular with geotechnical engineers. Its strength lies in its generality and flexibility to handle all types of load, sequence of construction and installation of supports.

The method essentially involves dividing the body into smaller elements of various shapes held together at the nodes, which are corner of elements. In general, the greater the number of elements used to model the problem and the better approximation to the real solution is obtained. Displacements at the nodes are

treated as unknowns and are calculated. Stresses are computed at one or more integration points inside each of the elements. Each element can have different material properties.

The major disadvantage of the method is that considerable effort is required in preparing data for a problem. This is particularly crucial in 3D problems and has led to "mesh generation" programs. These programs produce the input data required for the Finite Element program. Still considerable effort is needed in starting up the problem. FEM is also expensive in computer time. A large set of simultaneous equations has to be solved to obtain solutions, especially when the stress-strain relationship is nonlinear.

To model the rock fractures, Ngo & Scordelis (1967) proposed a two-node linkage element for rock joint. As an improvement, based on the lumped interface, Goodman et al. (1968) proposed a joint element in FEM. The Goodman joint element is a linear line element suitable for 2D analysis with four nodes and no thickness. The stiffness matrix for the joint element is derived in the same way as for the regular finite element. Mehtab & Goodman (1970) extended the formulation of the Goodman joint element to 3-D solution. Goodman (1976) presented another version of the joint element capable of modelling material non-linearity.

2.6.2 Boundary Element Method (BEM)

The Boundary Element Method (BEM) is becoming increasingly popular. The main reasons for this growth are: reduced set of equations, smaller amount of data, proper modelling of infinite domains, no interpolation errors inside the domain and valuable representation for stress concentration problems. BEM can be of as many different types as the domain methods, ranging from simple techniques such as indirect methods to the more versatile direct formulations.

Kupradeze (1965) established the foundations of the indirect boundary element method adopting the Kelvin fundamental solution to solve elastostatic problems. Watson, applying the same technique, has obtained a numerical solution for a pre-stressed concrete pressure vessel of a nuclear reactor treating the structure as a thick shell. The starting point of the direct formulation is due to Rizzo in 1967. His work, which presented the solution of the 2D elastostatic problem, was extended to the 3D case. The direct boundary element methods, which are more reliable than indirect techniques, are based on adopting the real physical variables of the problem as the unknown of the system.

In this method only the surface of the rock mass to be analyzed needs to be discretized, i.e. divided into smaller patches. BEM differs from FEM by the fact that approximations only occur on the boundary of the problem domain. The solution inside the domain will always satisfy the equations of equilibrium and compatibility exactly. For 2D solutions, line elements at the boundary represent the problem, while for fully 3D problems, surface elements are required. The data

preparation is relatively simple. However, the computer program is not so transparent.

Whenever there is a change of material properties, the surface defining the separation has to be discretized. Thus, if there are a number of layers of different materials, data preparation can still become complex. BEM appears to be a very efficient method for homogeneous, linear elastic problems, particularly in 3D conditions. For complex nonlinear material laws with a number of sets of materials, advantages of the method are considerably diminished. The matrices of equations arising in this method are not banded and symmetric as for FEM but are fully populated. Thus, though the number of equations to be solved is considerably reduced, computation time does not reduce in the same proportion. The method makes use of certain closed form relations of what may be called "elementary" problems. These solutions frequently contain trigonometric and logarithmic terms, which slow down the computations.

Recognizing the advantages and disadvantages of FEM and BEM, many researchers have combined the two methods. The coupled FEM/BEM method in which for a certain region, close to an opening or some other area of interest, FEM discretization is used, while for the remaining area BEM discretization is adopted.

2.6.3 Discrete Element Method (DEM)

A discrete element method (DEM), also called distinct element method, is any family of numerical methods for computing the motion of a large number of particles of micrometre-scale size and above. Though DEM is very closely related to molecular dynamics, the method is generally distinguished by its inclusion of rotational degrees-of-freedom as well as stateful contact and often complicated geometries (including polyhedra). With advances in computing power and numerical algorithms for nearest neighbor sorting, it has become possible to numerically simulate millions of particles on a single processor. Today DEM is becoming widely accepted as an effective method of addressing engineering problems in granular and discontinuous materials, especially in granular flows, powder mechanics, and rock mechanics.

The various branches of the DEM family are the Distinct Element Method proposed by Cundall in 1971, the Generalized Discrete Element Method proposed by Hocking, Williams and Mustoe in 1985, the Discontinuous Deformation Analysis (DDA) proposed by Shi in 1988 and the finite-discrete element method concurrently developed by several groups (e.g., Munjiza and Owen).

In the following we focus on three DEM methods that are widely used in engineering that are the Distinct Element Method (DEM), the Bonded Particle Model (BPM) and Discontinuous Deformation Analysis (DDA). A more comprehensive description of the Distinct Element Method will be given in Chapter 8.

Bonded Particle Model (BPM)

In the Bonded Particle Model (BPM), based on the Discrete Element Method - DEM (Cundall and Strack, 1979), the response of rock under a number of situations can be simulated by assemblies of a large number of circular or spherical particles with finite radius bonded by ball - ball contacts.

The relation between the model properties (assembly arrangement, particles' radius and contact characteristics) on a microscopic level and the rock macroscopic properties such as compressive strength or Young's modulus is not direct, as there is no complete theory to relate micro and macroscopic properties.

The constant and steady growth of computational capacities and a number of very successful applications of BPM to model complex rock behaviour has promoted the utilization of this method (e.g. Potyondy et al. 1996; Potyondy and Cundall, 2004). Not much attention, however, has been dedicated to the modelling of rock dynamic behaviour using particle models.

In the field of geophysics, some authors have used particle codes to model wave propagation in large scale, from hundreds of meters to tens of kilometres (Toomey and Bean, 2000; Abe et al., 2004). However, the model in question employed regular assemblies of particles, which do not mimic with realism the rock more complex behaviour.

Matsuoka et al. (2003) also used a regular arrangement of disks to model a Hopkinson bar test of rock capturing some of the main features of the experiment, namely the detachment of a piece of the bar extremity ejected due to the reflected tension wave. Hentz et al. (2004) employed a 3D particle model to investigate the effect of strain rate in the compressive and tensile strength of rock and several authors have used particle models to model blasting in several aspects.

Kim et al. (1997) and Donzè et al. (1997) modelled the crack generation caused by a blast charge in a cylindrical borehole, Donzè and Bernasconi (2004) modelled a shaft sinking blast in three dimensions obtaining patterns of rock damage around the shaft. Kim et al. (2006) investigated the influence of joint direction and spacing at a tunnel contour blasting. These works employ particle methods on blasting and rock dynamic applications managing to qualitatively capture the major phenomena at stake, namely fracture creation and propagation, rock fragmentation, movement of the blasted rock and damage due to high dynamic stress. However, the propagation of elastic stress waves outside the zone of rock fragmentation is not a relevant issue in these cases and has not been addressed so far.

Hazzard and Young (2004) used PFC3D to reproduce the anisotropic damage inflicted to a sandstone sample by triaxial deviatoric loading. This is the only work, to the knowledge of the authors, which investigates some of the characteristics of the propagation of stress waves in unorganized particle models of rock.

Discontinuous Deformation Analysis (DDA)

Discontinuous Deformation Analysis (DDA) is a type of discrete element method originally proposed by Shi in 1988. DDA is somewhat similar to the finite element method for solving stress-displacement problems, but accounts for the interaction of independent particles (blocks) along discontinuities in fractured and jointed rock masses.

DDA is typically formulated as a work-energy method, and can be derived using the principle of Minimum Potential Energy (e.g. Shi & Goodman 1985; Shi 1988; Shi & Goodman 1988) or by using Hamilton's principle. Once the equations of motion are discretized, a step-wise linear time marching scheme in the Newmark family is used for the solution of the equations of motion. The relation between adjacent blocks is governed by equations of contact interpenetration and accounts for friction.

DDA adopts a stepwise approach to solve for the large displacements that accompany discontinuous movements between blocks. The blocks are said to be "simply deformable". Since the method accounts for the inertial forces of the blocks' mass, it can be used to solve the full dynamic problem of block motion.

According to Sitar & McLaughlin (1997) contact detection logic is implemented in the code DDA similar to the DEM. Contact detection is performed in order to recognize the association between edges and corners between blocks. In this method interpenetration of blocks is avoided by a numerical iterative (algorithmic) procedure and thus the contacts are assumed to be rigid. The network of discontinuities, which are simulated by springs, creates and stores its own energy due to the above interpenetration cancelling technique.

The code tries to find the necessary compatible displacements of the blocks, so that this energy is minimized. The residual energy is then used to back calculate contact forces, element stresses, etc. DDA has been successful in simulating various geotechnical engineering problems such as rock slope stability, and underground excavations in fractured rock masses.

The DDA approach is applicable for rock masses in which the significant fractures affecting stability must be modelled explicitly using mean joint attitude, length, spacing, and bridge. This includes rock masses with more fractures than can be analyzed using the clamped beam model (Obert & Duvall, 1967) or the Voussoir bean analogue (Evans, 1941; Beer & Meek, 1982; Sofianos, 1996; Diederichs & Kaiser, 1999) for roof stability in mines, and rock masses where the number of

fractures is insufficient for application of particle flow codes (Cundall & Strack, 1979) or plastic continuum approximations (Klerck et al., 2004).

2.7 Summary

A review of the analytical and numerical methods for studying the effects of cracks, fractures and joints on wave propagation has been presented. The theoretical methods available in the literature are different depending on the type of problem to be considered. In fact, some methods are appropriate to treat the effects of microcracks on wave propagation, other methods are better suited for studying the effects of fractures or joints. Many numerical methods are available but not all of them allow one to study effectively wave propagation problems in discontinuous media. The most frequently used methods are DEM and DDA.

Chapter 3

The Scattering Matrix Method and the study of wave propagation in continuous media

3.1 Introduction

Wave propagation in continuous media is of interest in the design of underground structures and geotechnical works in general. This phenomenon has been studied by various authors. The first analysis is probably due to George Green (1839) who did not complete all the algebra necessary in the case of two half-spaces having different elastic constants and densities. This generalization was instead performed by Knott (1899) using potential theories and independently by Zoeppritz (1907).

The incident plane wave assumption may be appropriate to study the case of waves at great distances from their source. If reflection and refraction take place near the source, this phenomenon cannot be explained directly by Knott's theory, as in this case one considers a point source radiating spherical waves. An important indirect application of Knott's theory can be mentioned for studying spherical waves by decomposing them into a sum (or integral) of plane waves. Knott's theory is applied to each plane wave, and finally the result is obtained by superimposing the results for each plane wave.

In this chapter, we will introduce the classical theory of wave propagation through a stratified medium with welded interfaces between elastic media, i.e. a continuum by using the Scattering Matrix Method (SMM). We will analyze the simplest type of interface in which two homogeneous isotropic elastic media are in welded contact on a plane boundary. This type of interface can be considered like a discontinuity surface of mechanical properties. Details of the seismic source are avoided by considering the case of a plane wave incident on the boundary.

The SMM is based on the definition of the scattering matrix that is composed of reflection and transmission coefficients of a single interface or a set of interfaces. The SMM will be presented with some analytical and parametric analyses to evaluate the effects of the interfaces on wave propagation.

3.2 Properties of plane waves in elastic media and boundary conditions

The assumption, in the Scattering Matrix Method of an incident plane elastic wave, allows one to treat the problem of wave propagation through interfaces more easily than with spherical waves.

A physical quantity (such as particle acceleration or a stress component) propagates as a plane wave in direction $\mathbf{l}$ with speed c if (Aki & Richards, 2002):

- at a fixed time, the quantity is spatially unchanged over each plane normal to the unit vector $\mathbf{l}$, and if
- the plane associated with a particular value of the quantity moves with speed c in direction $\mathbf{l}$.

It follows that physical quantities propagating with these two properties must have a functional dependence on space and time only via the combination $t - (\mathbf{l} \cdot \mathbf{x})/c$. We call $\mathbf{l}/c$ the slowness vector $\mathbf{s}$. An advantage of using slowness (rather than velocity) to summarize the speed and direction of propagation of a wave is that slownesses may be added vectorially (velocities, in this context, cannot). Thus, using Cartesian coordinates *(x,y,z),* the slowness of a given wave is the vectorial sum of its components s_x, s_y, s_z along each coordinate direction: $\mathbf{s} = s_x\hat{\mathbf{x}} + s_y\hat{\mathbf{y}} + s_z\hat{\mathbf{z}}$ and the slowness in direction $\mathbf{n}$ is simply $\mathbf{s} \cdot \mathbf{n}$. In contrast, the velocity with which a plane wave advances in a particular direction is, in general, faster than its velocity in the direction of propagation (see Figure 3.1).

The two basic types of plane waves in a homogeneous isotropic medium are easily distinguished by substituting the general form $\mathbf{u}=\mathbf{u}(t - \mathbf{s} \cdot \mathbf{x})$ for displacement into the elastic displacement equation,

$$\rho\ddot{u}_i = (\lambda + \mu)\rho u_{j,ji} + \mu u_{i,jj} \tag{3.1}$$

to give

$$\left[\rho\delta_{ik} - (\lambda + \mu)s_i s_k + \mu s_j s_j \delta_{ik}\right]\ddot{u}_k = 0 \tag{3.2}$$

Forming the vector product and scalar product of (3.2) with $\mathbf{s}$, and using $s^2 = 1/c^2$, we obtain

$$\left(\rho - \frac{\mu}{c^2}\right)\ddot{\mathbf{u}} \times \mathbf{s} = \mathbf{0} \qquad \left(\rho - \frac{\lambda + 2\mu}{c^2}\right)\ddot{\mathbf{u}} \cdot \mathbf{s} = \mathbf{0} \tag{3.3}$$

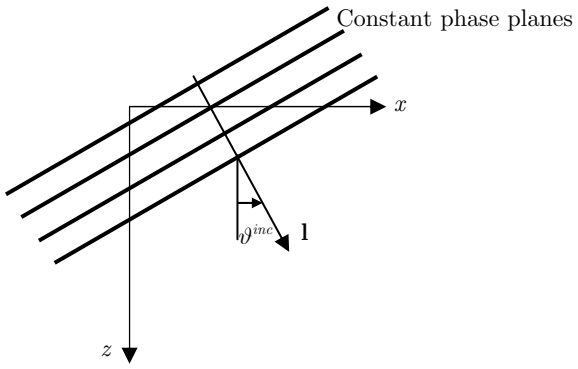

Figure 3.1 – Schematization of a plane wave (**l** is the direction of propagation and ϑ^{inc} is the angle of incidence, with respect the z-axis

Therefore, either $\ddot{\mathbf{u}} \times \mathbf{s} = \mathbf{0}$ and $c^2 = (\lambda + 2\mu)/\rho$, or $\ddot{\mathbf{u}} \cdot \mathbf{s} = \mathbf{0}$ and $c^2 = \mu/\rho$. It follows that the plane wave is either a P-wave, with longitudinal motion (parallel to **s**) and speed $[(\lambda + 2\mu)/\rho]^{1/2} = V_P$, or an S-wave with transverse motion and speed $(\mu/\rho)^{1/2} = V_S$. The longitudinal or transverse nature of P or S motion is exact, at all frequencies, for plane waves in homogeneous isotropic media.

To describe the energy associated with the elastic motion, we consider the concept of elastic strain-energy density. The strain energy of a medium is its capacity to do work by virtue of its configuration, and it is known (Aki & Richards, 2002) that the strain-energy density can be expressed as $1/2\tau_{ij}\varepsilon_{ij}$. For a plane wave $u_i = u_i(t - \mathbf{s} \cdot \mathbf{x})$, the strain tensor is $e_{ij} = -1/2[\dot{u}_i s_j + \dot{u}_j s_i]$, and recalling the stress-strain relations for an isotropic linearly elastic medium it is easy to show that

$$\frac{1}{2}\tau_{ij}\varepsilon_{ij} = \frac{1}{2}\left[\left(\lambda + \mu\right)\left(\mathbf{s} \cdot \dot{\mathbf{u}}\right)^2 + \mu\left(\dot{\mathbf{u}} \cdot \dot{\mathbf{u}}\right)\left(\mathbf{s} \cdot \mathbf{s}\right)\right] \tag{3.4}$$

In the case of either a P-wave (for which **s** is parallel to $\dot{\mathbf{u}}$, and $|s| = V_P^{-1}$) or an S-wave (**s** perpendicular to $\dot{\mathbf{u}}$, and $|s| = V_S^{-1}$) it follows from (3.4) that

$$\frac{1}{2}\tau_{ij}\varepsilon_{ij} = \frac{1}{2}\rho\dot{\mathbf{u}}^2 . \tag{3.5}$$

i.e., the strain-energy density equals the kinetic-energy density. The quantities in (3.5) are all real, and the energy densities depend on t and **x** only via the combination $t - \mathbf{s} \cdot \mathbf{x}$. Hence the speed of energy propagation is no different from

the speed with which a pulse shape in particle displacement is propagated: either V_P for P-waves or V_S for S-waves.

It follows that the flux rate of energy transmission in a plane wave (i.e., the amount of energy transmitted per unit time across unit area normal to the direction of propagation) is $\rho V_P \dot{u}^2$ for P-waves and $\rho V_S \dot{u}^2$ for S-waves. We have proved this result only for plane waves in homogeneous media, and it is a "local" property, depending on material properties and on the planar nature of the wave only at the point at which the flux rate is evaluated. We can therefore expect that flux rates are still given approximately by $\rho \dot{u}^2$ times the propagation velocity for the case of slightly curved wave-fronts in a medium with some spatial fluctuation in material properties. It follows that there is a physical interpretation of the results of geometrical ray theory for displacement amplitude (Aki & Richards, 2002).

3.3 Scattering Matrix Method (SMM)

The scattering phenomenon that takes place when an elastic wave impinges on a discontinuity is conveniently described by a scattering matrix. In the case of a planar interface between two media or a planar joint in a rock mass, incident, reflected and transmitted plane waves have the same transverse wave-vector. The respective amplitudes are related by a 2x2 block matrix

$$\mathbf{S} = \begin{pmatrix} \mathbf{S_{11}} & \mathbf{S_{12}} \\ \mathbf{S_{21}} & \mathbf{S_{22}} \end{pmatrix} \tag{3.6}$$

where
$\boldsymbol{S}_{ii}$ has the meaning of reflection coefficients at the two sides of the interface and $\boldsymbol{S}_{ij}$ of transmission coefficients. Since elastic waves have three possible polarization states (P, SV, SH), the submatrices have size 3x3.

When more parallel interfaces are present, the scattering matrices of each interface are combined according to a standard algorithm in order to describe the behaviour of the complete structure, with due consideration of all multiply reflected waves.

The method is borrowed from the study of electromagnetic waves propagation and the theory of transmission lines such as coaxial cables, optical fibres, strip-lines, etc (Collin, 1992).

The problem can be related to discontinuities of mechanical properties, between two different media, or joints as characteristic of rock masses. In this chapter we analyze the first type of discontinuities while in Chapter 4 we will consider typical

discontinuities as present in rock masses. As a first instance, we can consider the case of a planar welded interface between two homogeneous linear elastic media.

An earthquake generates waves that can be decomposed into a compressional wave (P-wave) and two shear waves (SV and SH). These three different elastic waves produce particle motion parallel to three spatial directions. In fact, a plane P-wave produces particle motion in the direction parallel to that of propagation; for a SV-wave the particle motion is normal to the direction of propagation but is in the plane of incidence while for a SH-wave the particle motion is normal to the plane of incidence. In this situation, we can simplify the problem by considering that, on reflection at an interface, P and SV-waves are coupled while the SH-waves are decoupled from them.

The description of the Scattering Matrix Method (SMM) can start by studying the propagation of a plane wave through a welded interface between two media with different mechanical properties (Figure 3.2). The wave-vector $\mathbf{k}$ represents the direction of propagation of the incident plane wave and its modulus is the propagation constant. The interface is represented by the z=0 plane in Figure 3.2.

We consider a 2D time harmonic problem by orienting the y axis perpendicular to both z and $\mathbf{k}$, so that $\partial / \partial y \equiv 0$.

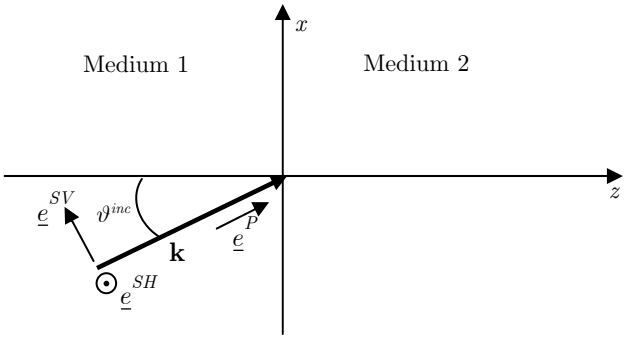

Figure 3.2 – Welded interface between two media - Geometry of the problem

As a first instance, we can consider that the wave vector $\mathbf{k}$ is relative to a P-wave that impinges on the interface at an angle ϑ^P. The wave vector $\mathbf{k}$ can be decomposed into x and z directions as:

$$\mathbf{k} = \xi \hat{\mathbf{x}} + k_{zP} \hat{\mathbf{z}} \tag{3.7}$$

where:

$\hat{\mathbf{x}}$ and $\hat{\mathbf{z}}$ are the unit vectors;

$\xi = k_P \sin \vartheta^P$ is the transverse wave-vector;

ω is the angular frequency;
$k_P = \omega / V_P$ is the propagation constant for P-waves;
V_P is the velocity of propagation of P-waves;
ϑ^P is the P-wave angle of incidence;
$k_{zP} = (k_P^2 - \xi^2)^{1/2}$ is the z component of the wave-vector $\mathbf{k}$.

The same considerations apply to shear waves but in this case we have to consider that k_S and k_{zS} are function of angular frequency, shear wave velocity and angle of incidence.

Snell's law shows the following relation between P and SV waves:

$$\xi = k_P \sin \vartheta^P = k_S \sin \vartheta^{SV} \tag{3.8}$$

where:
ϑ^{SV} is the angle of incidence for SV-wave.

It is well known (Van der Hÿden) that the state variables that characterize the elastic wave field are the velocity $\mathbf{v}$ and the traction $\mathbf{T} \cdot \hat{\mathbf{z}}$ on a plane orthogonal to $\hat{\mathbf{z}}$. Indeed these are the quantities that are continuous at a welded interface.

The stress field associated to a plane wave is computed by an impedance relation (Auld, 1973; Aki & Richards, 2002):

$$\begin{aligned} -\mathbf{T}^P \cdot \hat{\mathbf{l}} &= \frac{\rho\omega}{k_P}\mathbf{v} \qquad \text{for pressure waves (P-waves)} \\ -\mathbf{T}^S \cdot \hat{\mathbf{l}} &= \frac{\rho\omega}{k_S}\mathbf{v} \qquad \text{for shear waves (S-waves)} \end{aligned} \tag{3.9}$$

The left hand side of these equations yield the traction on planes orthogonal to the propagation direction $\hat{\mathbf{l}}$. The traction of interest is $\mathbf{T} \cdot \hat{\mathbf{z}}$ on the planes orthogonal to $\hat{\mathbf{z}}$ and is given by (Auld, 1973):

$$-\mathbf{T} \cdot \hat{\mathbf{z}} = \mathbf{Z} \cdot \mathbf{v} \tag{3.10}$$

with:

$$\mathbf{Z}^{+} = \frac{k_i}{\omega}\begin{bmatrix} C_{44}\cos\vartheta & 0 & C_{44}\sin\vartheta \\ 0 & C_{44}\cos\vartheta & 0 \\ C_{12}\sin\vartheta & 0 & C_{11}\cos\vartheta \end{bmatrix} = \frac{1}{\omega}\begin{bmatrix} C_{44}k_{zi} & 0 & C_{44}\xi \\ 0 & C_{44}k_{zi} & 0 \\ C_{12}\xi & 0 & C_{11}k_{zi} \end{bmatrix} \tag{3.11}$$

where the + sign is to be used for forward waves and the – sign for backward waves. Moreover k_{zi} is to be interpreted as k_{zS} for shear waves and k_{zP} for pressure waves while k_i as k_P and k_S.

We derive now the explicit expressions of the elastic wave field for each wave type:

Forward P-wave:

$$\mathbf{v}\big(x,z\big) = c^{P+}e^{-jk_{zP}z}e^{-j\xi x}\mathbf{e}^{P+} \tag{3.12}$$

with:

$$\mathbf{e}^{P+} = \Big(\sin\vartheta^P\hat{\mathbf{x}} + \cos\vartheta^P\hat{\mathbf{z}}\Big)N^{P+} = \left(\frac{\xi}{k_P}\hat{\mathbf{x}} + \frac{k_{zP}}{k_P}\hat{\mathbf{z}}\right)N^{P+} \tag{3.13}$$

where N^{P+} is a suitable normalization factor (see Appendix A).

$$\begin{aligned} -\mathbf{T}\cdot\hat{\mathbf{z}} &= c^{P+}e^{-jk_{zP}z}e^{-j\xi x}\mathbf{Z}^{P+}\cdot\mathbf{e}^{P+} = \\ &= c^{P+}e^{-jk_{zP}z}e^{-j\xi x}\,\frac{N^P}{\omega}\cdot\left[2C_{44}\,\frac{\xi k_{zP}}{k_P}\hat{\mathbf{x}} + \left(C_{11}k_P - 2C_{44}\,\frac{\xi^2}{k_P}\right)\hat{\mathbf{z}}\right] \end{aligned} \tag{3.14}$$

Backward P-wave:

$$\mathbf{v}\big(x,z\big) = c^{P-}e^{+jk_{zP}z}e^{-j\xi x}\mathbf{e}^{P-} \tag{3.15}$$

with:

$$\mathbf{e}^{P-} = \Big(\sin\vartheta^P\hat{\mathbf{x}} - \cos\vartheta^P\hat{\mathbf{z}}\Big)N^{P-} = \left(\frac{\xi}{k_P}\hat{\mathbf{x}} - \frac{k_{zP}}{k_P}\hat{\mathbf{z}}\right)N^{P-} \tag{3.16}$$

$$
\begin{aligned}
&-\mathbf{T}\cdot\hat{\mathbf{z}} = c^{P-}e^{+jk_{zP}z}e^{-j\xi x}\mathbf{Z}^{P-}\cdot\mathbf{e}^{P-} = \\
&= c^{P-}e^{+jk_{zP}z}e^{-j\xi x}\,\frac{N^P}{\omega}\cdot\left[-2C_{44}\,\frac{\xi k_{zP}}{k_P}\,\hat{\mathbf{x}} + \left(C_{11}k_P - 2C_{44}\,\frac{\xi^2}{k_P}\right)\hat{\mathbf{z}}\right]
\end{aligned}
\tag{3.17}
$$

Forward SV-wave:

$$
\mathbf{v}\big(x,z\big) = c^{SV+}e^{-jk_{zS}z}e^{-j\xi x}\mathbf{e}^{SV+}
\tag{3.18}
$$

with:

$$
\mathbf{e}^{SV+} = \Big(\cos\vartheta^{SV}\hat{\mathbf{x}} - \sin\vartheta^{SV}\hat{\mathbf{z}}\Big)N^{SV+} = \left(\frac{k_{zS}}{k_S}\,\hat{\mathbf{x}} - \frac{\xi}{k_S}\,\hat{\mathbf{z}}\right)N^{SV+}
\tag{3.19}
$$

$$
\begin{aligned}
&-\mathbf{T}\cdot\hat{\mathbf{z}} = c^{SV+}e^{-jk_{zS}z}e^{-j\xi x}\mathbf{Z}^{SV+}\cdot\mathbf{e}^{SV+} = \\
&= c^{SV+}e^{-jk_{zS}z}e^{-j\xi x}\,\frac{N^{SV}}{\omega}\cdot\left[C_{44}\,\frac{k_S^2 - 2\xi^2}{k_S}\,\hat{\mathbf{x}} - 2C_{44}\,\frac{\xi k_{zS}{}^2}{k_S}\,\hat{\mathbf{z}}\right]
\end{aligned}
\tag{3.20}
$$

Backward SV-wave:

$$
\mathbf{v}\big(x,z\big) = c^{SV-}e^{+jk_{zS}z}e^{-j\xi x}\mathbf{e}^{SV-}
\tag{3.21}
$$

with:

$$
\mathbf{e}^{SV-} = \Big(\cos\vartheta^{SV}\hat{\mathbf{x}} + \sin\vartheta^{SV}\hat{\mathbf{z}}\Big)N^{SV-} = \left(\frac{k_{zS}}{k_S}\,\hat{\mathbf{x}} + \frac{\xi}{k_S}\,\hat{\mathbf{z}}\right)N^{SV-}
\tag{3.22}
$$

$$
\begin{aligned}
&-\mathbf{T}\cdot\hat{z} = c^{SV-}e^{+jk_{zS}z}e^{-j\xi x}\mathbf{Z}^{SV-}\cdot\mathbf{e}^{SV-} = \\
&= c^{SV-}e^{+jk_{zS}z}e^{-j\xi x}\,\frac{N^{SV}}{\omega}\cdot\left[-C_{44}\,\frac{k_S^2 - 2\xi^2}{k_S}\,\hat{\mathbf{x}} - 2C_{44}\,\frac{\xi k_{zS}{}^2}{k_S}\,\hat{\mathbf{z}}\right]
\end{aligned}
\tag{3.23}
$$

Forward SH-wave:

$$
\mathbf{v}\big(x,z\big) = c^{SH+}e^{-jk_{zS}z}e^{-j\xi x}\mathbf{e}^{SH+}
\tag{3.24}
$$

where:

$$\mathbf{e}^{SH+} = \hat{\mathbf{y}} N^{SH+} \tag{3.25}$$

$$-\mathbf{T}\cdot\hat{\mathbf{z}} = c^{SH+} e^{-jk_{zS}z} e^{-j\xi x} \mathbf{Z}^{SH+}\cdot\mathbf{e}^{SH+} = c^{SH+} e^{-jk_{zS}z} e^{-j\xi x}\,\frac{N^{SH}}{\omega}\cdot\left(C_{44}k_{zS}\right)\hat{\mathbf{y}} \tag{3.26}$$

Backward SH-wave:

$$\mathbf{v}\left(x,z\right) = c^{SH-} e^{+jk_{zS}z} e^{-j\xi x}\mathbf{e}^{SH-} \tag{3.27}$$

with:

$$\mathbf{e}^{SH-} = \hat{\mathbf{y}} N^{SH-} \tag{3.28}$$

$$\begin{aligned} -\mathbf{T}\cdot\hat{\mathbf{z}} &= c^{SH-} e^{+jk_{zS}z} e^{-j\xi x}\mathbf{Z}^{SH-}\cdot\mathbf{e}^{SH-} = \\ &= c^{SH-} e^{+jk_{zS}z} e^{-j\xi x}\,\frac{N^{SH}}{\omega}\cdot\left(-C_{44}k_{zS}\right)\hat{\mathbf{y}} \end{aligned} \tag{3.29}$$

It can be noted that the x dependence of all the quantities is contained in the factor $e^{-j\xi x}$, which is no longer written explicitly from now on. Focusing our attention on the z dependence, it is convenient to define an abstract 6x1 state vector $\mathbf{\Psi}(z)$ as:

$$\boldsymbol{\Psi}\left(z\right)=\begin{pmatrix}\mathbf{v}\\ \mathbf{T}\cdot\hat{\mathbf{z}}\end{pmatrix}_{6\times1}=\begin{pmatrix}v_x\\ v_y\\ v_z\\ \hat{\mathbf{x}}\cdot\mathbf{T}\cdot\hat{\mathbf{z}}\\ \hat{\mathbf{y}}\cdot\mathbf{T}\cdot\hat{\mathbf{z}}\\ \hat{\mathbf{z}}\cdot\mathbf{T}\cdot\hat{\mathbf{z}}\end{pmatrix}=$$

$$=\mathbf{M}\cdot diag\left(e^{-jk_{zS}^{SH}z},e^{-jk_{zS}^{SV}z},e^{-jk_{zP}^{P}z},e^{jk_{zS}^{SH}z},e^{jk_{zS}^{SV}z},e^{jk_{zP}^{P}z}\right)\cdot\begin{pmatrix}c^{SH+}\\ c^{SV+}\\ c^{P+}\\ c^{SH-}\\ c^{SV-}\\ c^{P-}\end{pmatrix} \tag{3.30}$$

where:
M is the modal matrix (Aki & Richards, 2002).

The velocity and stress fields allow one to write the modal matrix $\mathbf{M}(\xi)$ (Aki & Richards, 2002):

$$\mathbf{M}\left(\xi\right)=\begin{bmatrix}\hat{\mathbf{e}}^{SH+}\cdot\hat{\mathbf{x}} & \hat{\mathbf{e}}^{SV+}\cdot\hat{\mathbf{x}} & \hat{\mathbf{e}}^{P+}\cdot\hat{\mathbf{x}} & \hat{\mathbf{e}}^{SH-}\cdot\hat{\mathbf{x}} & \hat{\mathbf{e}}^{SV-}\cdot\hat{\mathbf{x}} & \hat{\mathbf{e}}^{P-}\cdot\hat{\mathbf{x}}\\ \hat{\mathbf{e}}^{SH+}\cdot\hat{\mathbf{y}} & \hat{\mathbf{e}}^{SV+}\cdot\hat{\mathbf{y}} & \hat{\mathbf{e}}^{P+}\cdot\hat{\mathbf{y}} & \hat{\mathbf{e}}^{SH-}\cdot\hat{\mathbf{y}} & \hat{\mathbf{e}}^{SV-}\cdot\hat{\mathbf{y}} & \hat{\mathbf{e}}^{P-}\cdot\hat{\mathbf{y}}\\ \hat{\mathbf{e}}^{SH+}\cdot\hat{\mathbf{z}} & \hat{\mathbf{e}}^{SV+}\cdot\hat{\mathbf{z}} & \hat{\mathbf{e}}^{P+}\cdot\hat{\mathbf{z}} & \hat{\mathbf{e}}^{SH-}\cdot\hat{\mathbf{z}} & \hat{\mathbf{e}}^{SV-}\cdot\hat{\mathbf{z}} & \hat{\mathbf{e}}^{P-}\cdot\hat{\mathbf{z}}\\ M_{41} & M_{42} & M_{43} & M_{44} & M_{45} & M_{46}\\ M_{51} & M_{52} & M_{53} & M_{54} & M_{55} & M_{56}\\ M_{61} & M_{62} & M_{63} & M_{64} & M_{65} & M_{66}\end{bmatrix}_{6\times6} \tag{3.31}$$

where:

$$M_{41}=\mathbf{Z}^{SH+}\cdot\hat{\mathbf{e}}^{SH+}\cdot\hat{\mathbf{x}} \qquad M_{42}=\mathbf{Z}^{SV+}\cdot\hat{\mathbf{e}}^{SV+}\cdot\hat{\mathbf{x}} \qquad M_{43}=\mathbf{Z}^{P+}\cdot\hat{\mathbf{e}}^{P+}\cdot\hat{\mathbf{x}}$$
$$M_{51}=\mathbf{Z}^{SH+}\cdot\hat{\mathbf{e}}^{SH+}\cdot\hat{\mathbf{y}} \qquad M_{52}=\mathbf{Z}^{SV+}\cdot\hat{\mathbf{e}}^{SV+}\cdot\hat{\mathbf{y}} \qquad M_{53}=\mathbf{Z}^{P+}\cdot\hat{\mathbf{e}}^{P+}\cdot\hat{\mathbf{y}}$$
$$M_{61}=\mathbf{Z}^{SH+}\cdot\hat{\mathbf{e}}^{SH+}\cdot\hat{\mathbf{z}} \qquad M_{62}=\mathbf{Z}^{SV+}\cdot\hat{\mathbf{e}}^{SV+}\cdot\hat{\mathbf{z}} \qquad M_{63}=\mathbf{Z}^{P+}\cdot\hat{\mathbf{e}}^{P+}\cdot\hat{\mathbf{z}}$$
$$M_{44}=\mathbf{Z}^{SH-}\cdot\hat{\mathbf{e}}^{SH-}\cdot\hat{\mathbf{x}} \qquad M_{45}=\mathbf{Z}^{SV-}\cdot\hat{\mathbf{e}}^{SV-}\cdot\hat{\mathbf{x}} \qquad M_{46}=\mathbf{Z}^{P-}\cdot\hat{\mathbf{e}}^{P-}\cdot\hat{\mathbf{x}}$$
$$M_{54}=\mathbf{Z}^{SH-}\cdot\hat{\mathbf{e}}^{SH-}\cdot\hat{\mathbf{y}} \qquad M_{55}=\mathbf{Z}^{SV-}\cdot\hat{\mathbf{e}}^{SV-}\cdot\hat{\mathbf{y}} \qquad M_{56}=\mathbf{Z}^{P-}\cdot\hat{\mathbf{e}}^{P-}\cdot\hat{\mathbf{y}}$$
$$M_{64}=\mathbf{Z}^{SH-}\cdot\hat{\mathbf{e}}^{SH-}\cdot\hat{\mathbf{z}} \qquad M_{65}=\mathbf{Z}^{SV-}\cdot\hat{\mathbf{e}}^{SV-}\cdot\hat{\mathbf{z}} \qquad M_{66}=\mathbf{Z}^{P-}\cdot\hat{\mathbf{e}}^{P-}\cdot\hat{\mathbf{z}}$$

The columns of the modal matrix (3.31) contain the polarization vectors of forward and backward SH, SV, P waves. For example, the term 1,2 is the x component of the velocity for the forward SV polarization and the term 4,2 is the tangential stress τ_{zx}. The modal matrix is defined for a certain value of the transverse wave-vector ξ that is the x component of the wave-vector $\mathbf{k}$ (Figure 3.2).

At this point, we have a representation of the elastic fields at each side of an interface. The following step of the Scattering Matrix Method is the imposition of the boundary conditions along the interface, in order to relate the scattered wave amplitudes to the incident ones.

3.3.1 Wave scattering from a single interface

Consider a single welded interface between two media with different mechanical properties. In Figure 3.3 we can see the geometry of the problem. For generality there is also a wave incident from the right side, but with the same value ξ.

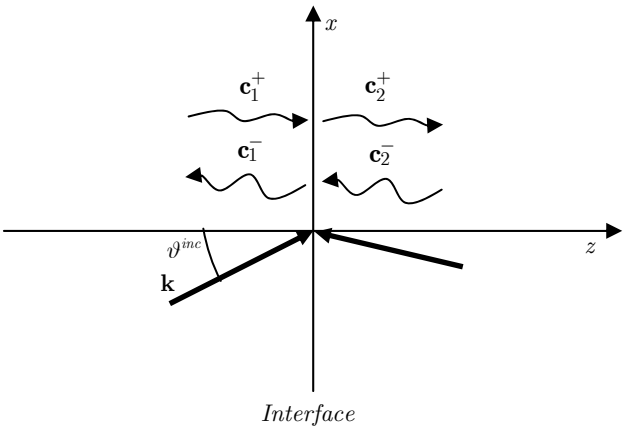

Figure 3.3 – Wave propagation through an interface ($\mathbf{k}$ is the wave direction vector)

At a welded interface, both velocity and traction on the interface must be continuous:

$$\mathbf{M_1} \cdot \begin{pmatrix} \mathbf{c_1}^+ \\ \mathbf{c_1}^- \end{pmatrix} = \mathbf{M_2} \cdot \begin{pmatrix} \mathbf{c_2}^+ \\ \mathbf{c_2}^- \end{pmatrix} \tag{3.32}$$

where:

$\mathbf{M}_1$, $\mathbf{M}_2$ are the modal matrices of the medium "1" and "2" respectively.

From Equation (3.32) we get:

$$\begin{pmatrix} \mathbf{c_1}^+ \\ \mathbf{c_1}^- \end{pmatrix} = \mathbf{M_1}^{-1} \cdot \mathbf{M_2} \cdot \begin{pmatrix} \mathbf{c_2}^+ \\ \mathbf{c_2}^- \end{pmatrix} \tag{3.33}$$

where:
$\mathbf{c}_1^+$ and $\mathbf{c}_2^-$ are the amplitudes of the left side and right side incident waves, $\mathbf{c}_1^-$ and $\mathbf{c}_2^+$ are the amplitudes of the scattered waves (reflected and transmitted). Equation (3.33) represents the relation between the elastic wave field at the right and at the left of the interface.

From Equation (3.33) we can define the transmission matrix $\mathbf{A}$ that relates the wave amplitudes at two sides of the interface:

$$\mathbf{A} = \mathbf{M_1}^{-1} \cdot \mathbf{M_2} \tag{3.34}$$

A more useful characterization of the interface is given by the scattering matrix, defined by:

$$\begin{pmatrix} \mathbf{c_1}^- \\ \mathbf{c_2}^+ \end{pmatrix} = \mathbf{S} \begin{pmatrix} \mathbf{c_1}^+ \\ \mathbf{c_2}^- \end{pmatrix} \tag{3.35}$$

Its expression is found by simple algebraic manipulations:

$$\mathbf{S} = \begin{pmatrix} \mathbf{A_{21}A_{11}^{-1}} & \left(\mathbf{A_{22}} - \mathbf{A_{21}A_{11}^{-1}A_{12}}\right) \\ \mathbf{A_{11}^{-1}} & -\mathbf{A_{11}^{-1}A_{12}} \end{pmatrix}_{6x6} \tag{3.36}$$

where:
$\mathbf{A} = \begin{pmatrix} \mathbf{A_{11}} & \mathbf{A_{12}} \\ \mathbf{A_{21}} & \mathbf{A_{22}} \end{pmatrix}_{6x6}$ and $\mathbf{A_{ij}}$ is a matrix with size 3x3.

Hence, for three wave polarization states, the expanded expression of the scattering matrix is:

$$\mathbf{S} = \begin{pmatrix} \mathbf{S_{11}} & \mathbf{S_{12}} \\ \mathbf{S_{21}} & \mathbf{S_{22}} \end{pmatrix} \tag{3.37}$$

and:

$$\mathbf{S_{11}} = \begin{pmatrix} \frac{c_1^{SH-}}{c_1^{SH-}} & 0 & 0 \\ 0 & \frac{c_1^{SV-}}{c_1^{SV+}} & \frac{c_1^{SV-}}{c_1^{P+}} \\ 0 & \frac{c_1^{P-}}{c_1^{SV+}} & \frac{c_1^{P-}}{c_1^{P+}} \end{pmatrix} \tag{3.38}$$

$$\mathbf{S_{21}} = \begin{pmatrix} \frac{c_2^{SH+}}{c_1^{SH+}} & 0 & 0 \\ 0 & \frac{c_2^{SV+}}{c_1^{SV+}} & \frac{c_2^{SV+}}{c_1^{P+}} \\ 0 & \frac{c_2^{P+}}{c_1^{SV+}} & \frac{c_2^{P+}}{c_1^{P+}} \end{pmatrix} \tag{3.39}$$

and so on.

The zeros make it clear that the SH polarization is uncoupled from the others. For this reason it is convenient to treat separately the case of SH and SV/P polarizations. In the following we will focus on the SV/P case, so that the submatrices of the **A** and **S** matrices are 2x2.

It can be proven that the scattering matrix is symmetric.

Some important energy considerations can be done for the scattering matrix **S**. It can be shown also that the scattering matrix of a lossless discontinuity is unitary, i.e.

$$\mathbf{S}^{*T} \cdot \mathbf{S} = \mathbf{I} \tag{3.40}$$

where:
$\mathbf{S}^{*T}$ is the complex conjugate of the transpose of **S**;
I is the identity matrix.

The Equation (3.40) is a consequence of conservation of energy. It implies that the power sensity leaving the interface in the $\hat{z}$ direction is equal to the incident one.

3.3.2 Wave propagation across *N* interfaces

In order to characterize the wave propagation across N parallel interfaces, we have to compute the global scattering matrix of the set of interfaces. This matrix can be obtained by applying a "chain rule" procedure to the scattering matrices of each interface.

However, the right reference plane of the scattering matrix of interface (1) must coincide with the left reference plane of interface (2) (see Figure 3.4). It can be shown that the scattering matrix $\mathbf{S}^{(1)}$ of interface (1) becomes:

$$\mathbf{S}^{(1)} = \begin{pmatrix} \mathbf{A_{21}A_{11}^{-1}} & \left(\mathbf{A_{22}} - \mathbf{A_{21}A_{11}^{-1}A_{12}}\right) diag\left(e^{-jk_{zi}d_1}\right) \\ diag\left(e^{-jk_{zi}d_1}\right)\mathbf{A_{11}^{-1}} & -diag\left(e^{-jk_{zi}d_1}\right)\mathbf{A_{11}^{-1}A_{12}} diag\left(e^{-jk_{zi}d_1}\right) \end{pmatrix} \tag{3.41}$$

instead of (3.36), where:
$\mathbf{A}_{ij}$ has size 2x2 and it is a sub-matrix of the transmission matrix $\mathbf{A}$ of the interface (a);

$k_{zi} = \begin{pmatrix} k_{zS} \\ k_{zP} \end{pmatrix}$ for coupled P and SV waves while for an incident SH wave $k_{zi} = k_{zS}$.

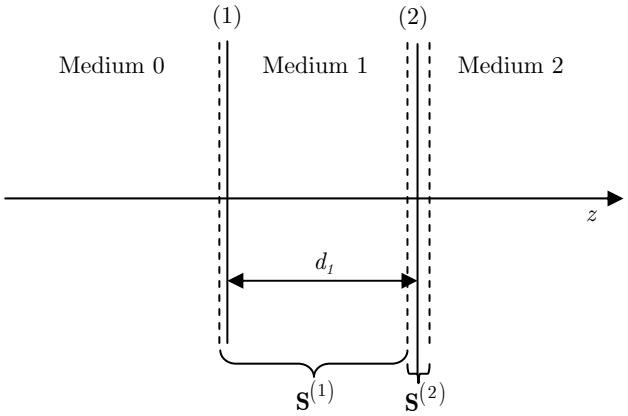

Figure 3.4 – Stratified structure with two interfaces

In Equation (3.41) relative to the shift of the reference plane, we can see that the scattering matrix of the interface (1) becomes function of the spacing (d_1) between two interfaces (Figure 3.4).

The last step of the construction of the global scattering matrix is the combination of the components of the scattering matrix for each interface. This procedure is named "chain rule" and it can be performed by using follows equations:

$$\begin{aligned}
\mathbf{S}_{11} &= \mathbf{S}_{11}^{(1)} + \mathbf{S}_{12}^{(1)}\mathbf{S}_{11}^{(2)}\left(\mathbf{I} - \mathbf{S}_{22}^{(1)}\mathbf{S}_{11}^{(2)}\right)^{-1}\mathbf{S}_{21}^{(1)} \\
\mathbf{S}_{12} &= \mathbf{S}_{12}^{(1)}\left(\mathbf{I} - \mathbf{S}_{11}^{(2)}\mathbf{S}_{22}^{(1)}\right)^{-1}\mathbf{S}_{12}^{(2)} \\
\mathbf{S}_{21} &= \mathbf{S}_{21}^{(2)}\left(\mathbf{I} - \mathbf{S}_{22}^{(1)}\mathbf{S}_{11}^{(2)}\right)^{-1}\mathbf{S}_{21}^{(1)} \\
\mathbf{S}_{22} &= \mathbf{S}_{22}^{(2)} + \mathbf{S}_{21}^{(2)}\left(\mathbf{I} - \mathbf{S}_{22}^{(1)}\mathbf{S}_{11}^{(2)}\right)^{-1}\mathbf{S}_{22}^{(1)}\mathbf{S}_{12}^{(2)}
\end{aligned} \tag{3.42}$$

where:
$\mathbf{S}_{ij}^{(1)}$ is the sub-matrix, with size 2x2, of the scattering matrix of the welded interface (1).

The global scattering matrix of the system of two parallel interfaces has the same form as that of a single interface (see Equation (3.37)).

This procedure can be easily applied to a system with N interfaces. The steps for computing the global scattering matrix of a set of 3 parallel interfaces is summarized in (Figure 3.5):

1. Definition of the scattering matrix for each of 3 interfaces ($\mathbf{S}^{(1)}$, $\mathbf{S}^{(2)}$, $\mathbf{S}^{(3)}$);
2. Shift of the reference plane, for $\mathbf{S}^{(1)}$ and $\mathbf{S}^{(2)}$.
3. Application of the "chain rule" procedure to the scattering matrices $\mathbf{S}^{(2)}$ and $\mathbf{S}^{(3)}$. From this combination of the components of two scattering matrices, we can obtain the global matrix $\mathbf{S}^{(23)}$ of the interfaces "1" and "2".
4. Application of the "chain rule" on the matrices $\mathbf{S}^{(1)}$ and $\mathbf{S}^{(23)}$. After this step we have the global scattering matrix of the set of three parallel interfaces.

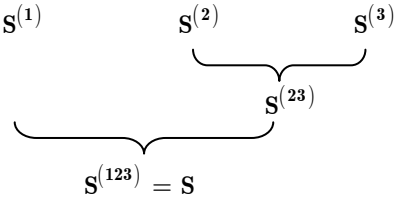

Figure 3.5 – Computation of the global scattering matrix for a set of 3 interfaces

The "chain rule" for the combination of the various scattering matrices is rather complicated. There is a simpler method that consists of the following steps:

1. Construction of the transmission matrix $\mathbf{A}^{(i)}$ for each interface;
2. Computation of the transmission matrix for each layer $\mathbf{A}_{str}{}^{(i)}$ between two interfaces:

$$\mathbf{A}_{str}^{(i)} = \begin{pmatrix} diag\left(e^{jk_{zi}d_1}\right) & 0 \\ 0 & diag\left(e^{-jk_{zi}d_1}\right) \end{pmatrix} \tag{3.43}$$

3. Computation of the global transmission matrix $\mathbf{A}$ as product of the transmission matrices of each interface $\mathbf{A}^{(i)}$ and of each layer $\mathbf{A}_{str}{}^{(i)}$:

$$\mathbf{A} = \prod_{k=1}^{n} \mathbf{A}^{(i)} \mathbf{A}_{str}^{(i)} \tag{3.44}$$

where:
n is the number of interfaces;

4. Computation of the global scattering matrix $\mathbf{S}$ from the global transmission matrix $\mathbf{A}$ of the set of interfaces. This operation may be done as follows:

$$\begin{aligned} \mathbf{S_{11}} &= \mathbf{A_{21}}\mathbf{A_{11}}^{-1} \\ \mathbf{S_{12}} &= \mathbf{A_{22}} - \mathbf{A_{21}}\mathbf{A_{11}}^{-1}\mathbf{A_{12}} \\ \mathbf{S_{21}} &= \mathbf{A_{11}}^{-1} \\ \mathbf{S_{22}} &= -\mathbf{A_{11}}^{-1}\mathbf{A_{12}} \end{aligned} \tag{3.45}$$

where:
$\mathbf{S}_{ij}$ and $\mathbf{A}_{ij}$ matrices are submatrices of the global scattering and transmission matrices.

This method is absolutely equivalent to the previous one if k_{zi} in all layers are all real. When some of them are imaginary, the ratio between the exponentials in (3.43) becomes so large as to lose significant digits in the computation. The result in this case is that the matrix $\mathbf{A}_{11}$ in (3.45) becomes singular and cannot be inverted.

The method based on the "chain rule" is stable and can be always used.

3.3.3 Free surface

For real problems, it may be necessary to model a free surface boundary condition that we suppose to be located at $z = 0$. In this situation it is well known that the tractions along a free surface are zero and then:

$$-\mathbf{T} \cdot \hat{\mathbf{z}} = 0 \tag{3.46}$$

Since there is no transmitted field, the scattering matrix of this interface reduces to the $\mathbf{S}_{11}$ element, i.e. to the reflection coefficient.

We recall that in a homogeneous medium at $z = 0$ we have:

$$\left.\begin{pmatrix} \mathbf{v} \\ -\mathbf{T} \cdot \hat{\mathbf{z}} \end{pmatrix}\right|_{z=0} = \mathbf{M}\begin{pmatrix} \mathbf{c}^+ \\ \mathbf{c}^- \end{pmatrix} = \begin{pmatrix} \mathbf{M_{11}} & \mathbf{M_{12}} \\ \mathbf{M_{21}} & \mathbf{M_{22}} \end{pmatrix}\begin{pmatrix} \mathbf{c}^+ \\ \mathbf{c}^- \end{pmatrix} \tag{3.47}$$

hence:

$$-\mathbf{T} \cdot \hat{\mathbf{z}} = \mathbf{M}_{21}\mathbf{c}^+ + \mathbf{M}_{22}\mathbf{c}^- \tag{3.48}$$

from which:

$$\mathbf{c}^- = -{\mathbf{M}_{22}}^{-1}\mathbf{M}_{21}\mathbf{c}^+ \tag{3.49}$$

where:
$\mathbf{C}^+$ is the amplitude of the incident wave on the free surface while $\mathbf{C}^-$ is the reflected one;
$\mathbf{M}_{21}$ and $\mathbf{M}_{22}$ are the sub-matries of the modal matrix of the medium.

In conclusion, the scattering matrix for a free surface is given by:

$$\mathbf{S} = -{\mathbf{M}_{22}}^{-1}\mathbf{M}_{21} \tag{3.50}$$

In the same way, in the case of a clamped surface $\mathbf{v} = 0$ and:

$$\mathbf{M_{11}}\mathbf{c}^+ + \mathbf{M_{12}}\mathbf{c}^- = 0 \rightarrow \mathbf{c}^- = -{\mathbf{M}_{12}}^{-1}\mathbf{M}_{11}\mathbf{c}^+ \tag{3.51}$$

In this case we have:

$$\mathbf{S} = -\mathbf{M_{12}}^{-1}\mathbf{M_{11}} \tag{3.52}$$

3.4 Attenuation in lossy media

When a wave travels through an elastic material, the total energy contained in the wave, partitioned between elastic strain energy and kinetic energy, is conserved. A plane wave will propagate without any change in amplitude. For waves that spread out radially, such as those emanating from spherical cavities or cylindrical boreholes, the amplitude will decrease, because a finite amount of energy is spread out over a wave front having ever-increasing area. This type of amplitude decay is known as geometric attenuation and is not associated with any loss of overall kinetic energy.

However, rocks do not behave entirely elastically under transient conditions. There are numerous mechanisms which cause the kinetic energy of seismic waves to be transformed into internal energy. This energy is not lost, but rather serves to raise the temperature of the rock slightly. However, from a purely mechanical point of view, this energy appears to be "lost" or "dissipated". Hence, part of the elastic energy of a wave propagating in a real material is always converted into heat. This conversion is accompanied by a decrease in wave amplitude. Viscous damping is often used to represent this dissipation of elastic energy. A viscoelastic medium is usually modelled as a Kelvin-Voigt solid (Figure 3.6).

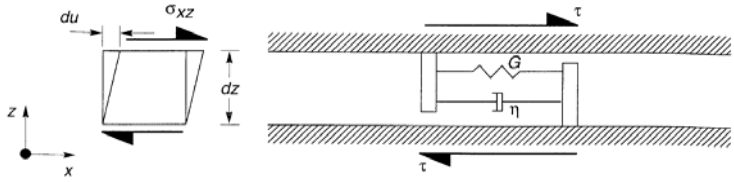

Figure 3.6 – Thin element Kelvin-Voigt solid subject to shear stress. The total resistance to shearing is the sum of an elastic component (spring) and a viscous component (damper)

The stress-strain relation, for the Kelvin-Voigt model, is assumed to be:

$$\tau = G\gamma + \eta\dot{\gamma} \tag{3.53}$$

where:
τ is the shear stress;

γ is the shear strain;
η is the viscosity of the material;
G is the shear modulus of the material;
$\dot{\gamma} = \dfrac{\partial \gamma}{\partial t}$ is the strain rate.

The shear stress is the sum of an elastic part (proportional to shear strains) and a viscous part (proportional to strain rate). For a harmonic shear strain

$$\gamma = \gamma_0 e^{j\omega t} \tag{3.54}$$

the shear stress will be:

$$\tau = \left(G + j\omega\eta\right)\gamma_0 e^{j\omega t} \tag{3.55}$$

The previous expressions show that the stress loop of Kelvin-Voigt solid is elliptical. The energy dissipation in a single cycle (Figure 3.7) is given by the ellipse area:

$$\Delta W = \int_{t_0}^{t_0 + 2\pi/\omega} \tau \frac{\partial \gamma}{\partial t} dt = \pi\eta\omega\gamma_0^2 \tag{3.56}$$

This equation shows that the dissipated energy is proportional to the frequency of the applied stress.

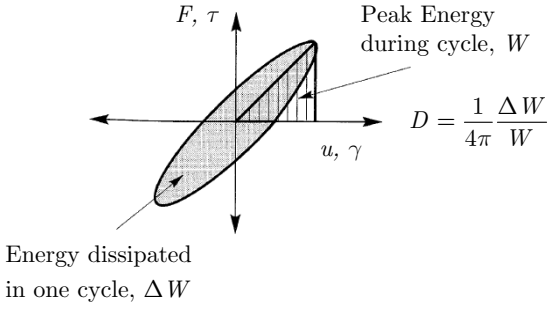

Figure 3.7 – Relation between hysteresis cycle and damping ratio

The peak of energy stored in a single cycle is:

$$W = \frac{1}{2} G \gamma_0^2 \tag{3.57}$$

Hence the damping ratio $D = \frac{1}{4\pi} \frac{\Delta W}{W}$ is given by:

$$D = \frac{1}{4\pi} \frac{\pi \eta \omega \gamma_0^2}{\frac{1}{2} G \gamma_0^2} = \frac{\eta \omega}{2G} \tag{3.58}$$

A Kelvin-Voigt solid can be represented by a series of infinitesimal elements as shown in Figure 3.6. The one-dimensional equation of motion for propagation of an S-wave can be written as:

$$\rho \frac{\partial v_y}{dt} = \frac{\partial \tau_{zy}}{dz} \tag{3.59}$$

and substituting (3.55) into the governing equation (3.59):

$$\rho \frac{\partial^2 v_y}{dt^2} = G \frac{\partial^2 v_y}{dz^2} + j\omega\eta \frac{\partial^2 v_y}{dz^2} \tag{3.60}$$

and differentiating we obtain:

$$-\rho\omega^2 V_y\left(z\right) = \left(G + j\omega\eta\right) \frac{\partial^2 V_y\left(z\right)}{dz^2} \tag{3.61}$$

where: $v_y\left(z,t\right) = V_y\left(z\right) e^{j\omega t}$.

We assume that the direction of propagation of an S-wave in an infinite extended medium coincides with z.

In these conditions, the propagation constant (or wave number) k_S is complex:

$$k_S^{*2}\left(G + j\omega\eta\right) = \rho\omega^2 \rightarrow k_S^* = \frac{\omega}{\sqrt{G^*/\rho}} = \frac{\omega}{V_S^*} \tag{3.62}$$

where:

$G^* = G + j\omega\eta$ is the complex shear modulus that can also be written as $G^* = G\left(1 + 2jD\right)$.

In order that the equation (3.62) is satisfied k_S^* must be complex and if we put it equal to $k_R + jk_I$ we obtain:

$$\begin{aligned}&\left(k_R + jk_I\right)^2\left(G + j\omega\eta\right) = \\ &= \rho\omega^2 \rightarrow k_R^2 G - k_I^2 G + 2jk_R k_I G - j\omega\eta k_R^2 + j\omega\eta k_I^2 + 2\omega\eta k_R k_I = \rho\omega^2\end{aligned} \tag{3.63}$$

and equating real and imaginary parts of (3.63) we find the following two equations:

$$\begin{aligned}G\left(k_R^2 - k_I^2\right) + 2\omega\eta k_R k_I &= \rho\omega^2 \\ 2k_R k_I G &= \omega\eta\left(k_R^2 - k_I^2\right)\end{aligned} \tag{3.64}$$

The expressions to compute the real and imaginary parts k_{zs}^* can be obtained by solving the equations (3.64) (Jaeger et al., 2007):

$$k_R = \left\{\frac{\rho G\omega^2}{2\left(G^2 + \omega^2\eta^2\right)}\left[\left(\frac{G^2 + \omega^2\eta^2}{G^2}\right)^{1/2} + 1\right]\right\}^{1/2} \tag{3.65}$$

$$k_I = \left\{\frac{\rho G\omega^2}{2\left(G^2 + \omega^2\eta^2\right)}\left[\left(\frac{G^2 + \omega^2\eta^2}{G^2}\right)^{1/2} - 1\right]\right\}^{1/2} \tag{3.66}$$

The positive root for k_R is chosen so that the wave propagates to the right, whereas the positive root must be chosen for k_I so as not to yield a wave whose amplitude grows as it propagates.

For a nonmolten rock, the elastic part of the stress would be expected to dominate the viscous part, which is to say η must in some sense be small. Expanding equations (3.65) and (3.66) for small values of η gives:

$$k_R \cong \frac{\omega}{V_S}\left[1 - \frac{3}{8}\left(\frac{\eta\omega}{G}\right)^2\right] \qquad k_I \cong \frac{\eta\omega^2}{2GV_S} \tag{3.67}$$

For lossless media the value of viscosity is zero and from the equation (3.67) we can obtain obviously that $k_R = \omega / V_S$ and $k_I = 0$.

The actual velocity, $V_{Si} = \omega / k_R$, varies with frequency, as it must for any dissipative medium, as required by the Kramers-Kroning relations (Mavko et al., 1998, pp. 75-77).

Using this further simplification, the wave (3.60) can be expressed as:

$$v\big(z,t\big) = v_0 e^{-jk_S^* z} e^{j\omega t} = v_0 e^{-k_R z} e^{-jk_I z} e^{j\omega t} \tag{3.68}$$

where:

$e^{-k_R z}$ is the attenuation factor and k_R is called attenuation constant;

$e^{-jk_I z}$ is the phase factor and k_I is the phase constant.

In Equations (3.62) and (3.68) we can see that the wave travels at velocity V_S but with an amplitude that decays exponentially with the distance. This represents the viscous attenuation, rather than the geometrical attenuation found in spherical or cylindrical waves.

According to the Kelvin model, the attenuation seems to increase with the square of the frequency. However, there are various mechanisms in rocks that give rise to viscous-like behaviour, and each has, in effect, its own dependence of η on frequency. Thus, each mechanism predicts a frequency-dependence of attenuation that will reflect both the ω^2 term from Equation (3.67) and the frequency dependence of η, usually giving rise to an exponent that differs from 2. Before discussing these dissipative mechanisms, we treat several standard definitions that are used to quantify attenuation.

The imaginary part of the wave number, k_I, is also denoted by α, the attenuation coefficient. Its inverse, $1/k_I$, is the length over which the amplitude will decay by a factor of $1/e \approx 0.37$. The mechanical energy (kinetic plus elastic strain energy) contained in a sinusoidal plane wave is proportional to the square of the amplitude so the fractional loss of energy over one wavelength is:

$$\frac{\Delta W}{W} = \frac{e^{-2\alpha z} - e^{-2\alpha(z+\lambda)}}{e^{-2\alpha z}} = 1 - e^{-2\alpha\lambda} \approx 2\alpha\lambda \tag{3.69}$$

The quality factor Q is defined in terms of this fractional energy loss as follows:

$$\frac{1}{Q} \equiv \frac{\Delta W}{2\pi W} = \frac{2\alpha\lambda}{2\pi} = \frac{2\alpha v_S}{\omega} \tag{3.70}$$

Substituting k_I from Equation (3.67) into Equation (3.70), we can shows that Q can also be expressed as:

$$\frac{1}{Q} = \frac{2\alpha v_S}{\omega} = \frac{2v_S \eta \omega^2}{2Gv_S \omega} = \frac{\eta\omega}{G} \tag{3.71}$$

It can also be shown that, if α is small, $1/Q$ is equal to the phase shift (in radians) between the stress and the strain, under sinusoidal oscillations such as described in Equation (3.55). Another parameter occasionally used to quantify attenuation in rocks is the logarithmic decrement, defined by $\delta = \pi/Q$.

Although α and Q contain the same information, α essentially measures the energy loss per distance travelled by the wave, whereas $1/Q$ measures the energy loss per wave cycle. Hence, as seen in Equation (3.71), these will vary with frequency in different ways.

Versions of the relations (3.69)-(3.71) that do not require the assumption of small attenuation are given by Bourbié et al. (1987, p. 113).

Same considerations presented in this paragraph can be done for a mono-dimensional propagation of a P-wave. Obviously normal stress τ_{zz} and complex Young's modulus $E^* = E\left(1 + 2jD\right)$ will be assumed.

3.5 Analytical solutions

In this part some analyses are presented for studying the behaviour of a welded interface between two different elastic half-spaces. We consider the effects of an interface on wave propagation by using the Scattering Matrix Method. Energy dissipation is here neglected.

The mechanical properties of the media are summarized in Table 3.1:

Table 3.1 – Properties of two media

Mechanical properties	Medium 1	Medium 2
Mass density	2000 kg/m^3	1800 kg/m^3
Velocity of the propagating P-wave	1560 m/s	700 m/s
Velocity of the propagating S-wave	955 m/s	430 m/s

The geometry of the problem can be illustrated as shown in Figure 3.8.

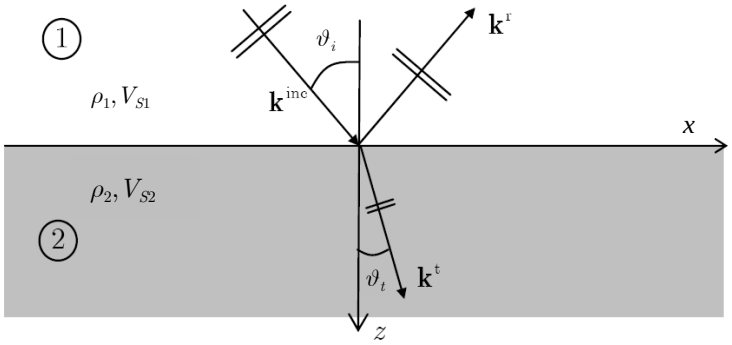

Figure 3.8 – Schematic representation of the wave propagation problem

The calculation is performed in the frequency domain and then a harmonic particle velocity input with unit amplitude and frequency $f_0 = 3Hz$ is assumed.

Figure 3.9a-b shows the magnitude of the transmission and reflection coefficients versus the angle of incidence for a SH plane wave. In Figure 3.9a, we can observe the trend of the transmission and reflection coefficients for a wave that propagates from a medium with higher stiffness to another with lower stiffness. In Figure 3.9b the opposite situation is shown. Since the media are lossless the principle of the energy conservation is satisfied:

$$\left|R_{SH}\left(\omega\right)\right|^2 + \left|T_{SH}\left(\omega\right)\right|^2 = 1 \tag{3.72}$$

where:

$R_{SH}(\omega)$ and $T_{SH}(\omega)$ are the reflection and transmission coefficients.

Obviously Equation (3.72) is true for any angle of incidence and for any frequency.

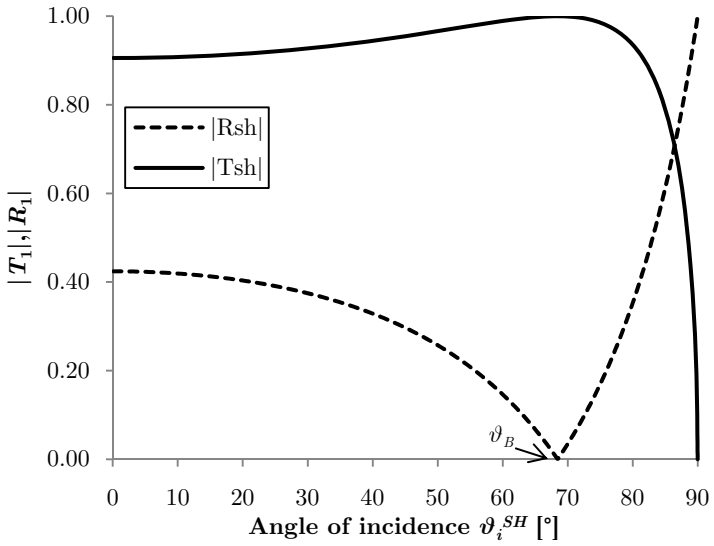

(a)

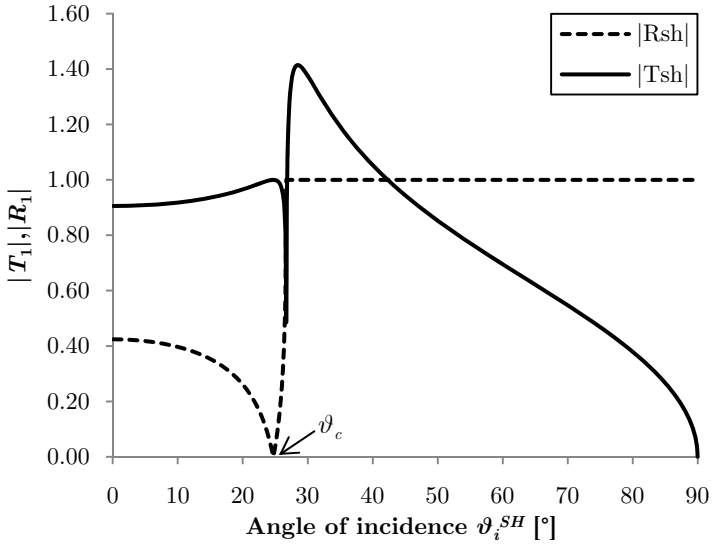

(b)

Figure 3.9 – Transmission and reflection coefficients, for a SH-wave, versus the angle of incidence ϑ_i^{SH}: wave propagation from a medium with higher stiffness to another with lower stiffness (a) and vice versa (b)

In Figure 3.9a we can see that the transmission coefficient reaches 1 ($|R_{SH}| = 0$) and for a particular angle of incidence called Brewster angle. It can be shown that this angle satisfies the condition:

$$\vartheta_B + \vartheta_t = \pi/2 \tag{3.73}$$

where:
ϑ_t is the angle between the normal at the interface and the direction of propagation of the transmitted wave.

From the refraction law we obtain:

$$\sin\vartheta_B = \sqrt{\frac{\dfrac{1}{C_{44_2}}\left(\dfrac{\rho_1}{C_{44_2}} - \dfrac{\rho_2}{C_{44_1}}\right)}{\rho_1\left(\dfrac{1}{C_{44_2}^2} - \dfrac{1}{C_{44_1}^2}\right)}} \tag{3.74}$$

Notice that the Brewster angle exists only for certain combinations of material parameters.

Developing step by step the calculation according to the Scattering Matrix Method, we can obtain the well known analytical expressions of the reflection and transmission coefficients:

$$\begin{aligned} R_{SH} &= \frac{C_{44_2}\cdot k_{zS_2} - C_{44_1}\cdot k_{zS_1}}{C_{44_2}\cdot k_{zS_2} + C_{44_1}\cdot k_{zS_1}} = \frac{\rho_2 V_{S_2}\cos\vartheta_t - \rho_1 V_{S_1}\cos\vartheta_i}{\rho_2 V_{S_2}\cos\vartheta_t + \rho_1 V_{S_1}\cos\vartheta_i} \\ T_{SH} &= \frac{2\cdot C_{44_2}\cdot k_{zS_2}}{C_{44_2}\cdot k_{zS_2} + C_{44_1}\cdot k_{zS_1}} = \frac{2\cdot\rho_2 V_{S_2}\cos\vartheta_t}{\rho_2 V_{S_2}\cos\vartheta_t + \rho_1 V_{S_1}\cos\vartheta_i} \end{aligned} \tag{3.75}$$

where:
C_{44i} is the shear modulus of medium i;
V_{Si} is the S-wave propagation velocity for medium i.

From Equations (3.75), we can see that the reflection and transmission coefficients are only function of the mechanical properties of two media and of the angle of incidence, but do not depend on frequency.

On the other hand, when a SH plane wave propagates from a less rigid medium to a more rigid medium, the trends of transmission and reflection coefficients versus

the angle of incidence change (see Figure 3.9b). It is possible to introduce a critical angle ϑ_c via

$$\vartheta_c = \arcsin \frac{V_{S_1}}{V_{S_2}} \tag{3.76}$$

If $\vartheta^{inc} < \vartheta_c$ reflection and transmission coefficients are real and satisfy (3.72). If $\vartheta^{inc} > \vartheta_c$ we have total reflection with $|R_{SH}| = 1$.

The elastic field in the second medium is an evanescent wave, i.e. a wave with exponentially decaying amplitude in the z direction. In this case (3.72) is not satisfied because $|T_{SH}|$ has no energy interpretation.

Next we have studied the same structure described in Figure 3.2 when the incident wave is P-polarized.

Two conditions were taken into account: wave propagation from a more rigid medium to a less rigid medium and vice versa (Figure 3.10a-b). As well known, an incident P-wave originates two couples of waves: reflected and transmitted P-waves and reflected and transmitted SV-waves.

In Figure 3.10, we can see the transmission and reflection coefficients vs. the P-wave angle of incidence. When the wave propagates from a less rigid medium to another more rigid, the transmission and reflection coefficients become complex.

In these conditions the definition of the critical angles is more complex and we can use the graphical method of the slowness surfaces to define them (Figure 3.11). In Figure 3.11 the radius of the cycles is the inverse of the P and S velocities of the media 1 and 2. When a P-wave impinges the interface with angle $\vartheta_c^{(1)}$ or $\vartheta_c^{(2)}$ critical transmitted P-wave or SV-wave respectively are generated.

The energy of the incident P-wave is distributed to other waves originated by the incidence with the interface. In the situation plotted in Figure 3.10a, the conservation energy equation for a P-wave that impinges on a welded interface between two media is:

$$\left|R_{PP}(\omega)\right|^2 + \left|T_{PP}(\omega)\right|^2 + \left|R_{PSV}(\omega)\right|^2 + \left|T_{PSV}(\omega)\right|^2 = 1 \tag{3.77}$$

where:

$R_{PP}(\omega)$ is the P-wave reflection coefficient for an incident P-wave;

$T_{PP}(\omega)$ is the P-wave transmission coefficient for an incident P-wave;

$R_{SVP}(\omega)$ is the SV-wave reflection coefficient for an incident P-wave;

$T_{SVP}(\omega)$ is the SV-wave transmission coefficient for an incident P-wave.

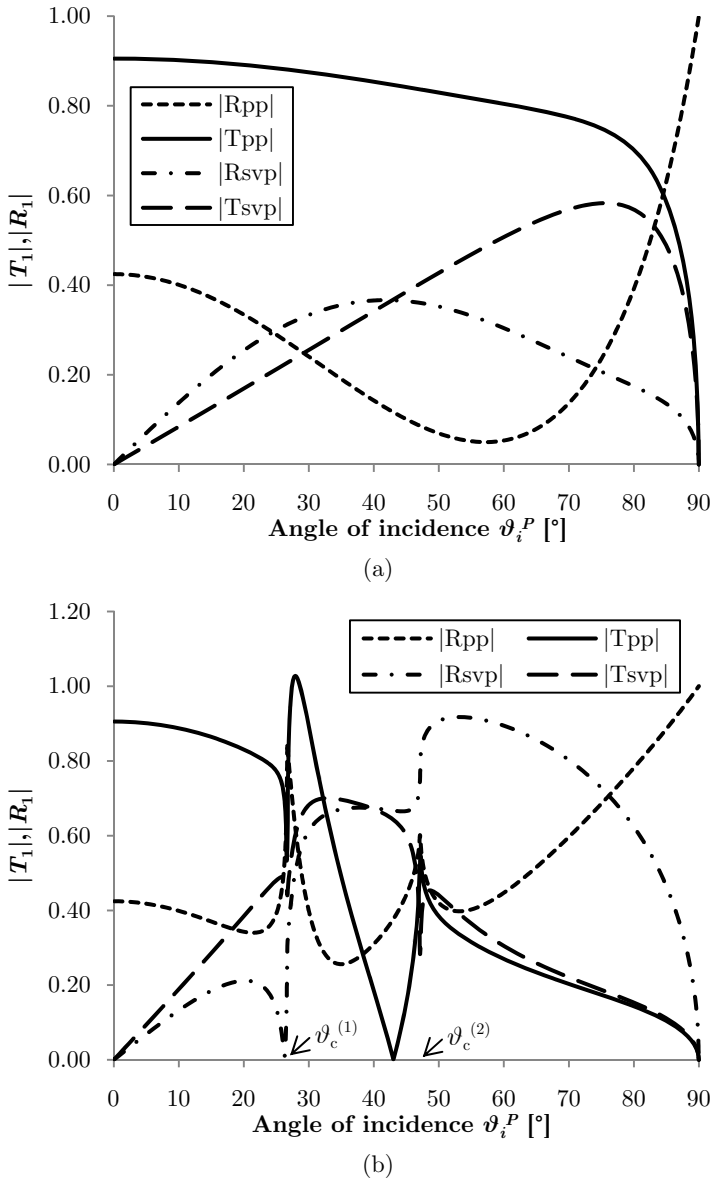

Figure 3.10 – Transmission and reflection coefficients, for a P-wave, versus the angle of incidence ϑ_i^P: wave propagation from a medium with higher stiffness to another with lower stiffness (a) and vice versa (b)

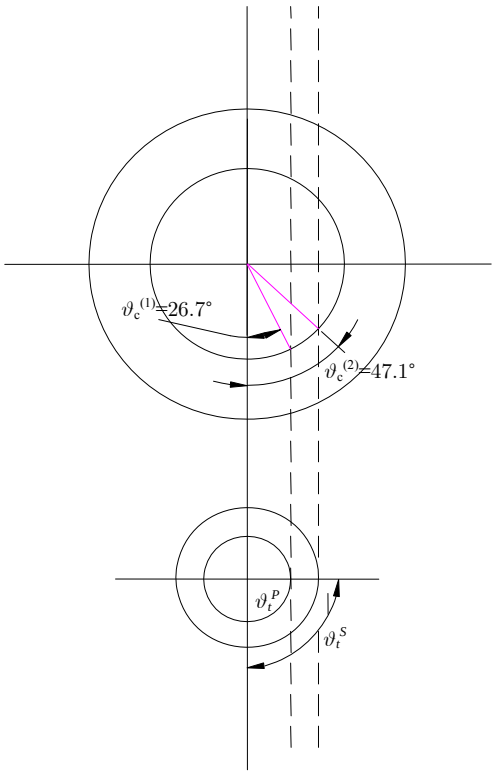

Figure 3.11 – Graphical representation of the critical angles for an incident P-wave

Similar considerations can be done for an incident plane elastic SV wave. In Figure 3.12 the magnitude of the transmission and reflection coefficients are plotted versus the angle of incidence of a SV-wave.

In Figure 3.16 the critical angles that are generated in these conditions are computed. If the SV-wave impinges the interface with an angle $\vartheta_c^{(3)}$ a critical reflected P-wave in the case (a) of Figure 3.12 is generated. In the other case, a critical transmitted P-wave and a critical transmitted SV-wave are originated respectively when the SV-wave impinges the interface with critical angles $\vartheta_c^{(4)}$ or $\vartheta_c^{(5)}$.

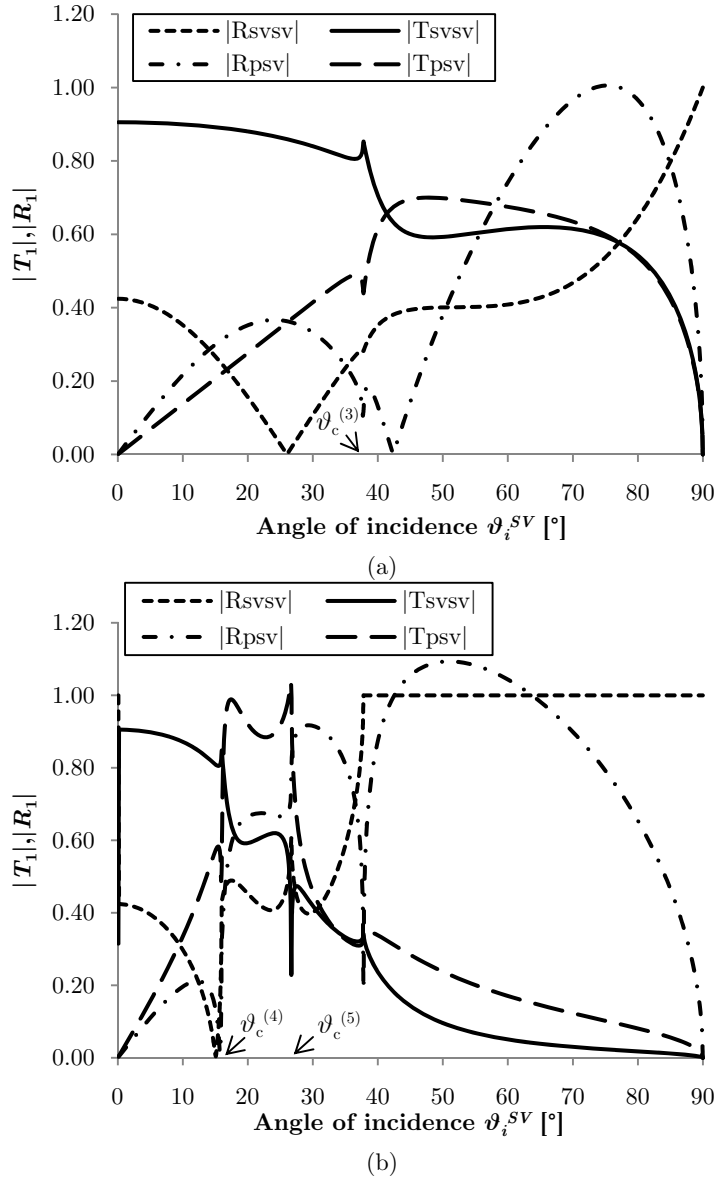

Figure 3.12 – Transmission and reflection coefficients, for a SV-wave, versus the angle of incidence ϑ_i^{SV}: wave propagation from a medium with higher stiffness to another with lower stiffness (a) and vice versa (b)

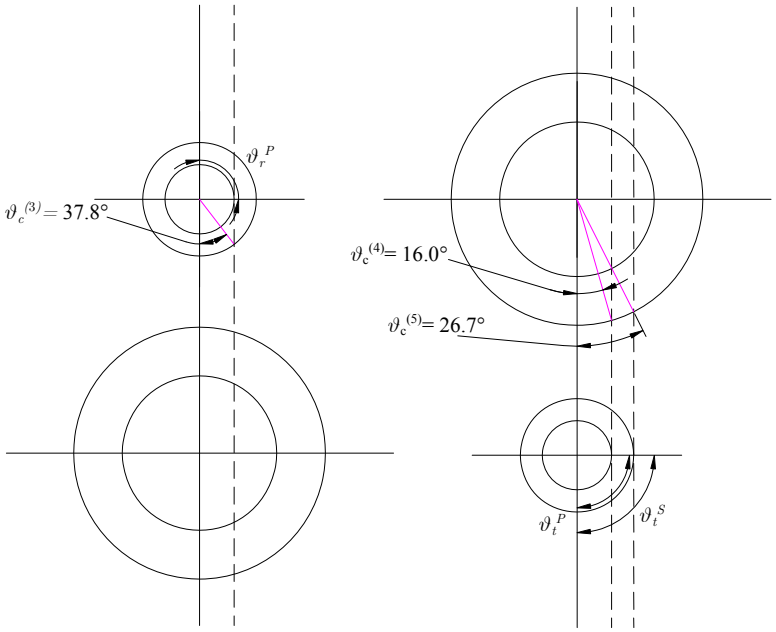

Figure 3.13 – Graphical representation of the critical angles for an incident SV-wave

3.6 Summary

In this chapter, we have presented the Scattering Matrix Method (SMM) for studying the effects of welded interfaces on wave propagation in linear elastic media. The assumption is that stresses, displacements and velocities are continuous across the welded interfaces between two adjacent media. All three wave polarizations are considered in the SMM. The SMM is extended to consider multiple reflections between N interfaces with any spacing.

The extension of the SMM to lossy media is then performed to consider the attenuation of the wave in these media. From a purely mechanical point of view, in these media part of the wave energy appears to be "dissipated" although the kinetic energy of the wave is transformed into internal energy.

Transmission and reflection coefficients versus the angle of incidence are computed for all three possible incident waves. Critical angles are found in SMM results and with the graphical method of the slowness surfaces.

These analyses highlight that when a plane elastic wave impinges on a welded interface the scattered waves are dependent on the impedance of two media and on the angle of incidence.

Finally, we have presented the SMM as used to study wave propagation across a continuous stratified or layered medium. In the next part (Chapter 4) we will describe the extension of this method to wave propagation in a discontinuous medium with non-welded interfaces.

Chapter 4

The Scattering Matrix Method and the study of wave propagation in discontinuous media

4.1 Introduction

The purpose of this chapter is to study the influence of rock joints on wave propagation by the Scattering Matrix Method. In Chapter 3 we have analysed the use of this method for the study of wave propagation in a continuum containing welded interfaces. In this chapter we will focus on non-welded interfaces representing the rock joints in a rock mass, i.e. a discontinuum.

The influence of rock joints on wave propagation is taken into account by using the displacement discontinuity method (DDM), whereby the displacements across a joint are discontinuous while the tractions are continuous. The joints are considered to be planar, large in extent and small in thickness compared to the wavelength.

Reflected and transmitted waves are calculated for one and more joints in dry or fluid filled conditions. Some analyses are also carried out for studying the influence of the characteristic parameters on wave propagation in a discontinuum.

4.2 Rock joint modelling

The Scattering Matrix Method (SMM) can model a rock joint by using the DDM. In this way one assumes that the displacements across a joint are discontinuous while the tractions are continuous. Moreover the amount of the discontinuity is assumed proportional to the traction. The general formulation of the SMM for a medium with joints is the same as used for continuous media with welded interfaces (Chapter 3). The presence of a discontinuity of displacement generates a change of its transmission matrix.

It is interesting to note that there is a formal analogy between the equations of elastic wave propagation and the equations of electrical transmission lines (Anderson, 1985 and Auld, 1973). In particular, the velocity can be identified with a current and the traction with a voltage, both of vector type. This implies that the joint has an "equivalent circuit" in the form of an admittance connected in parallel to the transmission line describing propagation in the homogeneous medium. This admittance depends of course on the characteristics of the joint, whether it is dry or fluid filled. The admittance can be also called compliance.

The geometry of the problem is shown in Figure 4.1.

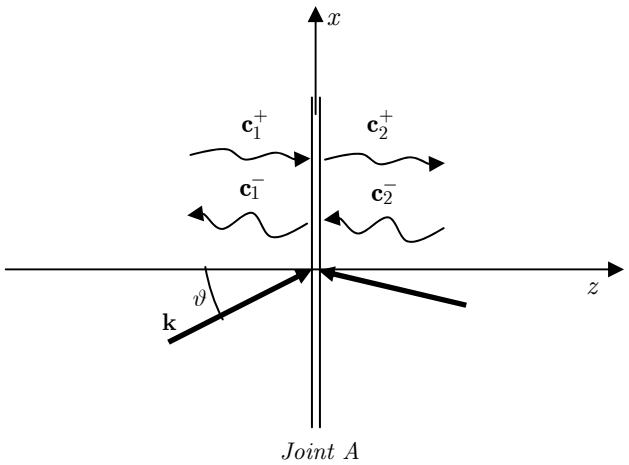

Figure 4.1 – Wave propagation through a single rock joint

Rock joints pertain to a type of discontinuity that is generally known as non-welded interface. In this part we consider two types of rock joints:

- Linear elastic, dry joint;
- Joints filled with fluid or soft material (Kelvin, Maxwell and Burger models).

The definition of the admittance (or compliance) $\mathbf{Y}$ for each type of joint is the fundamental step for obtaining the transmission matrix of the joint.

The boundary conditions along a joint, according to the displacement discontinuity model, are:

$$\begin{aligned} \left(\mathbf{u}_{A-} - \mathbf{u}_{A+}\right) &= \mathbf{B} \cdot \boldsymbol{\tau}_A \\ \boldsymbol{\tau}_A - \boldsymbol{\tau}_{A+} &= 0 \end{aligned} \tag{4.1}$$

The corresponding condition for the velocity is:

$$\left(\mathbf{v}_{A-} - \mathbf{v}_{A+}\right) = \mathbf{Y} \cdot \boldsymbol{\tau}_A \tag{4.2}$$

where:
$\mathbf{u}_{A-}$, $\mathbf{u}_{A+}$ are the displacements of the left side and of the right side of the joint A;

$\mathbf{v}_{A-}$, $\mathbf{v}_{A+}$ are the particle velocities of the two sides of the joint A;
$\mathbf{Y} = j\omega\mathbf{B}$ is the joint admittance;
$\boldsymbol{\tau}_A = \boldsymbol{\tau}_{A-} = \boldsymbol{\tau}_{A+} = -\mathbf{T}_A \cdot \hat{\mathbf{z}}$ is the traction on the joint surface A.

4.2.1 Linear elastic dry rock joint

Displacements and tractions across a linear elastic dry rock joint are linearly linked by a normal stiffness k_{nn} and a shear stiffness k_{ss} of the joint. These values of specific stiffness have units of stress over length. For obtaining the characteristic admittance $\mathbf{Y}$ of the discontinuity, it is necessary to rewrite Equation (4.1) of displacement discontinuity:

$$\mathbf{K}\left(\mathbf{u}_{A-} - \mathbf{u}_{A+}\right) = \boldsymbol{\tau}_A \tag{4.3}$$

where $\mathbf{K}$ is the matrix in which normal and shear dynamic joint stiffness are stored. The inverse of this matrix is the matrix $\mathbf{B}$ in which are stored the joint compliances. Taking the time derivative of the previous equation we can obtain the particle velocity discontinuity relation:

$$\Delta\mathbf{v} = \mathbf{v}_{A-} - \mathbf{v}_{A+} = \mathbf{Y} \cdot \boldsymbol{\tau}_A \tag{4.4}$$

from where we can derive the admittance of a linear elastic dry joint:

$$\mathbf{Y} = j\omega\mathbf{K}^{-1} \tag{4.5}$$

If the joint is of the simplest type, i.e. it is characterized by normal and shear stiffness only, the $\mathbf{K}$ matrix is diagonal:

$$\mathbf{K} = \begin{pmatrix} k_{ss} & 0 & 0 \\ 0 & k_{ss} & 0 \\ 0 & 0 & k_{nn} \end{pmatrix} \begin{matrix} \leftarrow x \\ \leftarrow y \\ \leftarrow z \end{matrix} \qquad \begin{matrix} \uparrow & \uparrow & \uparrow \\ x & y & z \end{matrix} \tag{4.6}$$

Clearly, also in this case SH-waves are decoupled from P and SV, and

$$\mathbf{Y} = j\omega\mathbf{K}^{-1} = \begin{pmatrix} j\omega\dfrac{1}{k_{ss}} & 0 & 0 \\ 0 & j\omega\dfrac{1}{k_{ss}} & 0 \\ 0 & 0 & j\omega\dfrac{1}{k_{nn}} \end{pmatrix} \tag{4.7}$$

Equation (4.7) highlights that, obviously, the compression waves are linked with the normal displacements along the discontinuity while the shear waves mobilize the shear displacement for a normal incident wave. When a P or SV-wave impinges not normally on a discontinuity the normal and shear displacements are mobilized.

4.2.2 Joints filled with fluid or soft material

A joint filled with fluid or a soft material can be modelled by using rheological models. These models have been presented in the literature in order to describe the time dependent behaviour of metals, steel (at high temperature) and fluids, and have been extended to geomaterials. They are generally formulated with reference to one-dimensional conditions and supply directly the fundamental relationships that govern the time dependency, either in a differential or in a closed form. A subgroup of rheological models is the analogical or mechanical rheological model. In this case the constitutive relations are constructed by combining, in series or in parallel, different elementary material models.

Therefore, rheological models are used to model joints with dissipation. In literature some models were proposed (e.g. Myer et al., 1990) to simulate the effects of joints filled with fluid or soft materials. Filled joints are generally represented by using the Kelvin-Voigt or Maxwell models. The Kelvin-Voigt model, also called the Voigt model, can be represented by a purely viscous damper and a purely elastic spring connected in parallel as illustrated in Figure 4.2a. The Maxwell model can be represented by a purely viscous damper and a purely elastic spring connected in series as shown in Figure 4.2b. In this study we consider also the Burger model shown in Figure 4.2c, which is obtained by connecting in series the Kelvin-Voigt and the Maxwell models.

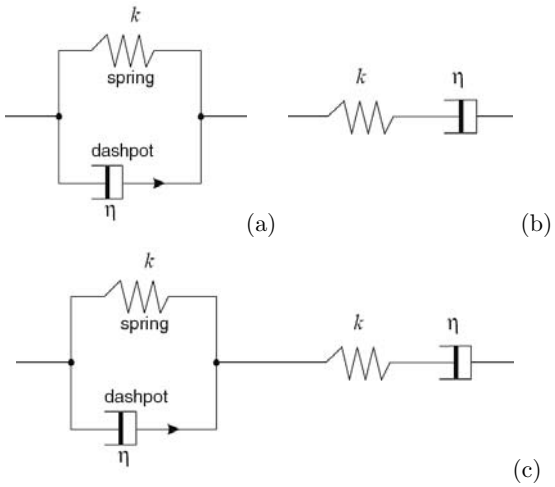

Figure 4.2 – Viscoelastic models of Kelvin-Voigt (a), of Maxwell (b) and of Burger (c)

The admittance of a filled joint depends on the type of rheological model. For simplicity, the process for computing the joint admittance is explained in detail for the SH-wave polarization while for P and SV-waves only the final expressions are reported.

The combined effect of the displacement discontinuity resulting from the fracture impedance, Equation (4.5), and the presence of a viscous fluid in the fracture can be expressed as a superposition of the two effects.

This can be accomplished in at least two simple ways. First, if we consider both the liquid film and the solid asperities as undergoing a common displacement under the effect of the applied stress, the averaged stress along the surfaces of contact is given by the sum of the stresses originating within the liquid film and within the contacting asperities. This case is commonly represented by the Kelvin-Voigt model.

If instead we assume the stress to be in common to both the solid asperities and the liquid film, the resultant overall displacement is expressed as the sum of the displacements in the two individual components. In this case, the representative model is the Maxwell viscoelastic model.

Starting from the Kelvin-Voigt model, the first step is the definition of the boundary conditions across the joint:

$$\text{displacement discontinuity:} \quad \begin{array}{l} k_{ss}\left(u_{A-}-u_{A+}\right)+\eta_y\left(v_{A-}-v_{A+}\right)=\tau_A \rightarrow \\ \rightarrow k_{ss}\left(u_{y-}-u_{y+}\right)+\eta_y\left(v_{y-}-v_{y+}\right)=\tau_{zy} \end{array} \tag{4.8}$$

$$\text{continuity of stress: } \tau_{A-} - \tau_{A+} = 0 \rightarrow \tau_{zy-} - \tau_{zy+} = 0$$

where $\eta_y = \mu/h$, is the fracture specific viscosity in the y direction of the fluid or the soft material that fills the joint. The specific viscosity η has units of viscosity over length (kg/m^2s), and represents the dissipative characteristic of the interface. μ is the dynamic viscosity (kg/ms) while h is the thickness of the liquid film between two faces.

From time derivation of the equation of displacement discontinuity we can obtain the discontinuity velocity relation:

$$k_{ss}\left(v_{y-} - v_{y+}\right) + j\omega\eta_y\left(v_{y-} - v_{y+}\right) = j\omega\tau_{zy} \tag{4.9}$$

and by introducing some simplifications we can derive the joint admittance for the Kelvin-Voigt model:

$$\left(v_{y-} - v_{y+}\right) = \frac{j\omega}{k_{ss} + j\omega\eta_y}\tau_{zy} = Y \cdot \tau_{zy} \longrightarrow Y = \frac{j\omega}{k_{ss} + j\omega\eta_y} \tag{4.10}$$

Similar expressions can be obtained for P and SV-wave polarizations:

$$\mathbf{Y} = \begin{pmatrix} \dfrac{j\omega}{k_{ss} + j\omega\eta_x} & 0 \\ 0 & \dfrac{j\omega}{k_{nn} + j\omega\eta_z} \end{pmatrix} \tag{4.11}$$

where η_x and η_z are the specific viscosity respectively in x and in z direction.

Instead, the boundary conditions for a Maxwell model are the following:

$$\begin{aligned} &\text{velocity discontinuity:} \quad \left(v_{y-} - v_{y+}\right) = \frac{j\omega\tau_{zy}}{k_{ss}} + \frac{\tau_{zy}}{\eta_y} \\ &\text{continuity of stress:} \quad \tau_{zy-} - \tau_{zy+} = 0 \end{aligned} \tag{4.12}$$

$$
\begin{aligned}
Y &= \left(\frac{j\omega}{k_{ss}} + \frac{1}{\eta_y} \right) \text{ for SH-waves} \\
\mathbf{Y} &= \begin{pmatrix} \left(\dfrac{j\omega}{k_{ss}} + \dfrac{1}{\eta_x} \right) & 0 \\ 0 & \left(\dfrac{j\omega}{k_{nn}} + \dfrac{1}{\eta_z} \right) \end{pmatrix} \text{ for P and SV-waves}
\end{aligned}
\tag{4.13}
$$

If the joint contains only a viscous liquid without any contact between the asperities of two faces, the stiffness can be assumed to be equal to zero and the admittance of the joint becomes $Y = 1/\eta$. Obviously, this result can be obtained with either the Kelvin-Voigt or the Maxwell model.

This methodology can be also implemented in the SMM by using a more complex model as the Burger model. The velocity for the Burger model is given by the sum of the velocities in the Kelvin-Voigt and Maxwell models:

$$
\begin{aligned}
&\left(v_{y-} - v_{y+} \right) = \left(v_{y-} - v_{y+} \right)_{kelvin} + \left(v_{y-} - v_{y+} \right)_{\max well} = \\
&= \left(\frac{j\omega}{k_{ss}^{(k)} + j\omega\eta_y^{(k)}} + \frac{j\omega}{k_{ss}^{(m)}} + \frac{1}{\eta_y^{(m)}} \right) \tau_{zy}
\end{aligned}
\tag{4.14}
$$

Hence, the admittance of the joint modelled with the Burger model is:

$$
\begin{aligned}
Y &= \left(\frac{j\omega}{k_{ss}^{(k)} + j\omega\eta_y^{(k)}} + \frac{j\omega}{k_{ss}^{(m)}} + \frac{1}{\eta_y^{(m)}} \right) \text{ for SH-waves} \\
\mathbf{Y} &= \begin{pmatrix} \left(\dfrac{j\omega}{k_{ss}^{(k)} + j\omega\eta_x^{(k)}} + \dfrac{j\omega}{k_{ss}^{(m)}} + \dfrac{1}{\eta_x^{(m)}} \right) & 0 \\ 0 & \left(\dfrac{j\omega}{k_{nn}^{(k)} + j\omega\eta_z^{(k)}} + \dfrac{j\omega}{k_{nn}^{(m)}} + \dfrac{1}{\eta_z^{(m)}} \right) \end{pmatrix} \\
&\qquad \text{for P and SV waves}
\end{aligned}
\tag{4.15}
$$

where with the apexes (k) and (m) indicate respectively the parameters of Kelvin-Voigt and Maxwell models. The admittance of the Burger model was obtained after the computation of the relative velocity between the two sides of the joint. This relative velocity is computed by the sum of two contributions: one from the Kelvin-Voigt model and the other one from the Maxwell model.

4.3 Application of the Scattering Matrix Method to wave propagation in jointed rock masses

With the admittance matrix for each type of joint being derived, we can develop the procedure to compute the transmission matrix for a non-welded interface. The state vector of the elastic fields at the two sides of a joint can be written as (see (3.30)):

$$\begin{pmatrix} \mathbf{v}_{A-} \\ \boldsymbol{\tau}_{A-} \end{pmatrix} = \mathbf{M_1} \cdot \begin{pmatrix} \mathbf{c_1}^{+} \\ \mathbf{c_1}^{-} \end{pmatrix} \qquad \begin{pmatrix} \mathbf{v}_{A+} \\ \boldsymbol{\tau}_{A+} \end{pmatrix} = \mathbf{M_2} \cdot \begin{pmatrix} \mathbf{c_2}^{+} \\ \mathbf{c_2}^{-} \end{pmatrix} \tag{4.16}$$

where:
$\mathbf{M}_1$, $\mathbf{M}_2$ are the modal matrices of the media 1 and 2;
$\mathbf{c}_1^{+}$, $\mathbf{c}_2^{-}$ are the amplitudes of the incident waves;
$\mathbf{c}_1^{-}$, $\mathbf{c}_2^{+}$ are the amplitudes of the scattered waves (reflected and transmitted).

By applying the boundary condition at (4.2), we get

$$\begin{pmatrix} \mathbf{v}_{A-} - \mathbf{Y} \cdot \boldsymbol{\tau}_A \\ \boldsymbol{\tau}_A \end{pmatrix} = \begin{pmatrix} \mathbf{I} & -\mathbf{Y} \\ 0 & \mathbf{I} \end{pmatrix} \cdot \begin{pmatrix} \mathbf{v}_{A-} \\ \boldsymbol{\tau}_{A-} \end{pmatrix} = \begin{pmatrix} \mathbf{v}_{A+} \\ \boldsymbol{\tau}_{A+} \end{pmatrix} = \mathbf{M_2} \cdot \begin{pmatrix} \mathbf{c_2}^{+} \\ \mathbf{c_2}^{-} \end{pmatrix} \tag{4.17}$$

where $\mathbf{I}$ is the identity matrix.

From this we obtain

$$\begin{pmatrix} \mathbf{C_1}^{+} \\ \mathbf{C_1}^{-} \end{pmatrix} = \mathbf{M_1}^{-1} \begin{pmatrix} \mathbf{v}_{A-} \\ \boldsymbol{\tau}_{A-} \end{pmatrix} = \mathbf{M_1}^{-1} \begin{pmatrix} \mathbf{I} & -\mathbf{Y} \\ 0 & \mathbf{I} \end{pmatrix}^{-1} \mathbf{M_2} \begin{pmatrix} \mathbf{c_2}^{+} \\ \mathbf{c_2}^{-} \end{pmatrix}. \tag{4.18}$$

Therefore, the transmission matrix of the joint is:

$$\mathbf{A} = \mathbf{M_1}^{-1} \begin{pmatrix} \mathbf{I} & \mathbf{Y} \\ 0 & \mathbf{I} \end{pmatrix} \mathbf{M_2} \tag{4.19}$$

This equation should be compared with Equation (3.34), which refers to a welded interface. As $\mathbf{Y}$ changes from 0 to ∞ the joint changes from a welded interface to an impenetrable free surface.

The scattering matrix can be derived from the transmission matrix in the same manner as described for a welded interface (see Equation (3.36)).

4.4 Evaluation of the effects of a single joint with the Scattering Matrix Method

In this paragraph, we discuss the effects of a single joint on wave propagation. The analytical SMM is presented step by step.

Analytical expressions of transmission and reflection coefficients for a wave that impinges a single joint are well known (e.g. Schoenberg, 1980; Myer et al., 1990; Pyrak-Nolte et al., 1990a). In this part, these analytical expressions of reflection and transmission coefficients will be obtained by using the SMM.

Firstly, we consider in the following the problem of wave propagation across a single rock joint (Figure 4.1) in a homogeneous medium.

The wave vectors of the two incident waves have the same components along the interface. Initially we consider the case of an incident SH-wave that impinges on a single joint. For SH polarization state the modal matrix (size 2x2) is the following:

$$\mathbf{M_1} = \begin{bmatrix} N^{SH+} & N^{SH-} \\ \dfrac{C_{44}k_{zS}}{\omega}N^{SH+} & -\dfrac{C_{44}k_{zS}}{\omega}N^{SH-} \end{bmatrix} = \mathbf{M_2} \tag{4.20}$$

(see equation (3.31)).

From Equation (4.19), we can write the transmission matrix **A**:

$$\mathbf{M_1}^{-1} = \begin{bmatrix} \dfrac{1}{2N^{SH}} & \dfrac{\omega}{2C_{44}k_{zS}N^{SH}} \\ \dfrac{1}{2N^{SH}} & -\dfrac{\omega}{2C_{44}k_{zS}N^{SH}} \end{bmatrix}$$

The transmission matrix is then:

$$\mathbf{A} = \begin{bmatrix} \dfrac{1}{2N^{SH}} & \dfrac{\omega}{2C_{44}k_{zS}N^{SH}} \\ \dfrac{1}{2N^{SH}} & -\dfrac{\omega}{2C_{44}k_{zS}N^{SH}} \end{bmatrix} \begin{bmatrix} 1 & Y \\ 0 & 1 \end{bmatrix} \begin{bmatrix} N^{SH} & N^{SH} \\ \dfrac{C_{44}k_{zS}}{\omega}N^{SH} & -\dfrac{C_{44}k_{zS}}{\omega}N^{SH} \end{bmatrix}$$

where the shear wave characteristic impedance (or acoustic impedance) is:

$$Z_S = \frac{C_{44} \cdot k_{zS}}{\omega} = \frac{C_{44} \cdot k_S \cdot \cos\vartheta}{\omega} = \frac{\left(\rho \cdot V_S^2\right) \cdot \left(\omega / V_S\right) \cdot \cos\vartheta}{\omega} = \rho \cdot V_S \cdot \cos\vartheta \ .$$

Hence, the final expression of the transmission matrix for a joint with admittance Y is:

$$\mathbf{A} = \begin{bmatrix} A_{11} & A_{12} \\ A_{21} & A_{22} \end{bmatrix} = \begin{bmatrix} 1 + \frac{Z_S}{2} Y & -\frac{Z_S}{2} Y \\ \frac{Z_S}{2} Y & 1 - \frac{Z_S}{2} Y \end{bmatrix} \tag{4.21}$$

Now we can obtain, from the transmission matrix and after some algebraic manipulations (see Equation (3.36) in Chapter 3), the scattering matrix **S** of a single joint. Hence the analytical expressions of the reflection R_{SH} and the transmission T_{SH} coefficients for a SH-wave that impinges a single joint are:

$$\begin{aligned} R_{SH}\left(\omega, \vartheta\right) &= \mathbf{S}(1,1) = A_{21} {A_{11}}^{-1} = \frac{Z_S Y}{2 + Z_S Y} \\ T_{SH}\left(\omega, \vartheta\right) &= \mathbf{S}(2,1) = {A_{11}}^{-1} = \frac{2}{2 + Z_S Y} \end{aligned} \tag{4.22}$$

The equations (4.22) define the reflection and transmission coefficients versus the angle of incidence ϑ and the frequency ω for a rock joint with admittance Y.

Analytical expressions of the transmission and reflection coefficients for the types of joints considered in this thesis are:

- Linear elastic dry joint:

  $$Y = j\omega \frac{1}{k_{ss}}$$

$$\begin{aligned} T_{SH}\left(\omega, \vartheta\right) &= \frac{2\left(\frac{k_{ss}}{Z_S}\right)}{j\omega + 2\left(\frac{k_{ss}}{Z_S}\right)} \\ R_{SH}\left(\omega, \vartheta\right) &= \frac{j\omega}{j\omega + 2\left(\frac{k_{ss}}{Z_S}\right)} \end{aligned} \tag{4.23}$$

- Joint filled with fluid or soft material:
  - Kelvin-Voigt model

$$Y = \frac{j\omega}{k_{ss} + j\omega\eta_y}$$

$$\begin{aligned} T_{SH}\left(\omega,\vartheta\right) &= \frac{2\left(k_{ss} + j\omega\eta_y\right)}{2k_{ss} + j\omega\left(2\eta_y + Z_S\right)} \\ R_{SH}\left(\omega,\vartheta\right) &= \frac{j\omega Z_s}{2k_{ss} + j\omega\left(2\eta_y + Z_S\right)} \end{aligned} \tag{4.24}$$

  - Maxwell model

$$Y = \frac{j\omega}{k_{ss}} + \frac{1}{\eta_y}$$

$$\begin{aligned} T_{SH}\left(\omega,\vartheta\right) &= \frac{\left(1 + \frac{Z_S}{2\eta_y}\right) + \frac{j\omega Z_S}{2k_{ss}}}{\left(1 + \frac{Z_S}{2\eta_y}\right)^2 + \left(\frac{\omega Z_S}{2k_{ss}}\right)^2} \\ R_{SH}\left(\omega,\vartheta\right) &= \frac{\frac{Z_S}{2\eta_y}\left(1 + \frac{Z_S}{2\eta_y}\right) + \frac{\omega Z_S}{2k_{ss}}\left(\frac{\omega Z_S}{2k_{ss}} + j\right)}{\left(1 + \frac{Z_S}{2\eta_y}\right)^2 + \left(\frac{\omega Z_S}{2k_{ss}}\right)^2} \end{aligned} \tag{4.25}$$

  - Burger model

$$Y = \frac{j\omega}{k_{ss} + j\omega\eta_y} + \frac{j\omega}{k_{ss}} + \frac{1}{\eta_y}$$

$$T_{SH}\left(\omega,\vartheta\right) = \frac{2\left(k_{ss} + j\omega\eta_y\right)}{k_{ss}\left(2 + \frac{Z_S}{\eta_y}\right) - \omega^2\eta_y\frac{Z_S}{k_{ss}} + j\omega\left(2\eta_y + 3Z_S\right)} \tag{4.26}$$

$$R_{SH}\left(\omega,\vartheta\right)=T_{SH}\left(\omega,\vartheta\right)\cdot\frac{Z_S\left(\dfrac{j\omega}{k_{ss}+j\omega\eta_y}+\dfrac{j\omega}{k_{ss}}+\dfrac{1}{\eta_y}\right)}{2}$$

The previous equations are the same, except from the sign of the imaginary part, as those presented by Myer L.R. et al. (1990). In fact, Myer uses the time convention $e^{-j\omega t}$ while we have assumed $e^{j\omega t}$, hence the final expressions have the imaginary part with opposite sign.

The magnitude and the phase angle of the transmission and reflection coefficients can be computed by the general expressions shown in Equations (4.23)-(4.26). The transmission and reflection coefficients in terms of their magnitudes and phase angles $\Theta(\omega,\vartheta)$ can be written as follows:

$$\begin{aligned}T_{SH}\left(\omega,\vartheta\right)&=\left|T_{SH}\left(\omega,\vartheta\right)\right|e^{i\omega\Theta_T}\\R_{SH}\left(\omega,\vartheta\right)&=\left|R_{SH}\left(\omega,\vartheta\right)\right|e^{i\omega\Theta_R}\end{aligned}\tag{4.27}$$

As an example, we only consider the linear elastic joint behaviour, but obviously the procedure is the same for the other models:

$$\begin{aligned}\left|T_{SH}\left(\omega,\vartheta\right)\right|&=\sqrt{\frac{\left(\dfrac{2k_{ss}}{Z_S}\right)^4+\omega^2\left(\dfrac{2k_{ss}}{Z_S}\right)^2}{\left[\left(\dfrac{2k_{ss}}{Z_S}\right)^2+\omega^2\right]^2}}\qquad\Theta_T\left(\omega,\vartheta\right)=arctg\left(\frac{\omega}{2\left(\dfrac{k_{ss}}{Z_S}\right)}\right)\\\left|R_{SH}\left(\omega,\vartheta\right)\right|&=\sqrt{\frac{\omega^2\left(\dfrac{2k_{ss}}{Z_S}\right)^2+\omega^4}{\left[\left(\dfrac{2k_{ss}}{Z_S}\right)^2+\omega^2\right]^2}}\qquad\Theta_R\left(\omega,\vartheta\right)=arctg\left(\frac{-2\left(\dfrac{k_{ss}}{Z_S}\right)}{\omega}\right)\end{aligned}\tag{4.28}$$

The group time delay for the transmitted and reflected waves can be computed as follows:

$$t_{gT} = \frac{d\Theta_T}{d\omega} = \frac{2\left(\frac{k_{ss}}{Z_S}\right)}{4\left(\frac{k_{ss}}{Z_S}\right)^2 + \omega^2}$$
$$t_{gR} = \frac{d\Theta_R}{d\omega} = \frac{2\left(\frac{k_{ss}}{Z_S}\right)}{4\left(\frac{k_{ss}}{Z_S}\right)^2 + \omega^2} \tag{4.29}$$

The transmitted and the reflected group time delays are equal and at zero frequency the group time delay becomes $t_{g0} = Z_S/2k_{ss}$. The group time delay is maximum when the frequency is zero and decreases with increasing the frequency as we can see in Equations (4.29).

On the other hand, if we have a SV or a P-wave that impinges a joint, the modal matrix has size 4x4 and it is the following:

$$\mathbf{M_1} = \begin{bmatrix} \frac{k_{zS}}{k_S} N^{SV+} & \frac{\xi}{k_P} N^{P+} & \frac{k_{zS}}{k_S} N^{SV-} & \frac{\xi}{k_P} N^{P-} \\ -\frac{\xi}{k_S} N^{SV+} & \frac{k_{zP}}{k_P} N^{P+} & \frac{\xi}{k_S} N^{SV-} & -\frac{k_{zP}}{k_P} N^{P-} \\ M_{1-31} & M_{1-32} & M_{1-33} & M_{1-34} \\ M_{1-41} & M_{1-42} & M_{1-43} & M_{1-44} \end{bmatrix} \tag{4.30}$$

where:

$$M_{1-31} = \frac{C_{44}k_{zS}}{\omega}\frac{k_{zS}}{k_S} N^{SV+} - \frac{C_{44}\xi}{\omega}\frac{\xi}{k_S} N^{SV+}$$
$$M_{1-41} = \frac{C_{12}\xi}{\omega}\frac{k_{zS}}{k_S} N^{SV+} - \frac{C_{11}k_{zS}}{\omega}\frac{\xi}{k_S} N^{SV+}$$
$$M_{1-32} = \frac{C_{44}k_{zP}}{\omega}\frac{\xi}{k_P} N^{P+} + \frac{C_{44}\xi}{\omega}\frac{k_{zP}}{k_P} N^{P+}$$
$$M_{1-42} = \frac{C_{12}\xi}{\omega}\frac{\xi}{k_P} N^{P+} + \frac{C_{11}k_{zP}}{\omega}\frac{k_{zP}}{k_P} N^{P+}$$

$$M_{1-33} = -\frac{C_{44}k_{zS}}{\omega}\frac{k_{zS}}{k_S}N^{SV-} + \frac{C_{44}\xi}{\omega}\frac{\xi}{k_S}N^{SV-}$$
$$M_{1-43} = \frac{C_{12}\xi}{\omega}\frac{k_{zS}}{k_S}N^{SV-} - \frac{C_{11}k_{zS}}{\omega}\frac{\xi}{k_S}N^{SV-}$$
$$M_{1-34} = -\frac{C_{44}k_{zP}}{\omega}\frac{\xi}{k_P}N^{P-} - \frac{C_{44}\xi}{\omega}\frac{k_{zP}}{k_P}N^{P-}$$
$$M_{1-44} = \frac{C_{12}\xi}{\omega}\frac{\xi}{k_P}N^{P-} + \frac{C_{11}k_{zP}}{\omega}\frac{k_{zP}}{k_P}N^{P-}$$

In this study, for simplicity, we consider that P or SV-waves impinge on a joint normally. In this condition we can consider separately the P and SV-waves. In fact, from an inclined incident P wave scattered P and SV-waves are generated and vice-versa. The general case of an inclined P or SV-wave was solved by implementing in Matlab the SMM algorithm.

The modal matrix, for normal P and SV incident waves ($\vartheta^{inc} = 0°$), can be simplified in two matrices:

$$\mathbf{M_1^P} = \begin{bmatrix} N^{P+} & -N^{P-} \\ \dfrac{C_{11}k_{zP}}{\omega}N^{P+} & \dfrac{C_{11}k_{zP}}{\omega}N^{P-} \end{bmatrix} = \mathbf{M_2^P} \text{ for P-wave}$$
$$\mathbf{M_1^{SV}} = \begin{bmatrix} N^{SV+} & N^{SV-} \\ \dfrac{C_{44}k_{zS}}{\omega}N^{SV+} & -\dfrac{C_{44}k_{zS}}{\omega}N^{SV-} \end{bmatrix} = \mathbf{M_2^{SV}} \text{ for SV-wave}$$

We can perform the following simplifications:

$$\xi = k_P \sin\vartheta^P = k_S \sin\vartheta^{SV} = 0$$
$$k_{zP} = k_P \cos\vartheta^P = k_P$$
$$k_{zS} = k_S \cos\vartheta^{SV} = k_S$$

By following the same computational procedure described above, we obtain the analytical expressions of the transmission and reflection coefficients for a P or SV-wave that normally impinges on a single joint:

$$R_P(\omega) = \frac{-Z_P Y_P}{2 + Z_P Y_P} \tag{4.31}$$

$$
\begin{aligned}
T_P\left(\omega\right) &= \frac{2}{2 + Z_P Y_P} \\
R_{SV}\left(\omega\right) &= \frac{Z_S Y_S}{2 + Z_S Y_S} \\
T_{SV}\left(\omega\right) &= \frac{2}{2 + Z_S Y_S}
\end{aligned}
\tag{4.32}
$$

where:
Y_P and Y_S are the joint admittance (or compliance) for compressional and shear waves which, for a linear elastic joint (e.g.), are given by:

$$Y_P = j\omega \frac{1}{k_{nn}}$$

$$Y_P = j\omega \frac{1}{k_{ss}}$$

The computation of the magnitude and the phase angle of the transmitted and reflection coefficients can be performed using the same procedure as for SH-waves. These coefficients obtained in this paragraph are the single components of the scattering matrix.

4.5 Analytical solutions

In this part, we present some solutions for evaluating the effects of a joint on wave propagation. This problem will be treated by computing the transmission and reflection coefficients for different values of the joint properties (stiffness, viscosity, etc), frequency and angle of incidence. The SMM has been implemented in Matlab.

In order to evaluate the effects of a single joint on wave propagation, we have taken a model composed of a single joint embedded in an elastic homogeneous medium. Material damping is set to zero for considering only the effect of the joints. The fundamental parameter of each joint is its admittance that is function of the behaviour of the joint. We will consider linear elastic dry rock joints and filled joints.

4.5.1 Linear elastic dry rock joint

When a wave impinges on a joint, transmitted and reflected waves are generated. The amplitude and the phase shift of these waves depend on the properties of the joint. In Figure 4.3, we can see the transmission and the reflection coefficients

versus the normalized shear joint stiffness (K). The normalized joint stiffness is defined as:

$$K = \frac{k}{\omega Z} \tag{4.33}$$

where k is the joint stiffness that for an incident S-wave is k_{ss} while for an incident P-wave is k_{nn}.

Figure 4.3 refers to a shear or pressure wave that impinges normally on the joint. The same figure applies to the two polarizations since normalized joint stiffnesses are used.

The Equations (4.31) and Figure 4.3 show that when a joint has a very high value of joint stiffness ($k \to \infty$) all energy is transmitted while when the stiffness is close to zero ($k \to 0$) all energy is reflected. When the first condition holds true we are in the typical case of a welded interface while in the second case we can assume the joint as a free surface.

We can evaluate the influence of the frequency on the transmission and reflection coefficients by assuming a fixed value of joint stiffness. With this assumption, when the frequency increases the normalized stiffness decreases and the transmission coefficient goes down very quickly. On the other hand, the reflection coefficient increases until 1 with the frequency increase. Hence, for high frequencies $K \to 0$, $|T_1| \to 0$ and $|R_1| \to 1$. Similar considerations hold true if we consider the influence of the joint stiffness for a fixed value of frequency.

In these conditions, the law of conservation of energy is satisfied:

$$\left|R_1(\omega)\right|^2 + \left|T_1(\omega)\right|^2 = 1 \tag{4.34}$$

The angle of incidence is another important parameter to consider. As well known, an obliquely incident SH-wave generates only SH scattered waves while for an incident P or SV-wave two pairs of P and SV scattered waves are originated.

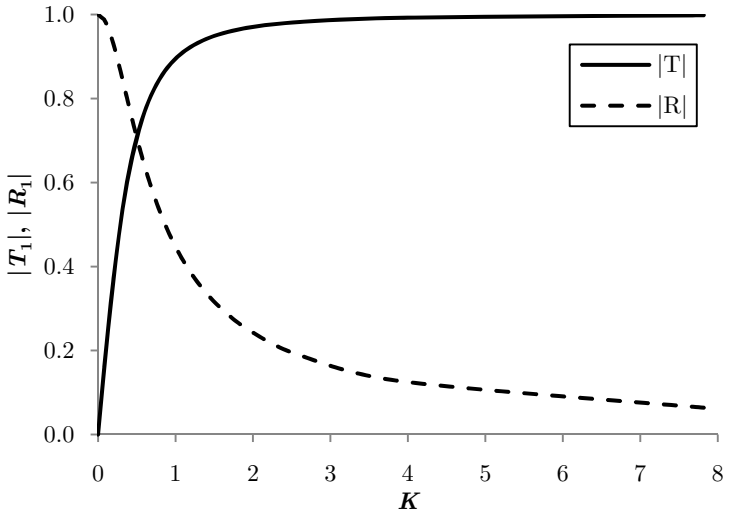

Figure 4.3 – Transmission and reflection coefficients versus the normalized joint shear stiffness: normal incident S or P-wave

Figure 4.4 shows the plots of the reflection and transmission coefficients versus the normalized stiffness computed for various values of the angle of incidence ϑ^{inc}. The normalized shear stiffness is calculated considering the medium impedance $Z_S = \rho V_S$. In this diagram, the different behaviour for each value of the angle of incidence ϑ^{inc} is well underlined.

In Figure 4.5, we can note that the behaviour of transmission and reflection coefficients versus the normalized joint stiffness, obtained by using the modal impedance $Z_S = \rho V_S \ cos\vartheta^{inc}$, is essentially the same for each angle of incidence. The modal impedance depends on the mass density, the S-wave velocity of the medium and the angle of incidence ϑ^{inc}.

Figure 4.4 and Figure 4.5 are also applicable to P or SV-wave normally incident on the joint.

When an obliquely incident P-wave impinges a joint the wave propagation problem becomes more complex. For studying this problem, we have assumed a medium with a single joint with the mechanical properties summarized in Table 4.1.

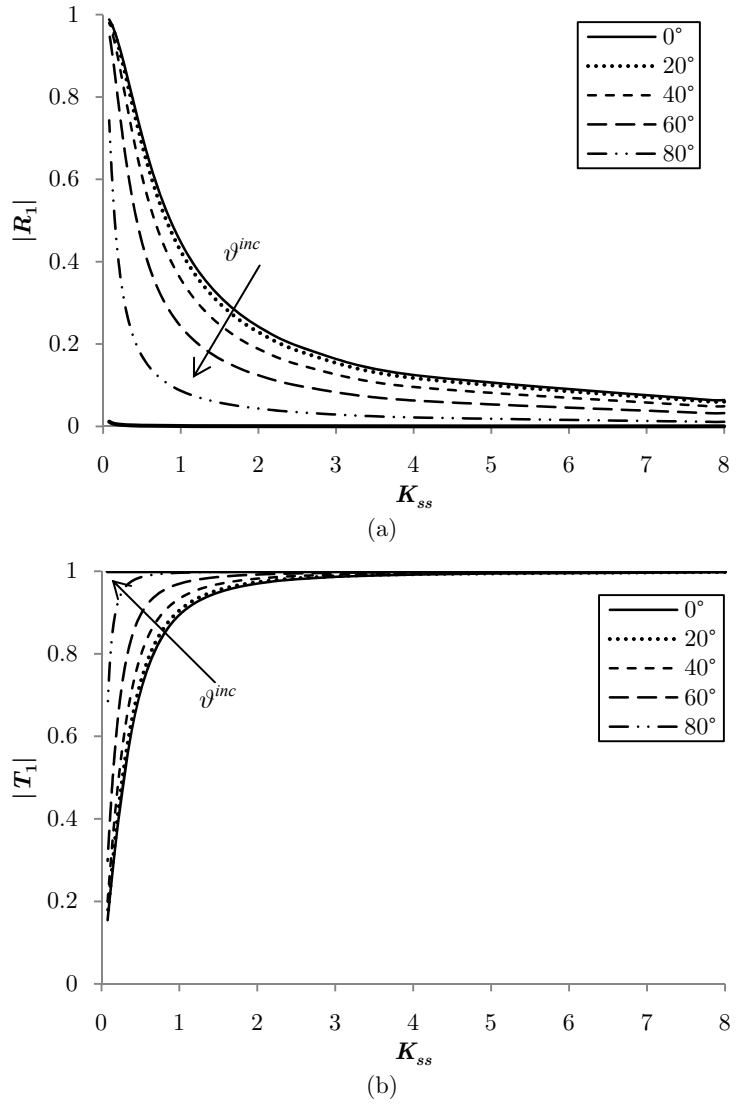

Figure 4.4 – Reflection (a) and transmission (b) coefficients versus the normalized joint shear stiffness K_{ss} (with $Z_S = \rho \cdot V_S$) and the angle of incidence

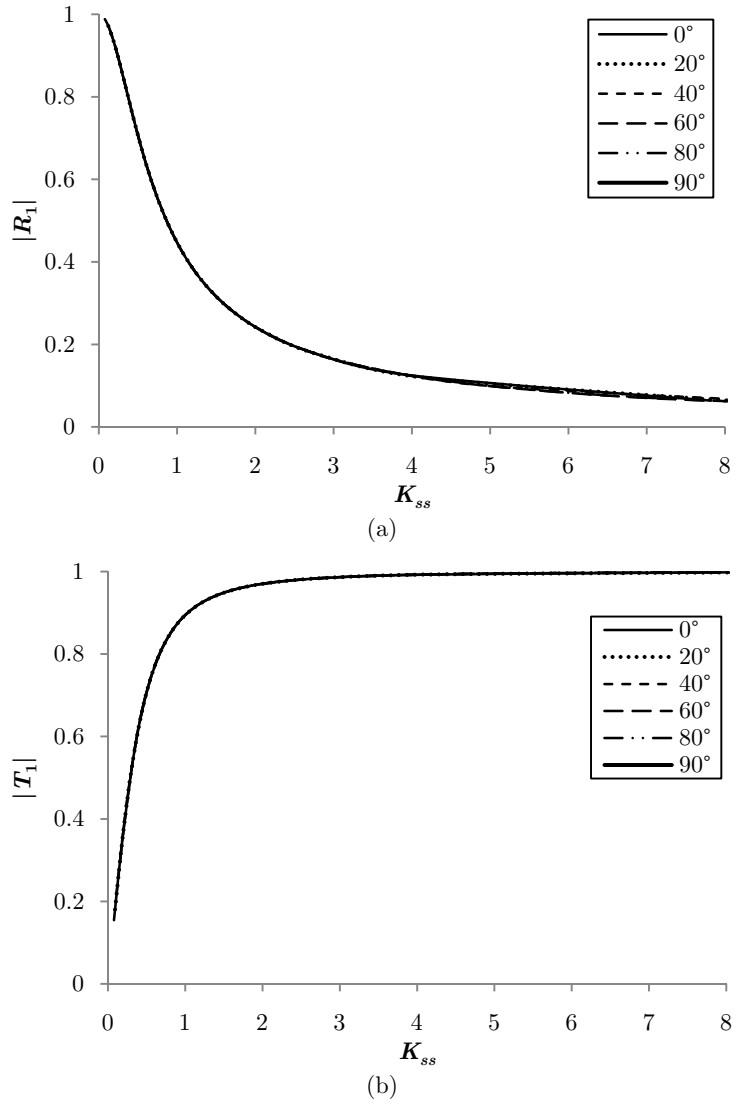

Figure 4.5 – Reflection (a) and transmission (b) coefficients versus the normalized joint shear stiffness K_{ss} (with $Z_S = \rho \cdot V_S \cdot cos\,\vartheta^{inc}$) and the angle of incidence

Two reflected waves (P and SV) and two transmitted waves (P and SV) are generated from an incident P-wave. In these conditions, both shear and normal joint stiffness are necessary to input in the SMM algorithm.

Table 4.1 – Mechanical properties of the rock mass

Properties of the intact rock:	
Mass density	2300 kg/m^3
Velocity of the propagating P-wave	2800 m/s
Velocity of the propagating S-wave	1400 m/s
Properties of the joint:	
Normal stiffness	400 MPa/m
Shear stiffness	200 MPa/m

The behaviour of the reflection and transmission coefficients for two types of waves is plotted in Figures 4.6 to 4.9. These values are stored in a column of the scattering matrix of a single joint. The energy conservation law in these conditions is obviously verified since the structure is lossless. $|R_{PSV}|$ denotes, for example, the ratio between the amplitude of the reflected SV-wave to that of the incident P-wave.

We can note in these figures that for low frequencies the joint is behaving as a welded interface. The reflected wave increases in amplitude if we increase the frequency or decrease the normal and shear stiffness of the joint. In fact an increase in frequency has the same effect as a decrease in stiffness.

Pyrak-Nolte et al. (1990a) showed that, for normally incident plane P-waves, the non-welded interface behaves somewhat like a low-pass filter for the transmitted P- wave, that is, at low frequencies, the transmitted P-wave has a high amplitude whereas the reflected P-wave has a low amplitude. Figures 4.6 to 4.9 confirm this and, in addition, show that the joint (non-welded interface) behaves like a low-pass filter for the transmitted P-wave at all angles of incidence except for those near 90° and that the filter also attenuates the scattered converted waves at low frequencies as well.

It is demonstrated in Figure 4.6 to Figure 4.9 that SV scattered waves are not generated by an incident P-wave perpendicular to the joint ($\vartheta = 0°$). In fact in this situation the amplitudes of reflected and transmitted SV-waves are zero. The reflection $|R_{PSV}|$ and transmission $|T_{PSV}|$ coefficients increase with the angle of incidence until a maximum value. After that, these coefficients decrease and become zero for an angle of 90° for which all energy is reflected as P-wave.

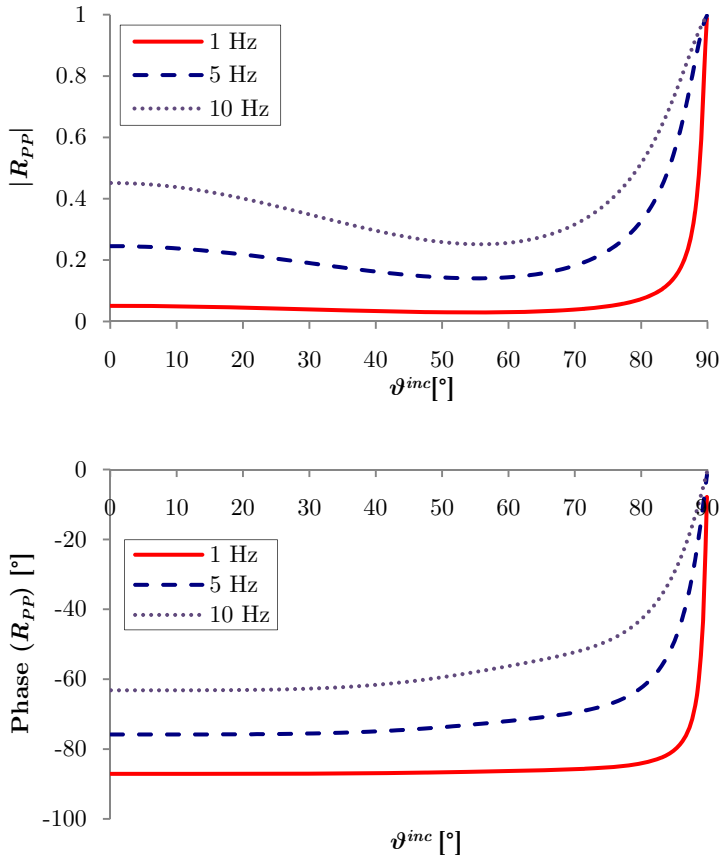

Figure 4.6 – Magnitude and phase of the reflection coefficient of the reflected P-wave versus the angle of incidence

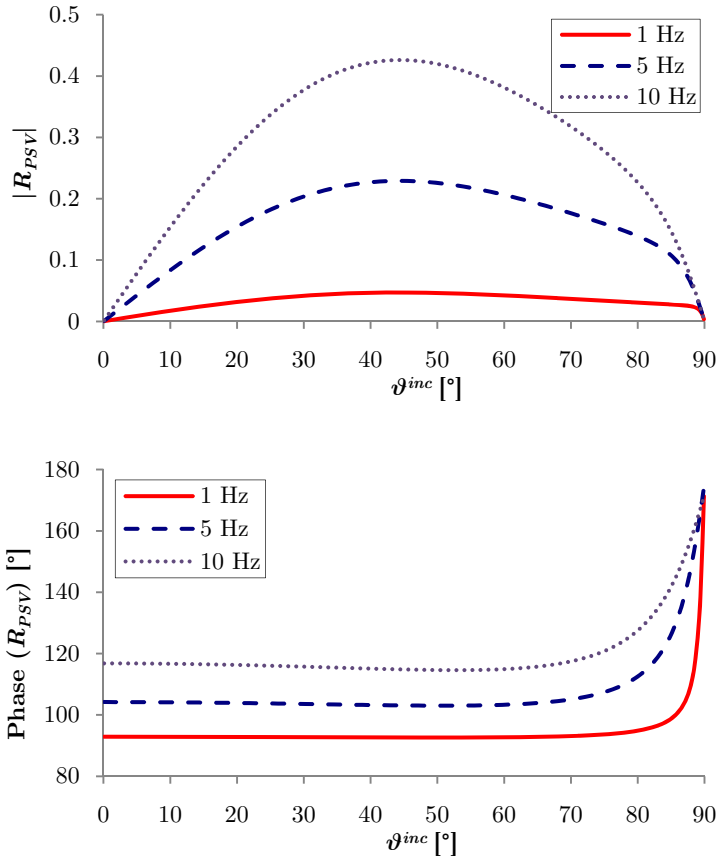

Figure 4.7 – Magnitude and phase of the reflection coefficient of the reflected SV-wave versus the angle of incidence

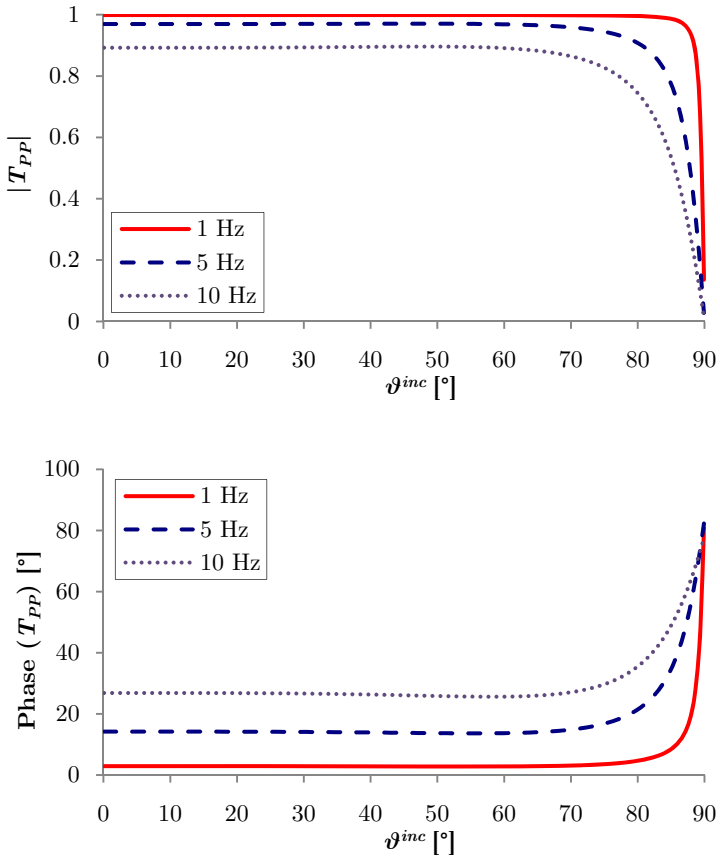

Figure 4.8 – Magnitude and phase of the transmission coefficient of the transmitted P-wave versus the angle of incidence

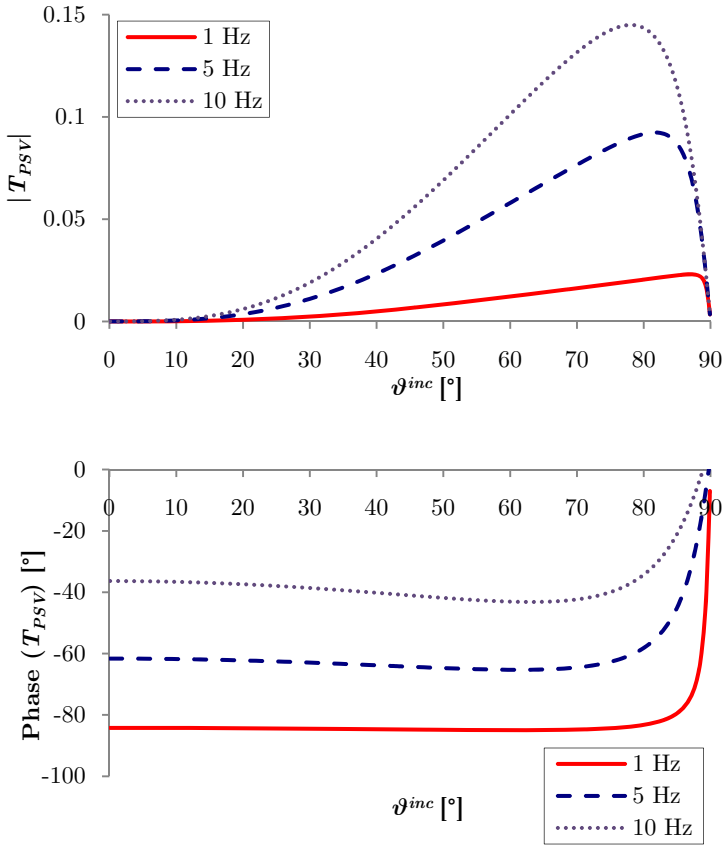

Figure 4.9 – Magnitude and phase of the transmission coefficient of the transmitted SV-wave versus the angle of incidence

The phase for each scattered wave is essentially constant for the angle of incidence less than 70-80°.

From the Kramers-Krönig relation (a consequence of causality), any changes in the amplitude of a wave must be accompanied by a change in phase.

Figures 4.6 to 4.9 also show that the coefficients have significant phase values, even for high values of normalized joint stiffness K. For example, the reflected P-wave, although small in amplitude at large K_{nn}, experiences a phase shift of about 90°. In the interpretation of seismic data the observation of small $|R_{PP}|$ reflections where none are expected, with 90° phase shifts, could be evidence of the presence of a small amount of non-welded contact.

The phase shift of the transmitted wave is related to time delay and it increases with the decrease of the joint stiffness and with the increase of the frequency.

4.5.2 Joints filled with fluid or soft material

A joint filled with fluid or soft material can be modelled, as previously described, with rheological models. In this paragraph we will consider the Kelvin-Voigt, the Maxwell and the Burger models.

For a joint with a viscoelastic behaviour the law of conservation of energy is not satisfied:

$$\left|R(\omega)\right|^2 + \left|T(\omega)\right|^2 \neq 1 \tag{4.35}$$

Hence, a part of energy of an incident wave is dissipated when impinges on a joint because it is simulated with viscous dampers. In fact, the fluid or the soft material layer, that fills the joints, produces a loss of energy due to their viscous properties.

The results of the analyses shown in Figures 4.10 and 4.11 are applicable for oblique SH-waves (by considering that $Z_s = \rho \cdot V_s \cdot cos\vartheta^{inc}$) and for normally incident P or SV-waves.

In Figure 4.10, we can note the trend of transmission and reflection coefficients versus the inverse of the normalized joint stiffness (η/K) and the normalized specific viscosity (η/Z) for a joint simulated with the Kelvin-Voigt model. The curve with η/Z=0 corresponds to the case of a linear elastic dry joint.

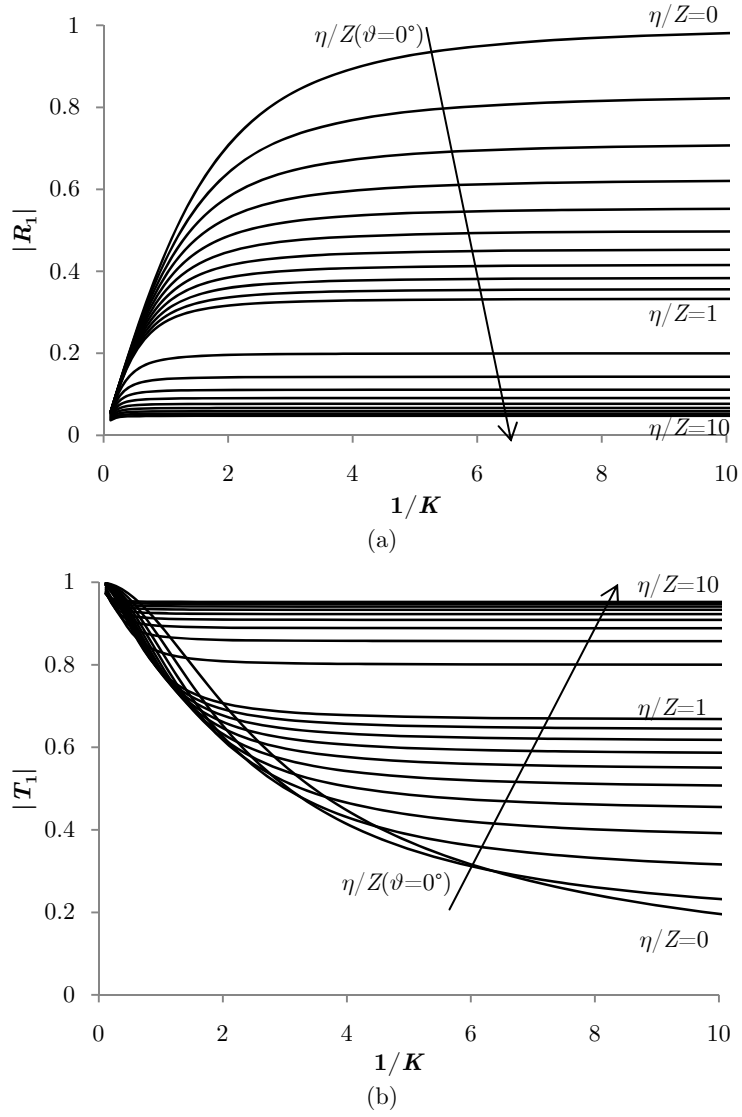

Figure 4.10 - Magnitude of reflection and transmission coefficients as predicted by Kelvin-Voigt model as a function of the normalized joint stiffness and the normalized specific viscosity

Figure 4.10 shows that for very large values of the joint stiffness k or of specific viscosity η all energy is transmitted ($|T_1| \to 1$, $|R_1| \to 0$) while for very low values of k and η all energy is reflected ($|T_1| \to 0$, $|R_1| \to 1$).

The transmission coefficient becomes frequency independent when the joint stiffness reaches zero while it remains non-zero. When the curves with $\eta/Z \neq 0$, approach a horizontal slope the specific viscosity becomes predominant. For low values of specific viscosity the behaviour is like that of a linear elastic discontinuity in which for low frequencies almost the entire wave is transmitted while by increasing the frequency the transmitted energy decreases.

If we compare the results obtained for an elastic joint, the specific viscosity reduces the energy transmitted at low frequencies and increases the energy transmitted at high frequencies. We obtain large values of the transmission coefficient $|T_1|$ with increasing the specific viscosity, if we take into account fixed values of joint stiffness and frequency. Hence, for high values of the specific viscosity there is a total transmission of energy at each frequency. In this condition the transmission and reflection coefficients become independent from the normalized joint stiffness, hence also from the frequency and from the joint stiffness.

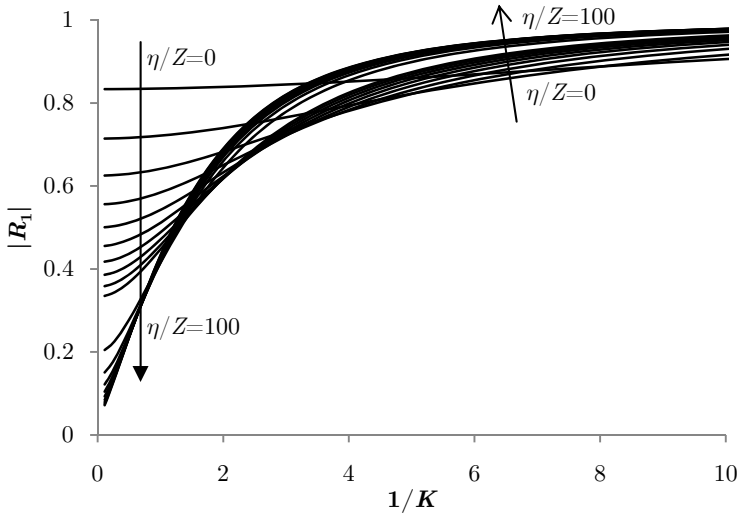

(a)

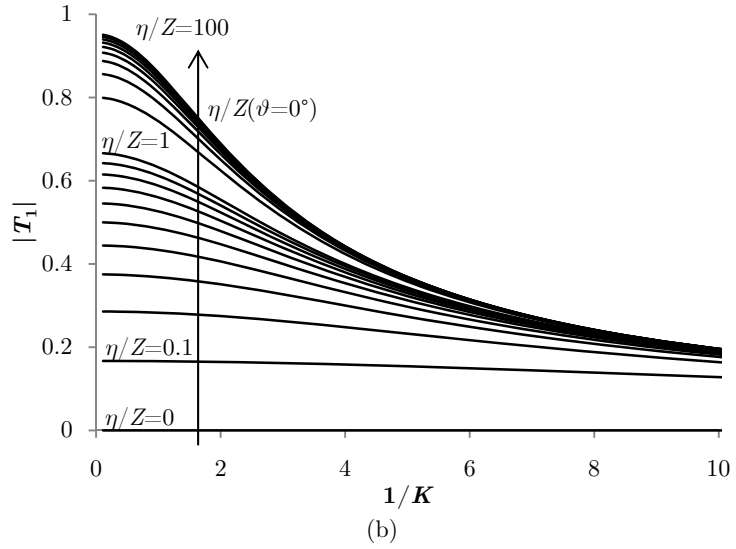

(b)

Figure 4.11 - Magnitude of reflection and transmission coefficients as predicted by Maxwell model as a function of the normalized joint stiffness and the normalized specific viscosity

On the other hand, the results obtained with the Maxwell model are summarized in Figure 4.11. In this case the results are different from those obtained with the Kelvin-Voigt model. The condition $\eta/Z \to \infty$, for the Maxwell model, corresponds to the case of an elastic joint. This previous situation is the opposite one of that obtained with the Kelvin-Voigt model. Curves of the transmission and reflection coefficients extend their area with horizontal slope for very low values of specific viscosity ($\eta/Z \to 0$). In this area, $|T_1|$ and $|R_1|$ become essentially independent from the frequency and the joint stiffness. The effects of high specific viscosity are large for Kelvin-Voigt model while are low for Maxwell model.

The Burger model was implemented in the SMM and the results are plotted in Figure 4.12. The Burger model is composed by the Kelvin and the Maxwell models in series and in this calculation the stiffnesses and the viscosities are assumed to be the same. In Figure 4.12, we can see as the transmission and reflection coefficients trends start from the same values of Maxwell model.

Figure 4.13 compares the transmission and reflection coefficients for an obliquely incident SH-wave or for a P or SV normal incident waves across a non-welded interface represented by a spring (linear elastic model), a dashpot (purely viscous model), a Kelvin-Voigt model, a Maxwell model and a Burger model. These

curves are the same also for SH-waves that impinge the joint with any angle of incidence.

Kelvin, Maxwell and Burger models have the same limiting behaviour, either an elastic (spring dominated) or purely viscous (dashpot dominated) interface. The Kelvin-Voigt model predicts the behaviour of an elastic interface when the viscosity of the layer becomes small while the Maxwell model predicts that the interface will behave as an elastic interface when the viscosity becomes large.

The behaviour of the Burger model is very similar to that of the Maxwell model for high and low values of normalized joint stiffness while for intermediate values the curve is different because its shape is similar to the Kelvin-Voigt model. Obviously, this behaviour is due to the fact that the Burger model is composed of a Kelvin-Voigt and a Maxwell model in series.

The Maxwell and Burger models are more sensitive to changes in the rheological properties of the interface at low frequencies; at high frequencies their behaviour for different values of the viscous parameter does not change considerably. The Kelvin-Voigt model is more sensitive to the rheological properties of the interface at high frequencies; at low frequencies these differences becomes small.

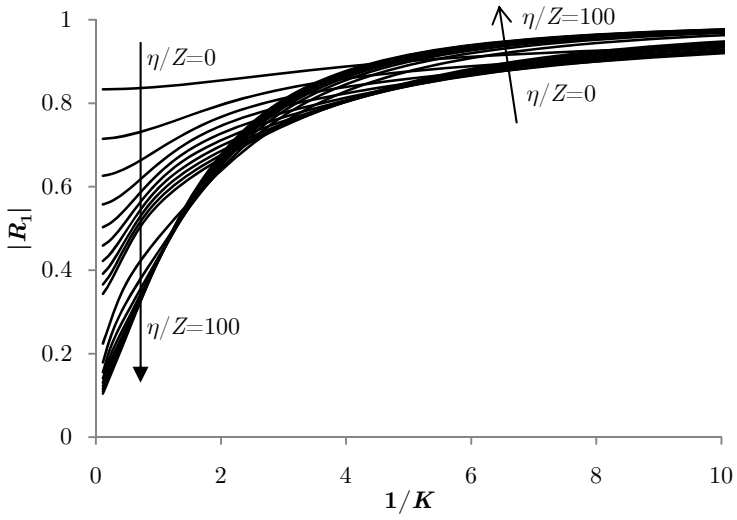

(a)

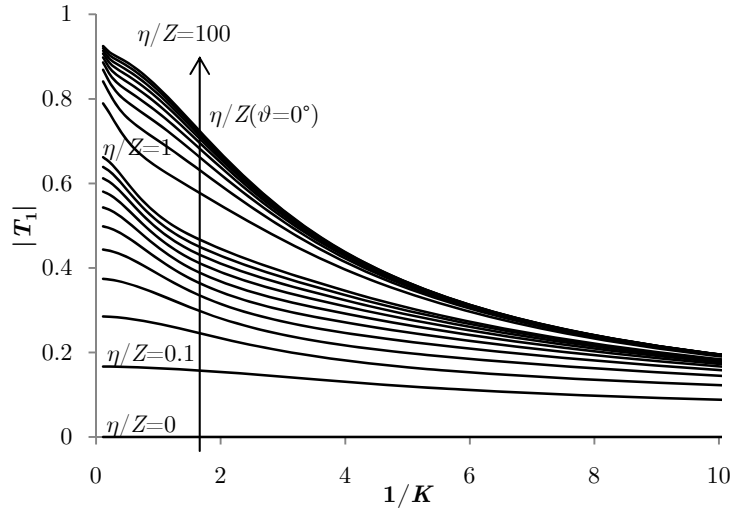

(b)

Figure 4.12 – Magnitude of reflection and transmission coefficients as predicted by Burger model as a function of the normalized joint stiffness and the normalized specific viscosity

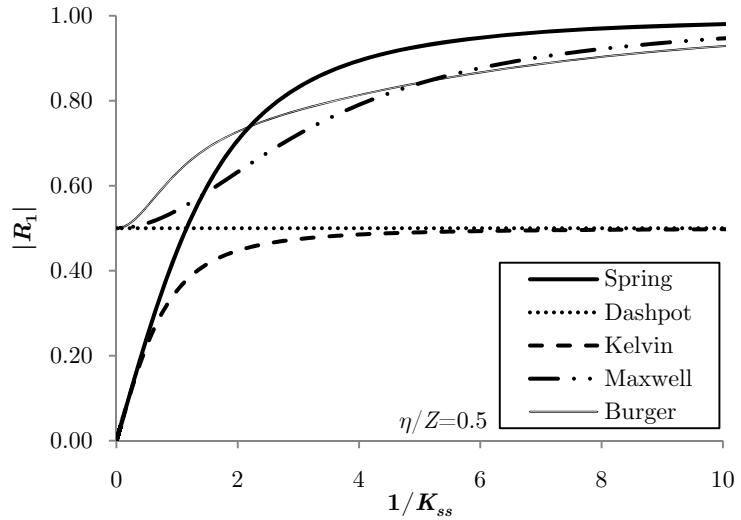

(a)

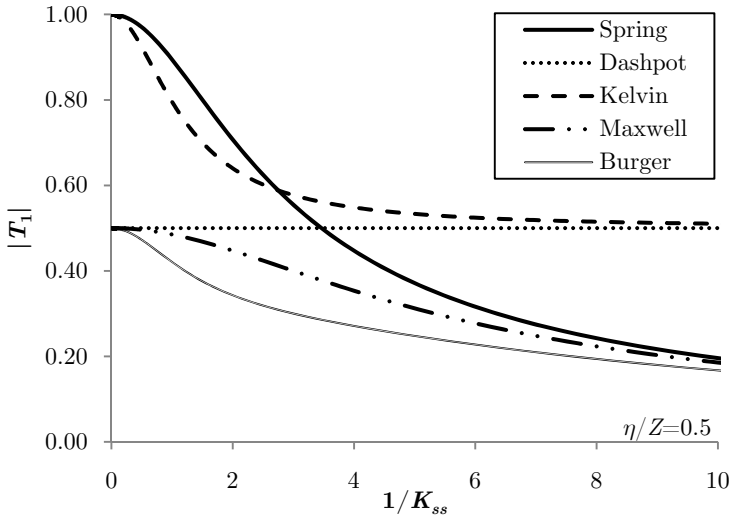

(b)

Figure 4.13 – Comparison of reflection and transmission coefficients for a wave impinging a fracture represented by a spring (linear elastic model), dashpot (purely viscous model), Kelvin-Voigt model, Maxwell model and Burger model (η/Z=*0.5*)

4.6 Evaluation of the effects of a set of joints

The SMM method allows one to compute the global scattering matrix of a set of joints through a series of algebraic matrices computations. This method has been implemented in Matlab.

In order to explain the SMM procedure, we examine the case of a set of two parallel joints with the same mechanical characteristics. The SMM will be developed step by step.

The model used for studying the problem of wave propagation across two parallel joints is shown in Figure 4.14.

The aim of this analysis is to obtain the global scattering matrix of the set of two discontinuities as shown in Figure 4.14. The first step is the computation of the scattering matrix of each joint:

$$\mathbf{S^{(1)}} = \begin{bmatrix} R_{SH} & T_{SH} \\ T_{SH} & R_{SH} \end{bmatrix} = \begin{bmatrix} \dfrac{Z_S Y}{2+Z_S Y} & \dfrac{2}{2+Z_S Y} \\ \dfrac{2}{2+Z_S Y} & \dfrac{Z_S Y}{2+Z_S Y} \end{bmatrix} = \mathbf{S^{(2)}} \tag{4.36}$$

where $\mathbf{S^{(1)}}$ and $\mathbf{S^{(2)}}$ are the scattering matrices of the joint "1" e "2".

In this analysis we consider a SH-wave that impinges on a joint.

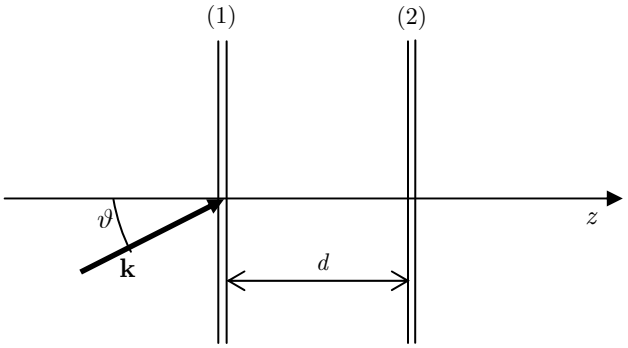

Figure 4.14 – Wave propagation across two parallel joints

The second step is the application of the "chain rule" procedure, to the two scattering matrices, for obtaining the global scattering matrix. The reference plane of the first joint "1" has to be moved on the joint "2" for using the "chain rule" procedure. The scattering matrix for the joint "1", after the translation of the reference plane, is the following:

$$\mathbf{S^{(1)}} = \begin{bmatrix} \dfrac{Z_S Y}{2+Z_S Y} & \dfrac{2}{2+Z_S Y} e^{-jk_{zS}d} \\ \dfrac{2}{2+Z_S Y} e^{-jk_{zS}d} & \dfrac{Z_S Y}{2+Z_S Y} e^{-2jk_{zS}d} \end{bmatrix} \tag{4.37}$$

where d is the joint spacing.

By applying the "chain rule" procedure (see Equations (3.42)), transmission and reflection coefficients can be defined as follows:

$$\begin{aligned} T_{SH}^{(2)}\left(\omega,\vartheta\right) = S_{21} &= \frac{4e^{-jk_{zS}d}}{\left(2+Z_S Y\right)^2 - \left(Z_S Y\right)^2 e^{-2jk_{zS}d}} \\ R_{SH}^{(2)}\left(\omega,\vartheta\right) = S_{11} &= \frac{Z_S Y}{2+Z_S Y}\left(1+T_{SH}^{(2)}e^{-jk_{zS}d}\right) = R_{SH}^{(1)}\left(1+T_{SH}^{(2)}e^{-jk_{zS}d}\right) \end{aligned} \tag{4.38}$$

where $R_{SH}^{(1)}$ is the reflection coefficient for the case of SH-wave propagation across a single joint.

Equations (4.38) show the dependence of the transmission and reflection coefficients on the joint spacing d, the joint properties Y, medium properties Z_s and angular frequency ω.

From Equations (4.38), we can obtain the same expression of the global transmission coefficient for a set of N joints obtained with a recursive approach (e.g., Boadu,1997; Fokkema and Ziolkowski, 1987).

Figure 4.15 shows the magnitude of the transmission and reflection coefficients versus the joint spacing ratio computed with a constant value of normalized joint stiffness K_{ss} of 1.6 and deduced from the Equations (4.38). A linear elastic joint is assumed.

In Figure 4.15, we can note that transmission and reflection coefficients are periodic functions of the joint spacing ratio ζ, that is:

$$\zeta = \frac{d}{\lambda / \cos \vartheta^{inc}} \tag{4.39}$$

where the joint spacing is divided by the ratio between the wavelength and the cosine of the angle of incidence. The results shown in Figure 4.15 are applicable for oblique SH-waves and for normally incident P or SV-waves. The points where the transmission coefficient reaches 1 while the reflection coefficient becomes zero are located each 0.5ζ.

4.7 Analytical expressions of the transmission and reflection coefficients for a medium with parallel equi-spaced discontinuities

In this paragraph the effects of a set of parallel equi-spaced discontinuities on wave propagation will be analysed. Wave propagation through N discontinuities is a very complex problem if it is studied by the plane wave method. The complexity of this problem is essentially due to the multiple reflections between the discontinuities.

To address more easily this problem, we have adopted an approach used in the field of microwaves circuits. This approach is based on the Bloch waves, i.e. elementary waves very suitable to simulate wave propagation through periodic media. Therefore, this approach is applicable only on parallel equi-spaced discontinuities (periodic medium). Bloch waves are an appropriate combination of a forward and a backward wave that does not undergo any change from the input to the output plane of the periodic cell but only a phase-shift, hence a time delay.

Bloch waves are reflected from the interface between the elastic periodic medium and the elastic homogeneous one. Indeed plane waves are very good to treat problems of wave propagation in homogeneous media, while Bloch waves are a useful tool for studying wave propagation through periodic media.

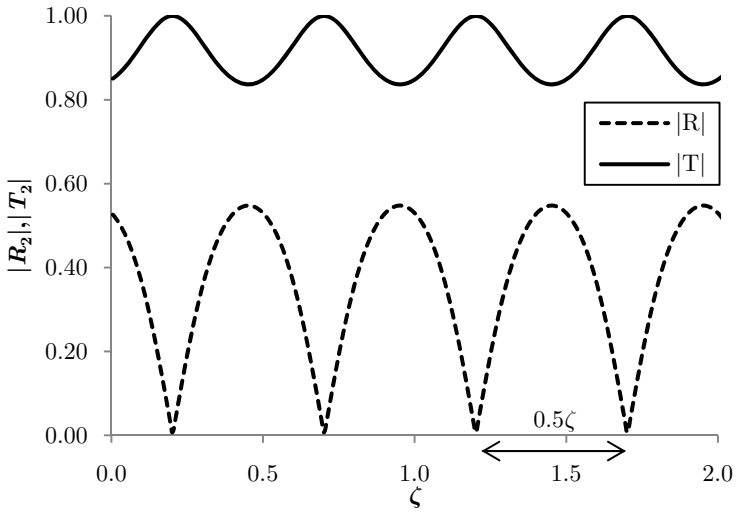

Figure 4.15 – Magnitude of the transmission and reflection coefficients for a set of two parallel elastic joints (K_{ss}= 1.6) versus the normalized joint spacing ratio ζ

4.7.1 Periodic discontinuities, SH polarization

The aim of this part is to compute the effects of a set of parallel equi-spaced discontinuities on SH-wave propagation.

The characteristics of the periodic medium are shown in Figure 4.16. The periodic medium is composed of N unit cells (see Figure 4.16).

The media on the left and on the right of the zone with parallel discontinuities are two half-spaces. The mechanical properties of the layers between the discontinuities are the same. The medium is characterized by the impedance Z_S and the propagation constant k_S.

For each discontinuity we can define an admittance Y that is function, as shown in the paragraph 4.2, of the mechanical properties of the joint and of the frequency. By varying the joint admittance we can simulate linear elastic dry joints and joints filled with fluid or soft materials.

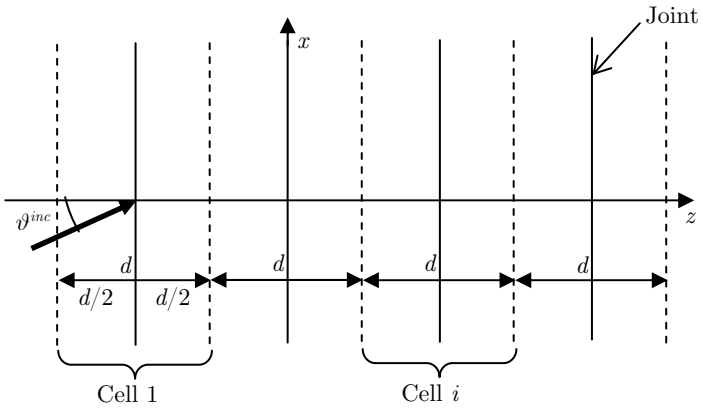

Figure 4.16 – Schematization of periodic medium

It is necessary to define the transmission matrix of the unit cell, shown in Figure 4.16, for introducing the theory of Bloch waves. It is known that this transmission matrix at terminal planes close to the fracture is given by Equation (4.19).

We need the expressions of the SH-wave modal matrix. Either we extract it from the Equation (3.31) in Chapter 3 or we compute it directly.

Stress and velocity components of the elastic field in the unit cell are defined as follows (see Equation (3.30) in the Chapter 3):

$$\begin{aligned} v_y &= \left(c^+ - c^-\right)\sqrt{Y_S^m} \;\rightarrow\; \text{velocity} \\ \tau_{zy} &= \left(c^+ + c^-\right)\sqrt{Z_S} \;\rightarrow\; \text{stress} \end{aligned} \tag{4.40}$$

where:

c^+ and c^- are the amplitude of the incident and the reflected waves;
$Y_S^m = 1/Z_S$ is the admittance of the medium;
τ_{yz} is the tangential shear stress.

Then, we can write:

$$\begin{pmatrix} v_y \\ \tau_{zy} \end{pmatrix} = \begin{pmatrix} \sqrt{Y_S^m} & \sqrt{Y_S^m} \\ \sqrt{Z_S} & -\sqrt{Z_S} \end{pmatrix} \begin{pmatrix} c^+ \\ c^- \end{pmatrix} = \mathbf{M} \begin{pmatrix} c^+ \\ c^- \end{pmatrix} \tag{4.41}$$

The inverse of the modal matrix, necessary for computing the transmission matrix $\mathbf{A}'$ is:

$$\mathbf{M^{-1}} = \frac{1}{2}\begin{pmatrix} \sqrt{Z_S} & \sqrt{Y_S^m} \\ \sqrt{Z_S} & -\sqrt{Y_S^m} \end{pmatrix} \tag{4.42}$$

Then the transmission matrix of the fracture, at the terminal planes to the joint, is:

$$\mathbf{A}' = \frac{1}{2}\begin{pmatrix} \sqrt{Z_S} & \sqrt{Y_S^m} \\ \sqrt{Z_S} & -\sqrt{Y_S^m} \end{pmatrix}\begin{pmatrix} 1 & Y \\ 0 & 1 \end{pmatrix}\begin{pmatrix} \sqrt{Y_S^m} & \sqrt{Y_S^m} \\ \sqrt{Z_S} & -\sqrt{Z_S} \end{pmatrix} = \begin{pmatrix} 1 + y_p/2 & -y_p/2 \\ y_p/2 & 1 - y_p/2 \end{pmatrix} \tag{4.43}$$

where $y_p = Y \cdot Z_S$.

The transmission matrix of the unit cell can be obtained by moving the planes terminal to the cell boundaries. The transmission matrix of the unit cell is:

$$\mathbf{A} = \begin{pmatrix} e^{j\frac{\psi}{2}} & 0 \\ 0 & e^{-j\frac{\psi}{2}} \end{pmatrix}\mathbf{A}'\begin{pmatrix} e^{j\frac{\psi}{2}} & 0 \\ 0 & e^{-j\frac{\psi}{2}} \end{pmatrix} = \begin{pmatrix} \left(1 + y_p/2\right)e^{j\psi} & -y_p/2 \\ y_p/2 & \left(1 - y_p/2\right)e^{-j\psi} \end{pmatrix} \tag{4.44}$$

where:

$\psi = k_{zS} \cdot d = \dfrac{\omega}{V_S}\cos\vartheta^{inc} d$ with d being the size of the unit cell and the discontinuity spacing.

At this point, it is possible to introduce the theory of the Bloch waves that are related to the eigenvectors of the transmission matrix **A** of the unit cell. The matrix **A** has the following representation:

$$\mathbf{A} = \mathbf{V}\boldsymbol{\lambda}\mathbf{V}^{-1} \tag{4.45}$$

where:
V is the matrix of the eigenvectors of the transmission matrix of the unit cell;
λ is the diagonal matrix of the eigenvalues.

The transmission matrix of the periodic medium with N cells can be obtained by:

$$\mathbf{A}^N = \mathbf{V}\boldsymbol{\lambda}^N\mathbf{V^{-1}} = \mathbf{V}\begin{pmatrix} \lambda_1^N & 0 \\ 0 & \lambda_2^N \end{pmatrix}\mathbf{V^{-1}} \tag{4.46}$$

The eigenvalues of **A** have the physical meaning of phase-shift per cell of suitably defined waves: we are introducing Bloch waves, defined by the eigenvectors of **A**. The "natural basis" here is that of the forward and backward plane waves.

Bloch waves can be defined only at the terminal planes of the periodic medium and not inside the periodic medium.

The eigenvalues of **A** are the roots of the characteristic polynomial:

$$\lambda^2 - Tr\big(\mathbf{A}\big)\cdot\lambda + \det\big(\mathbf{A}\big) = 0 \tag{4.47}$$

where $Tr(\mathbf{A})$ and $\det(\mathbf{A})$ are respectively the trace and the determinant of the transmission matrix **A**.

Since the structure is reciprocal, the determinant of **A** is 1. Hence the roots are reciprocal:

$$\lambda = \frac{1}{2}Tr\big(\mathbf{A}\big) \pm \sqrt{\left(\frac{Tr\big(\mathbf{A}\big)}{2}\right)^2 - 1} = \frac{1}{2}Tr\big(\mathbf{A}\big) \pm j\sqrt{1 - \left(\frac{Tr\big(\mathbf{A}\big)}{2}\right)^2} \tag{4.48}$$

with $\lambda_1 = 1/\lambda_2$.

This form suggests to introduce an angle φ such that

$$Tr\big(\mathbf{A}\big) = A_{11} + A_{22} = \lambda_1 + \lambda_2 = e^{-j\varphi} + e^{j\varphi} = 2\cos\varphi \tag{4.49}$$

The trace of the transmission matrix can be also obtained from the equation (4.44)

$$\begin{aligned} Tr\big(\mathbf{A}\big) &= \big(1 + y_p/2\big)e^{j\psi} + \big(1 - y_p/2\big)e^{-j\psi} = \\ &= \big(1 + y_p/2\big)\big(\cos\psi + j\sin\psi\big) + \big(1 - y_p/2\big)\big(\cos\psi - j\sin\psi\big) = \\ &= 2\left(\cos\psi + j\frac{y_p}{2}\sin\psi\right) = 2\left(\cos\psi - \frac{b}{2}\sin\psi\right) \end{aligned} \tag{4.50}$$

where $y_p = jb$

Finally by equating expressions (4.49) and (4.50) of $Tr(\mathbf{A})$, we obtain the phase-shift per cell:

$$2\cos\varphi = 2\left(\cos\psi - \frac{b}{2}\sin\psi\right) \longrightarrow \varphi = \arccos\left(\cos\psi - \frac{b}{2}\sin\psi\right) \tag{4.51}$$

After long algebraic manipulations, we can write the transmission matrix for the periodic medium composed of N cells in the following form:

$$\mathbf{A}^N = \begin{pmatrix} A_{11}U_{N-1} - U_{N-2} & A_{12}U_{N-1} \\ A_{21}U_{N-1} & A_{22}U_{N-1} - U_{N-2} \end{pmatrix} \tag{4.52}$$

where:

$$U_N = \frac{\sin\left[\left(N+1\right)\varphi\right]}{\sin\varphi}$$

By recalling the conversion expressions of the elements of the transmission matrix into those of the scattering matrix, we obtain the reflection and the transmission coefficients (R_N and T_N) of the periodic medium:

$$\begin{aligned} R_N &= S_{11} = A_{21}^N\left(A_{11}^N\right)^{-1} = \frac{A_{21}U_{N-1}}{A_{11}U_{N-1} - U_{N-2}} = \\ &= -\frac{1}{2}\frac{y_p}{\left(1 + \dfrac{y_p}{2}\right)e^{j\psi} - \dfrac{\sin\left[\left(N-1\right)\varphi\right]}{\sin\left(N\varphi\right)}} \end{aligned} \tag{4.53}$$

$$\begin{aligned} T_N &= S_{21} = \left(A_{11}^N\right)^{-1} = \frac{1}{A_{11}U_{N-1} - U_{N-2}} = \\ &= \frac{\sin\varphi}{\sin\left(N\varphi\right)}\frac{1}{\left(1 + \dfrac{y_p}{2}\right)e^{j\psi} - \dfrac{\sin\left[\left(N-1\right)\varphi\right]}{\sin\left(N\varphi\right)}} \end{aligned} \tag{4.54}$$

Equations (4.53) and (4.54) are the general expressions of the reflection and transmission coefficients for a set of N parallel joints. These coefficients are applicable for an incident SH-wave and for each angle of incidence ϑ^{inc} by remembering that:

$$y_p = Y \cdot Z_S \text{ and } Z_S = \rho V_S \cos\vartheta^{inc}$$

These expressions, which are related to the fracture impedance Y, are applicable to different types of fracture (see Paragraph 4.2).

4.7.2 Additional considerations

In this section some analyses have been performed with the SMM implemented in Matlab. The results obtained are explained by using Bloch wave theory.

We can rewrite the trace of the transmission matrix of the unit cell as:

$$Tr\left(\mathbf{A}\right) = 2D\cos\left(\psi + \alpha\right) = 2D\cos\psi\cos\alpha - 2D\sin\psi\sin\alpha \tag{4.55}$$

and equating the components of (4.50) and (4.55) we obtain:

$$\begin{cases} D\cos\alpha = 1 \\ D\sin\alpha = \dfrac{b}{2} \end{cases} \longrightarrow \begin{array}{l} \alpha = arctg\dfrac{b}{2} \\ D = \dfrac{1}{\cos\left(arctg\dfrac{b}{2}\right)} \end{array} \tag{4.56}$$

Figure 4.17 shows the positions of stop-bands that are located in the intervals where the curve raises above 1 or falls below -1.

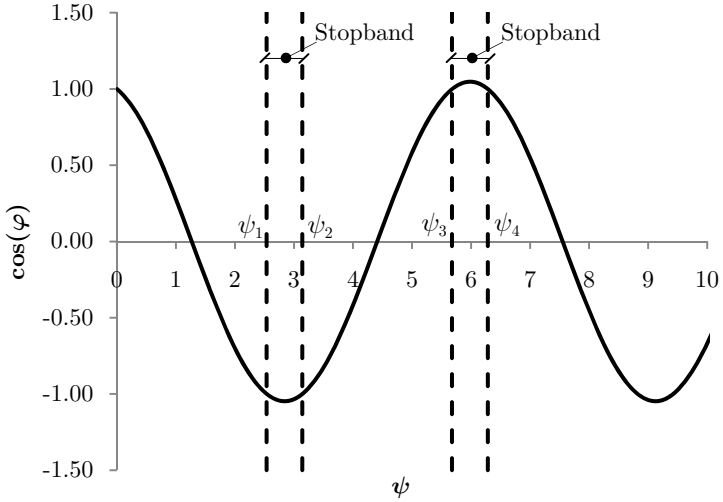

Figure 4.17 – Localization of stopbands

The band edges (defined by $|\cos\varphi| = 1$) of the first stop-band (see Figure 4.17) are:

$$D\cos\big(\psi+\alpha\big) = -1 \longrightarrow \cos\big(\psi+\alpha\big) = -\frac{1}{D} = -\cos\big(\alpha\big)$$
$$\psi+\alpha = \pi \pm \alpha \longrightarrow \begin{cases} \psi_1 = \pi - 2\alpha \\ \psi_2 = \pi \end{cases} \tag{4.57}$$

For the second stop-band the band edges are:

$$D\cos\big(\psi+\alpha\big) = 1 \longrightarrow \cos\big(\psi+\alpha\big) = \frac{1}{D} = \cos\big(\alpha\big)$$
$$\psi+\alpha = 2\pi \pm \alpha \longrightarrow \begin{cases} \psi_3 = 2\pi - 2\alpha \\ \psi_4 = 2\pi \end{cases} \tag{4.58}$$

In the same manner it is possible to compute the position of all stop-bands.

It is clear from Equations (4.57) and (4.58) that the width of stopbands is 2α.

The phase-shift per cell φ is function of the frequency and of ξ ($= k_S \sin\vartheta^{inc}$) and it represents the dispersion relation of Bloch waves.

In Figure 4.17, the zones in which $|\cos\varphi| < 1$ correspond to real value of φ. These zones are defined as pass-bands. On the other hand the stop-bands are located where $|\cos\varphi| > 1$. In these zones φ is complex and thus Bloch waves are evanescent (i.e. attenuated). The maximum attenuation is reached at $\psi = m\pi - \alpha$ and $\varphi = j\varphi''$ (with $\varphi'' = \cosh^{-1}\big(D\big) = \ln\Big(D + \sqrt{D^2-1}\Big) =$

$$= \ln\left(\frac{b}{2} + \sqrt{1+\left(\frac{b}{2}\right)^2}\right).$$

Figure 4.18 shows the plot of the real and imaginary part of φ versus ψ. Dashed curves yield the imaginary part of φ in m^{-1}.

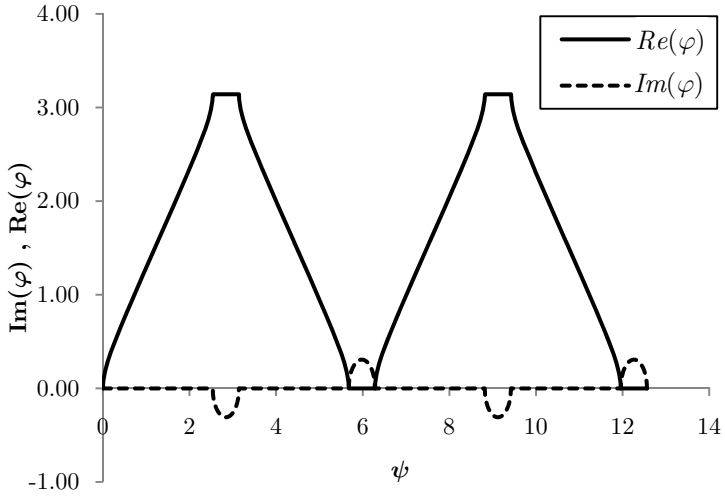

Figure 4.18 – The dispersion relation of Bloch waves between φ and ψ

Some parametric analyses have been performed for linear elastic dry discontinuities.

Figure 4.19 shows a plot of the reflection and transmission coefficients, for a discontinuous medium with *N=10* parallel equi-spaced discontinuities, in function of the joint spacing ratio ζ (see Equation (4.39)) for a normalized discontinuity stiffness ($K_{ss} = k_{ss}/\omega Z_S$) equal to 1.6. In this case we consider a SH wave that impinges on the discontinuities. The results plotted are obtained by varying the joint stiffness and keeping constant the frequency or vice versa.

The parameter b is related to the normalized joint stiffness K_{ss} (K_y) as follows:

$$b = \frac{y_p}{j} = \frac{Y \cdot Z_S}{j} = \frac{j\omega}{k_y}\frac{Z_S}{j} = \frac{\omega Z_S}{k_y} = \frac{1}{K_{ss}} \tag{4.59}$$

while the ratio ζ is related to ψ:

$$\psi = k_{zS}d = k_S \cos\vartheta^{inc} d = \frac{\omega}{V_S} d \cos\vartheta^{inc} = \frac{2\pi f}{V_S} d \cos\vartheta^{inc} = 2\pi \frac{d}{\lambda} \cos\vartheta^{inc} = 2\pi\zeta$$

so

$$\frac{\psi}{2\pi} = \frac{d}{\lambda}\cos\vartheta^{inc} = \zeta \tag{4.60}$$

Hence, for the case studied in Figure 4.19 we have:

$$\alpha = arctg\frac{1}{2K_{ss}} = arctg\frac{1}{2\cdot 1.6} = 0.303^{rad} \longrightarrow$$

$$\frac{\psi_2 - \psi_1}{2\pi} = \frac{2\alpha}{2\pi} = 0.096 \longrightarrow \text{width of stopbands}$$

$$l = \frac{\psi_3 - \psi_1}{2\pi} = \frac{\pi}{2\pi} = \frac{1}{2} \longrightarrow \text{stopbands period}$$

where the results are applicable for a SH-wave that impinges on a discontinuity with any angle of incidence ϑ^{inc} or for normally incident P or SV-waves.

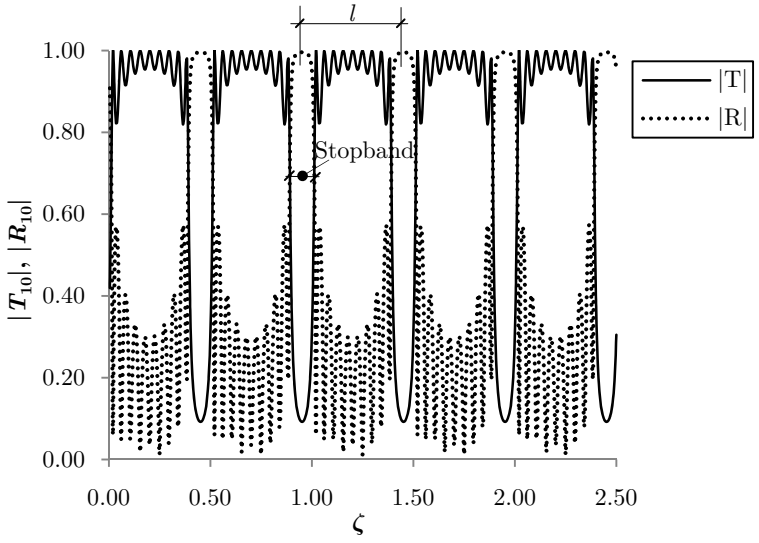

Figure 4.19 – Reflection and transmission coefficients, for a discontinuous medium with N=10 parallel equispaced discontinuities, versus the ratio between fracture spacing and wavelength ($\zeta = d/(\lambda/\cos\vartheta^{inc})$) with $K_{ss} = 1.6$

If we do not normalize the joint spacing with the cosine of ϑ^{inc} we obtain:

- if ϑ^{inc} increases the period of the stopbands increases;
- the width of the period $(l) \rightarrow \infty$ for $\vartheta^{inc} = 90°$.

Figure 4.19is defined for a value of $b = 1/K_y = 1/1.6$.

In Figure 4.20, the plots of the transmission and reflection coefficients versus the normalized joint spacing are defined for a stiffness ratio $K_{ss} = 0.47$. In this situation the width of the stop-bands is 0.260 while the stop-bands period (l) is 0.500, that is constant with respect to K_{ss}.

Finally, it is possible to say that by decreasing the discontinuity or joint stiffness (K_{ss}), b and α increase. Hence the width of the stop-band increases. For $K_{ss} \rightarrow 0$ the width of the stopband $\rightarrow \infty$ and hence there is a complete reflection of the SH-wave. On the other hand if $K_{ss} \rightarrow \infty$ the width of the stop-band $\rightarrow 0$ and the wave is completely transmitted (welded interface).

Characteristics of the stop-band are influenced by the number N of discontinuities. The increase of the number N of joints leads to an increase of the reflectivity within the stop-band and enlargement of its width. The band edges become also sharper. We can observe form Figure 4.20 and Figure 4.21 that when N increases, the band edges are sharper and the reflection coefficient tends to the unity exponentially with N. If the number N of discontinuities is high enough we can obtain reflection coefficient near 1 and the band edges are essentially vertical (Figure 4.20 and Figure 4.21). This last statement is confirmed by the fact that, for a very large N (Figure 4.22), the band edges maintain their position. Moreover the number of oscillations between two successive stop-bands is N-1.

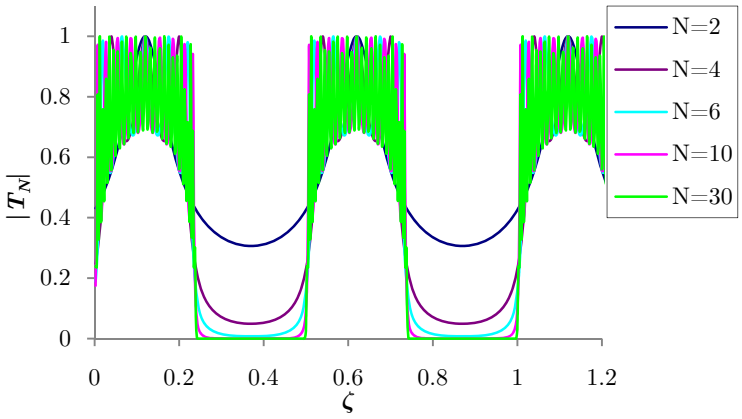

(a)

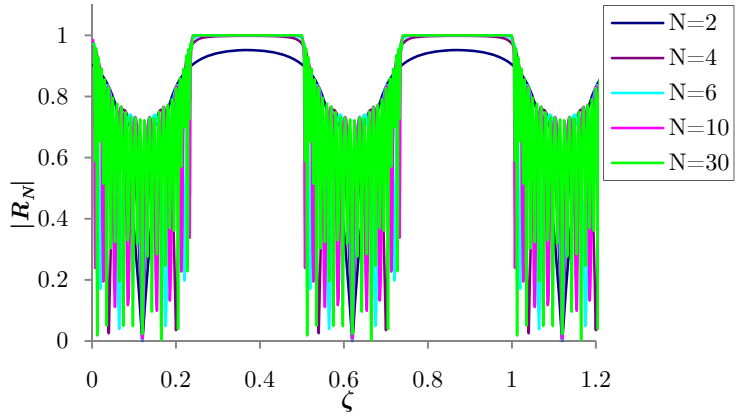

(b)

Figure 4.20 – Magnitude of the transmission and reflection coefficients versus the joint spacing ratio ζ and with $K_{ss} = 0.47$, for a medium with N parallel equispaced discontinuities and with SH-wave normally incident

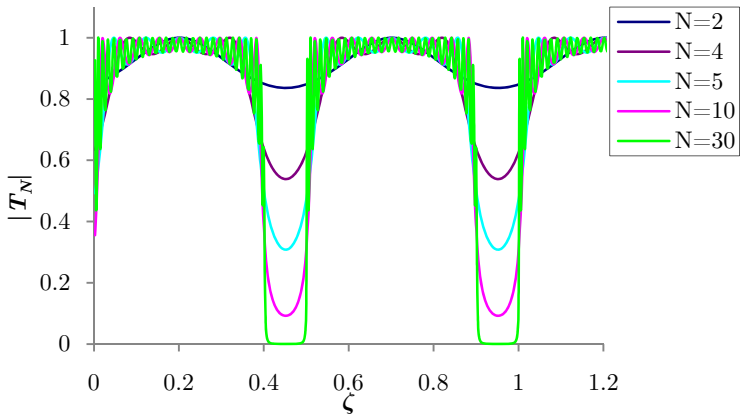

(a)

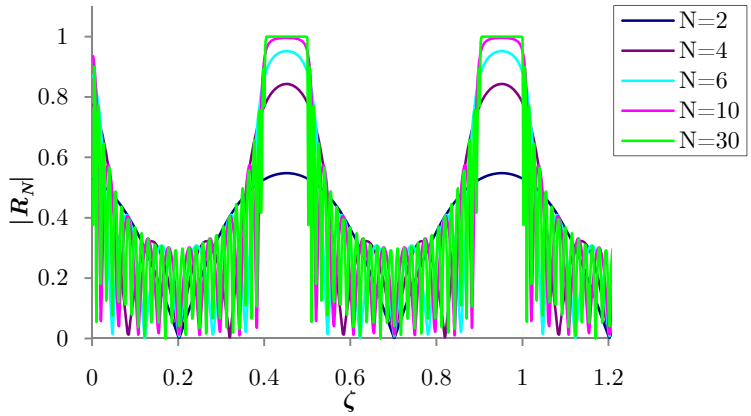

(b)

Figure 4.21 – Magnitude of the transmission and reflection coefficients versus the joint spacing ratio ζ and with $K_{ss} = 1.6$, for a medium with N parallel equispaced discontinuities and with SH-wave normally incident

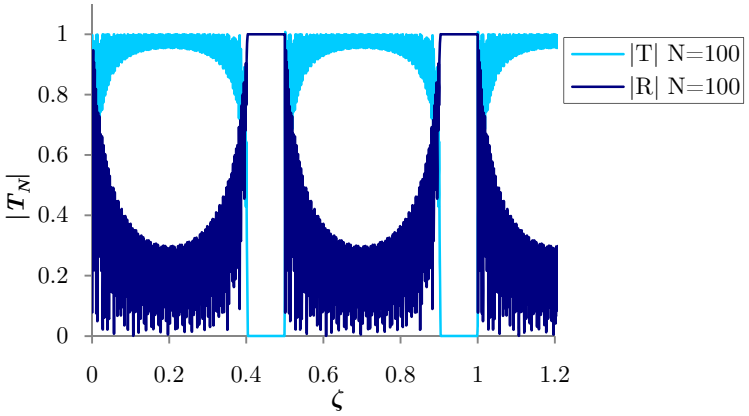

Figure 4.22 – Magnitude of the transmission and reflection coefficients versus the ratio ζ with $K_{ss} = 1.6$ and with a very large number of discontinuities

In the end, this paragraph develops a well known methodology (especially in optical physics) that allows understanding the behaviour of discontinuous media with parallel equi-spaced discontinuities. We have derived simple analytical expressions of the reflection and transmission coefficients. These coefficients are function of:

- number N of discontinuities,
- joint stiffness,
- angle of incidence and frequency of the SH-wave.

For certain values of frequency or the ratio ζ, the SH-wave is completely reflected (stop-bands).

From the previous results, we can say that by increasing the number N of joints the magnitude of the transmission coefficient decreases while the magnitude of the reflection coefficient increases. Another important parameter is the normalized joint stiffness. When this value increases the magnitude of the transmission coefficient increases while the magnitude of the reflection coefficient decreases.

For a certain number of joints (some tens), depending on the joints stiffness, in the stop-bands and then for certain ranges of normalized joint spacing ratio there is a total reflection of the incident wave.

Additional analyses are performed in Chapters 5 to 8 for each type of joint behaviour considered in this thesis.

4.8 Summary

The application of the SMM to wave propagation through discontinuous media has been presented with interest in different types of joint behaviour (e.g. linear elastic, or viscoelastic).

The expressions of the transmission and reflection coefficients for one joint and for N parallel equi-spaced joints has been obtained. Bloch wave theory has been used to understand the behaviour of a periodic medium and then of a medium with N equi-spaced parallel joints.

The fundamental parameter for describing a joint with SMM is the admittance of the joint or discontinuity. By applying the analogy with the transmission lines, we have considered a relevant equivalent circuit in which the admittance is connected in parallel on the transmission line representing wave propagation in the z direction. The joint admittance is function of the frequency and of the properties of the joint (normal and shear stiffness and specific viscosity of the fluid or the soft material that fills the joint).

The increase in the number of joints produces an increase of the reflected wave and a decrease of the transmission coefficient. The transmission coefficient increases with the increasing of the joint stiffness and with the decreasing of the frequency. Moreover, the transmission coefficient is more or less influenced by the number of joints as a function of the normalized joint spacing ratio.

The behaviour of a medium with a set of parallel joints is periodic in the frequency domain (application of a harmonic incident wave).

Chapter 5

Comparative study of wave propagation across multiple rock joints by different analytical methods

5.1 Introduction

The theoretical methods proposed by different Authors for the study of wave propagation through discontinuous media (also see Chapter 2), in addition to the Scattering Matrix Method (SMM) developed in the previous two chapters, are briefly reviewed in the following.

These methods may be classified as pertaining to either the Displacement Discontinuity Method (DDM) or to the Equivalent Medium Method (EMM). Firstly, we will introduce the Method of Characteristics (MC) and the Virtual Wave Source Method (VWSM) that belong to the DDM. Then, the Equivalent Medium Method (EMM), recently developed by Li et al. (2010), will be described.

With reference to these methods a comparative study of wave propagation across multiple rock joints, where multiple wave reflections are taken into account, is presented. The advantages and disadvantages of these methods with respect to SMM will also be discussed.

5.2 Method of Characteristics (MC)

MC has been widely used to study one-dimensional wave propagation in continuous media (Ewing et al. 1957; Courant and Hilbert 1962; Bedford and Drumheller 1994). Based on the one-dimensional wave equation, relations between particle velocity and stress along right- and left-running characteristics can be built.

As shown in Figure 5.1, the quantity $(Zv + \sigma)$ is a constant along any straight line with slope $1/\alpha$ (right-running characteristic) in the x-t plane, where σ is the normal stress, v is the wave velocity, $Z = \rho\alpha$ is the impedance of the material, ρ is the rock density, and α the wave velocity. Similarly, the quantity $(Zv - \sigma)$ is a constant along any straight line with slope of $-1/\alpha$ (left-running characteristic) in the x-t plane. It is noted that the normal stress is defined to be positive for compressive stress, and negative for tensile stress. The definition is consistent with that commonly used in rock mechanics.

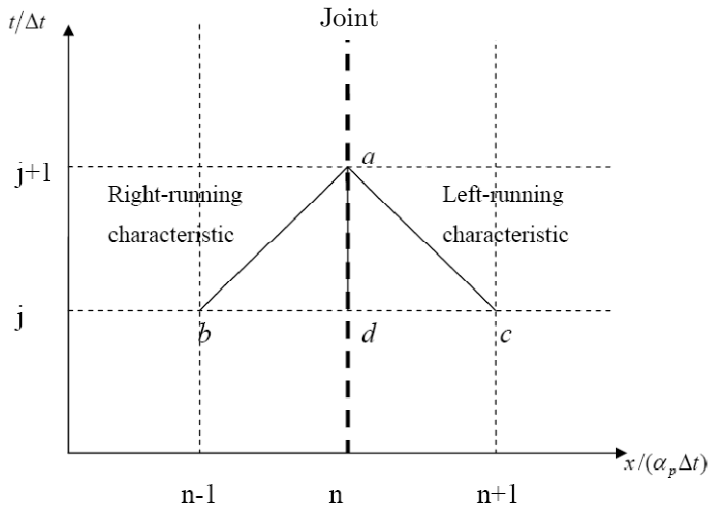

Figure 5.1 - Characteristics in the non-dimensional x-t plain (Cai and Zhao, 2000)

MC can also be used to study wave propagation across discontinuous jointed rock masses (Cai and Zhao, 2000; Zhao J. et al., 2006). When a wave propagates in a jointed rock mass, multiple reflections occur between joints. Actually, the transmitted wave across parallel joints can be treated as wave superposition of differently arriving transmitted waves caused by the multiple reflections. In the x - t plane, new variables, non-dimensional distance (n) and non-dimensional time (j), are used:

$$j = t \,/\, \Delta t \tag{5.1}$$

$$n = x \,/\, (\alpha \Delta t) \tag{5.2}$$

where Δt is the time interval.

It is assumed that a finite number of interfaces are located at integral values of non-dimensional distance in a half space with its left boundary at n=0, the first interface at n=1, the second interface at n=2, and the last interface at n=l (l is an integer). The interface could be a joint or a welded interface, which can be treated as a joint with infinite joint specific stiffness.

Figure 5.1 shows conjunction points of right- and left-running characteristics at integral values of non-dimensional distance and non-dimensional time. Particle velocities and normal stresses are evaluated at these points. However, this does not mean that solutions can be obtained only at the interface positions. If the field between two adjacent interfaces is further divided into a certain number of layers,

solutions can be obtained at these layers' boundaries, which are treated as joints with infinite joint specific stiffness.

In the analysis, it is assumed that joints and elastic media on both sides of the joints have identical properties. Along the right-running characteristic *ab* and the left-running characteristic *ac* shown in Figure 5.1, two relations between particle velocities and normal stresses at points *a*, *b* and *c* are built:

$$Zv^{-}(n, j+1) + \sigma^{-}(n, j+1) = Zv^{+}(n-1, j) + \sigma^{+}(n-1, j) \tag{5.3}$$

$$Zv^{+}(n, j+1) - \sigma^{+}(n, j+1) = Zv^{-}(n+1, j) - \sigma^{-}(n+1, j) \tag{5.4}$$

where $v^{-}(n, j+1)$ and $v^{+}(n, j+1)$ are particle velocities at time $j + 1$ before and after the joint at distance n, $\sigma^{-}(n, j+1)$ and $\sigma^{+}(n, j+1)$ are normal stresses at time $j + 1$ before and after the joint at distance n.

Based on the DDM, the stresses at the joint are continuous, while the displacements are discontinuous. Therefore, the response at point *a* can be derived:

$$\sigma^{-}(n, j+1) = \sigma^{+}(n, j+1) = \sigma(n, j+1) \tag{5.5}$$

$$u^{-}(n, j+1) - u^{+}(n, j+1) = \sigma(n, j+1) \,/\, k_{nn} \tag{5.6}$$

where k_{nn} is the normal joint specific stiffness, $u^{-}(n, j+1)$ and $u^{+}(n, j+1)$ are displacements at time j+1 before and after the joint at distance n.

With Equation (5.5), the addition of Equations (5.3) and (5.4) gives:

$$\begin{aligned} &Zv^{-}(n, j+1) + Zv^{+}(n, j+1) = \\ &= Zv^{+}(n-1, j) + \sigma^{+}(n-1, j) + Zv^{-}(n+1, j) - \sigma^{-}(n+1, j) \end{aligned} \tag{5.7}$$

The differentiation of Equation (5.6) with respect to t is:

$$v^{-}(n, j+1) - v^{+}(n, j+1) = \frac{1}{k_{nn}} \frac{\partial \sigma(n, j+1)}{\partial t} \tag{5.8}$$

If Δt is small enough, Equation (5.8) can be expressed as:

$$v^{-}(n,j+1)-v^{+}(n,j+1)=\frac{\sigma(n,j+1)-\sigma(n,j)}{k_{nn}\Delta t} \tag{5.9}$$

Equation (5.9) can be rewritten as:

$$\sigma(n,j+1)=\sigma(n,j)+k_{nn}\Delta t[v^{-}(n,j+1)-v^{+}(n,j+1)] \tag{5.10}$$

Substituting Equation (5.10) into Equation (5.3) gives:

$$\begin{aligned}&(k_{n}\Delta t+Z)v^{-}(n,j+1)-k_{nn}\Delta t v^{+}(n,j+1)+\sigma(n,j)=\\&=Zv^{+}(n-1,j)+\sigma(n-1,j)\end{aligned} \tag{5.11}$$

Equations (5.7) and (5.11) form a linear equation group with respect to particle velocities at point a before and after the joint. After it is solved, expressions of particle velocities at point a are obtained:

$$\begin{aligned}&v^{-}(n,j+1)=(Zv^{+}(n-1,j)+\sigma(n-1,j)-\sigma(n,j)+\frac{k_{nn}\Delta t}{Z}(Zv^{-}(n+1,j)\\&+Zv^{+}(n-1,j)+\sigma(n-1,j)-\sigma(n+1,j)))\,/\,(2k_{nn}\Delta t+Z)\end{aligned} \tag{5.12}$$

$$\begin{aligned}&v^{+}(n,j+1)=\\&=(Zv^{+}(n-1,j)-\sigma(n+1,j)+\sigma(n-1,j)+Zv^{-}(n+1,j))\frac{k_{nn}\Delta t+Z}{Z}+\\&-Zv^{+}(n-1,j)+\sigma(n,j)-\sigma(n-1,j))\,/\,(2k_{nn}\Delta t+Z)\end{aligned} \tag{5.13}$$

By substituting Equations (5.12) and (5.13) into Equation (5.10), the expression of normal stress is derived as follows:

$$\begin{aligned}&\sigma(n,j+1)=\sigma(n,j)+\frac{k_{nn}\Delta t}{2k_{nn}\Delta t+Z}(Zv^{+}(n-1,j)+\sigma(n-1,j)\\&-Zv^{-}(n+1,j)+\sigma(n+1,j)-2\sigma(n,j))\end{aligned} \tag{5.14}$$

Equations (5.12) to (5.14) show that the responses at point a are determined by those at points b, c and d. Meanwhile, it indicates that responses at time $j+1$ can be calculated from those at time j. With input velocity of $v(0, j)$ and initial conditions of $v^{+}(n,0)$, $v^{-}(n,0)$ and $\sigma(n,0)$, Equations (5.11) to (5.13) are applied

to determine particle velocities and stress at any point through an iterative computation.

5.3 Virtual Wave Source Method (VWSM)

Li et al. (2010) introduced a new concept of virtual wave source (VWS) with a viscoelastic medium model to establish an equivalent viscoelastic model, which can describe the dynamic properties of the rock mass and derived an explicit expression for the wave propagation equation. Here, the VWS concept is extended to the study of a discontinuous rock mass.

The VWS exists at the joint position and produces new waves when the incident wave approaches the joint. The transmitted wave across the rock mass can be treated as the superposition of different transmitted waves created by the VWS. Combined with the DDM, VWS can also be used to study wave propagation across a discontinuous rock mass, where the discreteness of the joints can be taken into account.

If an incident harmonic P-wave with the form of:

$$v_I = I \exp(i\omega t) \tag{5.15}$$

transmits across a joint, the reflection and transmission coefficients across it can be written as (Equations 4.23):

$$R_1 = \frac{i}{-i + 2k_{nn} \,/\, (Z_P \omega)} \tag{5.16}$$

$$T_1 = \frac{2k_{nn} \,/\, (Z_P \omega)}{-i + 2k_{nn} \,/\, (Z_P \omega)} \tag{5.17}$$

where I is the amplitude of the incident wave.

Equations (5.16) and (5.17) show that reflection and transmission coefficients are dependent on a combined parameter $K_{nn} = k_{nn} \,/\, (Z_P \omega)$ which is named as normalized normal joint stiffness.

In order to obtain the theoretical solution of the transient wave transmitting across a joint set, the incident transient wave (v_I) is first transformed into frequency domain by FFT (Fast Fourier Transform). In the frequency domain, the incident transient wave can be transformed as the sum of a series of harmonic waves with different amplitudes and frequencies:

$$v_I = \sum_{i=-\infty}^{\infty} v_{Ii} = \sum_{i=-\infty}^{\infty} A_i e^{i\omega_i t} \tag{5.18}$$

where v_{Ii} is one harmonic wave, A_i and ω_i are the amplitude and angular frequency of the harmonic wave v_{Ii}.

When the rock is characterized by the presence of two or more joints, the transmitted wave can be treated as wave superposition of transmitted waves arriving at different times. In order to take into account wave superposition, the method of VWS is used. The VWS exists at each joint position and produces two new waves with opposite directions when an incident wave impinges the VWS.

The concept of VWS can be re-explained as there are one 'reflected' wave and one 'transmitted' wave created from the VWS, when the wave arrives at the VWS's position. The reflected and transmitted waves from one joint can be obtained by Equations (5.16) and (5.17) when the incident harmonic wave is known.

Figure 5.2 illustrates the scheme of wave propagation across a jointed rock mass with VWS. The transmitted harmonic wave across one joint set is the result of the wave superposition of different transmitted waves created by the VWS:

$$v_{Ti} = \sum_{j=1}^{\infty} v_{Tij} \tag{5.19}$$

where v_{Ti} is the transmitted wave for the incident harmonic wave v_{Ii}, v_{Tij} is the transmitted wave arriving at different time, as shown in Figure 5.2.

Then, an inverse transform for these transmitted harmonic waves is conducted to get the transmitted transient wave (v_T) by IFFT (Inverse Fast Fourier Transform), which can transform one series of harmonic waves into a transient wave:

$$v_T = \sum_{i=-\infty}^{\infty} v_{Ti} \tag{5.20}$$

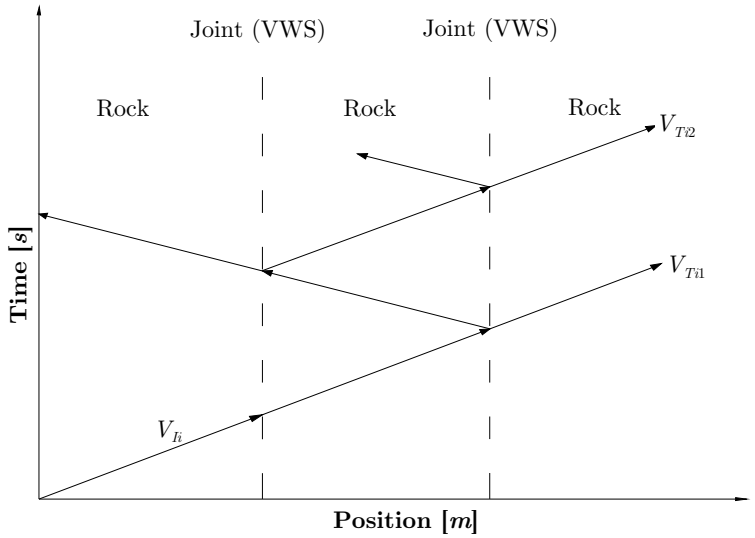

Figure 5.2 - Scheme of jointed rock mass with VWS (2 joints)

5.4 Equivalent Medium Method (EMM)

The equivalent medium method (EMM) (Li et al. 2010) is a continuous medium model which describes the dynamic property of the discontinuous rock mass. This model consists of a viscoelastic medium model and the concept of virtual wave source (VWS). The viscoelastic medium model is an auxiliary spring placed in series with the Kelvin-Voigt model (Figure 5.3), which can display both the attenuation and the frequency dependence of the transmitted wave. The concept of VWS is to consider the effect of discreteness of a rock mass on wave propagation, i.e., the wave reflections between two joints.

As for the longitudinal motion equation for one-dimensional problems, the equivalent model of the auxiliary spring placed in series with the Kelvin-Voigt model can be mathematically expressed as:

$$\rho\eta_v \frac{\partial^2 v}{\partial t^2} + \rho(E_a + E_v)\frac{\partial v}{\partial t} - \eta_v E_a \frac{\partial^2 v}{\partial x^2} - E_v E_a \int \frac{\partial^2 v}{\partial x^2} dt = 0 \tag{5.21}$$

where v is the particle velocity, E_a is the Young's modulus of the intact rock, while E_v represents the stiffness contributed by the joints; η_v is the viscosity.

Define $\tau = \eta_v / E_v$ as the time of retardation of the Kelvin-Voigt element, and:

$$\frac{1}{E_c} = \frac{1}{E_a} + \frac{1}{E_v} \tag{5.22}$$

E_v and η_v need to be determined by comparing the transmitted wave through the equivalent medium with the existing solutions of a discontinuous rock mass. E_v is obtained for each joint section (including one joint and rock material having thickness equal to the joint spacing). Therefore, joint spacing is involved in the determination of E_v, while the joint thickness is not since the joint is very thin and the thickness is considered to be zero.

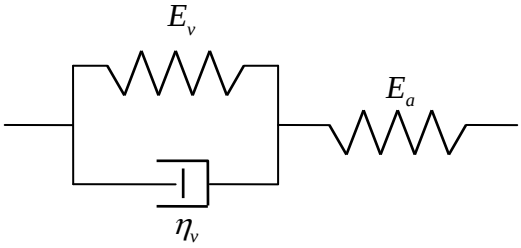

Figure 5.3 - Equivalent mechanical model of an auxiliary spring in series with Kelvin-Voigt model

The solution for Equation (5.21) has the following form:

$$v = A \cdot \exp(\beta x) \exp[i(-\omega t + \alpha x)] \tag{5.23}$$

and

$$\begin{cases} \alpha = \left\{ \dfrac{\rho\omega^2}{2E_cE_a} \left[\left(\dfrac{{E_a}^2 + {E_c}^2\omega^2\tau^2}{1+\omega^2\tau^2} \right)^{1/2} + \dfrac{E_a + E_c\omega^2\tau^2}{1+\omega^2\tau^2} \right] \right\}^{\frac{1}{2}} \\ \beta = -\left\{ \dfrac{\rho\omega^2}{2E_cE_a} \left[\left(\dfrac{{E_a}^2 + {E_c}^2\omega^2\tau^2}{1+\omega^2\tau^2} \right)^{1/2} - \dfrac{E_a + E_c\omega^2\tau^2}{1+\omega^2\tau^2} \right] \right\}^{\frac{1}{2}} \end{cases} \tag{5.24}$$

where α gives the phase shift per unit length and the minus sign of β indicates the wave attenuation.

Across the joint set, the final transmitted wave is the superposition of two parts. The first one is from the direct transmission of the initial incident wave and the other one is from the multiple reflections among the joints. Although the frequency-dependence and wave attenuation have been shown in Equations (5.23) and (5.24), the effect of the discreteness of joints on wave propagation in the viscoelastic solid still cannot be reflected in the two equations.

In order to solve this problem, the concept of virtual wave source (VWS) is proposed in the equivalent medium model. The VWS exists at each joint surface and produces a new wave (in the opposite direction of the incident wave) at each time when an incident wave propagates across the VWS. The distance between two adjacent VWSs is equal to the joint spacing d. The equivalent length of the medium is defined as the product of joint number N and the joint spacing d, i.e., Nd. Figure 5.4 shows a rock mass with three parallel joints and the corresponding equivalent medium with and without VWS, where the equivalent length is $3d$. The concept of VWS can be interpreted as that a reflected wave is created from the virtual wave source when either a positive wave or a negative wave arrives at the VWS.

Assume there is an incident P-wave:

$$v_I(t,0) = A\exp(-i\omega t) \tag{5.25}$$

from the left side A of the equivalent medium in Figure 5.4. According to Equation (5.22), along the direction of the incident wave the particle velocity at point B is:

$$v_e(t,d) = A\exp(\beta d)\exp[i(-\omega t + \alpha d)] \tag{5.26}$$

where the phase shift of $v_e(t,d)$ and $v_I(t,0)$ is αd. According to the energy conservation of the simple harmonic waves (Cook 1992), the amplitude of the reflected wave at the interface B is $A\{1-[\exp(\beta d)]^2\}^{1/2}$, if the interface B is a discontinuous boundary.

From the Kramer-Kronig relation (a statement of causality), any changes in the amplitude of a wave must be accompanied by a change in phase. Since the phase shift between the reflected and transmitted waves is $\pi/2$ (Pyrak-Nolte et al. 1990a; Cook 1992), the reflected wave at B can be expressed as:

$$v_e'(t,d) = A\sqrt{1-[\exp(\beta d)]^2}\,\exp[i(-\omega t + \alpha d - \pi\,/\,2)] \tag{5.27}$$

where $v_e'(t,d)$ is regarded as the wave produced from the VWS at B. Then, $v_e(t,d)$ and the created wave $v_e'(t,d)$ propagate along two opposite directions as new incident waves to the adjacent interfaces C and A, where new waves are repeatedly

created and propagate to their adjacent interfaces. The transmitted wave at the right side D of the equivalent medium is a wave superposition of $v_e(t,3d)$ arriving at different times, which is the summation of multiple waves created from the three VWSs and the transmitted wave from the incident wave $v_I(t,0)$ propagating across the viscoelastic medium.

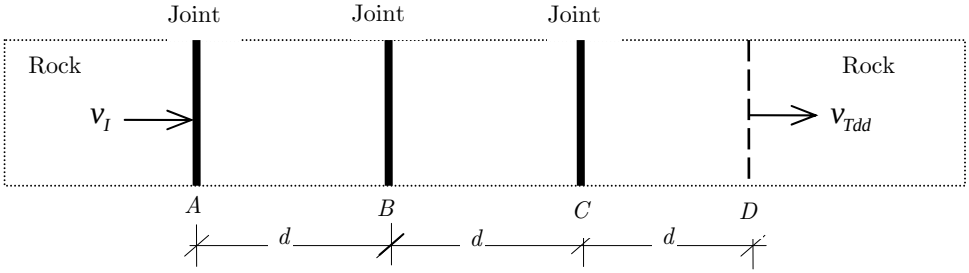

(a) Jointed rock mass

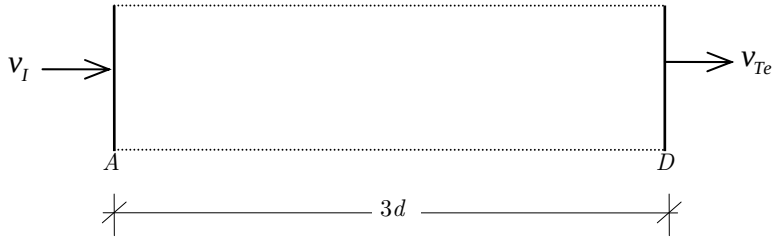

(b) Equivalent medium model without virtual wave source (VWS)

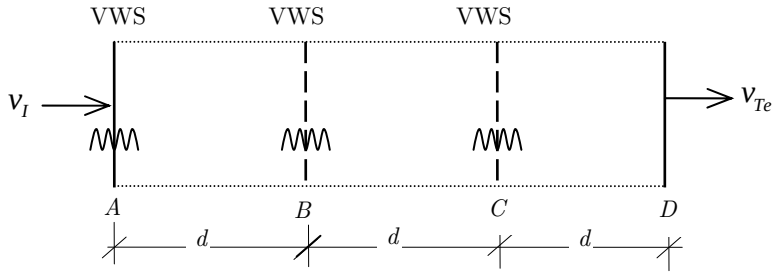

(c) Equivalent medium model with virtual wave source (VWS)

Figure 5.4 - Scheme of jointed rock mass and equivalent medium

5.5 Comparative study

In order to compare the four different methods, the SMM and the three methods briefly described above (MC, VWSM, and EEM), a one-dimensional P-wave propagation analysis through a rock mass with parallel joints is performed. The joints considered in the analysis are planar, large in extent and small in thickness compared to the wavelength. The material damping is considered because we only study the effects of joints on wave propagation.

The model is the same for all the methods considered as shown in Figure 5.4a. A normally incident half-cycle sinusoidal P-wave is assumed to be applied at the boundary of the model with a frequency of f_0=*100Hz* and unit amplitude (Figure 5.5). Hence, the incident wave is applied at the boundary "*A*" while the transmitted wave is recorded at the boundary "*D* " (Figure 5.4a). The assumed mechanical properties of the rock mass are listed in Table 5.1.

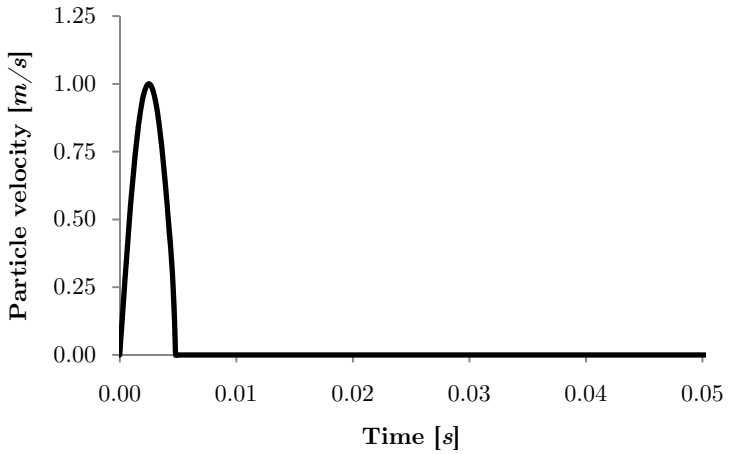

Figure 5.5 - Incident wave (half-cycle sinusoidal wave)

Transmitted waveforms across 1, 2, 3 and 4 parallel joints with joint spacing d= $1/10\lambda$ and normalized joint stiffness K_{nn} = 0.36 are plotted in Figure 5.6. The transmission coefficient is defined as the ratio of the amplitude of the transmitted wave to that of the incident wave. The transmitted wave is shown to decreases in amplitude with increasing number of joints. Therefore, the incident wave is attenuated from the jointed rock mass, and this attenuation increases with the number of joints. Each joint causes a time delay of the transmitted wave. This time delay increases with the joint number and it results in a phase shift. Hence the phase shift ϑ for a compressional wave normally incident upon a joint (Schoenberg, 1980) is a function of the normalized joint normal stiffness K_{nn} and

$\vartheta = \arctan(1 / 2K_{nn})$. Obviously, there is also another part of this time delay that is caused by the medium between joints.

Table 5.1- Mechanical properties of the rock mass

Model	Parameters from curve fit
Density	2650 kg/m^3
Velocity of the propagating P-wave	5830 m/s
Joint normal stiffness	3.5 GPa/m^3

Moreover, it is clear from Figure 5.6 that the transmitted waveforms obtained with all four methods are almost coincident. We can only note negligible differences for later arriving transmitted waves.

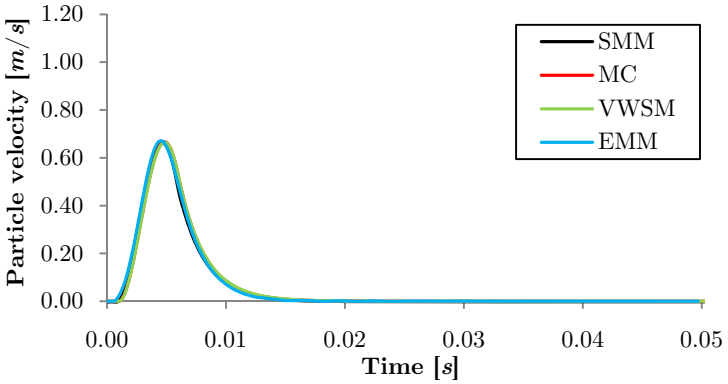

(a) Single joint

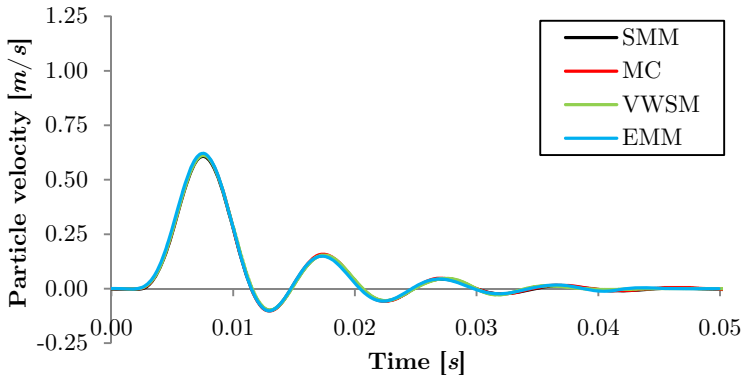

(b) Two joints

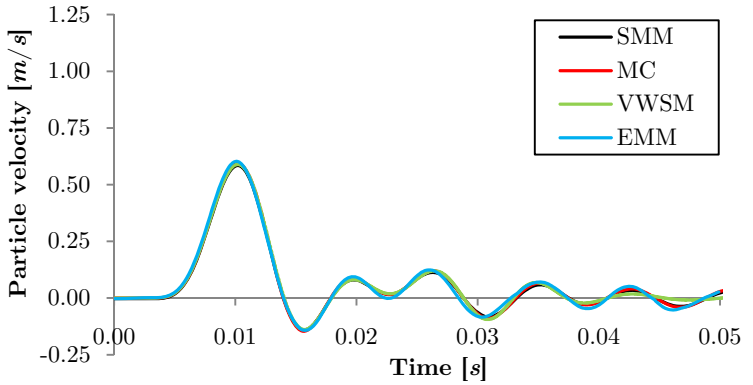

(c) Three joints

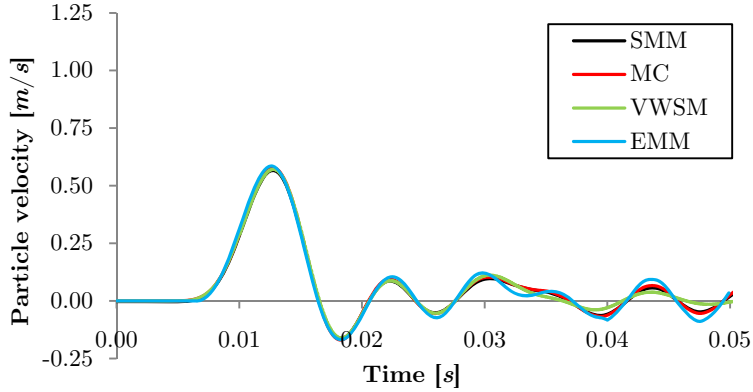

(d) Four joints

Figure 5.6 - Comparison of transmitted waves obtained from four methods with different joint number N (K_{nn}=0.36 and d=1/10λ)

Wave propagation across a single fracture is simulated as shown in Figure 5.7. By showing the trend of the transmission coefficient $|T_1|$ versus the normalized joint normal stiffness $|K_{nn}|$, it is found that the four methods agree well with each other. In Figure 5.7 we can see that if the value of $|K_{nn}|$ approaches infinity, $|T_1|$ approaches 1. While $|K_{nn}|$ approaches 0, $|T_1|$ approaches 0. These two limit conditions correspond respectively to the case of a welded and free interface. Between these two extreme conditions, $|T_1|$ increases with increasing $|K_{nn}|$.

Figure 5.8 shows the transmission coefficient $|T_2|$ evaluated for a model with two parallel joints by varying the non-dimensional ratio (ζ) of joint spacing to wavelength for different values of K_{nn} (0.3, 1). The following remarks are made:

1. The four methods agree well with each other.
2. $|T_2|$ increases with increasing K_{nn}.
3. When $\zeta > 0.19$ for K_{nn} and $\zeta > 0.26$ for $K_{nn} = 0.3$, $|T_2|$ is constant.
4. For smaller ζ values, $|T_2|$ reaches a maximum value. The trends of $|T_2|$ versus ζ are essentially the same for the two values of K_{nn} analysed.
5. $|T_2|$ increases with K_{nn}.

Figure 5.9 shows the magnitude of transmission coefficients across N (2, 4 and 6) joints as a function of ζ with $K_{nn} = 0.36$. We can note that:

1. The four methods agree well. There is only a small gap between EMM and other DDMs between $\zeta = 0.31$ and $\zeta = 0.57$.
2. $|T_N|$ decreases with the increasing of N.
3. When $\zeta > 0.24$ for $N = 2$, $\zeta > 0.46$ for $N = 4$ and $\zeta > 0.66$ for $N = 6$, $|T_N|$ is constant. In this zone, $|T_N|$ strongly decreases with N according to the exponential function $|T_N| = |T_1|^N$, as proposed by Pyrak-Nolte et al. (1990a).
4. For smaller ζ values, $|T_N|$ reaches the maximum value. In this area, $|T_N|$ decreases more slowly with increasing N. Moreover, in the range of ζ between 0 and 0.04 (0.04 corresponds to the max value of $|T_N|$), $|T_N|$ is approximately the same with increasing N.

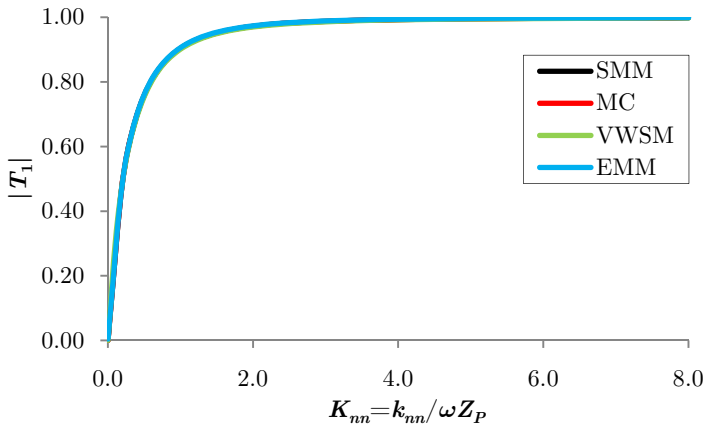

Figure 5.7 - Transmission coefficient for a single joint versus K_{nn}

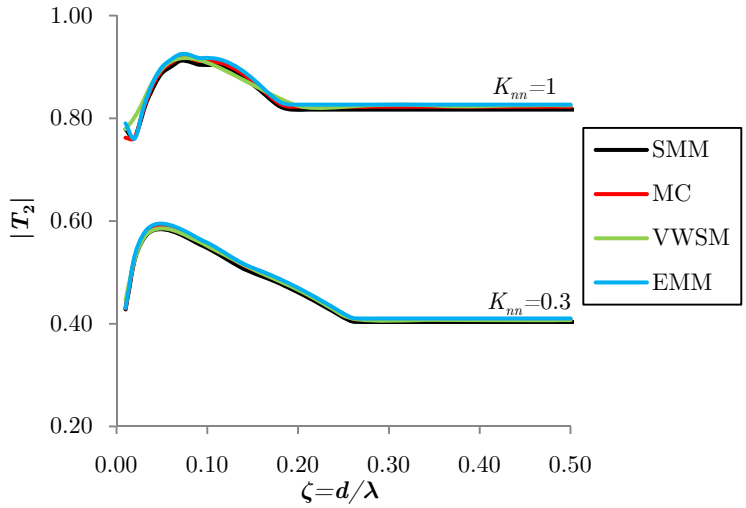

Figure 5.8 - Transmission coefficient for two parallel joints versus the non-dimensional joint spacing ζ

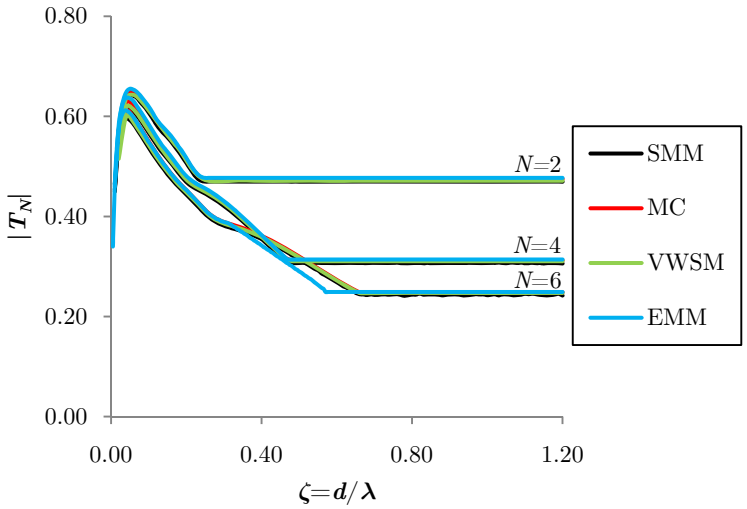

Figure 5.9 - Transmission coefficient for N parallel joints versus the non-dimensional joint spacing ζ with a $K_{nn} = 0.36$

Finally, wave attenuation across jointed rock masses is mainly due to the presence of joints, although there is wave attenuation due to rock material damping (not considered in these analyses).

In fact, if the stiffness of the joint decreases, the amplitude of the transmitted wave decreases. If the frequency increases, the amplitude of the transmitted wave decreases. The reduction of the amplitude of the transmitted wave increases with the increasing of the number of joints because at each joint some energy of the wave is reflected.

5.6 Discussion

The MC, SMM and VWSM methods use the displacement discontinuity model for representing the joint as a discontinuity in displacements, while EMM adopts a different approach to model the rock mass.

MC is widely used in solving particle one-dimensional wave propagation problems and also helps to explain the boundary and initial problems that must be prescribed in such cases. The method works directly in the time domain. Therefore, FFT and IFFT cannot shorten computation time.

With MC, wave interaction with different joint behaviour can be studied, e.g., joints with nonlinear behaviour (the static BB model, Zhao XB et al. 2006a) and joints with Coulomb slip behaviour (Zhao XB et al. 2006b). MC can also be used

to study wave propagation across a large number of joints and joints with different spacing. MC cannot be used in frequency domain.

The MC uses differential equations to calculate the dynamic response and therefore it is affected by inherent computation errors. With smaller time interval, the results will be more accurate, but the computation efficiency will be lower. In addition, it is hard to study with MC obliquely incident wave propagation across jointed rock masses.

With SMM, all multiple wave reflections between joints are taken into account. This method works in frequency domain. Transmission and reflection coefficients for a single joint or for many joints can be derived analytically. With SMM, we can derive the analytical expressions available in literature (e.g., Pyrak-Nolte et al. 1990a). With this method, material damping can be considered, which in previous analyses was set equal to zero, in order to better evaluate the influence of joints on wave propagation.

SMM can also allow to study various joint conditions (e.g. dry, filled or frictional joints) and to treat obliquely incident waves across a joint set. Additionally, wave propagation across a large number of joints in a rock mass and joints with different spacing can be studied. However, in order to study wave propagation in time domain, FFT and IFFT are to be used to transform harmonic wave to transient wave. Thus, there will be additional computation time, and the time interval will result in computational errors. For an obliquely incident wave, some difficulties can be found in comparing the transmitted wave computed by using SMM and that measured in experiments or obtained by numerical modelling. These difficulties are due to the limited transversal size of the specimen or of the numerical model, which results in a limited number of transmitted waves from multiple wave reflections between joints.

VWSM uses a virtual concept in order to represent the influence of joints on wave propagation. VWS exists at each joint position and produces new waves (2 in opposite directions) each time an incident wave propagates across the VWS. With the transmission and reflection coefficients obtained for one single joint in frequency domain, wave propagation across one joint set can be studied, where multiple wave reflections are considered. Material damping can also be taken into account. The method can be extended to study obliquely incident waves across one joint set with different joint spacing.

In addition, with VWSM, different arriving transmitted waves can be separated, and the analytical results can be compared with experiments, numerical modelling and in situ tests, especially for obliquely incident waves. However, in the time domain, FFT and IFFT should be used to transform harmonic wave to transient wave. Thus, there will be additional computation time, and the time interval will result in computational errors. Besides, the times of multiple wave reflections are controlled by the time duration used in the computation. With longer time, the times of multiple wave reflections will be larger and the results will be more accurate but the computational time will be longer.

Unlike previous methods, the EMM adopts an equivalent viscoelastic medium model and the concept of VWS to solve the problem. The VWS is to reflect the discreteness of rock mass, or to describe the multiple reflections among joints. With this method, effective moduli of the jointed rock mass can be accurately obtained. It is convenient to adopt the effective moduli to quantitatively compute the wave attenuation across the jointed rock mass in engineering application. However, this method requires some additional steps for computing the input parameters (stiffness contributed by the joints (E_v) and viscosity (η_v)) that are function of the incident wave frequency and the joint spacing. The EMM also needs to carry out further study for some other problems, such as the obliquely incident wave propagation problems and the wave propagation across a great number of joints with different spacing.

5.7 Summary

The methods described above can be used to simulate wave propagation across a set of rock joints, where multiple wave reflections can be taken into account. All of them have advantages or disadvantages. Depending on the problem to be solved (type of input signal or joint conditions), a specific method can be chosen and adopted.

In particular, SMM is very good to solve wave propagation problems through a large number of joints because the time required for computations is small and the accuracy remain the same of that for a single joint. Particularly efficient for this type of analysis is the method of Bloch waves (see Chapter 4) that gives, for a periodic distribution of joints, the same results of the SMM. It is important to say that although the SMM work in frequency domain gives results that are very near to those obtained with a completely different method operating in the time domain as MC.

On the other hand, MC and VWS are not very good if the number of joints is large because the computational time becomes very large and if the incident plane wave impinges obliquely the joints. EMM is the most simplified approach and many difficulties may be found if we increase the number of joints or we consider a oblique incident wave.

Chapter 6

Filled joints

6.1 Introduction

Many studies have been performed on wave propagation across non-filled joints (Cai and Zhao, 2000; Schoenberg, 1980). However, natural joints, are often filled with materials such as sand or clay or are water saturated. Therefore, the study of wave propagation across filled joints is of great interest.

In the present chapter, this problem is analysed by using the SMM as developed in Chapter 4. Parametric analyses are performed to evaluate the effects of joint properties and of the impedance ratio between the filling material and the rock on wave propagation. The results obtained with the SMM are compared with those derived with other analytical solutions and numerical methods.

Consideration is finally given to the results of tests performed with the modified split Hopkinson pressure bar of P-wave propagation across a joint filled with saturated sand (Li and Ma, 2009). These results are back analysed with the SMM by using Kelvin, Maxwell and Burger viscoelastic models.

6.2 Analytical solutions for wave propagation across a single filled joint with SMM

The simulation of wave propagations through a filled joint can be performed by using different analytical methods. The most accurate method is the "thin plane layer model TPLM" (Fehler, 1982) where the joint is modelled as a thin layer and composed of two welded interfaces between the intact rock and the filling material and between the filling material and the intact rock. Another method is an approximation of the first one and uses the DDM (Schoenberg, 1980 and Pyrak-Nolte, 1990) as modified by Rokhlin and Wang (1991). Also used is the EMM which simplifies the problem significantly.

With the SMM a rock joint can be modelled according to different approaches: the "thin plane layer model TPLM" and the "displacement discontinuity model DDM" modified with the introduction of a stress discontinuity. The choice of one method or the other one is dependent on the joint conditions and the accuracy required for the computations to be performed.

6.2.1 Thin Plane Layer Model (TPLM)

The TPLM simulates the filling material as a thin layer with thickness h composed by two interfaces with the intact rock (Figure 6.1) and characterized by continuity of velocities and stresses. With this model, we are in the typical condition of a continuum and the theory of wave propagation as described in Chapter 3 can be applied.

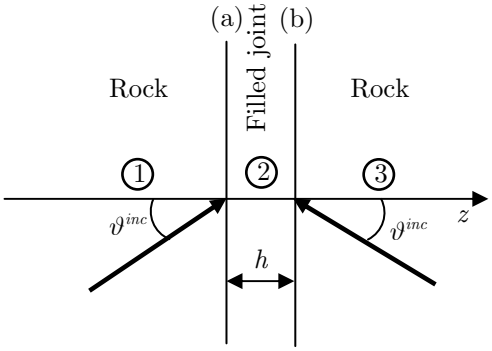

Figure 6.1 – Thin plane layer model

Analytical expressions of the transmission and reflection coefficients can be derived by computing the transmission matrices of the two welded interfaces that form the joint. For the SH-wave polarization we have:

$$\mathbf{A}^{(a)} = \mathbf{M_1^{-1}M_2} = \begin{pmatrix} \frac{1}{2}+\frac{F}{2} & \frac{1}{2}-\frac{F}{2} \\ \frac{1}{2}-\frac{F}{2} & \frac{1}{2}+\frac{F}{2} \end{pmatrix} \tag{6.1}$$

$$\mathbf{A}^{(b)} = \mathbf{M_2^{-1}M_3} = \begin{pmatrix} \frac{1}{2}+\frac{1}{2F} & \frac{1}{2}-\frac{1}{2F} \\ \frac{1}{2}-\frac{1}{2F} & \frac{1}{2}+\frac{1}{2F} \end{pmatrix} \tag{6.2}$$

where:
$\mathbf{A}^{(a)}$, $\mathbf{A}^{(b)}$ are the transmission matrices of the welded interfaces (a) and (b) (see Chapter 3);

$F = \dfrac{C_{44_2} k_{zS_2}}{C_{44_1} k_{zS_1}}$ is the impedance ratio between the filling material and the rock.

To obtain the global transmission matrix of the filled joint we can compute the scattering matrix of layer 2 with thickness h:

$$\mathbf{A}_{str}^{(2)} = \begin{pmatrix} diag\left(e^{jk_{zS}h}\right) & 0 \\ 0 & diag\left(e^{-jk_{zS}h}\right) \end{pmatrix} \tag{6.3}$$

The global transmission matrix of the filled joint is:

$$\mathbf{A} = \mathbf{A}^{(a)}\mathbf{A}_{str}^{(2)}\mathbf{A}^{(b)} \tag{6.4}$$

and with some algebraic manipulations (see Equations 3.45) we can obtain the scattering matrix and then the reflection and transmission coefficients of the filled joint represented with the TPLM:

$$R_{SH}\left(\omega,\theta\right) = S_{11} = \frac{\left(\frac{1}{4F} - \frac{F}{4}\right)\phi}{\frac{1}{2}\varphi + \left(\frac{1}{4F} + \frac{F}{4}\right)\phi} \tag{6.5}$$

$$T_{SH}\left(\omega,\theta\right) = S_{21} = \frac{1}{\frac{1}{2}\varphi + \left(\frac{1}{4F} + \frac{F}{4}\right)\phi} \tag{6.6}$$

where:

$\phi = e^{jk_{zS_2}h} - e^{-jk_{zS_2}h}$ and $\varphi = e^{jk_{zS_2}h} + e^{-jk_{zS_2}h}$;

k_{zS_2} is the z wave vector component in the filling material.

Equations (6.5) and (6.6) show that the reflected and transmitted waves are function of the impedance ratio F and the thickness h of the joint. If we consider the filled of the joint as viscoelastic (Chapter 3) the shear modulus becomes complex ($G_f^* = G_f + j\omega\eta_f$ for Kelvin-Voigt model).

6.2.2 Displacement Discontinuity Method (DDM)

When the density of the filled material is not negligible compared with the rock density, the initial mass of the filled joint can affect wave propagation (Rokhlin

and Wang, 1991). With consideration given to the initial mass terms of the filled joint, besides the displacements, the stresses across it are also discontinuous. In fact, the density of the filled material, which is usually saturated sand or clay, is comparable with the rock density. Therefore, the simple displacement discontinuity model (Pyrak-Nolte et al., 1990a; Schoenberg, 1980) is not appropriate to study wave propagation and a displacement and stress discontinuity model need be introduced.

There are numerous models to represent the viscoelastic behavior of a joint filled with soft materials. The Kelvin model (one spring and one dashpot in parallel) is usually adopted to describe the dynamic and seismic response of saturated soils (Braja and Ramana, 2011; Verruijt, 2010). However, Suárez-Rivera (1992) found that the Maxwell model (one spring and one dashpot in series) is more appropriate to study shear wave propagation across a thin clay layer. In the present study, both the Kelvin and the Maxwell models will be used. Also adopted is the Burger model.

The boundary conditions along a joint, according to the displacement and stress discontinuity model, are:

$$\begin{aligned} \left(\mathbf{v}_{A-} - \mathbf{v}_{A+}\right) &= \mathbf{Y} \cdot \boldsymbol{\tau}_A \\ \boldsymbol{\tau}_{A-} - \boldsymbol{\tau}_{A+} &= -\omega^2 \mathbf{M}\mathbf{u}_{A+} = j\omega\Pi\mathbf{v}_{A+} \end{aligned} \tag{6.7}$$

where:

$\Pi = \begin{pmatrix} m_t & 0 \\ 0 & m_n \end{pmatrix}$ for coupled P-SV waves and $\Pi = m_t$ for SH-waves. m_n is termed as the normal mass, m_t is called as the tangential mass (termed as the plate mass by Rokhlin and Wang, 1991).

Here, $m_n = \rho_0 h$, which determines the stress difference in the normal direction, is the mass of the filled medium of a unit area of the joint plane and named as the normal mass, where ρ_0 is the density of the filled medium, h is the joint thickness. $m_t = qm_n = [1\text{-}(C_{plate}/V_i)^2 \sin^2\vartheta^{inc}]m_n$, which determines the stress difference in the tangential direction, is the effective mass in the tangential direction and is named as the tangential mass. q is a parameter dependent on the plate velocity of the filled medium $C_{plate} = \{[E_0/[(\rho_0\ (1\text{-}\ \nu_0^2)]\}^{0.5}$, where E_0 and ν_0 are Young's modulus and Poisson's ratio of the filled medium, respectively, the incident angle ϑ^{inc} and the wave velocity of the rock corresponding to the type of the incident wave V_i, $V_i = V_P$ for P-wave or $V_i = V_S$ for S-wave. When the wave is normally incident upon the joint, $q = 1$ and thus $m_t = m_n$.

The analytical expressions of the reflection and transmission coefficients are also computed.

The transmission matrix $\boldsymbol{A}$ of the non-welded interface is obtained from the boundary conditions (6.7):

$$\begin{pmatrix} \mathbf{v}_{A-} \\ \boldsymbol{\tau}_{A-} \end{pmatrix} = \begin{pmatrix} \mathbf{v}_{A+} + \mathbf{Y}\boldsymbol{\tau}_{A+} \\ \boldsymbol{\tau}_{A+} + j\boldsymbol{\omega}\Pi\mathbf{v}_{A+} \end{pmatrix} = \begin{pmatrix} 1 & \mathbf{Y} \\ j\boldsymbol{\omega}\Pi & 1 \end{pmatrix} \begin{pmatrix} \mathbf{v}_{A+} \\ \boldsymbol{\tau}_{A+} \end{pmatrix} = \mathbf{M_1} \begin{pmatrix} \mathbf{C_1}^{+} \\ \mathbf{C_1}^{-} \end{pmatrix} \tag{6.8}$$

and in the same manner, as shown in the Chapter 4, we can obtain:

$$\mathbf{A} = \mathbf{M_1}^{-1} \begin{pmatrix} 1 & \mathbf{Y} \\ j\omega\Pi & 1 \end{pmatrix} \mathbf{M_2} \tag{6.9}$$

For SH polarization state, the extended expression of the transmission matrix is the following:

$$\mathbf{A} = \begin{bmatrix} 1 + \dfrac{Z_S}{2}Y + j\dfrac{\omega\Pi}{2Z_S} & -\dfrac{Z_S}{2}Y + j\dfrac{\omega\Pi}{2Z_S} \\ \dfrac{Z_S}{2}Y - j\dfrac{\omega\Pi}{2Z_S} & 1 - \dfrac{Z_S}{2}Y - j\dfrac{\omega\Pi}{2Z_S} \end{bmatrix} \tag{6.10}$$

and from Equation (3.36) we can compute the scattering matrix and then the reflection and the transmission coefficients of the filled joint:

$$R_{SH}\left(\omega, \vartheta\right) = \frac{Z_S Y - j\dfrac{\omega\Pi}{Z_S}}{2 + Z_S Y + j\dfrac{\omega\Pi}{Z_S}} \tag{6.11}$$

$$T_{SH}\left(\omega, \vartheta\right) = \frac{2}{2 + Z_S Y + j\dfrac{\omega\Pi}{Z_S}} \tag{6.12}$$

By comparing the Equations (6.11) and (6.12) with Equations (4.22) we can see that the introduction of the discontinuity of stress consists in introducing in the expressions the term function of the mass. The admittance expressions (Y) for various models are the same of those shown in Chapter 4. The curves of the transmission and reflection coefficients versus the normalized joint stiffness and normalized joint viscosity are similar to those introduced in Chapter 4 because the contribution of the ratio $\omega\Pi/Z_S$ is very small. In nature, this ratio is very small

because the rock impedance at the denominator is much larger than the numerator. In fact, the thickness of the joint is normally of the order of millimetres and then the numerator becomes very small compared with the denominator.

6.2.3 Comparison of TPLM and DDM

In order to compare TPLM and DDM, it is of interest to analyze the case of a SH-wave impinging obliquely a filled joint. A comparison of the results obtained is shown in Figure 6.2 where the magnitude of the transmission coefficient is plotted versus the ratio between the joint thickness and the wavelength in the filling material (λ_f) divided for the cosine of the angle of incidence (ϑ^{inc}).

It is noted that the joint in Figure 6.2 is given a linear elastic behaviour. To perform this comparison we state that:

$$k_{ss} = \frac{G_f}{h} \tag{6.13}$$

and if we consider a Kelvin joint the viscosity term becomes:

$$\eta = \frac{\eta_f}{h} \tag{6.14}$$

Equations (6.13) and (6.14) show the correlations between DDM and TPLM and justify the unit system of the specific shear stiffness k_{ss} and the specific viscosity η used in the DDM. In fact, the unit system of the joint specific stiffness is Pa/m that is different from the usually stiffness defined as the ratio of force to displacement with unit N/m. On the other hand, the specific joint viscosity is in $Pa{\cdot}s/m$ that is different from that defined as the ratio of stress to flow velocity gradient expressed in $Pa{\cdot}s$.

In Figure 6.2, with the two approaches representing the same problem, a very good agreement is obtained for a joint thickness ratio less than 0.1. The plot is for an impedance ratio F=1/25 that is a typical value for rock joints filled with soft materials.

For the joint thickness ratio greater than 0.1 the behaviour of the filling layer changes and the displacement discontinuity model is no longer applicable. In fact, a series of peaks are found with the magnitude of the transmission coefficient equal to 1. These peaks identify the typical resonance frequencies of the Fabry-Perot interferometer, as well known in optics (Iizuka, 2008). In this interferometer, the resonant frequencies are spaced $n\lambda_f/2$ as shown in Figure 6.2.

These results show that the displacement discontinuity model is an approximation of the thin plane layer model. In fact, the first model is applicable when the wavelength is very large compared with the joint thickness. Similar results can be obtained with the Kelvin-Voigt model.

These considerations are also valid for an oblique P/SV wave but in this case also the joint normal stiffness k_{nn} is mobilized and, for the comparison DDM-TPLM, it can be written as C_{11f}/h.

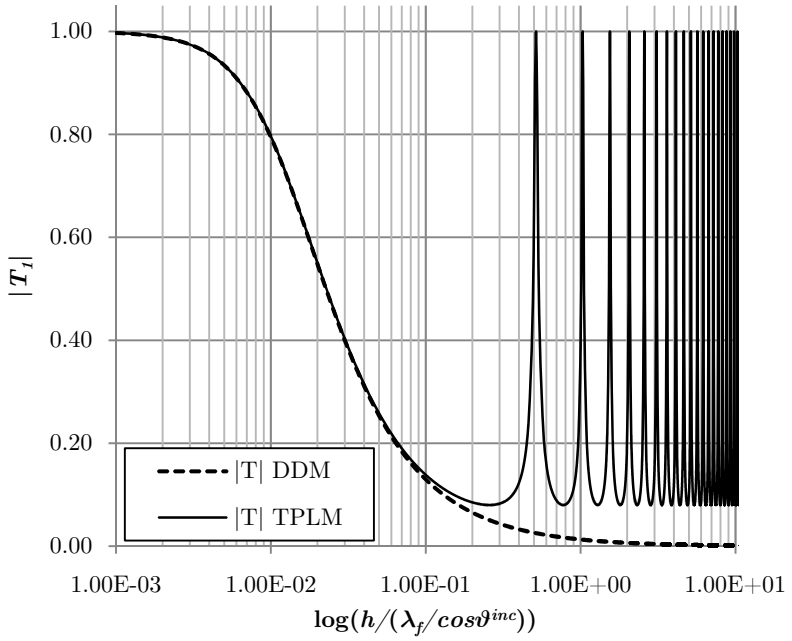

Figure 6.2 - Comparison of DDM and TPLM for different values of the transmission coefficient versus the ratio between the joint thickness and the wavelength in the filling material divided for the cosine of the angle of incidence

6.3 Numerical analyses with TPLM

It is now of interest to perform some numerical analyses to study the influence of the filled joints on wave propagation. The analyses are for a linear elastic joint. The dependence of the impedance ratio, the joint thickness and the joint spacing on the transmitted wave are investigated.

Without losing generality, a half-cycle sinusoidal wave is assumed to be the incident wave, in the form of:

$$v_I(t,0) = I\sin(\omega_0 t) \tag{6.15}$$

where:
I=1m/s,
ω_0*=10kHz.*

In cooperation with EPFL, Lausanne and NTU, Singapore, the analyses performed with SMM were also carried out with both MC and VWSM, as described in Chapter 5. In all the methods the TPLM has been implemented.

The transmitted wave forms for a one-dimensional wave propagation through a column composed by N parallel joints are plotted in Figure 6.3a-d. The incident wave is put at the first joint and the transmitted wave is recorded immediately after the last joint.

For one joint, we have assumed a non-dimensional joint thickness of δ_0=0.5 and an impedance ratio *F=1/6*. δ_0 is the ratio between the joint thickness h and the wavelength in the filling material. For 2, 5, 8 joints, δ_0=0.05, the joint spacing ratio ζ=0.2 and F=1/6. We can say that the magnitude of the transmitted wave decreases with the increasing of the number of fractures.

Figure 6.4 shows the magnitude of the transmission coefficient for a single joint versus the impedance ratio between the rock and the filling material. The graph is obtained by assuming δ_0=0.05. It can be found that with increasing $1/F$, $|T_1|$ first increases from zero to one, and then it decreases to zero when $1/F$ approaches infinity. Obviously, when $1/F$=1, the phenomenon of impedance matching takes place and all waves will be transmitted. However, in nature, $1/F$ usually varies from units to tens, and therefore, we can state that $|T_1|$ decreases with increasing $1/F$.

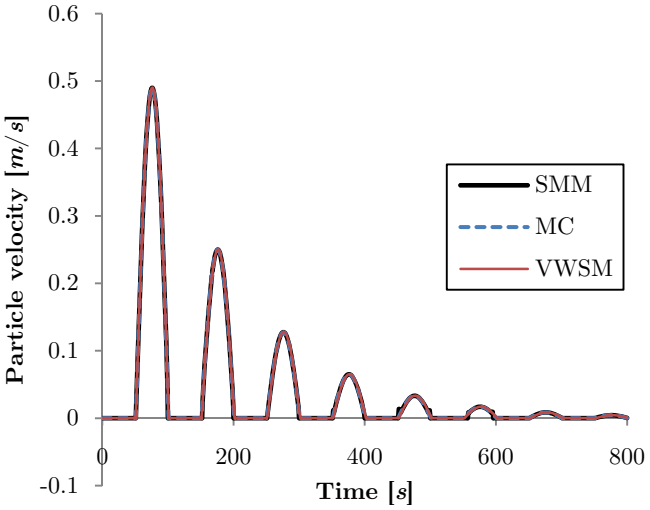

(a) 1 joint

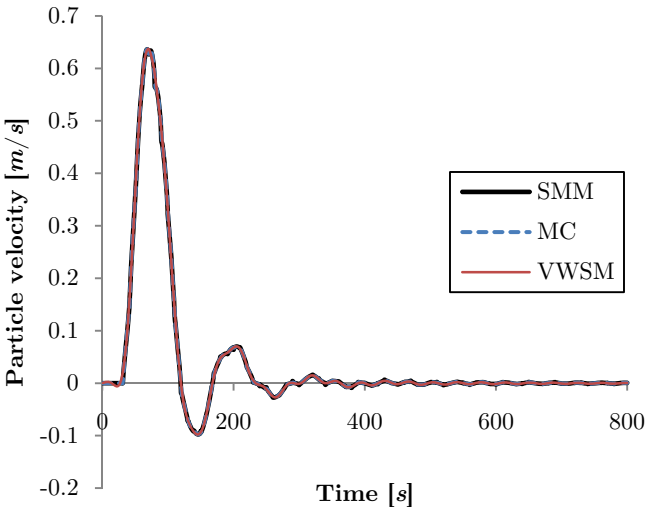

(b) 2 joints

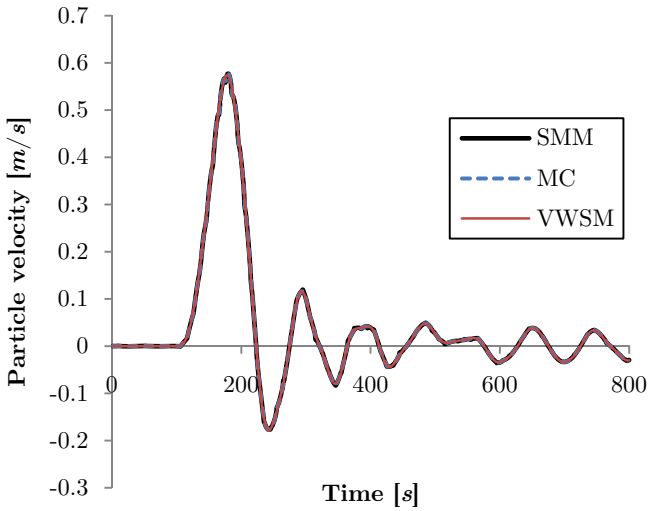

(c) 5 joints

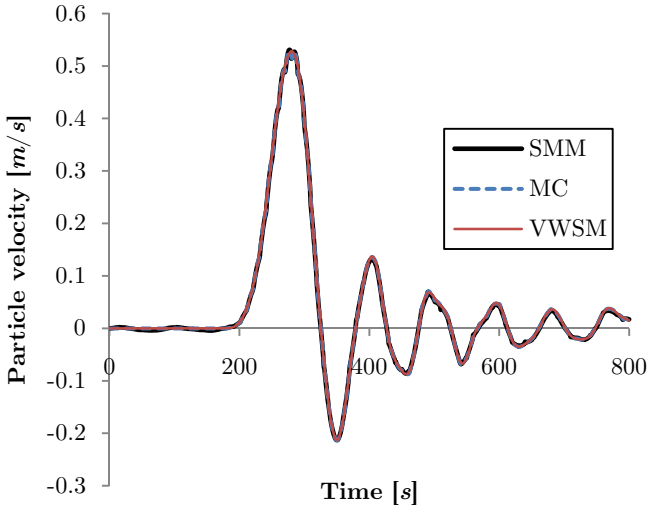

(d) 8 joints

Figure 6.3 - Transmitted waveforms across (a) 1 joint, (b) 2 joints, (c) 5 joints, (d) 8 joints with SMM, MC and VWSM

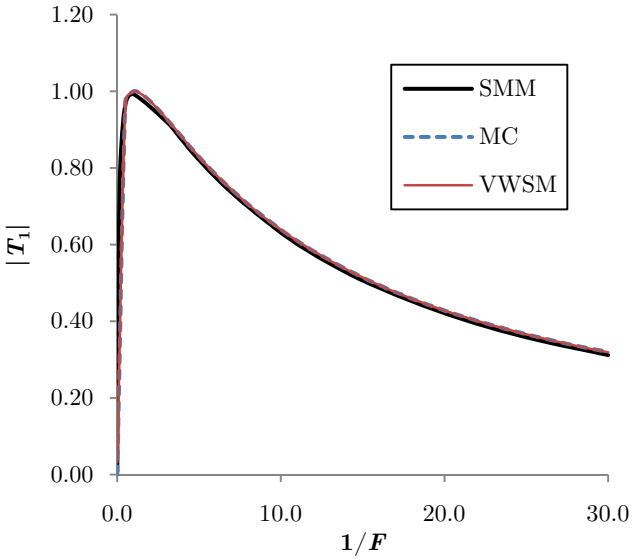

Figure 6.4 – Magnitude of the transmission coefficient for a single joint versus the impedance ratio

The influence of the joint thickness on wave propagation has been analysed as shown in Figure 6.5. It is found that $|T_1|$ decreases from unit to a constant with increasing δ_0. When δ_0 approaches zero, there will be no filled medium, and all the wave will be transmitted. When δ_0 is larger than one the threshold value δ_{0thr}, $|T_1|$ will not change with δ_0. This is because when the joint thickness is large enough, the arriving time difference between the first transmitted wave and later transmitted waves from multiple wave reflections between the two interfaces of the filled joint is so large that later arriving transmitted waves have no affect on the amplitude of the first transmitted wave. When $0< \delta_0< \delta_{0thr}$, the effects of multiple wave reflections between the two interfaces of the joint become weaker with increasing δ_0, which is consistent with the experimental results obtained by Li et al. (2009).

The plot of Figure 6.5 is obtained in time domain but is essentially the same as shown in Figure 6.2 computed in frequency domain. In frequency domain we considered a harmonic incident wave and then the response is also harmonic. In this analysis we applied an impulsive input that generates a non harmonic response.

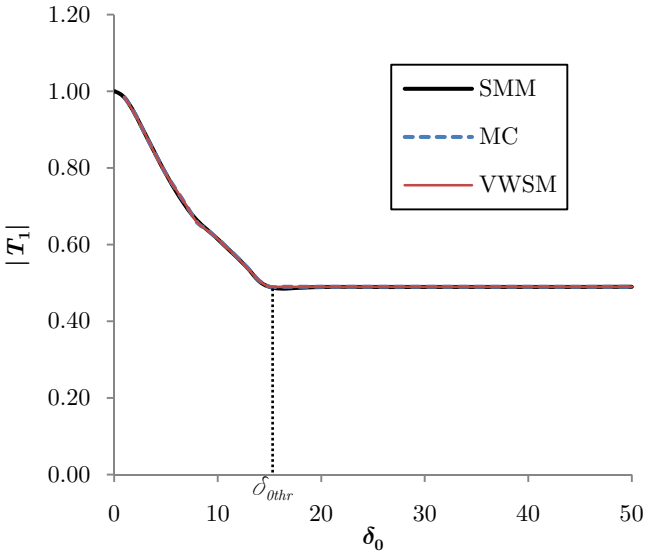

Figure 6.5 – Magnitude of the transmission coefficient for a single joint versus the non-dimensional joint thickness

Figure 6.6 shows $|T_N|$ as a function of ζ for different number of joints (N=2, 3, 5, 8) with MC, SMM and VWSM, where F=1/6, δ_0=0.05. With increasing ζ, $|T_N|$ first increases to the maximum value prior to decreasing to a constant value. When ζ is large enough, the arriving time of the first transmitted wave and later transmitted waves is so large that later transmitted waves have no effects on $|T_N|$, and therefore, $|T_N|$ does not change with ζ. When ζ is small, ζ has great effects on $|T_N|$. When ζ approaches zero, the N joints will act as one single joint with non-dimensional thickness of $N\zeta$. In most cases, $|T_N|$ decreases with increasing N, which accords with common sense. However, in certain cases, $|T_N|$ increases with increasing N, which is strange. This is caused by the time difference between the amplitude of the first transmitted wave and the later transmitted waves. When the time difference is small, the later transmitted waves have great effects on $|T_N|$. While the time difference is large, the later transmitted waves have no effect on $|T_N|$. The strange phenomenon happens when the time difference is small for large N but large for small N with the same ζ.

This behaviour is essentially the same as obtained in Chapter 5 with the displacement discontinuity method. This statement is obvious because the DDM is an approximation of the TPLM which is valid for small values of joint thickness compared to the wavelength of the filling material (see Figure 6.2). As widely described in Chapter 5 the SMM, MC and VWSM implemented with the TPLM

produce results that are essentially the same although the methods are very different.

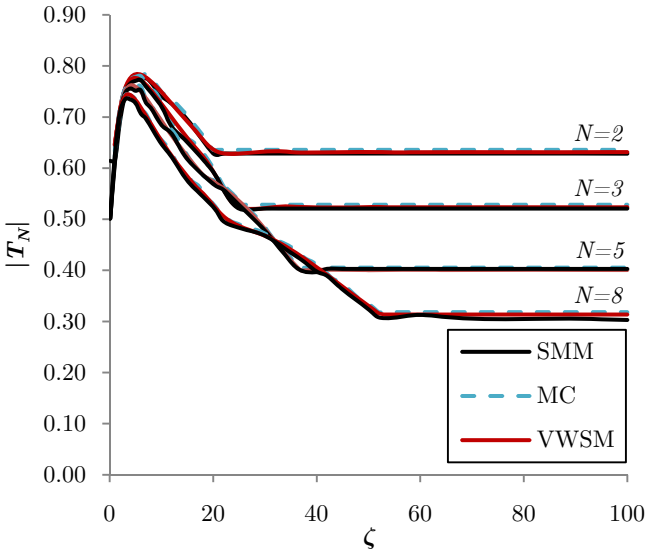

Figure 6.6 – Magnitude of the transmission coefficient for N joints versus the non-dimensional joint spacing

6.4 Comparison with the results of tests performed with the Hopkinson pressure bar

A modified split Hopkinson pressure bar (SHPB) test was recently performed to study wave propagation across a joint filled with sand (Li and Ma, 2009). It is therefore of interest to verify if the joint models as developed above are adequate to reproduce the available experimental data.

6.4.1 Description of the Modified SHPB test

The Split-Hopkinson Pressure Bar (SHPB), named after Bertram Hopkinson, sometimes also called a Kolsky bar, is an apparatus for testing the dynamic stress-strain response of materials. SHPB is commonly used for testing different materials and to obtain material properties at higher strain rates. Moreover, the governing principles of SHPB include one dimensional wave propagation equation, uniaxial

stress relations, deformations and momentum of conservation. After development of the Hopkinson's bar in early 1900's by Bertram Hopkinson, who developed the device to test steel cylindrical bars (Kolsky, 1949) with very high velocity impacts, many derivatives were followed. Among them, the SHPB development is the most popular one.

In the tests performed by Li and Ma (2009) a pendulum hammer generates a pulse loading. The intensity of the pulse loading can be changed by varying the swing-angles of the hammer. As shown in Figure 6.7, a sand layer was sandwiched between the incident and transmitted granite pressure bars. The two bars have the same diameter of 5 *cm*, and length of 97 and 100.5 *cm*. A pendulum hammer is used to generate a P-wave pulse applied to the left boundary of the incident bar. The sand layer is contained in a plastic tube to prevent outflow of the sand.

The compressive stress waves generated from the hammer in the incident bar travel in a uniaxial direction to hit the sand layer. At this instance, the generated compressive stress wave by the incident bar is partially transmitted into the transmitted bar through the sand layer. However, some of the compressive stress waves in the incident bar would reflect back into it as a tensile stress wave. Strains are recorded from both the incident and transmitted bars with the help of four strain gages mounted on the bars. The strain gauges are glued on the incident and transmitter bar. The output of this test would generally be in the form of a plot of strain versus time or in the form of stress versus strain or stress versus strain rate.

SHPB is commonly used to evaluate the mechanical properties of materials at higher strain rates up to 10^4 s^{-1}. This is for the following reasons:

1. Bars used in the experiments are longer to make sure the incident signal separates and transmits.
2. To maintain one dimensional wave propagation the ratio between the length and diameter of the bars are generally high.
3. Sensitiveness of mechanical dispersion towards signal resolution.

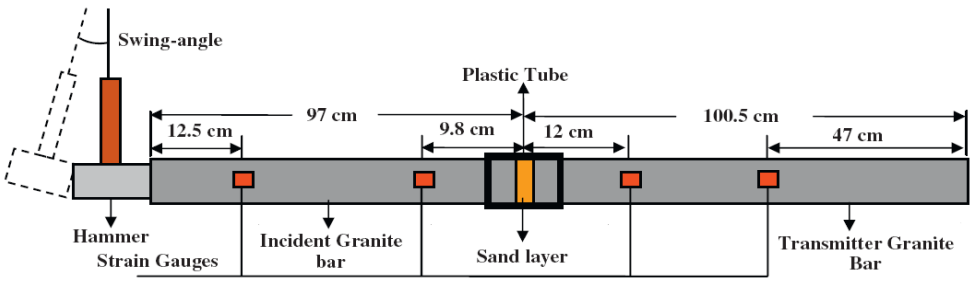

Figure 6.7 – Schematics of modified split Hopkinson pressure bar (SHPB) (Li and Ma, 2009)

The impact caused by the hammer on the incident bar excites different frequencies on the incident bar which lead to different velocities within it. The velocity variations with respect to time are recorded by the strain gauges. The oscillations on the strain gauge recordings make the data difficult to obtain peaks of strain rates.

As mentioned above the pressure bars geometry is more important in the SHPB set up. Among all the pressure bars, the incident bar is more sensitive to the geometry variations as this is the bar which transmits the stress wave to the test sample. The dimensions of the incident bar are important in terms of length and diameter so as to maintain a uniaxial stress state, homogeneous deformation in the sample or specimen while maintaining the elastic behaviour inside the pressure bar.

To make it sure that a uniaxial, homogeneous deformation within the elastic limit of the pressure bar takes place, the equation below (Kaiser, 1998 and Swantek, 2000) has to be satisfied.

$$\frac{L}{\phi} \geq 11 \tag{6.16}$$

where L is the length and ϕ is the diameter of the bar.

Equation (6.16) states that length should be greater than equal to 10 times the diameter. Moreover, the diameter of the incident bar has to be greater than twice the wavelength of the generated compressive wave, to ensure that the pulses generated from the incident bar be separated as incident and reflected waves.

The strain rates of the specimen are inversely proportional to the length of the incident bar. Thus we have:

$$\dot{\varepsilon} \propto \frac{C^*}{L} \tag{6.17}$$

where C^* is a constant of proportionality.

SHPB strain rates are approximately in the range of 10^4 s^{-1}. To achieve this, the pressure bars have to be very small with respect to length and diameter. However, pressure bars with such small size make experiments practically impossible.

Along with the geometric specifications discussed above, it is important to position and align the specimen precisely to capture the deformations in the experiments. Accurate positioning of the specimen in the centre has to be maintained in order to achieve separation and compressive of the stress waves.

6.4.2 Mechanical properties of the samples

In this part, we consider the results obtained by Li and Ma (2009) with a swing-angle of the hammer of 40°, a thickness of the filled sand of 3 *mm*, a water content of 5% and a density of 1592.2 kg/m^3. The sand layer is composed by particle with size between 0.25 and 0.5 *mm*. The density of the granite is 2650 kg/m^3 and the P-wave velocity of the granite bar is 4758 *m/s*. The interfaces between the granitic bar and the sand layer were smooth and contacted firmly.

The stress, strain rate and strain on the interfaces of the sand layer and the pressure bar are computed from the separated incident, reflected and transmitted strain waves according to the basic theory of the SHPB test. The stress-strain plot is shown in Figure 6.8. We can note that the trend of the curve is in accordance with the following exponential form (Li and Ma, 2009):

$$\sigma = a_1\left[e^{a_2\varepsilon} - 1\right] \tag{6.18}$$

where a_1 and a_2 are the curve-fitting coefficients that in this case are equal to $1.39 MPa$ and 12.53 respectively.

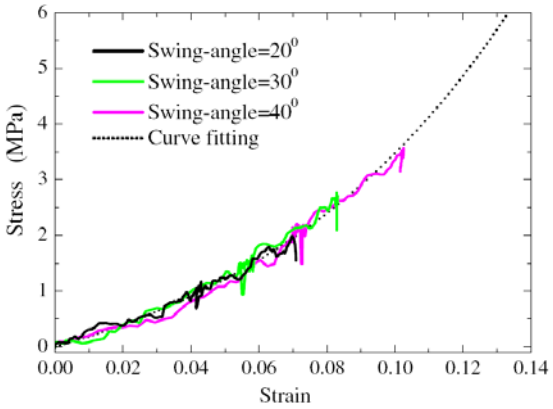

Figure 6.8 – Stress-strain curves of the single sand layer under different input energies (Li and Ma, 2009)

6.4.3 Experimental results and curve fitting

Figure 6.9 shows the incident, reflected and transmitted waves through the filled joint as obtained by Li and Ma (2009).

To examine the spectral contents of the measured pulses, a window function (also known as the tapering function) is used to extract a particular pulse from the original one. The amplitude of the windowing function is zero everywhere except along a finite time interval with unit amplitude, defined as the width of the

window. The product of the windowing function and the original pulse results in the desired isolated pulse.

It should be noted that the same windowing function is used for the measured incident and transmitted waves to ensure that the results of the spectral contents are comparable with each other. In the present study, Hann window, whose function is $0.5 \times \{1 - \cos[2\pi n \,/\, (N-1)]\}$, where n varies from 0 to N-1, is used as the window function (Harris, 1978). The amplitude spectra are then calculated by performing a fast Fourier transform (FFT) on the tapered waveforms.

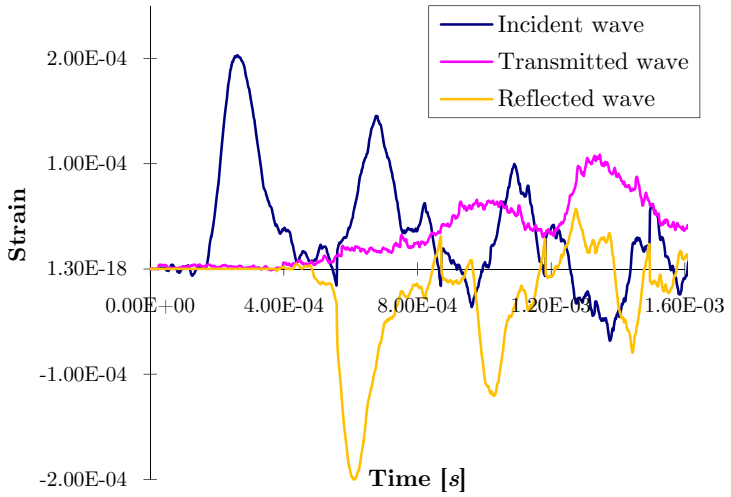

Figure 6.9 – Incident, reflected and transmitted waves through a filled joint (Li and Ma, 2009)

An algorithm that minimizes the least squares differences between these two series of values is used to achieve the best fit between the measured transmitted wave and the calculated transmitted wave derived from the analytical solutions. From these iterative computations, we have obtained, for each joint model assumed, the mechanical parameters that generate the best fit of the measured transmitted wave. The fitting computations are performed in frequency domain and the theoretical transmitted wave is obtained multiplying the FFT of the measured incident tapered wave and the transmission coefficient corresponding to the analytical model assumed.

Figure 6.10 plots the curve fitting of the measured transmitted tampered wave obtained for various analytical models and in Table 6.1 the curve fitting parameters are shown.

The first model used for fitting is the linear elastic model. Also used have been the TPLM and the transmitted wave has been obtained from the transmitted coefficient shown in Equation (6.6). In the latter model the P-wave velocity of the filling material have been changed to perform the best fit. From this velocity we can compute the normal stiffness of the joint as follows:

$$\begin{aligned} C_{11} &= K + \frac{4}{3}G = \rho \cdot V_P^2 = 1592{,}20 \cdot 269{,}70^2 = 115.81\text{MPa} \\ \mathrm{k}_{nn} &= \frac{C_{11}}{h} = \frac{115.81 \cdot 10^6}{0.003} = 38{,}60\text{GPa/m} \end{aligned} \tag{6.19}$$

The results obtained by using Equation (6.19) highlight that the joint normal stiffness computed from the P-wave velocity obtained from the curve fit with the TPLM is essentially the same as that deduced directly with the spring model (see Table 6.1). This proves that either the TPLM or DDM can be used when the joint thickness ratio is small ($<0.1\lambda_f$).

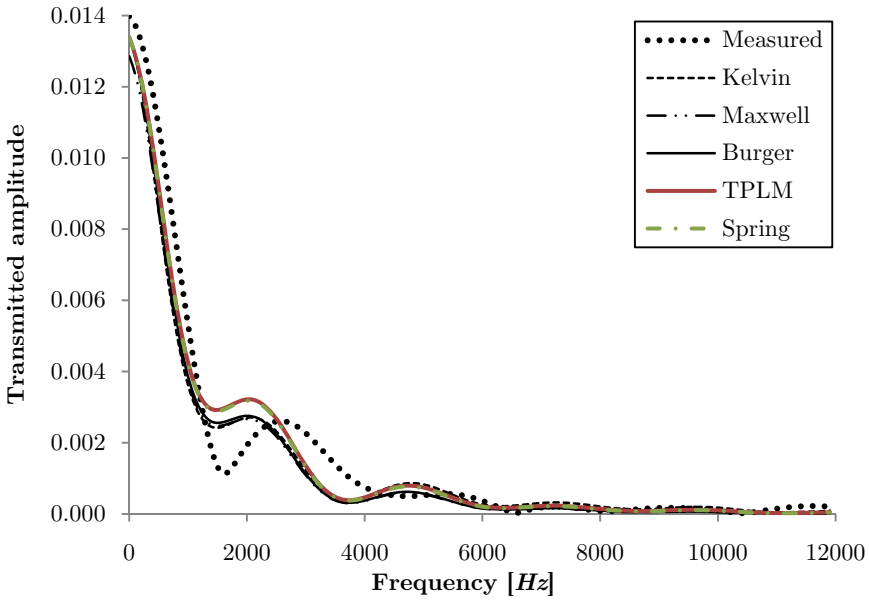

Figure 6.10 – Spectra of the measured and predicted transmitted waves

Figure 6.10 shows the results obtained by using the Kelvin-Voigt, Maxwell and Burger models. It is noted that the differences between the three models are small. Table 6.1 shows that the model that simulates better the filled joint behaviour is

the Burger model. We have found that a better curve fit is obtained with the Burger model if one adopts the same values of the parameters used in the Kelvin-Voight and Maxwell models.

However, a good accuracy in fitting is also obtained with the Kelvin-Voight and Maxwell models. The linear elastic models are also shown to give a good fitting when the viscosity part is small.

Table 6.1 - Model parameters obtained from best fitting

Model	Parameters from curve fit	Goodness of fit		
		SSE	R-square	RMSE
Linear elastic (DDM)	k_{nn}= 38,201 GPa/m	8.42E-05	0.952499	6.57E-04
TPLM	V_P= 269,700 m/s	8.41E-05	0.952518	6.57E-04
Kelvin-Voigt (DDM)	k_{nn}= 33,748 GPa/m η_{nn}= 1,2919 $MPa{\cdot}s/m$	8.06E-05	0.960346	6.38E-04
Maxwell (DDM)	k_{nn}= 31,566 GPa/m η_{nn}= 150 $MPa{\cdot}s/m$	8.13E-05	0.956094	6.64E-04
Burger (DDM)	k_{nn_kelv}= 32,616 GPa/m η_{nn_kelv}= 5,536 $GPa{\cdot}s/m$ k_{nn_max}= 32,616 GPa/m η_{nn_max}= 5,536 $GPa{\cdot}s/m$	1.41E-05	0.992063	2.71E-04

In addition, the filled joint modelled in the present study also functions as a high-frequency filter. The high frequency components across the joint attenuate much more than the low frequency components.

6.4.4 Numerical analyses

The effects on wave propagation of a set of filled joints with the same properties as used above are now studied by using the SMM in which the DDM has been modified to account for the discontinuity of stresses (see Paragraph 6.2.2).

Without losing generality, a normally incident half-cycle sinusoidal P-wave is applied at the boundary of a filled joint set with viscoelastic behaviour

$$v_I(t,0) = I\sin(\omega_0 t) \tag{6.20}$$

where:
$I=1$,
$\omega_0= 2\pi$ kHz.

The analyses are performed for Kelvin and Maxwell joint models.

The specific joint stiffness and viscosity of the Kelvin and the Maxwell joints are the same as those determined through the best fit in the previous section. With these parameters the normalized joint stiffness $K_{nn}=k_{nn}/\omega Z_P$ and the normalized joint viscosity $H_n=\eta_n/Z_P$ are:

- $K_{nn}=0.4$ and $H_n=0.1$ for the Kelvin model;
- $K_{nn}=0.4$ and $H_n=11.9$ for the Maxwell model.

The influence of the joint viscosity and the joint stiffness on the magnitude of the transmission coefficient for two joints $|T_2|$ represented with Kelvin and Maxwell models is shown in Figure 6.11. We have assumed a joint spacing ratio $\zeta=1/10$. We can see that increasing the normalized stiffness of the joint $|T_2|$ increases. This means that $|T_2|$ increases with increasing the normal joint stiffness and with the decreasing of the frequency. In fact, this proves that the high frequency components across the joint attenuate much more than the low frequency components.

Figure 6.11 also shows that the transmission coefficient $|T_2|$, for the joint simulated with the Kelvin model first decreases to the minimum and then it increases with the increasing of H_n. $|T_2|$ is the same as that derived for dry joint when $H_n=0$. On the other hand $|T_2|$ approaches 1 if H_n is sufficiently large. The situation is different if we represent the joint with the Maxwell model: the transmission coefficient always increases with increasing the normalized joint viscosity and for high H_n the behaviour become the same as that of dry joints.

Figure 6.12 and Figure 6.13 show the magnitude of transmission coefficients ($|T_N|$) across N (N = 2, 3, 5, 8) Kelvin joints and N Maxwell joints, respectively, as a function of the non-dimensional joint spacing (ζ). The non-dimensional joint spacing is defined as the ratio of the joint spacing d to the incident wavelength for the intact rock λ.

It is found that although the general changing trend of $|T_N|$ versus ζ is the same for the Kelvin and the Maxwell joints, the amplitudes are somewhat different. It indicates that even though both the Kelvin and the Maxwell models can be used to study P-wave propagation across a single viscoelastic joint filled with sand, the

seismic response of multiple parallel Kelvin and Maxwell joints is somewhat different.

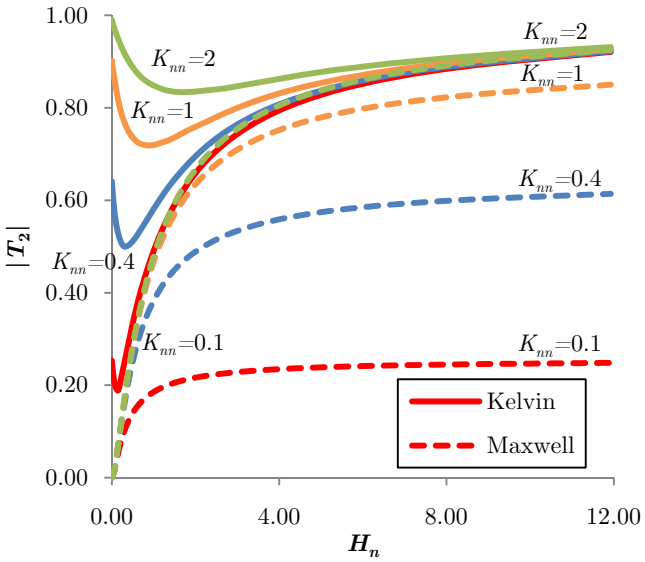

Figure 6.11 – Magnitude of transmission coefficients across 2 joints for Kelvin and Maxwell joint models versus the normalized joint viscosity H_n with $\zeta = 1/10$

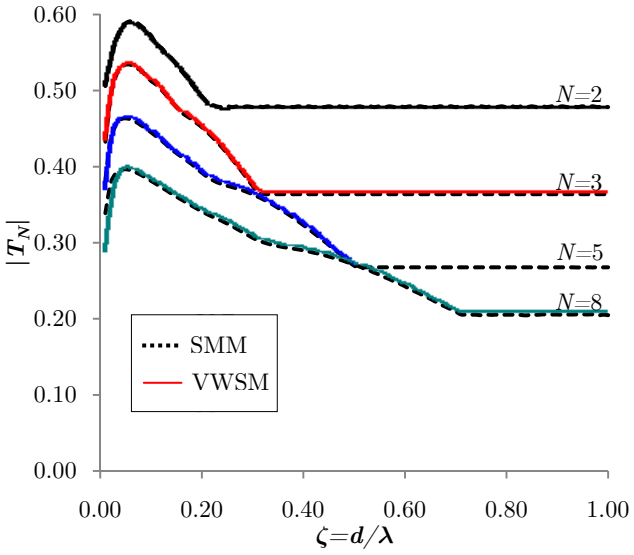

Figure 6.12 – Magnitude of transmission coefficients across N (N = 2, 3, 5, 8) Kelvin joints versus the non-dimensional joint spacing (ζ) with $K_{nn} = 0.4$

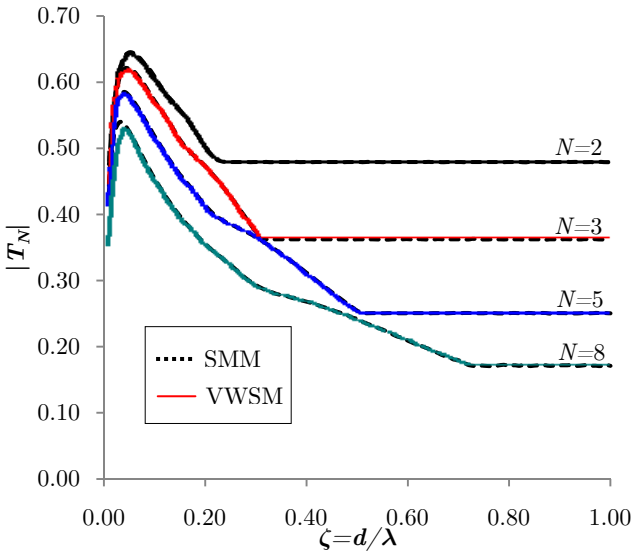

Figure 6.13 – Magnitude of transmission coefficients across N (N = 2, 3, 5, 8) Maxwell joints versus the non-dimensional joint spacing (ζ) with $K_{nn} = 0.4$

Further experiments on wave propagation across multiple parallel joints filled with saturated sand are needed to determine which model is better. For both the Kelvin and the Maxwell joints, with increasing ζ, $|T_N|$ first increases to the maximum value before it decreases to a constant. When ζ is sufficiently large, it has no effect on $|T_N|$, which indicates that the multiple wave reflections among joints have no effect on $|T_N|$. This is because the arriving time difference between the first transmitted wave and later transmitted waves is large enough to eliminate the influence of later arriving transmitted waves on $|T_N|$. While ζ is small, the multiple wave reflections among the joints have great effects, and $|T_N|$ is dependent on ζ. It is also noted that $|T_N|$ decreases with increasing number of joints.

Figures 6.12 and 6.13 give the results obtained for linear elastic joints. It is shown that the SMM and VWSM compare very satisfactorily.

6.5 Summary

The effects of filled joints on wave propagation are of considerable significance and engineering interest.

It is found that the TPLM is the best approach to model a filled joint and the DDM is an approximation. The two models can however be used indifferently when the joint thickness is about 0.1 of the wavelength of the filling material. In this case the loss in accuracy with the DDM is very small compared with the TPLM.

As the density of the filled medium, e.g. a saturated clay or sand, is not negligible compared with the rock density, the DDM, with the stress discontinuity introduced, is found to be suitable to describe the seismic response of the filled joint. The stress discontinuity across the filled joint is caused by the normal and tangential mass, which further determine the acoustic impedance ratio of the filled joint. The displacement discontinuity across the filled joint results from the specific joint stiffness and viscosity, which further determine the normalized joint stiffness and viscosity. It should be noted that the physical implication and unit of the specific joint stiffness and specific joint viscosity are different from those of normally used stiffness and viscosity.

The reflection and transmission coefficients across a single filled joint with viscoelastic behaviour are determined by the choice of the parameters being introduced, including the incident angle, the normalized joint stiffness, the non-dimensional joint viscosity and the acoustic impedance ratio of the filled joint. The acoustic impedance ratio of the filled joint and the normalized joint stiffness are frequency dependent, while the normalized joint viscosity is not. In addition, the wave energy is dissipated due to the viscosity and the initial mass of the filled joint.

The most significant difference between the seismic responses of the Kelvin and the Maxwell joint relates to the role played by both the normalized joint stiffness and the normalized joint viscosity in the wave reflection and transmission. When a wave propagates across a filled joint set, due to the presence of multiple wave reflections, the normalized joint spacing ratio is a dominating parameter.

The satisfactory comparison between the results obtained with the modified SHPB tests and with the SMM shows that this method can well be used to represent the effects of filled joints on P-wave propagation. It is found that the best model to represent the behaviour of sand filled joints is the Burger model. Acceptable results can be obtained with the linear elastic DDM or TPLM models if the viscosity of the infilling is small.

Chapter 7

Frictional joints

7.1 Introduction

If the shear stress along a joint reaches the shear strength, a non linear behaviour is generated. This is the case when we are near to a seismic source or in the presence of waves originated by explosions.

In this chapter, the Coulomb slip behaviour is implemented in the SMM by using an equivalent linearization procedure. Obviously, an approximation of the non linear behaviour is obtained, which allows one to better understand the effects of frictional joints on wave propagation.

As already mentioned in Chapter 2, Miller (1977-1978) used an equivalent linearization approach to analyse the wave propagation of an elastic plane wave through a frictional boundary. He assumed a Coulomb slip model of a fracture with infinite elastic shear stiffness.

In this chapter, we extend the equivalent linearization to a general Coulomb slip model with finite elastic joint stiffness. The results obtained with the SMM will be compared with those derived numerically with the MC.

7.2 Basic formulation of the equivalent linearization approach

In general, linear systems are much easier than nonlinear ones to handle, but they also allow for a better understanding of the dynamic characteristics. For this reason, the equivalent linearization techniques (Caughey, 1960 and Iwan, 1973) have been utilized for determining the steady-state response of nonlinear hysteretic systems.

Vestroni & Noori (2002) showed that a system is endowed with hysteresis if there is a lag in the arrival of the output with respect to the input, or if the output depends, in a rate-independent way, on the history of the input. The dependence on the history of the input manifests itself in the "non-local memory" character of hysteresis. The hysteretic friction is not a unique function of the displacement but depends on the previous history of the movement.

The hysteretic frictional behaviour of a mass moving on ground as shown in Figure 7.1 can be represented with the single-degree-of-freedom system (SDOF) shown in Figure 7.2. The non linear frictional stress can be linearized as follows:

$$\tau_F\left(x,\dot{x}\right) \rightarrow k_{eq}x + c_{eq}\dot{x} \tag{7.1}$$

where:
x are displacements relative to the base;
k_{eq} and c_{eq} are the equivalent stiffness and damping parameters that will be defined later.

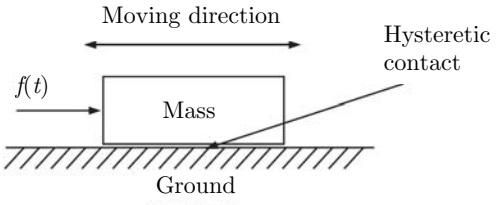

Figure 7.1 – The hysteretic behaviour in the friction force for a mass moving on a ground

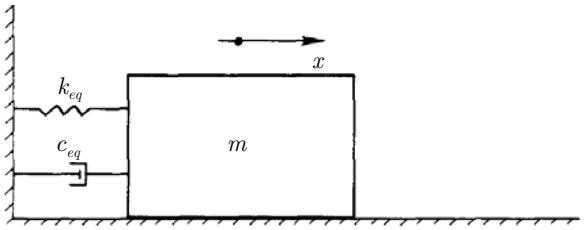

Figure 7.2 – Single-degree-of-freedom model of a mass moving on a ground

Hence, the behaviour of the SDOF system (Figure 7.2) is represented by

$$m\ddot{x} + \tau_F\left(x,\dot{x}\right) = -m\ddot{x}_g \tag{7.2}$$

where $\ddot{x}_g$ is the ground surface acceleration due for example to an earthquake.

The nonlinear Equation (7.2) is equivalently linearized with the two parameters, k_{eq} and c_{eq}, introduced with the Equation (7.1):

$$m\ddot{x} + c_{eq}\dot{x} + k_{eq}x + \varepsilon = -m\ddot{x}_g \tag{7.3}$$

where ε represents the resulting residue from the linearization.

Hence, the equivalent linear system is modelled by the Kelvin-Voigt model in which the equivalent stiffness and damping are connected in parallel.

One of the techniques for properly determining the two key parameters in the above linearized equation is to minimize the mean square of the resulting residue. With the mean square of the residue denoted as $E[\varepsilon^2]$, the conditions for determining the linearized parameters are:

$$\begin{aligned} \frac{\partial E\left[\varepsilon^2\right]}{\partial k_{eq}} &= 0 \\ \frac{\partial E\left[\varepsilon^2\right]}{\partial c_{eq}} &= 0 \end{aligned} \tag{7.4}$$

From the above conditions we obtain:

$$c_{eq}E\left[x\dot{x}\right] + k_{eq}E\left[x^2\right] - E\left[\tau_F\left(x,\dot{x}\right)x\right] = 0 \tag{7.5}$$

$$c_{eq}E\left[\dot{x}^2\right] + k_{eq}E\left[x\dot{x}\right] - E\left[\tau_F\left(x,\dot{x}\right)\dot{x}\right] = 0 \tag{7.6}$$

The operator $E[\cdot]$ must satisfy certain conditions which assure the uniqueness of the approximate solution.

When the system is excited by a stationary process, the linear response also becomes stationary, i.e. $E[x\dot{x}] \equiv 0$. In this case, the linearized stiffness and damping are given by:

$$k_{eq} = \frac{E\left[\tau_F\left(x,\dot{x}\right)x\right]}{E\left[x^2\right]} \tag{7.7}$$

$$c_{eq} = \frac{E\left[\tau_F\left(x,\dot{x}\right)\dot{x}\right]}{E\left[\dot{x}^2\right]} \tag{7.8}$$

The procedure based on the least square method, which has been briefly presented above, is called "Dynamic Stiffness Method" (DSM) (Jennings, 1968).

Now we consider a SDOF system (Figure 7.2) exhibiting a type of bilinear hysteresis as depicted in Figure 7.3. This hysteresis is the most typical one for base isolation systems for buildings consisting of rubber bearings and dampers. This is the most general bilinear model that can be simplified in the Coulomb slip model by assuming $k_2 = 0$.

Consider the case in which this nonlinear system is excited by a steady-state sinusoidal acceleration, i.e. $\ddot{x}_g = B\cos\omega t$. By assuming that such an excitation results in a steady-state response, the equation becomes:

$$m\ddot{x} + \tau_F\left(x,\dot{x}\right) = -mB\cos\omega t \tag{7.9}$$

with:

$$x = X\cos\left(\omega t - \varphi\right) \tag{7.10}$$

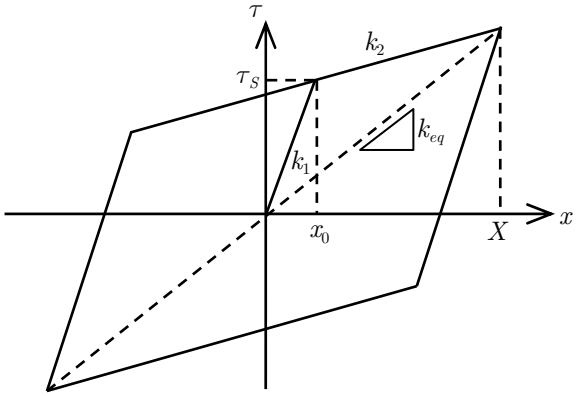

Figure 7.3 – Bilinear hysteresis

The equivalent linear parameters are found by the harmonic analysis of Caughey (1960) applying the averaging principle of Krylov and Bogolyubov (1947). This approach is also defined as the "method of the describing function" (Al-Bender et al., 2004).

The required parameters for the linearized model are obtained based on the same procedure presented in the previous subsection, by utilizing the average principle for estimating $E[x]$ and $E[\dot{x}]$. If Equation (7.10) is assumed, $E[x\dot{x}]$ becomes zero. $E[\cdot]$ is a logic averaging operator that is simply the average over one period of the solution (Iwan, 1973). Then we have:

$$k_{eq} = \frac{\int_0^{2\pi} x\cdot\tau_F\left(x,\dot{x}\right)d\theta}{\int_0^{2\pi} x^2 d\theta} = \frac{1}{\pi X}\int_0^{2\pi}\tau_F\left(X\cos\theta,-\omega X\sin\theta\right)\cos\theta d\theta \tag{7.11}$$

$$c_{eq} = \frac{\int_0^{2\pi} \dot{x} \cdot \tau_F\left(x, \dot{x}\right) d\theta}{\int_0^{2\pi} \dot{x}^2 d\theta} = -\frac{1}{\pi\omega X}\int_0^{2\pi} \tau_F\left(X\cos\theta, -\omega X \sin\theta\right)\sin\theta d\theta \tag{7.12}$$

where $\theta = \omega t$ - φ.

The solution of the Equations (7.11) and (7.12) is conveniently expressed in terms of the parameter Θ^*, related to the amplitude via:

$$\cos\Theta^* = 1 - 2\frac{x_0}{X} \tag{7.13}$$

Evaluation of the integrals gives the following expressions for the stiffness and damping parameters:

$$k_{eq} = \begin{cases} k_1 = k_{ss} & \rightarrow X \le x_0 \\ \dfrac{1}{\pi}\left[\left(k_1 - k_2\right)\Theta^* + k_2\pi - \dfrac{k_1 - k_2}{2}\sin 2\Theta^*\right] & \rightarrow X > x_0 \end{cases} \tag{7.14}$$

$$c_{eq} = \begin{cases} 0 & X \le x_0 \\ \dfrac{4\left(k_1 - k_2\right)}{\pi\omega} \cdot \dfrac{x_0}{X}\left(1 - \dfrac{x_0}{X}\right) & \rightarrow X > x_0 \end{cases} \tag{7.15}$$

The linearized parameters given above clearly depend upon the maximum response value, X. The solutions of Equations (7.14) and (7.15) can be obtained iteratively.

The bilinear model is composed by a first part (linear elastic) in which the slope of the line in Figure 7.3 is the joint shear stiffness k_{ss} while in the second part the behaviour is plastic and the slope of the line is k_2. Equations (7.14) and (7.15) show that when the shear stress along the joint is smaller than τ_S the behaviour is elastic while when τ is greater than τ_S the behaviour is plastic. In the plastic part, the relative sliding between two surfaces of the joint occurs.

A representative definition of the equivalent stiffness of the bilinear model shown in Figure 7.3 is the secant stiffness at the extremal displacements. Similarly, equivalent damping can be defined using the energy dissipated per cycle which is determined by the extremal displacement. Hence, the equivalent damping is given by: $c_{eq}\omega$ = *loop area*/πX^2 , i.e. the damping force is equal to $c_{eq}\omega X$ = *loop area*/πX.

This amount of energy dissipation per cycle does not depend on the velocity, as in the case of viscous damping, but depends on the amplitude of the motion. The loop area per cycle is indeed independent of the velocity at which the cycle is traversed (Al-Bender et al., 2004).

Now, we assume that the hysteretic contact between the mass and the ground of Figure 7.1 is represented by the Coulomb slip model (Figure 7.4).

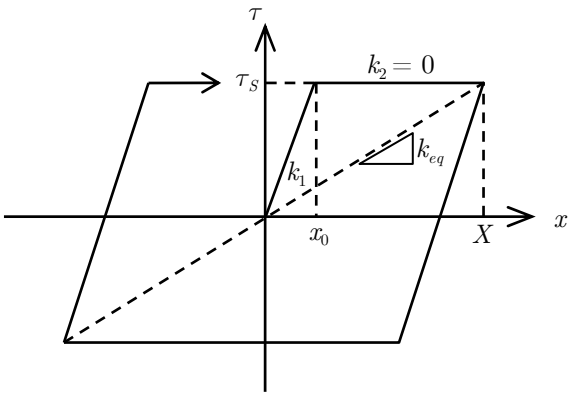

Figure 7.4 – Stress-displacement diagram for Coulomb frictional boundary

In Figure 7.4, τ_S and x_0 are the fracture shear strength and the corresponding shear displacement. k_1 is equal to the joint shear stiffness k_{ss}. The Coulomb slip model is a bilinear model composed by two parts: a linear deformation portion and a slip portion with k_2=0. When τ reaches τ_S the joint surfaces undergo relative sliding.

The Coulomb slip model assumes k_2=0 and the Equations (7.14) and (7.15) can be simplified as follows:

$$k_{eq} = \begin{cases} k_1 = k_{ss} & \rightarrow X \le x_0 \\ \dfrac{1}{\pi} k_{ss} \left[\Theta^* - \dfrac{1}{2} \sin 2\Theta^* \right] & \rightarrow X > x_0 \end{cases} \tag{7.16}$$

$$c_{eq} = \begin{cases} 0 & X \le x_0 \\ \dfrac{4k_{ss}}{\pi\omega} \cdot \dfrac{x_0}{X} \left(1 - \dfrac{x_0}{X} \right) & \rightarrow X > x_0 \end{cases} \tag{7.17}$$

Miller (1977) has used a simplified Coulomb slip model in which k_{ss} is infinite. With this assumption, we can obtain the equivalent parameters of Miller from the Equations (7.16) and (7.17):

$$k_{eq} = 0 \tag{7.18}$$

$$c_{eq} = \frac{4k_{ss}}{\pi\omega} \cdot \frac{x_0}{X}\left(1 - \frac{x_0}{X}\right) = \frac{4\tau_S}{\pi\omega X}\left(1 - \frac{\tau_S}{k_{ss}X}\right) = \frac{4\tau_S}{\pi\omega X} \tag{7.19}$$

where $\tau_S = k_{ss} \cdot x_0$.

Thus, we have obtained the most general and appropriate Coulomb slip model to study rock joints. In this chapter, we will use this model with $k_1 = k_{ss}$.

7.3 Implementation in SMM

Firstly, we assume that the media at both sides of the joint have the same mechanical elastic properties (Figure 7.5). A harmonic normal incident shear displacement wave $u = Ue^{j\omega t}$ is introduced ($\vartheta^{inc} = 0$).

As described in Chapter 4, the stress field in one of the two media is composed by the sum of the incident component and the reflected one:

$$T_{zx} = T_{zx}^{inc}\left(1 + R_{SH}\right) \tag{7.20}$$

and the reflection coefficient for the joint A (Figure 7.5) is:

$$R_{SH} = -\frac{Z_S Y}{2 + Z_S Y} = -\frac{Y}{Y + 2Y_S^m} \tag{7.21}$$

where:
T_{zx} is the amplitude of the shear stress τ_{zx};
Y_S^m is the shear medium admittance;
Y is the shear joint admittance.
As described in the previous paragraph Y becomes:

$$Y = \frac{j\omega}{k_{eq} + j\omega c_{eq}} \tag{7.22}$$

that is the typical admittance of a Kelvin-Voigt joint model (see Equation 4.10) but with the equivalent stiffness and damping obtained with the linear equivalent model.

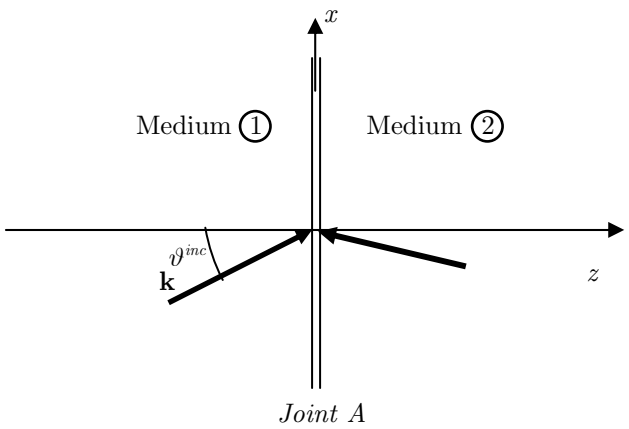

Figure 7.5 – Plane wave that impinges a joint with frictional behaviour

As well known, we can write the stress as function of the incident velocity:

$$T_{zx} = T_{zx}^{inc}\left(1 - \frac{Y}{Y + 2Y_S^m}\right) = Z_S V_x^{inc}\left(1 - \frac{Y}{Y + 2Y_S^m}\right) = V_x^{inc}\frac{2}{Y + 2Y_S^m} \tag{7.23}$$

At this point we can write that:

$$U = \frac{V_x^{inc}}{j\omega} \tag{7.24}$$

where:
V_x^{inc} is the amplitude of the incident particle velocity v_x;
U is the amplitude of the incident harmonic displacement wave u.

We can assume that the linearized system has a steady-state solution of the form

$$x = Xe^{j(\omega t - \varphi)} \tag{7.25}$$

where x is the relative displacement between two faces of the joint.

The velocity field along the interface becomes:

$$V_x = j\omega X = Y \cdot T_{zx} = V_x^{inc} \frac{2Y}{Y + 2Y_S^m} = j\omega U \frac{2Y}{Y + 2Y_S^m} \tag{7.26}$$

and by substituting into the Equation (7.26) the Equations (7.22) and (7.25) we obtain:

$$Xe^{-j\varphi} = U \frac{2Y}{Y + 2Y_S^m} = U \frac{j\omega Z_S}{k_{eq} + j\omega \left(\frac{Z_S}{2} + c_{eq} \right)} \tag{7.27}$$

The square modulus of Equation (7.27) provides:

$$X^2 = \frac{\omega^2 {Z_S}^2 U^2}{{k_{eq}}^2 + \left(\frac{\omega Z_S}{2} + \omega c_{eq} \right)} \rightarrow X^2 {k_{eq}}^2 + \left(X \frac{\omega Z_S}{2} + X\omega c_{eq} \right) = \omega^2 {Z_S}^2 U^2 \tag{7.28}$$

The equivalent stiffness and damping are also function of X and for this reason X can be obtained by inserting the Equations (7.16) and (7.17) into Equation (7.28). In this way we obtain an equation with only one unknown that can be solved iteratively. Obviously, this iterative computation of the amplitude X of the displacements along the joint makes sense only if τ reaches τ_S.

The phase angle φ is equal to the phase of the denominator of the Equation (7.27):

$$\varphi = \tan^{-1} \left(\frac{\frac{\omega Z_S}{2} + \omega c_{eq}}{k_{eq}} \right) \tag{7.29}$$

The implementation of the Coulomb slip model in SMM can be performed in the following steps:

1. Computation of the relative displacement amplitude X (Equation (7.28)).
2. Computation of the equivalent stiffness and damping (Equations (7.16) and (7.17)).

3. Calculation of the joint admittance (Equation (7.22)).
4. Definition of the transmission matrix **A** and then computation of the scattering matrix **S**.

This approach can be generalized for all wave polarizations and for any angle of incidence. The boundary conditions are as follows:

$$\begin{gathered} k_{eq}\left(X\right)\left(u_{x-}-u_{x+}\right)+c_{eq}\left(X\right)\left(v_{x-}-v_{x+}\right)=\tau_{zx} \\ k_{nn}\left(u_{z-}-u_{z+}\right)=\tau_{zz} \\ \tau_{zx-}-\tau_{zx+}=0 \\ \tau_{zz-}-\tau_{zz+}=0 \end{gathered} \tag{7.30}$$

If we have an oblique P or SV-wave impinging on a frictional joint, the normal behaviour is linear elastic while the shear behaviour is represented by Coulomb slip model. In this case the joint admittance Y becomes a 2x2 matrix:

$$\mathbf{Y}=\begin{pmatrix} \dfrac{j\omega}{k_{eq}+j\omega c_{eq}} & 0 \\ 0 & \dfrac{j\omega}{k_{nn}} \end{pmatrix} \tag{7.31}$$

At this point we have all the tools needed to compute the incident, reflected and transmitted waves. In presence of a frictional joint, part of the energy of the incident wave is absorbed by the friction along the joint. If E_I, E_R and E_T represent the energy flux per unit area per cycle of oscillation associated with the incident, transmitted and reflected waves, respectively, we may compute the amount of energy absorbed (E_A) from the frictional interface as follows:

$$E_I+E_R+E_T+E_A=1 \tag{7.32}$$

We can compute the transmission (T_1), reflection (R_1) and absorption (A_1) coefficients from the corresponding energies:

$$R_1=\sqrt{\frac{E_R}{E_I}} \tag{7.33}$$

$$T_1 = \sqrt{\frac{Z_{S1}}{Z_{S2}}} \cdot \sqrt{\frac{E_T}{E_I}}$$

$$A_1 = \sqrt{\frac{E_A}{E_I}} = \sqrt{1 - R_1^2 - \left(\frac{Z_{S1}}{Z_{S2}}\right) T_1^2}$$

7.4 Numerical analyses with SMM

Numerical analyses with the SMM can now be performed in the frequency domain to understand the effects of a frictional joint on wave propagation. In accordance with Miller (1977), Figure 7.6 gives the plot of the transmission, reflection and absorption coefficients versus the shear stress ratio $\omega Z_s U/\tau_S$. The numerator of the shear stress ratio represents the maximum shear stress of the incident wave (τ_{imax}) and then this ratio can be written more simply as τ_{imax}/τ_S. This ratio is the rate between the maximum stress of the incident wave and the shear strength.

We have applied a harmonic shear displacement wave with frequency ω and amplitude U. Figure 7.6 is obtained for a joint with Coulomb slip behaviour and with $k_{ss} = \infty$. When the shear stress ratio is smaller than 1, $|T_1|$ is equal to 1 and $|R_1|$ equal to zero. In this zone no slip occurs and the behaviour is linear elastic (welded interface). Miller (1977) has shown that the equivalent linearization provides results which are very close to the exact solution.

As an extension of previous studies we have assumed a joint with Coulomb slip behaviour and with shear stiffness. Figures 7.7 to 7.9 show the transmission, reflection and absorption coefficients versus the shear stress ratio for different values of normalized shear joint stiffness (K_{ss}=$k_{ss}/\omega Z_s$).

The relative slip along the surfaces of the joint starts when $|A_1|$ becomes different from zero and then when $c_{eq} \neq 0$. At this point the maximum incident stress $\tau_{i,max}$ reaches the joint strength τ_S and then X becomes equal to x_0. Hence, transmission and reflection coefficients may be computed by using Equations (4.23) for linear elastic joints. We can note as in the linear elastic zone the coefficients are constant until the stress along the joint reaches the shear strength. When the τ_S is mobilized along the joint the maximum amplitude τ_{trasm} of the transmitted wave becomes equal to τ_S. Hence, we can write:

$$\tau_{trasm} = \left|T_1^{el}\right| \tau_{i\max} \rightarrow \text{if } \tau_{trasm} = \tau_S \rightarrow \frac{\tau_{i\max}}{\tau_S} = \frac{1}{\left|T_1^{el}\right|} \tag{7.34}$$

where $|T_1^{el}|$ is the transmission coefficient when the joint is linear elastic.

Equation (7.34) identifies the transition point from the linear elastic behaviour to the slip behaviour. This point changes position with the change of the normalized joint shear stiffness as shown in Figures 7.7 to 7.9 and computed in Table 7.1. The stress ratio, for which the frictional behaviour occurs, increases with decreasing the normalized joint shear stiffness and then with decreasing the joint shear stiffness and with increasing the incident frequency.

Table 7.1 – Location of the transition points

Normalized joint shear stiffness	Transmission coefficient $\lvert T_1^{el} \rvert$	Stress ratio τ_{imax}/τ_S
0.1	0.196	5.102
0.25	0.447	2.237
0.63	0.783	1.277
1.6	0.954	1.048
∞	1	1

When slip along the joints occurs, the transmission coefficient decreases with increasing the shear stress ratio and the curves, computed for different K_{ss}, converge to the same curve (Figure 7.7). A similar behaviour is exhibited by the reflection coefficient (Figure 7.8) which increases with increasing the stress ratio. Figure 7.9 shows that the absorption coefficient decreases with decreasing the normalized joint shear stiffness.

From Equation (7.19) we may find that c_{eq} is maximum when the ratio $\tau_S/k_{ss}X$ is equal to zero and this condition is achieved when $k_{ss} \to \infty$. Now, we can state that, for high values of τ_{imax}/τ_S, the transmission, reflection and adsorption coefficients become independent from the shear joint stiffness.

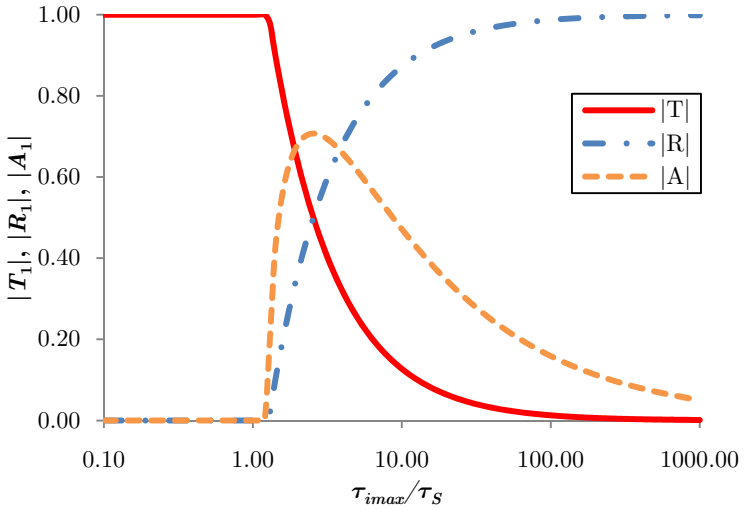

Figure 7.6 – Transmission, reflection and absorption coefficients versus the shear stress ratio for a Coulomb slip interface with $k_{ss} = \infty$

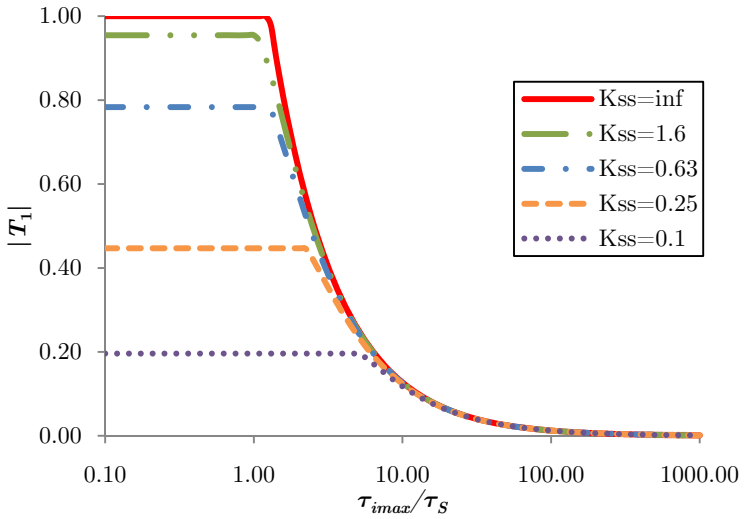

Figure 7.7 – Transmission coefficient versus the shear stress ratio for different values of K_{ss}

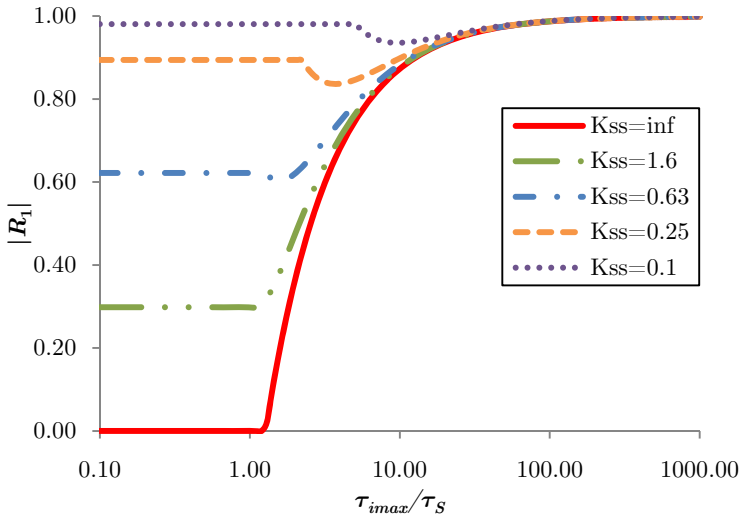

Figure 7.8 – Reflection coefficient versus the shear stress ratio for different values of K_{ss}

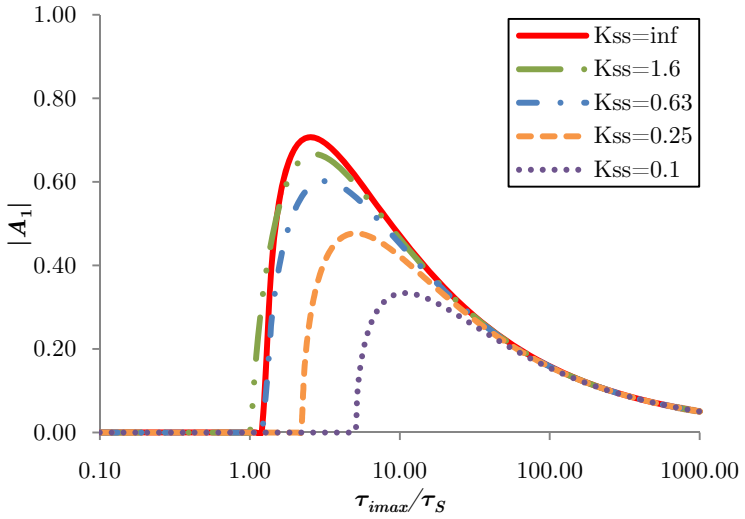

Figure 7.9 – Absorption coefficient versus the shear stress ratio for different values of K_{ss}

7.5 Comparison between SMM and MC

Some numerical analyses performed with the SMM have been compared with the results obtained by Zhao et al. (2006) who used the MC to study the Coulomb slip joint behaviour. As already described, the MC is a method that solves numerically the wave equation in time domain.

A one-cycle sinusoidal incident shear displacement wave $u = U \cdot \sin(\omega t)$ which impinges a frictional joint with Coulomb slip behaviour is applied. The incident wave has frequency $f = 50$ Hz and amplitude $U = 1$.

The incident wave in time domain is transformed in the frequency domain with the FFT. At this point, in SMM, we apply the equivalent linearization theory and we compute the scattering matrix for all frequencies. Then, we perform the IFFT to obtain the transmitted and reflected wave forms.

Figures 7.10 to 7.12 give the transmission, reflection and absorption coefficients versus the shear stress ratio τ_{imax}/τ_S. It is shown that the magnitude of the transmission coefficient decreases with increasing the shear stress ratio (Figure 7.10). In this situation the energy transmitted decreases and the remaining part of energy is reflected and dissipated from the frictional joint. $|T_1|$ increases with increasing the normalized joint shear stiffness K_{ss} as occurs for linear elastic joints.

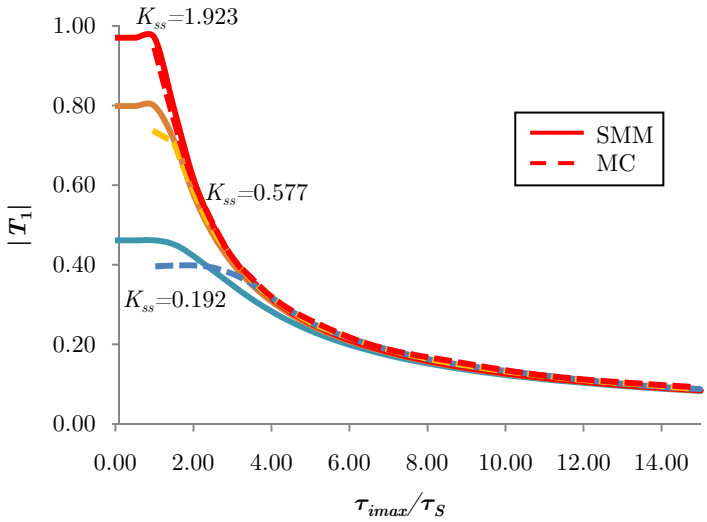

Figure 7.10 – Magnitude of the transmission coefficient versus the shear stress ratio: comparison between SMM and MC

The magnitude of the reflection coefficient versus the ratio τ_{imax}/τ_S is plotted in Figure 7.11. Obviously, $|R_1|$ increases with increasing of the shear stress ratio and

decreases with increasing K_{ss}. For low K_{ss} the variation with τ_{imax}/τ_S is less evident and less energy is adsorbed as shown in Figure 7.12. The absorption coefficient firstly increases with τ_{imax}/τ_S and after a peak decreases. The peak values move toward the right with decreasing of the normalized shear joint stiffness.

Figures 7.10 to 7.12 also highlight the favourable comparison between SMM and MC. Obviously, the MC, being a numerical method which accounts for the non linear behaviour more accurately, provides results that are more accurate than those obtained with the linear equivalent approach implemented in SMM.

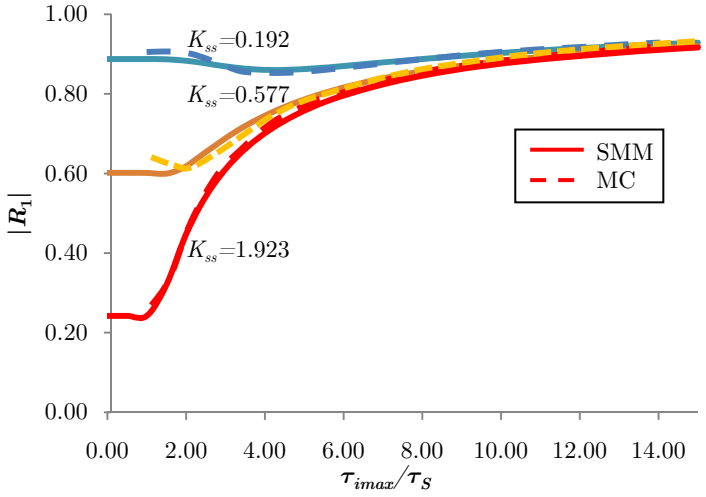

Figure 7.11 – Magnitude of the reflection coefficient versus the shear stress ratio: comparison between SMM and MC

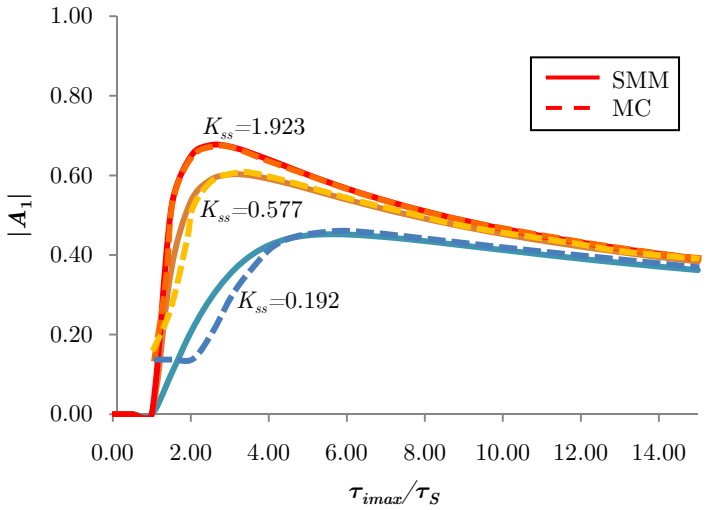

Figure 7.12 – Magnitude of the absorption coefficient versus the shear stress ratio: comparison between SMM and MC

7.6 Summary

Wave propagation across a frictional joint has been studied in this chapter. An equivalent linearization technique has been used to implement the frictional joint behaviour in the SMM.

This linearization of a non linear problem has shown to provide quite accurate results based on the comparison with the MC. Moreover, we have demonstrated that SMM can be used to analyse with good accuracy wave propagation across a frictional joint of a harmonic or a transient wave.

An extension of the problem studied by Miller (1977) has been also given. We have implemented in the SMM the linear elastic behaviour that the joint exhibits before the relative slip between the surfaces of the joint occurs.

Chapter 8

Discrete Element Modelling

8.1 Introduction

The purpose of this chapter is to compare the Scattering Matrix Method (SMM) with the Discrete Element Method (DEM) as implemented in the UDEC and 3DEC codes of the Itasca Consulting Group. This is done by focussing on the evaluation of the effects of joints on wave propagation.

Given that the SMM has been effectively developed, as shown in the previous chapters, to compute in a number of cases wave propagation in a medium containing discontinuities, this method will also be used in the following to optimize the discretized numerical model as adopted in the DEM codes.

8.2 Distinct Element Codes: UDEC and 3DEC

8.2.1 Universal Distinct Element Code (UDEC)

The Distinct Element Method (DEM) was presented and developed by Cundall (1971) and was later implemented in the numerical code UDEC (Universal Distinct Element Code), (Cundall 1980; Cundall & Hart 1985) for both static and dynamic analyses of rock mechanics problems. Later on, research by Cundall (1983) yielded to the development of the three dimensional distinct element code 3DEC (Cundall 1988; Hart et al. 1988). For rock mechanics problems, a key issue is the behaviour of discontinuous masses that include one or more joint sets or other discontinuity features.

This behaviour is difficult if not impossible to be included in a continuum formulation. Some numerical codes are able to implement certain features using interface elements or incorporate ubiquitous joint formulations. Despite this fact, the full simulation of the true mass is not achieved and often numerical difficulties may occur since these models may not be able to handle efficiently multiple discontinuities (Itasca, 2006). According to the architects of the method the main aspects behind the formulation of the distinct element analysis are:

- Ability to calculate infinitesimal strains, rotational behaviour of blocks including complete separation.

- Automatic recognition of new contacts between the blocks.

In this method, the domain is simulated by a group of "discrete" blocks and joints which are introduced as boundary conditions between the blocks, thus representing explicitly a fractured rock mass behaviour. The independent blocks can be rigid or deformable. For the latter case the blocks are discretized into elements following a finite element or finite difference formulation. In the Distinct Element Method, the governing differential equations dictate the kinematics of the blocks in the assemblage. The numerical solution targets in converging to an acceptable displacement in order for grid forces to equilibrate. At that state out of balance forces are minimized. Therefore, the individual blocks can interact following some behavioural model and deformations can also occur in the blocks thus the complete mass can be better modelled approximating the true conditions. Gutierrez & Barton (1994)) advice the use of the DEM method for rock mechanics problems when $0.1<Q<100$.

The distinguishing features of UDEC are described below (Stephansson et al., 1996):

- Simulation of large displacements (slip and opening) along distinct surfaces in a discontinuous medium (e.g., jointed rock masses);
- Discontinuous medium treated as an assemblage of discrete (convex or concave) polygonal blocks with rounded corners;
- Explicit solution scheme, giving a stable solution to unstable physical processes;
- Rigid or deformable blocks (can be mixed);
- Library of material models for deformable blocks (e.g., elastic, Mohr-Coulomb plasticity, ubiquitous joint, double-yield and strain-softening);
- Library of material models for discontinuities (e.g., Coulomb slip, continuously-yielding and Barton-Bandis);
- Full dynamic capability, with absorbing boundaries and wave input;
- "Null" blocks for excavation and backfill simulation;
- Coupled fluid flow in joints and pressure in cavities;
- Boundary-element coupling for "infinite domain" problems;
- Structural elements (including non-linear cables), with general coupling to continuum blocks (spatially extensive) or discontinuities (local reinforcement);
- Tunnel generator and statistically based joint-set generator.

8.2.2 3-Dimensional Distinct Element Code (3DEC)

3DEC (3-Dimensional Distinct Element Code) is a three-dimensional numerical program based on the distinct-element method (DEM) for discontinuum modelling. The basis for this code is the extensively tested numerical formulation used by UDEC (2006). The distinguishing features of 3DEC (Itasca, 2007) are described below:

- Simulation of large displacements (slip and opening) along distinct surfaces in a discontinuous medium (e.g., jointed rock masses);
- Discontinuous medium treated as an assemblage of discrete (convex or concave) polyhedra;
- Discontinuities treated as boundary conditions between blocks; six modes of contact automatically recognized;
- Relative motion along discontinuities governed by linear and non-linear force-displacement relations for movement in both the normal and shear directions;
- Explicit solutions to unstable physical processes;
- Rigid or deformable blocks (cannot be mixed);
- Five basic block constitutive models types of material models for deformable blocks (null; elastic, isotropic; elastic, anisotropic; Mohr-Coulomb plasticity and bilinear strain-hardening/softening ubiquitous-joint plasticity;
- Two types of material models for discontinuities (Coulomb-slip or continuously-yielding);
- Full dynamic capability, with absorbing boundaries and wave input;
- "Null" blocks for excavation and backfill simulation;
- Pre-processor program available to read AutoCAD (from Autodesk) files of solid objects and output 3DEC data files to generate polyhedra;
- Joint structure viewed separately from block structure; vectors and contours plotted on joint plane;
- Interactive manipulation of screen images (shaded perspective views, cross-sections, wire frames, vectors, tensors, contours, etc.);
- Inner/outer region coupling and automatic, radially graded mesh generation within polyhedra for modelling "infinite domain" problems;
- Structural elements (including grouted cables), with general coupling to continuum blocks (spatially extensive) or discontinuities (local reinforcement) and triangular plate elements to model concrete or shotcrete linings;
- Tunnel generator and statistically based joint-set generator.

8.3 Numerical models developed

The impedance concept is fundamental for understanding the procedure to define the maximum size of each element discretizing the numerical model. In the first part of this paragraph the meaning of the impedance of a system will be specified.

8.3.1 Definition of the impedance

In general, the impedance of a system is the ratio between the force applied in a point and the velocity in that point. The impedance influences the wave propagation phenomenon. There are different types of impedance depending on the field of analysis:

- Mechanical impedance is used in the study of the vibrating mechanical systems, i.e. studies of rigid vibrating bodies or loaded with forces but with only one value of velocity in each point.
- Acoustic impedance is used in the coupled study between an acoustic source and a fluid in contact; the source is characterized by a global parameter that is the acoustic discharge (equal to the product between the velocity and the source area) and a uniform value of pressure.
- Electrical impedance: is the ratio between the electric voltage and the electric current.

In general, the impedance generates two main effects:

1. Attenuation: the magnitude of the signal in output depends on the frequency of the input signal;
2. Phase-shift: the output signal cannot be in phase with the input signal but it can be forward or backward in function of frequency of the signal.

In dispersive systems, not all of the input energy is converted in the output signal. Each system has its own "reaction time" that produces a phase-shift. Part of energy is stored to be transferred in another form.

Two components compose the impedance:

1. Resistance: is the part of total impedance responsible of the energy dissipation;
2. Reactance: is the part of total impedance responsible of the energy transformation without dissipation.

The attenuation of the response of a physical system is due to the simultaneous presence of resistance and reactance terms. The phase-shift is only due to reactive terms. We can identify two types of reactance:

- capacitive reactance: attenuates low frequencies but not the high frequencies (the phase-shift of the output is in forward of 90° than the input);
- inductive reactance: attenuates high frequencies but not the low frequencies (the phase-shift of the output is in backward of 90° than the input).

8.3.2 Definition of the mesh element size

Transient forces, such as generated from earthquake sources, usually contain a wide band of significant frequencies. For this reason, it is necessary to choose a correct size of the finite element mesh to model the wave propagation carefully.

Shipley et al. (1968) observed that the finite element models behave like low pass filters having definite passing bands and cut-off frequencies which depend upon the wave type and the finite element mesh. It was noted also that wave propagation through a continuum at frequencies above the cut-off frequency cannot propagate through the finite element mesh associated with the particular cut-off frequency.

Take as an example, a semi-infinite elastic homogeneous rod (Figure 8.1a). As well known in an infinite rod a harmonic P-wave travelling in the positive direction would impose normal stresses on a fictitious boundary that separates the rod in two semi-infinite rods: $\tau_{zz}=\rho V_P\ \dot{u}$. These normal stresses are identical to those which would exist if the semi-infinite rod on the right side of the boundary were replaced by a dashpot of coefficient $c_p=\rho V_P$. Hence a dashpot is applied at the right side of the rod to simulate the perfect absorption of the normally incident elastic wave imposed to the left side. The constant of this dashpot (Figure 8.1a) coincides with the characteristic impedance of the not discretized media and then the dashpot simulates the infinite extent of the rod.

The study of the response of a continuous, homogeneous, isotropic and perfectly elastic semi-infinite rod (Figure 8.1a) in the mechanical field is more complex. It is convenient to build up the equivalent electric circuit (Figure 8.1b) of the mechanical model of the rod to simplify the problem. Characteristic equations of the mechanical field are formally the same of those that represent the equivalent electric systems. The electric systems can be represented by models with concentrated parameters composed by inductive and capacitive elements.

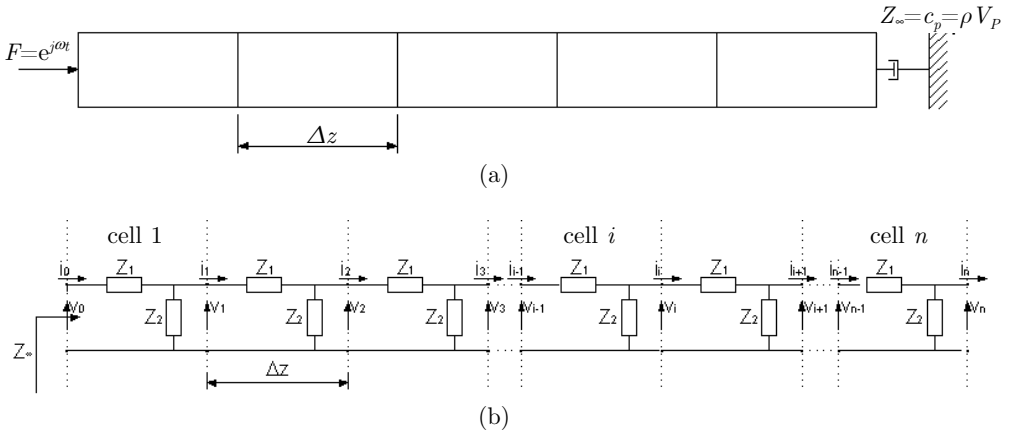

Figure 8.1 – (a) Finite element model and (b) equivalent electric circuit

A physical system subjected to wave propagation can be studied by analyzing the equivalent electric circuit that is called "ladder network".

The "ladder network" is an infinite electric circuit that is composed by n cells. The electric iterative impedance of the single cell i (Figure 8.2) can be computed as follows:

$$Z_\infty = Z_1 + \frac{Z_2 Z_\infty}{Z_2 + Z_\infty} \tag{8.1}$$

from which:

$$Z_\infty = \frac{Z_1}{2} + \sqrt{\frac{Z_1^2}{4} + Z_1 Z_2} \tag{8.2}$$

where:
Z_∞ is the characteristic impedance that in this case is also the input impedance of the line (Figure 8.2);
Z_1 and Z_2 are two local impedances.

For simplicity, we can rebuild the "ladder network" of Figure 8.1b as plotted in Figure 8.3. In these conditions, the input impedance at the point B-B is as follows:

$$Z_\infty = \sqrt{\frac{Z_1^2}{4} + Z_1 Z_2} \tag{8.3}$$

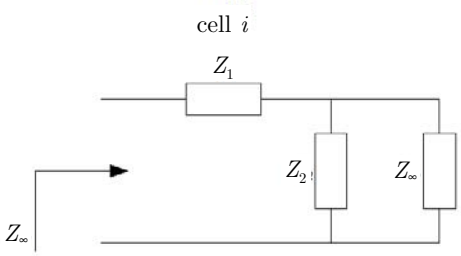

Figure 8.2 – Electric circuit for the computation of the iterative impedance of the cell i

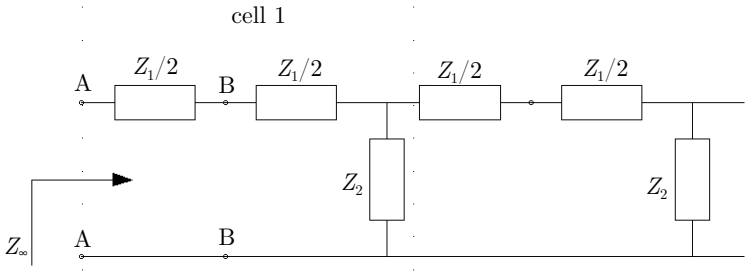

Figure 8.3 - Equivalent circuit of that shown in Figure 8.1b

At this point, we can transform the ladder network of Figure 8.3 in a LC ladder network (Figure 8.4), composed by inductors and capacitors, by considering:

$$Z_1 = j\omega L \qquad Z_2 = \frac{1}{j\omega C} \tag{8.4}$$

where L is the inductance and C the capacitance.

If we substitute the Equations (8.4) in the Equation (8.3), we obtain the characteristic impedance of the LC ladder network:

$$Z_\infty = \sqrt{\frac{L}{C} - \frac{\omega^2 L^2}{4}} \tag{8.5}$$

From Equation (8.5), we can identify a critical circular frequency ω_c for which:

$$Z_\infty \text{ is real if } \omega < \frac{2}{\sqrt{LC}} = \omega_c \tag{8.6}$$

$$Z_\infty \text{ is imaginary if } \omega > \frac{2}{\sqrt{LC}} = \omega_c$$

$$Z_\infty = 0 \text{ if } \omega = \frac{2}{\sqrt{LC}} = \omega_c$$

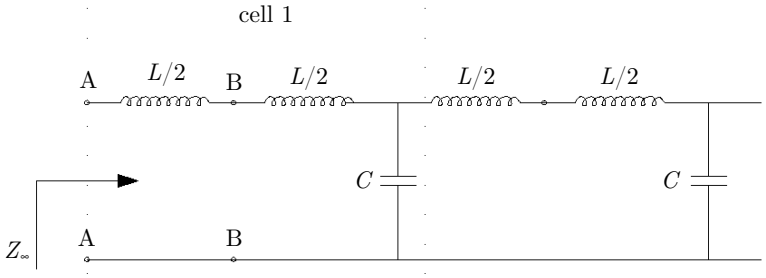

Figure 8.4 – Ladder network LC

The characteristic impedance shown in Equation (8.2) can also be obtained for the mechanical system by using the Maxwell analogy. The Maxwell analogy relates the electrical quantities with mechanical quantities as follows:

Capacitance $C \Leftrightarrow$ spring $1/k$
Inductance $L \Leftrightarrow$ mass m
Resistance $R \Leftrightarrow$ damping coefficient c
Current $I \Leftrightarrow$ velocity v
Voltage $V \Leftrightarrow$ stress T

If we consider the semi-infinite rod shown in Figure 8.1a, the equivalent single cell i, for the mechanical system, is represented by the system shown in Figure 8.5 that is analogous to the single cell of the electric circuit in Figure 8.2.

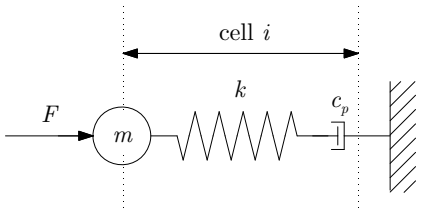

Figure 8.5 – Mechanical circuit for computation of the iterative impedance of the cell i

The equation of motion of the mechanical system, shown in Figure 8.5, is as follows:

$$m\ddot{z} + f_{kc} = f \rightarrow \left(j\omega m + \frac{1}{\frac{j\omega}{k} + \frac{1}{c_p}} \right) V = F \tag{8.7}$$

where:

$v = Ve^{j\omega t}$ is the velocity;

$f = Fe^{j\omega t}$ is the sinusoidal force;

f_{kc} is the force related to the spring and dashpot connected in series.

We can assume that the constant of the dashpot, in Equation (8.7), is equal to the characteristic impedance Z_∞. Hence, the input impedance of the single cell i is equal to the output one in the semi-infinite bar. In this way we can obtain the expression of the characteristic impedance of the single cell i:

$$j\omega m + \frac{1}{\frac{j\omega}{k} + \frac{1}{c_p}} = \frac{F}{V} \rightarrow Z_1 + \frac{1}{\frac{1}{Z_2} + \frac{1}{Z_\infty}} = Z_\infty \tag{8.8}$$

From the Equation (8.8), we can obtain the same equation of the characteristic impedance of the system previously derived for the equivalent electric circuit (see Equation (8.1)).

We have shown the analogy between the mechanical and the electrical systems. By the Maxwell analogy, we can rewrite the Equation (8.3) as follows:

$$Z_\infty = \sqrt{mk - \frac{\omega^2 m^2}{4}} \tag{8.9}$$

and the critical frequency becomes:

$$\omega_c = \frac{2}{\sqrt{m/k}} \tag{8.10}$$

Going back to the electric circuit, we take the cell n of the "ladder network", plotted in Figure 8.1b, to compute the ratio between the electric voltages in input V_n and in output V_{n+1} in a unit cell n:

$$V_n = Z_\infty I_n \rightarrow I_n = \frac{V_n}{Z_\infty} \text{ and } V_n - V_{n+1} = I_n Z_1 = V_n \frac{Z_1}{Z_\infty} \text{ and then}$$

$$\frac{V_n}{V_{n+1}} = 1 - \frac{Z_1}{Z_\infty} = \frac{Z_\infty - Z_1}{Z_\infty} \tag{8.11}$$

These electric voltages are equivalent to the stress before and after the cell i for a mechanical system.

At this point, we can compute the propagation factor of the "ladder network":

$$\alpha = \frac{\sqrt{\frac{Z_1^2}{4} + Z_1 Z_2} - \frac{Z_1}{2}}{\sqrt{\frac{Z_1^2}{4} + Z_1 Z_2} + \frac{Z_1}{2}} = \frac{\sqrt{\frac{L}{C} - \frac{\omega^2 L^2}{4}} - j\frac{\omega L}{2}}{\sqrt{\frac{L}{C} - \frac{\omega^2 L^2}{4}} + j\frac{\omega L}{2}} \tag{8.12}$$

where the factor α has modulus 1 if $\omega < \omega_c = \frac{2}{\sqrt{LC}}$.

We can write:

$$\alpha = e^{-j\delta} \tag{8.13}$$

with:

$$\delta = 2arctg\left[\frac{\frac{\omega L}{2}}{\sqrt{\frac{L}{C} - \frac{\omega^2 L^2}{4}}}\right] \tag{8.14}$$

On the other hand, if $\omega > \omega_c$, α becomes a real value < 1:

$$\alpha = \frac{\sqrt{\frac{\omega^2 L^2}{4} - \frac{L}{C}} - \frac{\omega L}{2}}{\sqrt{\frac{\omega^2 L^2}{4} - \frac{L}{C}} + \frac{\omega L}{2}} \tag{8.15}$$

which can be written as in Equation (8.13) but with δ imaginary ($Im\ (\delta) < 1$):

$$\delta = j \ln \left[\frac{\sqrt{\frac{\omega^2 L^2}{4} - \frac{L}{C}} - \frac{\omega L}{2}}{\sqrt{\frac{\omega^2 L^2}{4} - \frac{L}{C}} + \frac{\omega L}{2}} \right] \tag{8.16}$$

This means that V_n tends to zero exponentially with increasing n. The signal cannot propagate because the inductances and the capacitances are not matched. Hence, this ladder network is a low pass filter.

Now we can define the maximum allowable size Δz_{lim} (evaluated in the direction of wave propagation) of the single element discretizing a mechanical system for correctly representing the wave propagation through the semi-infinite rod plots in Figure 8.1a. We can assume for the mechanical system that:

$$m = \rho \Delta z \qquad k = \frac{C_{jj}}{\Delta z} \tag{8.17}$$

where $C_{jj} = C_{11}$ for compressional waves and $C_{jj} = C_{44}$ for shear waves.

The mass in the Equation (8.17) is computed assuming a unitary transversal area of the single element. After substituting in the Equation (8.10) we can obtain the maximum allowable element size:

$$\omega_c = 2\pi f_c = \frac{2}{\sqrt{\rho \Delta z \frac{\Delta z}{C_{jj}}}} = \frac{2V_{P,S}}{\Delta z} \rightarrow \Delta z_{\lim} = \frac{1}{\pi} \lambda \tag{8.18}$$

The equation of characteristic impedance of the mechanical system obtained by substituting the terms (8.17) in the Equation (8.9) is the following:

$$Z_{\infty} = \sqrt{\rho C_{jj} - \frac{\omega^2 \left(\rho \Delta z\right)^2}{4}} \tag{8.19}$$

which can be expressed as function of the element size ratio $\Delta z/\lambda$ as follows:

$$Z_{\infty} = \sqrt{\rho C_{jj} - \frac{\omega^2 \left(\rho \Delta z\right)^2}{4}} = \sqrt{\rho C_{jj}\left(1 - \pi^2 \left(\frac{\Delta z}{\lambda}\right)^2\right)} = Z_{\infty ND}\sqrt{1 - \pi^2 \left(\frac{\Delta z}{\lambda}\right)^2} \tag{8.20}$$

where $Z_{\infty ND}$ is the characteristic impedance of the not discretized mechanical system.

Similar considerations can be developed for the propagation factor α and for the phase-shift δ (on the tract Δz):

- If $\omega < \omega_c$, $|\alpha| = 1$

$$\alpha = \frac{\sqrt{1 - \pi^2 \left(\frac{\Delta z}{\lambda}\right)^2} - j\pi\left(\frac{\Delta z}{\lambda}\right)}{\sqrt{1 - \pi^2 \left(\frac{\Delta z}{\lambda}\right)^2} + j\pi\left(\frac{\Delta z}{\lambda}\right)} \tag{8.21}$$

$$\delta = 2arctg\frac{\pi\left(\frac{\Delta z}{\lambda}\right)}{\sqrt{1 - \pi^2 \left(\frac{\Delta z}{\lambda}\right)^2}} \tag{8.22}$$

- If $\omega > \omega_c$, $\alpha < 1$

$$\alpha = \frac{\sqrt{\pi^2 \left(\frac{\Delta z}{\lambda}\right)^2 - 1} - \pi\left(\frac{\Delta z}{\lambda}\right)}{\sqrt{\pi^2 \left(\frac{\Delta z}{\lambda}\right)^2 - 1} + \pi\left(\frac{\Delta z}{\lambda}\right)} \tag{8.23}$$

$$\delta = j \ln \left[\frac{\sqrt{\pi^2 \left(\frac{\Delta z}{\lambda} \right)^2 - 1} - \pi \left(\frac{\Delta z}{\lambda} \right)}{\sqrt{\pi^2 \left(\frac{\Delta z}{\lambda} \right)^2 - 1} + \pi \left(\frac{\Delta z}{\lambda} \right)} \right] \tag{8.24}$$

When $\Delta z \to 0$, $\omega_c \to \infty$ there is not the attenuation band and the stress and velocity becomes continuous. In these conditions $\pi \Delta z \ll 1$ and then the phase-shift δ (Equation (8.22)) can be approximated as:

$$\delta \simeq 2\pi \left(\frac{\Delta z}{\lambda} \right) \left(1 + \frac{1}{2} \pi^2 \left(\frac{\Delta z}{\lambda} \right)^2 \right) \tag{8.25}$$

Equation (8.25) is obtained from the Equation (8.22) by remembering that for small values $arctg(x) \simeq x$ and $1/\sqrt{1-y} \simeq 1 + 1/2\, y$.

Kuhlmeyer & Lysmer (1973) stated that the maximum element length equal to one-eighth of the wavelength of the slowest body wave propagating in the elastic material is recommended (based upon the experience) for analysis of layered media.

The above analysis is related to a model that is discretized with concentrated parameters (masses and stiffnesses).

Let us now give an example of definition of the element size. Take the model as composed of a semi-infinite rod (see Figure 8.1a) loaded by a harmonic P-wave and with the mechanical properties shown in Table 8.1.

Figures 8.6 to 8.8 show the comparison between the quantities obtained for the not discretized and discretized models for a fixed value of input frequency of $50Hz$. The dashed lines highlight the position of the element size ratios 1/8 (as suggested by Kuhlemeyer & Lysmer (1973)) and $1/\pi$.

In order to have a general expression, the characteristic impedance, shown in Figure 8.6, is divided by the characteristic impedance of the not discretized system:

$$\frac{Z_\infty}{Z_{\infty ND}} = \sqrt{1 - \pi^2 \left(\frac{\Delta z}{\lambda} \right)^2} \tag{8.26}$$

The curves of the characteristic impedance versus element size ratio are shown in Figure 8.6. As previous mentioned, the characteristic impedance of the not discretized model is $Z_{\infty ND} = \rho V_P$. The gap between the curves of the impedance for the not discretized and the discretized systems increases with the increasing of

$\Delta z/\lambda$. Moreover we can note that the characteristic impedance of the discretized system decreases with the increasing of the element size ratio.

Table 8.1 – Properties of the discontinuous medium

Mass density	2650 kg/m^3
Bulk modulus	44 GPa
Shear modulus	39 GPa
Velocity of the propagating P-wave	5830 m/s
Velocity of the propagating S-wave	3840 m/s

If we pay attention to Figure 8.7 it is evident that over the limit value $\Delta z_{lim} = 1/\pi\lambda$ the wave is attenuated and then the magnitude of the propagation factor becomes smaller than 1. These results prove the correctness of using an element size $\Delta z = 1/8\lambda$ as Kuhlmeyer & Lysmer (1973) suggested. In fact for this element size the accuracy of the wave propagation across the discretized model is good because the error done is minimal (about 8%).

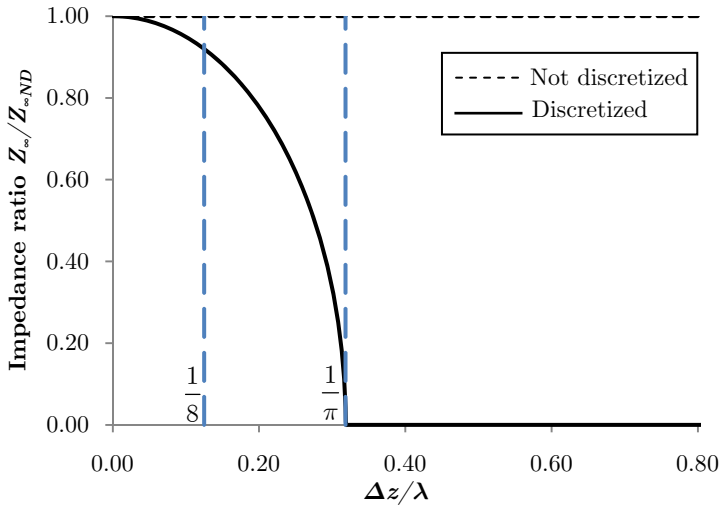

Figure 8.6 – Impedance ratio versus the ratio between the element size and the wavelength ($f = 50Hz$)

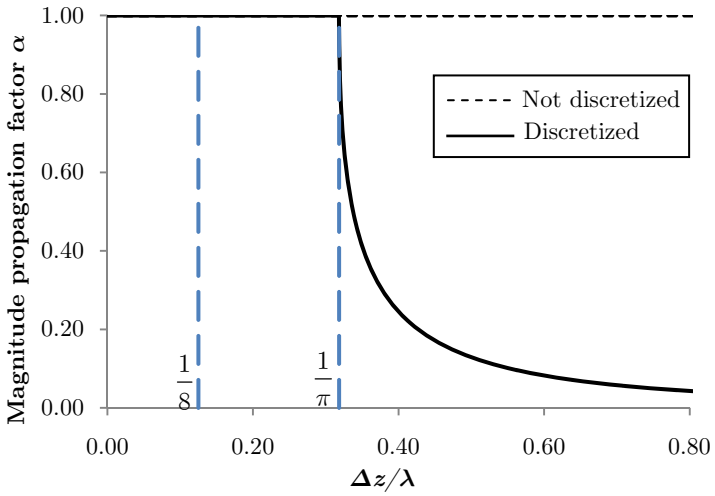

Figure 8.7 – Magnitude of the propagation factor versus the ratio between the element size and the wavelength ($f = 50Hz$)

If we divide the phase-shift δ on the tract Δz for λ, we can obtain an equivalent propagation constant k_e. The variation of k_e versus the element size ratio is shown in Figure 8.8. In this graph we can see that k_e is constant for the not discretized system because it becomes equal to the well known propagation constant $k_P = \omega / V_P$ (that for shear waves the propagation constant becomes $k_S = \omega / V_S$).

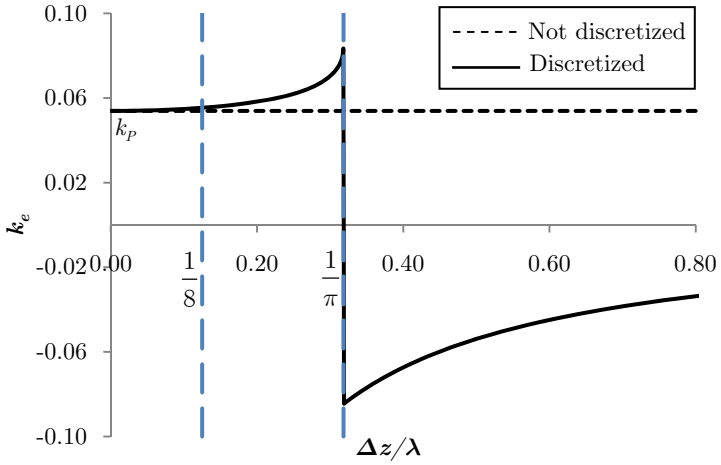

Figure 8.8 – Equivalent propagation constant versus the ratio between the element size and the wavelength (f=50Hz)

In summary, we can say that the element size of the discretized model must be smaller than $\Delta z = 1/8\lambda$. After that the error in the accuracy of the wave propagation in the discretized model increases exponentially. Over the $\Delta z = 1/\pi\lambda$, the wave travelling across the discretized model undergoes an attenuation that grows exponentially.

Then the correct element size which ensures the accuracy of the numerical model is defined. It is found that the element size and the time step observe Courant-Freidrichs-Lewy (CFL) Stability Criterion:

$$\Delta t < \frac{1}{V_{P,S}\sqrt{1/\Delta x^2 + 1/\Delta y^2 + 1/\Delta z^2}} \tag{8.27}$$

where the time increment Δt has a specific bound relative to the spatial discretization Δx, Δy and Δz.

8.3.3 Boundaries of the model

To prevent the reflection of outward propagating waves back into the model, absorbing boundaries are applied along the base and the top of the models. UDEC and 3DEC use the quiet-boundary scheme developed by Lysmer and Kuhlemeyer (1969): it is based on the use of dashpots attached independently to the boundary in the normal and shear directions. They provide viscous normal and shear tractions given by:

$$\begin{aligned} \tau_n &= -\rho V_P v_n \\ \tau_s &= -\rho V_S v_s \end{aligned} \tag{8.28}$$

where v_n and v_s are the normal and shear components of the velocity at the boundary.

In fact, when a wave hits a viscous boundary, a symmetric wave that cancels the incoming one is generated. This symmetric wave is materialized by imposition of equivalent forces such as in the velocity-stress equation (8.28). These viscous terms can be introduced directly into the equations of motion of the grid points lying on the boundary.

A different approach, however, was implemented in UDEC and 3DEC, whereby the tractions τ_n and τ_s are calculated and applied at every time-step in the same way as boundary loads are applied. This is more convenient than the former approach, and tests have shown that the implementation is equally effective. The only potential problem concerns numerical stability, because the viscous forces are

calculated from velocities lagging by half a time-step. In practical analyses to date, no reduction of time-step has been required by the use of the non-reflecting boundaries. Time-step restrictions demanded by small zones are usually more important.

Taking into account that quiet boundaries are not completely effective at absorbing body waves approaching the boundary at angles of incidence smaller than 30° or for surface waves, we need to place the boundaries at some distance from the region of interest to minimize the effect of reflected waves. In fact, it is well known that viscous absorbing boundaries loose efficiency as the angle of incidence decreases.

One restriction when using quiet boundaries is that one cannot apply a velocity record along the same boundary because the effect of the quiet boundary would be nullified. To input seismic motion at a quiet boundary, the velocity wave is converted to a stress wave using the formula:

$$\begin{aligned} \sigma_n &= 2\rho V_P v_n \\ \sigma_s &= 2\rho V_S v_s \end{aligned} \tag{8.29}$$

Hence, if a dynamic load is to be introduced simultaneously in the same place of an absorbing boundary, it must be set as a force loading. Because half of the load will be absorbed by a viscous boundary the load magnitude must be doubled.

8.3.4 Geometrical and mechanical properties

The models implemented in UDEC and in 3DEC in order to study wave propagation in a jointed medium are shown in Figure 8.9 and 8.10 for the case of a single joint. The DEM models were built with deformable blocks, which were subdivided into a mesh of finite difference elements, which satisfies the requirement of accuracy.

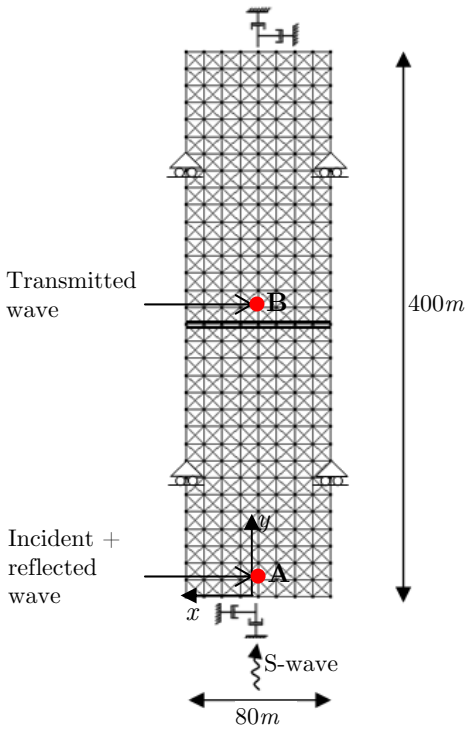

Figure 8.9 – UDEC two-dimensional model with a single joint

The UDEC model size is $400m$ in y direction and $80m$ in x direction. On the other hand, the three-dimensional 3DEC model has the same size of the UDEC one in the xy plane, but in addition it has a width of $10m$ in z direction.

The medium was modelled with elastic, fully deformable blocks. The blocks are separated by planar discontinuities extending in the xz plane for the 3DEC model and parallel to x in the UDEC model. The blocks were internally discretized into tetrahedral zones.

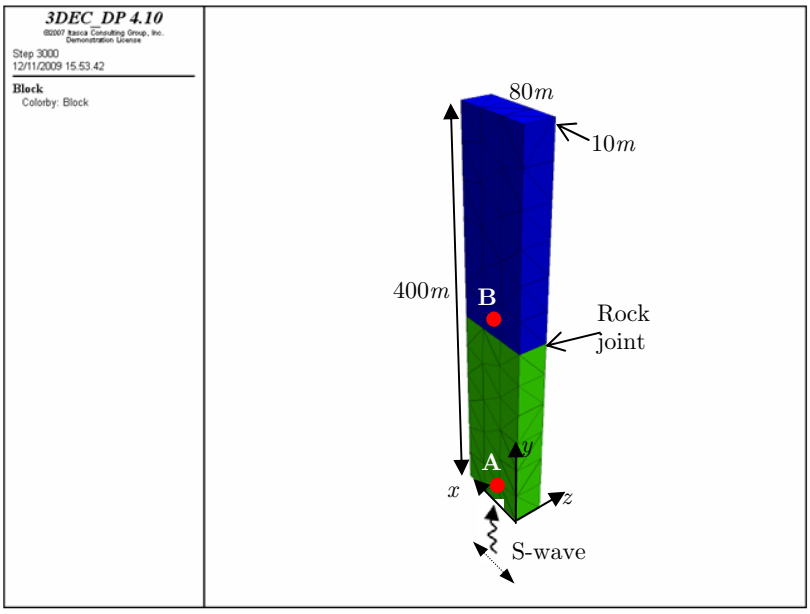

Figure 8.10 – 3DEC model for the case of a single joint

As described in the previous paragraph, no-reflection boundaries are applied at the bottom and top of the UDEC model, while the lateral boundaries are fixed in the y direction (direction normal to the wave propagation). Vertical movement at the lateral boundaries is constrained to prevent formation of surface waves. No-reflection boundaries were applied to consider an infinite medium in the y direction.

In the 3DEC model, non-reflecting boundary conditions were introduced at the top and bottom of the model. Displacements were restrained in the z direction in the xy plane at z=0 and z=10m to simulate plane strain conditions. In UDEC only P or SV-plane elastic waves can be applied (the code does not allow for SH-wave propagation).

The input is applied at the bottom of two numerical models and it is a one-cycle sinusoidal incident shear stress wave with amplitude of 1MPa and frequency of 50Hz (Figure 8.11).

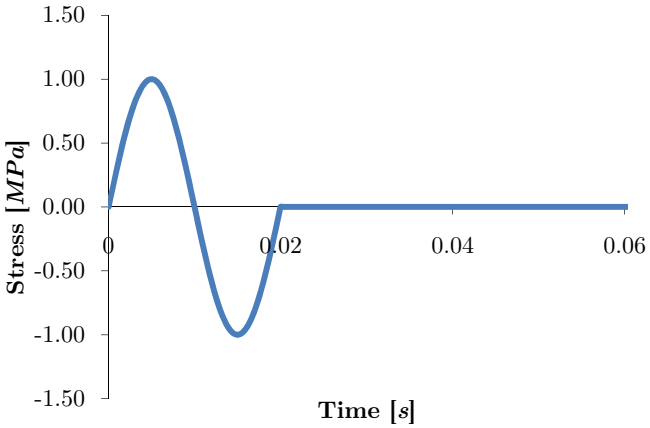

Figure 8.11 – Input shear stress wave

As discussed in the previous paragraph, the magnitude of the incident shear stress wave has been doubled in the numerical models to account for the simultaneous presence of the non-reflecting boundary at the bottom of the models.

The properties of the discontinuous medium are summarized in Table 8.1.

No material and geometrical damping is considered because the object here is to study only the changes in the wave form due to the joints.

8.4 Wave propagation across linear elastic joints

With the intent to compare the results obtained with the UDEC and 3DEC models with those given by the Scattering Matrix Method (SMM), joints with a linear elastic behaviour are considered. As in Chapter 5, the reflection and transmission coefficients are computed versus the joint stiffness (k_{ss}), the number of joints (N) and the joint spacing (d).

Single joint

Let us consider first a one-dimensional wave propagation through a model with a single joint. The shear stress wave impinges normally the joint. The magnitude of the reflection $|R_1|$ and transmission $|T_1|$ coefficients for a single joint are plotted in Figure 8.12 versus the normalized joint shear stiffness $K_{ss} = k_{ss}/\omega Z_S$. A very good agreement between the DEM and SMM results is found.

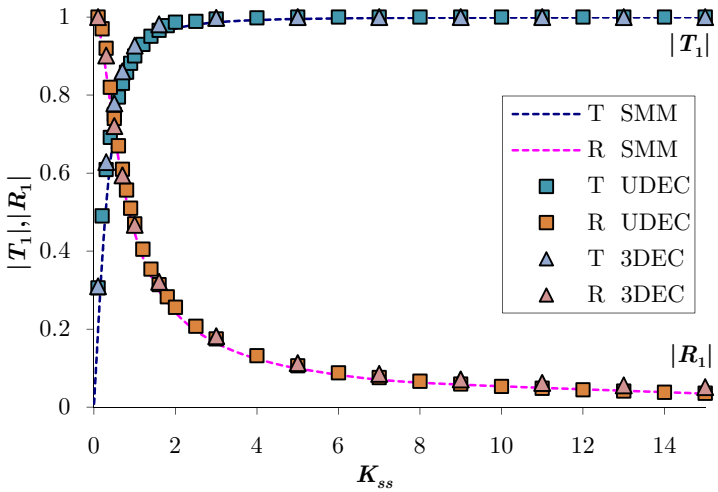

Figure 8.12 – Magnitude of the transmission and reflection coefficients as function of the normalized joint shear stiffness for a single joint

The transmission and reflection coefficients were defined respectively from the ratio between the maximum amplitudes with the corresponding waves and the incident waves. The transmitted wave is recorded at the point B while the reflected one at the point A (see Figures 8.9 and 8.10). The point A is located at $1m$ from the bottom of the model while point B is at $1m$ from the joint.

Set of N parallel equi-spaced joints

Let us take the case of a set of N parallel equi-spaced linear elastic joints. A large number of simulations for different values of the joint spacing ratio $\zeta = d/\lambda$, K_{ss} and number N of joints has been considered.

Figure 8.13 plots some transmitted wave forms obtained for different values of the joint parameters. The transmitted shear stress waves are recorded in UDEC and in 3DEC at $1m$ following the last joint. The models, with more joints, are built from the same model used for a single joint. The other joints are added above and below the joint in the middle of the model.

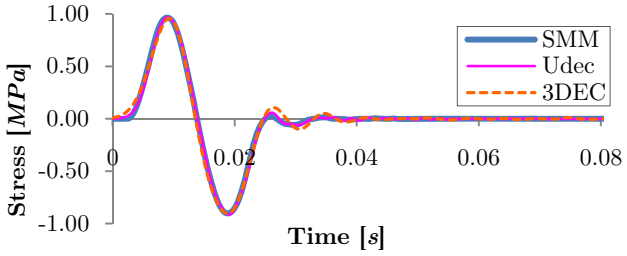

(a) K_{ss}=1.6 ζ=0.081 N=2

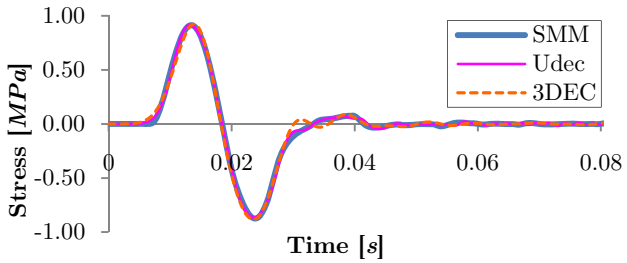

(b) K_{ss}=1.6 ζ=0.326 N=2

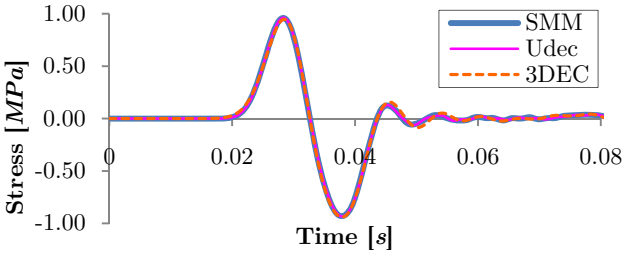

(c) K_{ss}=1.6 ζ=0.081 N=10

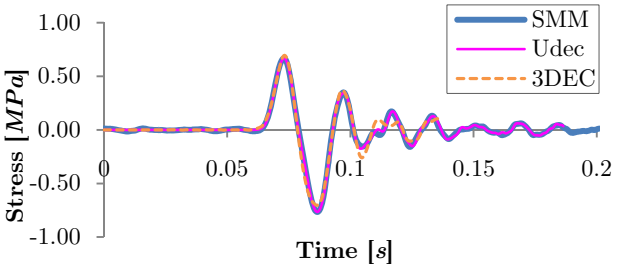

(d) K_{ss}=1.6 ζ=0.326 N=10

Figure 8.13 – Transmitted wave forms - Comparison between analytical and numerical results obtained with different values of K_{ss}, ζ and number of joints

The results obtained with UDEC and 3DEC which are plotted in Figure 8.13 are shown to be very close to those obtained with the SMM. In particular, the transmitted wave from a set of N=2 and N=10 joints for two different value of ζ with an assumed K_{ss} = 1.6 is shown.

Of interest are the results shown in Figure 8.14 and 8.15 which have been obtained with a great number of numerical analyses (performed with an half-cycle sinusoidal incident shear stress wave). Figure 8.14 plots the magnitude of the transmission coefficient of a set of two parallel joints as a function of ζ for different values of the normalized joint shear stiffness. The results obtained with UDEC and 3DEC, which are essentially the same as shown by the square symbols, are in close agreement with those given by the SMM solution.

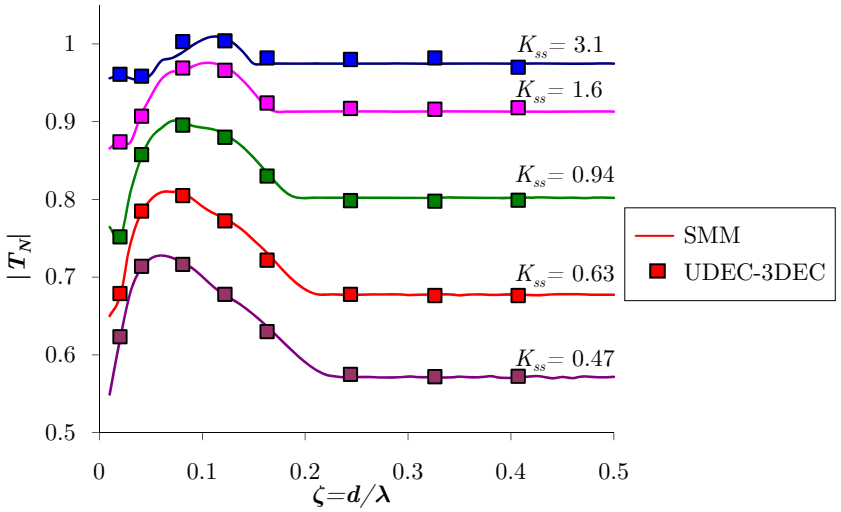

Figure 8.14 – Magnitude of the transmission coefficient for two joints versus the joint spacing ratio for various K_{ss} values. Comparison between DEM and SMM results

The transmission coefficient $|T_N|$ for a set of N joints versus the joint spacing ratio as computed with UDEC and 3DEC is plotted in Figure 8.15. Once again the results obtained are shown to agree satisfactorily with those given by the SMM solution. It is of interest to note that as for the case of two joints the peak value of the transmission coefficient increases with the increasing of the number of joints unlike what happens after the peak.

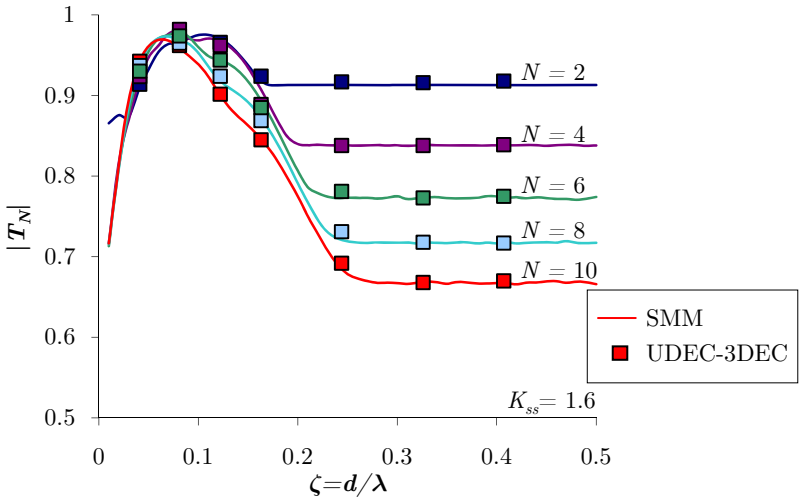

Figure 8.15 – Magnitude of the transmission coefficient for N joints versus the joint spacing ratio with $K_{ss} = 1.6$. Comparison between DEM and SMM results

Additional analyses

At this point, we have performed the same analyses with UDEC and 3DEC by applying a one-cycle sinusoidal normal stress P-wave with frequency $50Hz$ and unit amplitude. The models shown in Figures 8.9 and 8.10 have been modified to simulate P-wave propagation. Quiet boundaries were applied along the bottom and the top of the models. Lateral boundaries were fixed only in the x direction in the UDEC model rather than in the y direction (Figure 8.16). Same considerations were done for the 3DEC model.

As expected, the results of these analyses have shown that the diagrams of Figures 8.12 to 8.15 can be also applied for a P-wave that impinges normally the joints. In fact, it is sufficient to replace the value of the joint shear stiffness with the normal stiffness and the impedance Z_S with Z_P.

Discussion

In conclusion, we have shown that the results obtained with SMM, UDEC and 3DEC compare very satisfactorily. Hence the SMM can be considered as an excellent tool to evaluate, in first approximation, the correctness of the numerical models. These results are indeed of special interest as the SMM, although operating in the frequency domain, provides results that are very near to those obtained with DEM which operates in the time domain. On the other hand, we can state that DEM codes simulate very well wave propagation through jointed media.

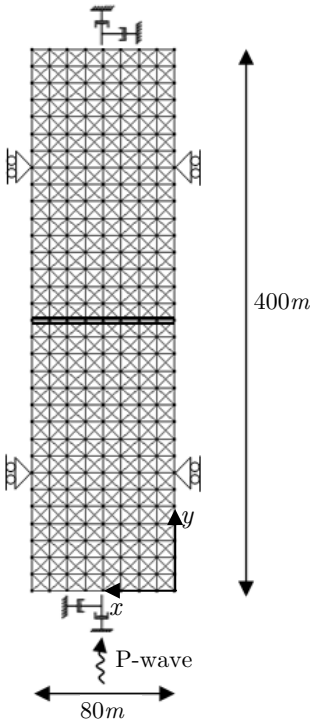

Figure 8.16 – UDEC model for mono-dimensional P-wave propagation analyses

8.4.1 Plane wave with oblique incidence

The wave propagation of an SH-wave with oblique incidence is analysed in the following. This problem is studied with the 3DEC code and the results obtained are compared again with the SMM.

The creation of the numerical model is now more complex than in the case of a normally incident wave. Particular attention need be placed on the boundary conditions and on the application of the oblique incident wave.

The geometry of the model is shown in Figure 8.17. The size of the model has been chosen so as to limit the computational time. An element size of the mesh of $6m$ has been taken in order to ensure accurate wave propagation through the numerical model.

A linear elastic joint has been generated in the middle of the model. In this case the material and the geometrical damping are not considered as the interest is now to study the effect of the joint on wave propagation.

Quiet boundary conditions have been applied on the planes yz and xy. The direction z on the plane xz has been taken as fixed. These boundary conditions allow one to model correctly the wave propagation of an SH-wave with particle velocity in the y direction.

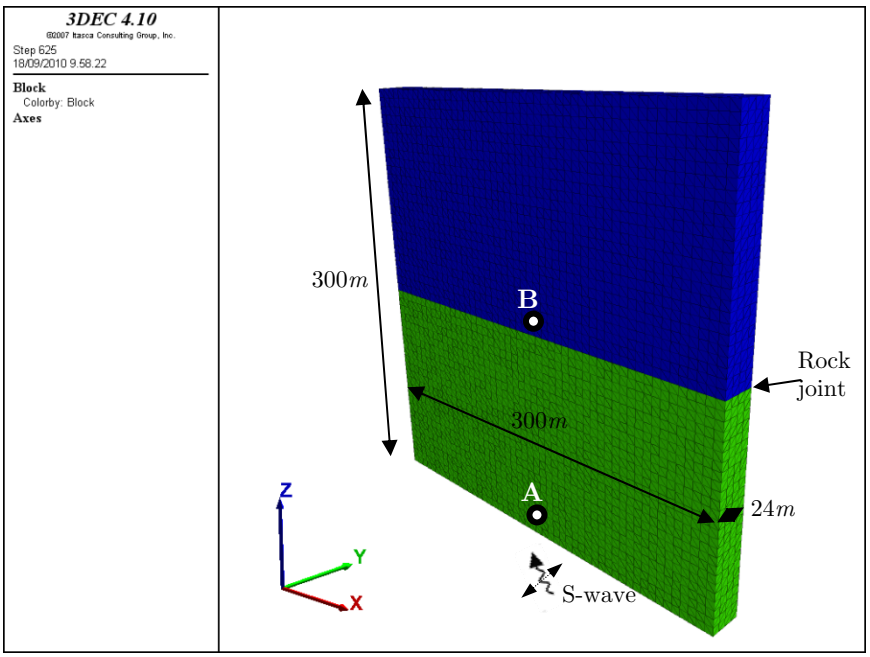

Figure 8.17 – 3DEC model for oblique SH-wave propagation

Particular attention has to be taken in this case to the application of the plane SH-wave at the bottom plane xy of the model. Along this boundary a one-cycle sinusoidal shear wave velocity has been applied as follows:

$$v^{inc}\left(x,t\right) = \sin\left(\omega_0 t - \xi_0 x\right)\hat{y} \tag{8.30}$$

where:
$\omega_0 = 314.16\ rad/s$ with $f = 50Hz$;
$\xi_0 = k_s \cdot \sin\vartheta^{inc}$ is the transverse wave vector.

It is noted that the incident wave applied along the bottom of the model depends not only on the time t but also on the space x. Thus, in order to apply correctly the oblique incident wave, it is necessary to consider that at the same time the input wave is different at any node of the bottom of the model (Figure 8.18). Hence, a "fish" function in 3DEC has been built that allows one to apply a different input for each node of the bottom along the x direction.

Moreover, due to the limited extension of the model in the x direction, the applied SH-wave is not exactly a plane wave. In fact, for each node of the model the wave is not applied exactly with an angle of incidence ϑ^{inc} but waves are introduced with different directions close to ϑ^{inc}.

On the other hand, if the extension of the model was infinite these directions converged all in the correct direction ϑ^{inc}. For this reason, some modifications in the SMM needed be introduced in order to allow the comparison with the 3DEC results. In the SMM, the input wave (see Equation (8.30)) is normally transformed in the frequency domain with the FFT. In this case another FFT in space has been performed to move from x to ξ space.

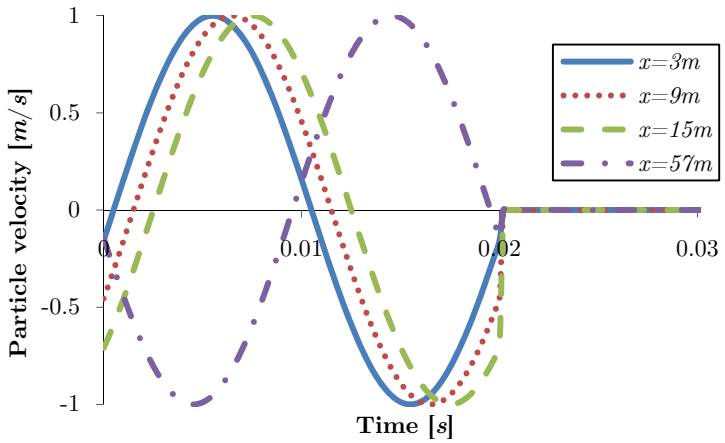

Figure 8.18 – Example of variation of the input wave ($\vartheta^{inc} = 40°$) with the position x along the bottom of the 3DEC model

The plot of the magnitude of the transmission coefficient versus the angle of incidence is shown in Figure 8.19. It is observed that the results obtained with 3DEC (square symbols) are very close to those computed with the SMM. It is noted that the SMM results are obtained for a joint stiffness ratio $K_{ss} = 0.25$ and normalized with respect to the cosine of the angle of incidence ($\cos \vartheta^{inc}$). For this reason, we should obtain a constant transmission coefficient with the variation of the angle of incidence. However, the transmission coefficient is not perfectly constant because we have not applied a pure plane wave.

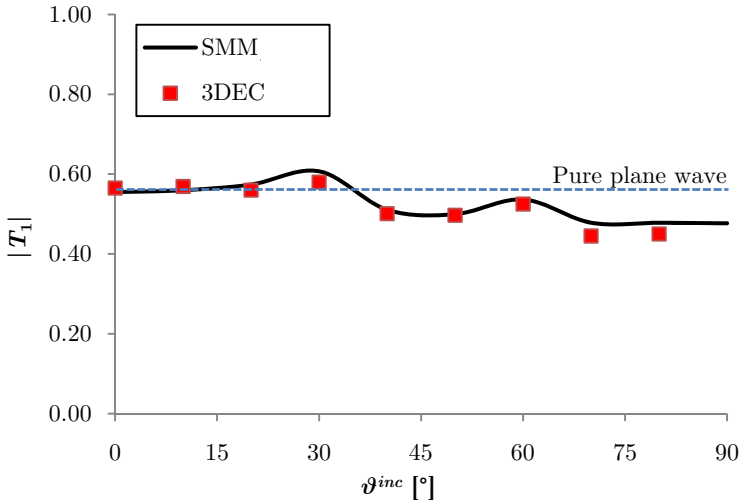

Figure 8.19 – Magnitude of the transmission coefficient versus the angle of incidence

In conclusion, we can say that the 3DEC model allows one to simulate oblique wave propagation, although some difficulties in the definition of the size and boundary conditions of the model have been encountered.

8.5 Wave propagation across frictional joints

Finally, in line with the theoretical developments given in Chapter 7, the case of wave propagation through a Coulomb slip joint is considered in the following. Once again the interest is to compare the results obtained with the UDEC code and those derived with the SMM.

Two homogeneous, isotropic, semi-infinite elastic regions separated by a planar discontinuity with given shear strength have been considered. The geometry and boundary conditions of the DEM model are the same as shown in Figure 8.9. The properties of the medium are summarised in Table 8.1.

A one-cycle sinusoidal shear stress wave, with amplitude $0.1 MPa$, is applied at the bottom of the model. The direction of propagation is assumed to be normal to the bottom boundary.

Figures 8.20 and 8.21 show the recorded wave form at the points A and B (see Figure 8.9). The wave forms obtained by both the SMM and DEM with a normalized joint stiffness of 1.6 and a shear strength of 0.05 *MPa* are compared. In this case the shear stress ratio between the maximum amplitude of the incident shear stress wave and the shear strength (τ_{imax}/τ_S) is equal to 2. It is clear that the

SMM results approximate those obtained with the UDEC code. In fact, the transmitted wave in the DEM analysis, when it reaches the shear strength of the joint, does not exceed this value but it remains constant until the incident stress decreases below the shear strength. In this zone the slip develops between the two surfaces of the joint.

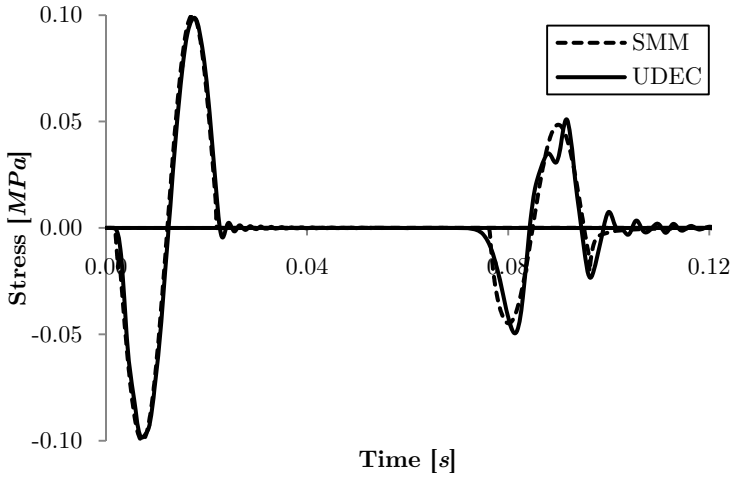

Figure 8.20 – Incident and reflected wave forms recorded at the point A (K_{ss}=1.6 and τ_{imax} /τ_S=2)

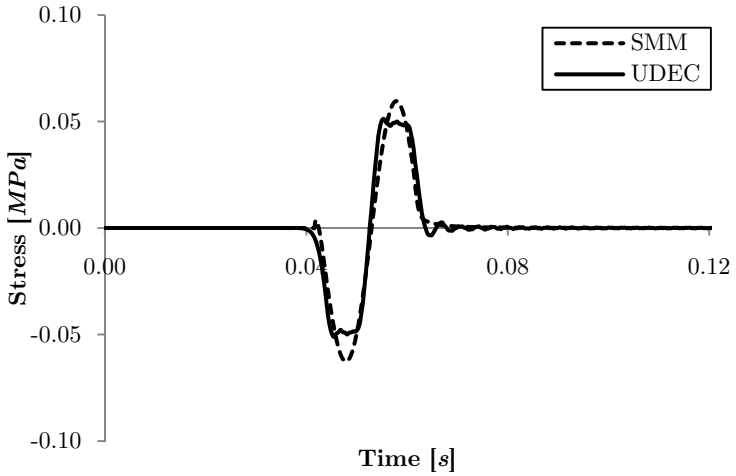

Figure 8.21 – Transmitted wave form recorded at the point B (K_{ss}=1.6 and τ_{imax}/τ_S=2)

Figures 8.22 to 8.24 illustrate the magnitude of the transmission, reflection and absorption coefficients versus the shear stress ratio for various values of K_{ss}. When the amplitude of the transmitted shear stress wave τ_{trasm} reaches the τ_S value, slip occurs. In the linear elastic zone the transmission and reflection coefficients are constant and they are located where $\tau_{trasm} < \tau_S$.

The last step of this study was the computation of the transmitted, reflected and absorbed waves from a set of N parallel joints. Figures 8.25 to 8.27 show the magnitude of the transmission, reflection and absorption coefficients versus the shear stress ratio as function of the number of the joints.

Here, we have assumed that in a set of joints only the first one reaches the joint shear strength while the others remain with linear elastic behaviour. It is clear from Figure 8.27 that most of the incident energy is absorbed from the first joint. The influence of the number of joints on the transmission and reflection coefficients decreases with the shear stress ratio increasing, i.e. when the shear strength of the joints is mobilized. In fact, the greatest influence is where the behaviour is linear elastic.

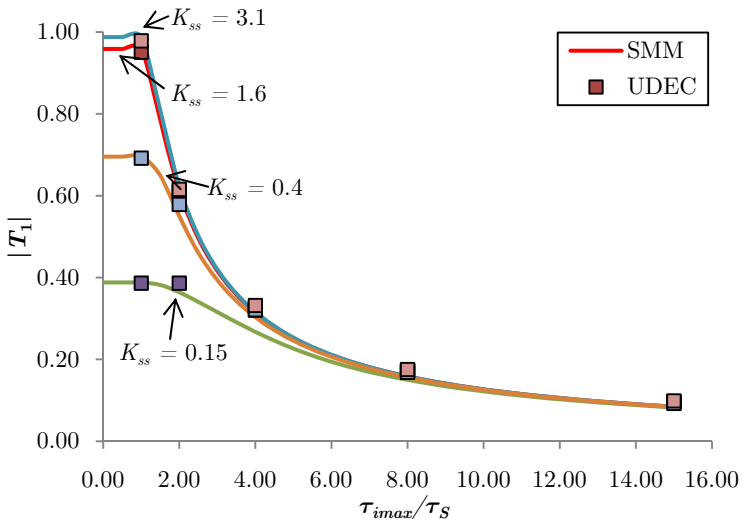

Figure 8.22 – Magnitude of the transmission coefficient versus the shear stress ratio as function of the normalized shear joint stiffness

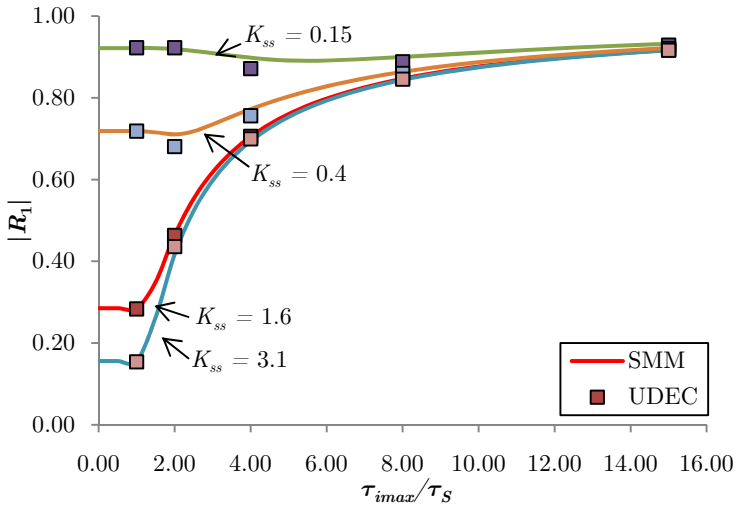

Figure 8.23 – Magnitude of the reflection coefficient versus the shear stress ratio as function of the normalized shear joint stiffness

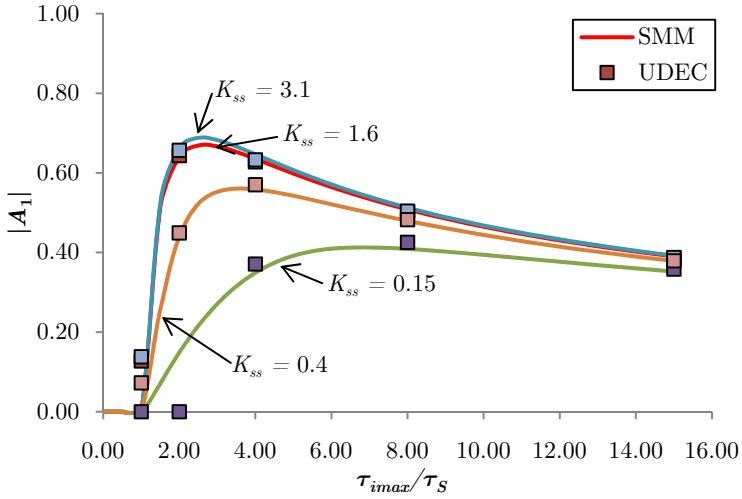

Figure 8.24 – Magnitude of the absorption coefficient versus the shear stress ratio as function of the normalized shear joint stiffness

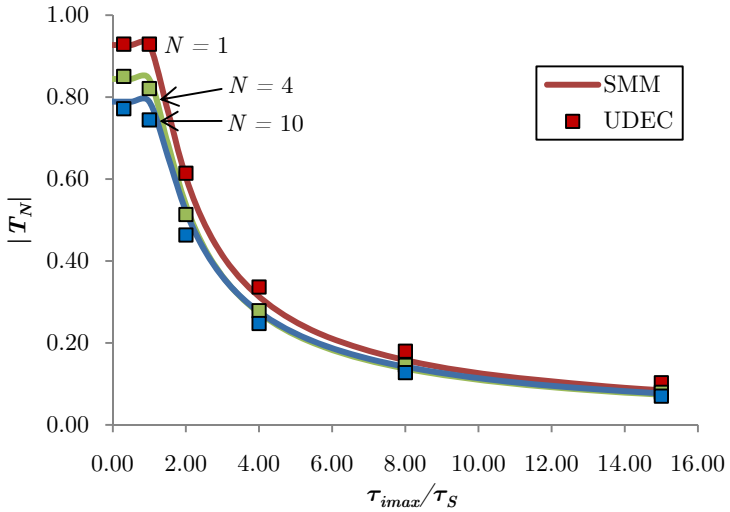

Figure 8.25 – Magnitude of the transmission coefficient versus the shear stress ratio as function of the number N of joints ($K_{ss} = 1.154$, $\zeta = 0.3$)

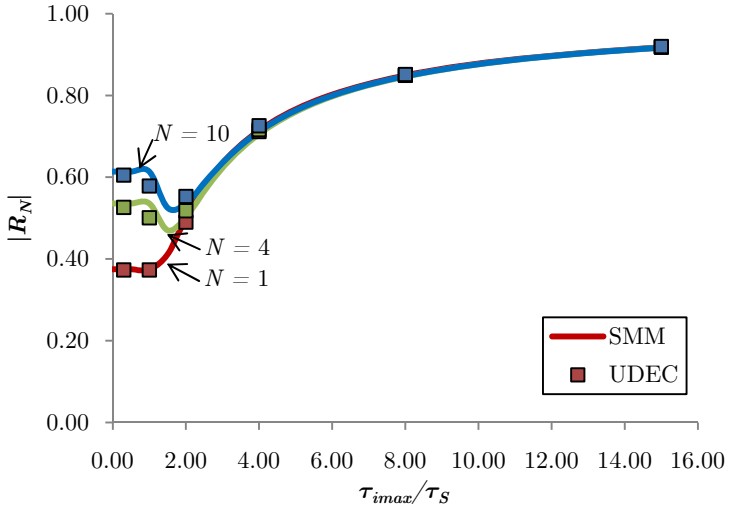

Figure 8.26 – Magnitude of the reflection coefficient versus the shear stress ratio as function of the number N of joints ($K_{ss} = 1.154$, $\zeta = 0.3$)

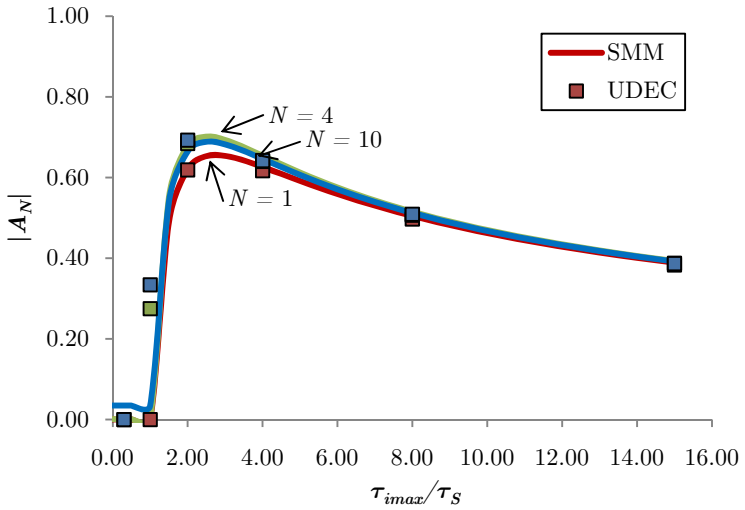

Figure 8.27 – Magnitude of the absorption coefficient versus the shear stress ratio as function of the number N of joints ($K_{ss} = 1.154$, $\zeta = 0.3$)

Figures 8.22 to 8.27 show that once again the SMM and DEM results compare very satisfactorily. Then we can state that the DEM code (UDEC or 3DEC) is a valid tool in order to study the wave propagation problems considered. Also the SMM is a good tool of analysis although it uses an equivalent linear approximation of the Coulomb slip behaviour of the joint.

8.6 Summary

The Scattering Matrix Method (SMM) as developed in this thesis has been compared with the Discrete Element Method (DEM) as implemented in the UDEC and 3DEC codes of the Itasca Consulting Group. This has been done by focussing on the evaluation of the effects of joints on wave propagation. Given that the SMM has been effectively developed to compute in a number of cases wave propagation in a medium containing discontinuities, the method has also been used to optimize the discretized numerical model as adopted in the DEM codes.

The definition of the size of the mesh for a dynamic problem is an important point to allow for correct wave propagation studies. We have therefore proven analytically that the element size of $1/8\lambda$, prescribed by Kuhlemeyer & Lysmer (1973), can be used to avoid wave attenuation across the mesh. In particular, we have used a transmission line approach and transformed the electrical quantities into mechanical ones by using the Maxwell analogy.

SMM results have been compared with DEM (UDEC and 3DEC) in the case of linear elastic and Coulomb slip joints. The analyses performed highlight that the SMM is a good tool for the study of wave propagation through discontinuous media and it can be effectively used to check the numerical models and to evaluate if the element size is adequate to allow for a correct wave propagation and if the boundary conditions are appropriate.

Chapter 9

Use of the Resonant Column Apparatus for wave propagation studies

9.1 Introduction

The SMM has been developed in Chapters 3 to 7 for the study of wave propagation in a discontinuous rock mass containing a single joint or a set of parallel joints having different types of behaviour. The DEM in either 2D or 3D conditions has been used successfully for the purpose of comparative analyses with the SMM.

The obvious interest in the research programme carried out so far has been to look for a testing equipment which could allow for the evaluation of the effects of joints on wave propagation. Such a system used for the first time in rock dynamics testing is the Resonant Column Apparatus (RCA) which allowed one to test intact and jointed rock specimens.

In this chapter, following a description of the mechanical properties of the rock specimens used for testing, the results obtained by using the RCA are discussed in terms of the shear wave velocity and material damping. Then, a 3D DEM model is described which allows one to compare the numerical results with the experimental data. Finally, the comparison is extended to the use of the SMM.

9.2 Mechanical and physical properties of the rock tested

The tests were performed on specimens of "Diamante Bateig stone". This rock is a biocalcarenite extracted in the Alicante Province (Spain) which is used as an ornamental stone in new-building construction and as a cladding for existing buildings. It is homogeneous and isotropic.

Biocalcarenites are rich in foraminifers (mainly Globigerinae) ranging in size from 0.2 to $0.5mm$. Foraminifera shells are generally filled with glauconite and/or siliceous cement. The terrigenous fraction comprises quartz, feldspars, micas, dolostone and other rock fragments. Both interparticle and intraparticle porosity vary. The most abundant type of cement present is equant-equicrystalline mosaics of calcite spar.

Uniaxial compression tests (Figure 9.1a) and ultrasonic tests (Figure 9.1b) were performed on 5 intact rock specimens to obtain the static and dynamic mechanical

properties of the rock investigated. Uniaxial compression tests performed under radial strain controlled conditions allowed one to the Young's modulus and the Poisson's ratio. Ultrasonic tests were performed with the ultrasonic pulse technique method to obtain the P-wave velocity. The physical and mechanical properties obtained with these laboratory tests are summarized in Table 9.1 and 9.2.

Table 9.1 – Physical properties of the Diamante Bateig stone

Physical properties	
Porosity 7-0.005ium (%)	17.79
Porosity 200-7ium (%)	0.41
Mineral	cal,c
$CaCO_3$ (%)	>87
$MgCO_3$ (%)	>1
A. absorption (%)	5.8
Density (kg/m^3)	2169

Table 9.2 – Mechanical properties of the Diamante Bateig stone

Mechanical properties	
Uniaxial compressive strength (MPa)	42.1
Tangent Young's modulus (MPa)	15316
Average Young's modulus (MPa)	15615
Secant Young's modulus (MPa)	18302
Poisson's ratio	0.244
P-wave velocity (m/s)	3416.8

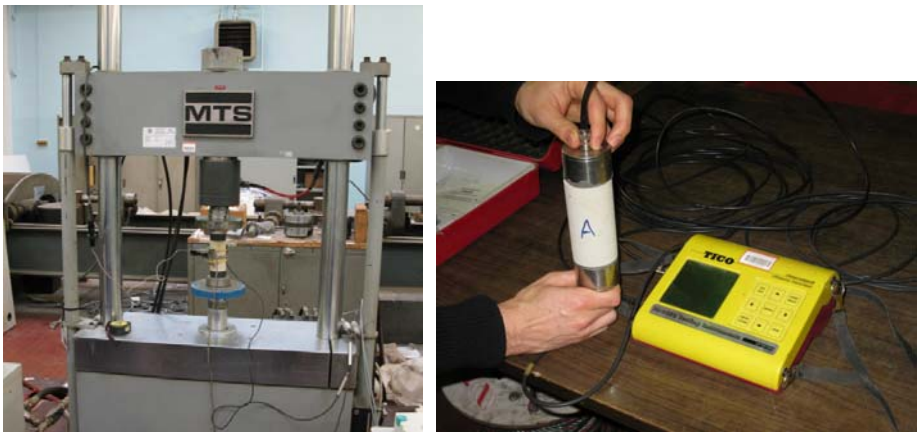

(a) (b)

Figure 9.1 – Laboratory apparatus for (a) uniaxial compression and (b) ultrasonic tests

9.2.1 Rock specimens used for RCA tests

Intact and jointed rock specimens were prepared to perform the resonant column tests as follows:

- A: intact cylindrical specimens with height $100mm$ and diameter $50mm$ (Figure 9.2);
- B: cylindrical specimens with smooth fractures;
- C: cylindrical specimens with tooth fractures.

The B specimens were prepared with one, two and three parallel smooth fractures, named B1, B2 and B3 respectively, as shown in Figure 9.3. The C specimens (Figure 9.4) were prepared with one (C1) and two (C2) tooth fractures with the following geometrical characteristics (Figure 9.5):

- Height of teeth: $1.5mm$;
- Spacing between teeth: $6mm$;
- Width of teeth: $5mm$;
- Contact width of the tooth: $1mm$.

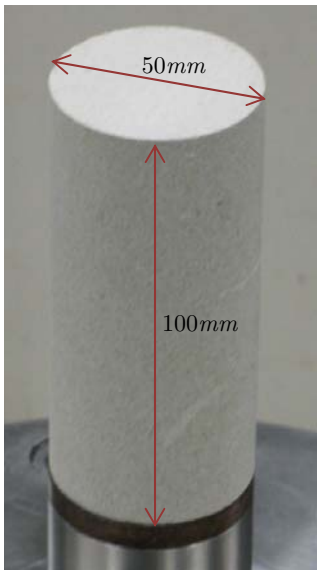

Figure 9.2 – Intact specimen A

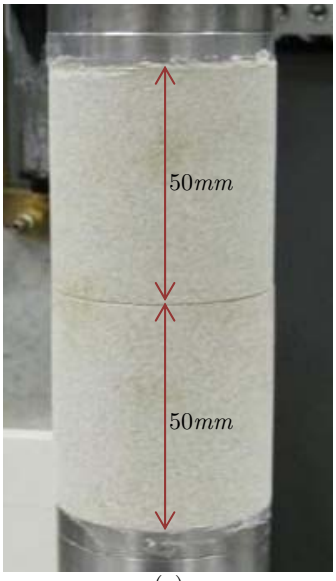

(a)

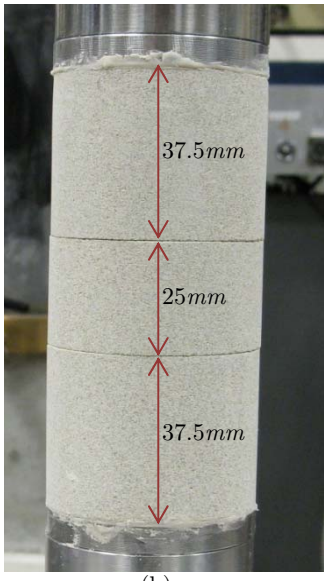

(b)

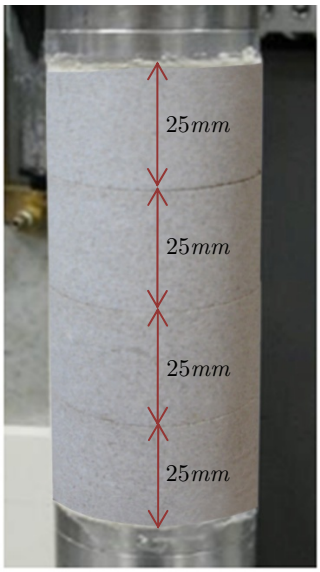

(c)

Figure 9.3 – Specimens with smooth fractures (B): (a) specimen B1, (b) specimen B2 and (c) specimen B3

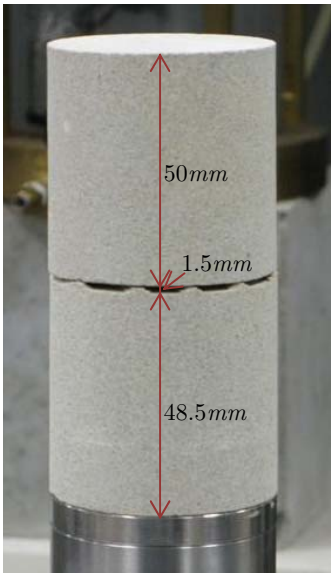

(a)

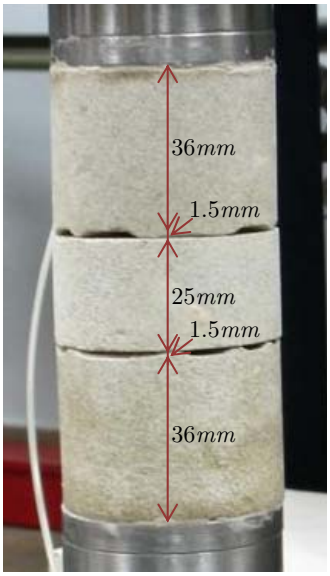

(b)

Figure 9.4 – Specimens with tooth fractures (C): (a) specimen C1 and (b) specimen C2

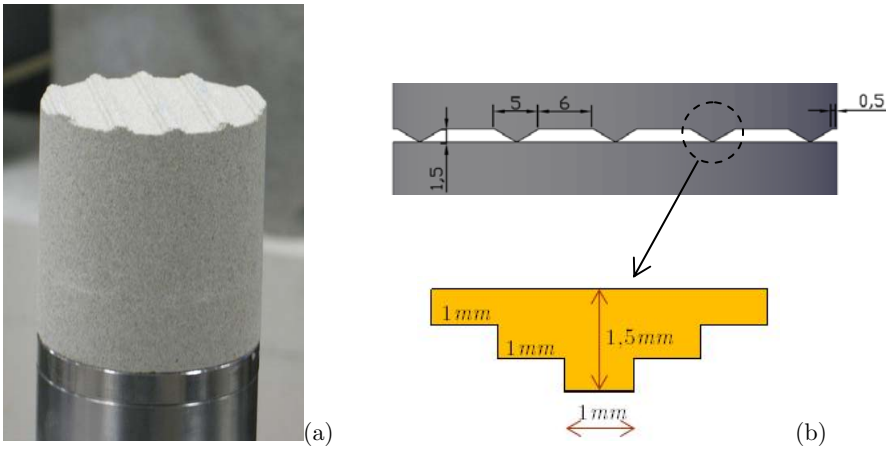

(a) (b)

Figure 9.5 – Detail of the tooth fracture: (a) photo of the fracture and (b) geometric dimensions

9.3 The Resonant Column Apparatus (RCA)

The Resonant Column Apparatus (RCA) used is that available at the DIPLAB (DIsaster Planning LABoratory) of the Structural and Geotechnical Engineering Department of the Politecnico di Torino.

As well known, a resonant column test is used to measure the dynamic properties of soils. The basic principle of the resonant column test is to vibrate a cylindrical soil specimen in a fundamental mode of vibration, usually in torsion. Once the fundamental mode is established, measurements of resonant frequency and amplitude of vibration are made.

Shearing strain amplitude during vibration is determined using measurements of acceleration and frequency of vibration. Velocities of wave propagation and elastic moduli are calculated using the measurements of resonant frequency, specimen size and drive-system mass using relationships derived from the theory of elasticity. Viscous damping is measured from the decay of free vibrations.

The resonant column apparatus (Figure 9.6) used is of the type fixed-free with the specimen fixed at the base and free at the top. The excitation system is composed by a structure with magnets and coils (Figure 9.7). These magnets interact with the coils when the coils are crossed from current and transfer to the specimen a cyclic torsion of equal frequency to that of the arrival signal. The response of the system is measured by an accelerometer that is placed over the head of the specimen in the drive-system.

The resonant column apparatus was modified suitably to perform tests on intact and fractured rock specimens. The first problem to solve was the connection

between the ends of the specimen and the apparatus. To this end the two porous stones were substituted with two disks of stainless steel which were used to allow pasting the ends of the specimen (Figure 9.8). In this way we have realized a glued connection between the bottom of the specimen and the base of the apparatus and between the head of the specimen and the top cap. This procedure was to ensure that the ends of the specimen do not slip on the "porous stones" during testing.

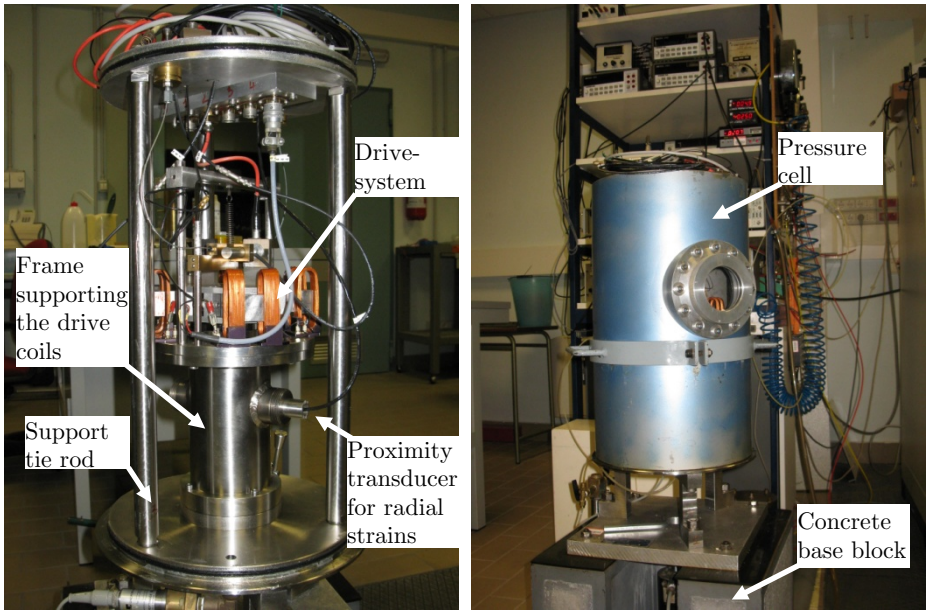

(a) (b)

Figure 9.6 – Views of the resonant column apparatus

With the membrane placed around the specimen (Figure 9.9), three o-rings were positioned to fix the membrane to the apparatus. In the tests performed with specimens C1 and C2, the fractures were filled with water to ensure that the membrane does not enter into the fractures. The next step is the mounting of the components of the resonant column apparatus and the connection with the acquisition data system.

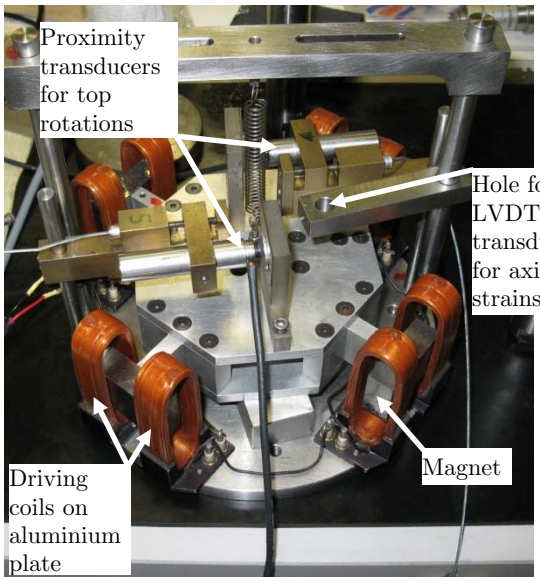

Figure 9.7 – Particular of the drive-system

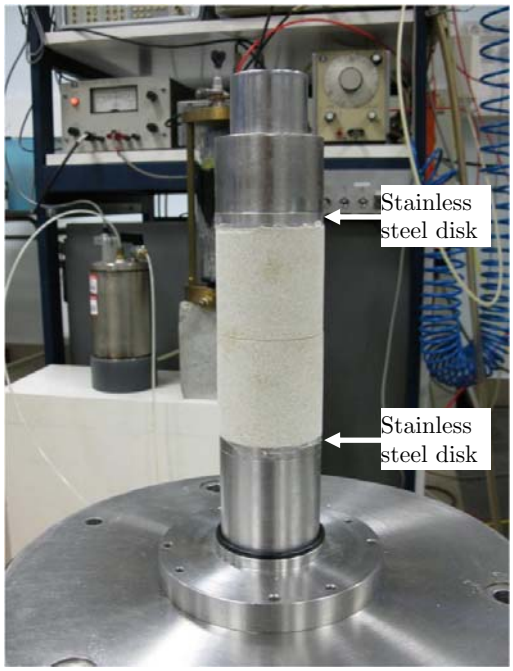

Figure 9.8 – Detail of the specimen with the ends pasted to the test apparatus

Figure 9.9 – Specimen preparation before the test

9.4 Dynamic properties of the biocalcarenite with RCA

In the RCA tests, a sinusoidal torque was applied at the head of the specimen. The amplitude was kept constant while the frequency was changed to find the resonant frequency of the system. The electrical signal applied and the correspondent torsional moment generated are shown in Figure 9.10. The input motion is composed by a cycle of rest, 20 load cycles and 20 free vibration cycles. The first step was the definition of the shear modulus at small strains of the biocalcarenite.

The measured transfer function obtained with the resonant column test for the intact specimen A is shown in Figure 9.11. The measured spectra have some irregularities probably due to small lacks in the connection of the specimen to the RCA. A fitting curve was drawn to define more accurately the frequency of resonance f_n. We can see that the resonant frequency where we have the maximum amplitude of the response spectra is about $374 Hz$ for the intact specimen. The RCA tests were repeated four times to check the repetitiveness of the experimental results.

By using the classical interpretation procedure of the RCA, we can compute the shear modulus and the shear wave propagation velocity of the biocalcarenite rock:

- $G = 3489.00\ MPa$ ($\gamma = 1.56 \cdot 10^{-6}$)

- $V_S = 1268.24\ m/s$

Then, the material damping ratio D was calculated by using the half-power bandwidth method and the amplitude decay method.

The half-power bandwidth method requires one to compute the frequencies f_1 and f_2 for which the amplitude of the response spectra (see Figure 9.11) is $1/\sqrt{2}$ times the amplitude at the resonance frequency f_n. In this case the material damping ratio is 2.941% that it is computed with $f_1 = 362.5Hz$ and $f_2 = 384.5Hz$.

On the other hand, the amplitude decay method allows one to compute the damping ratio from the attenuation of free vibrations. Figure 9.12a shows the recorded free vibration decay response curve and the diagram used to compute the logarithmic decrement δ. δ is equal to the slope of the line of best fit through the data points (Figure 9.12b). The material damping ratio obtained from the decrement $\delta = 0.1561$ is 2.484%. The damping ratio derived with the two methods is quite similar and it is typical for this type of rock.

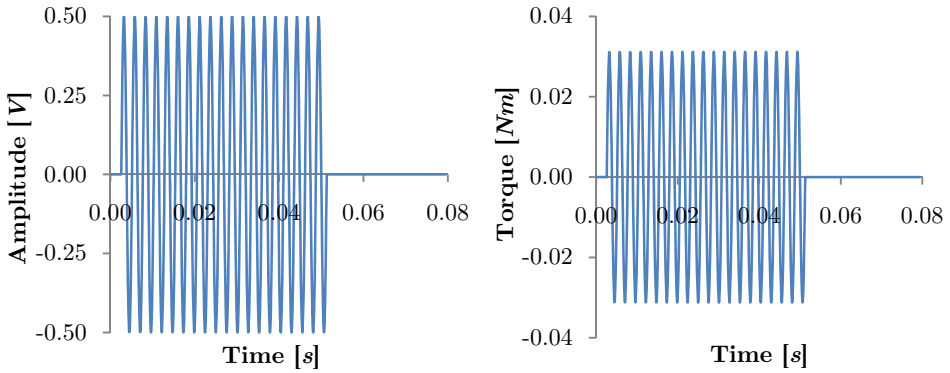

(a) (b)

Figure 9.10 – Torsional wave applied to the head of the specimen: (a) electrical signal in volt and (b) torque in Nm

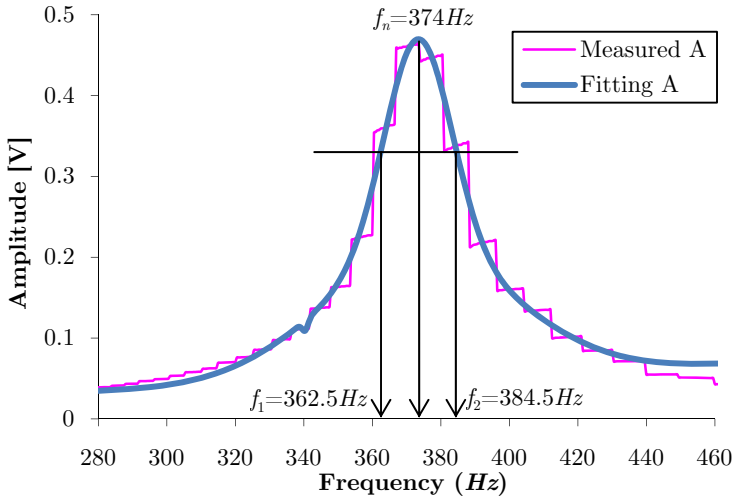

Figure 9.11 – Measured transfer function for intact specimen A

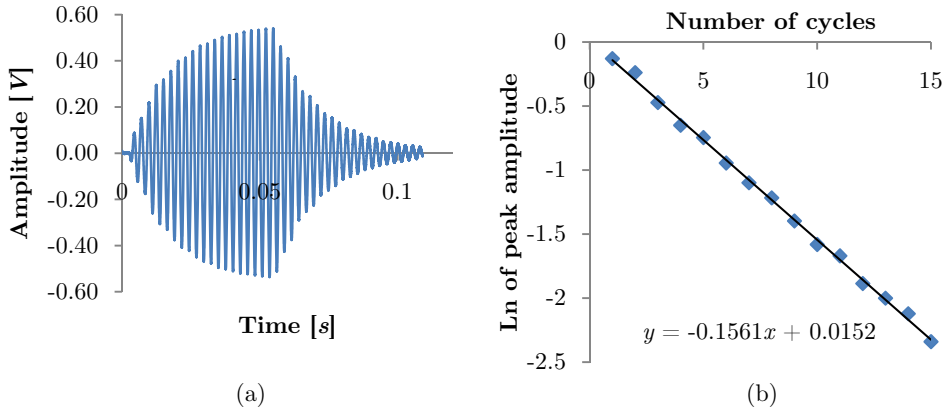

(a) (b)

Figure 9.12 – Computation of the logarithmic decrement: (a) free vibration decay response curve; (b) the slope of the least-squares regression line fitted to the data provide the logarithmic decrement δ

9.5 DEM modelling of the resonant column apparatus

To interpret the results of the RC tests a DEM model was created. This model was generated with the 3DEC code in 3D conditions, with the purpose to reproduce quite closely the resonant column apparatus. The numerical simulations were

performed so as to apply as closely as possible the same procedure used in the laboratory tests.

The numerical model is composed by joined deformable blocks. The head of the specimen was joined with the drive-system while the bottom was fixed in all directions. The excitation was generated by forces applied at each node of the blocks that compose the magnets. Forces were computed by dividing the torque applied in the laboratory tests (Figure 9.10b) for the distance between the point of force application and the axis of rotation. The geometry of the tooth fracture in the specimens C1 and C2 has been faithfully reproduced as shown in Figure 9.14.

A Rayleigh material damping was assumed and it was defined from the damping ratio obtained in the RCA tests.

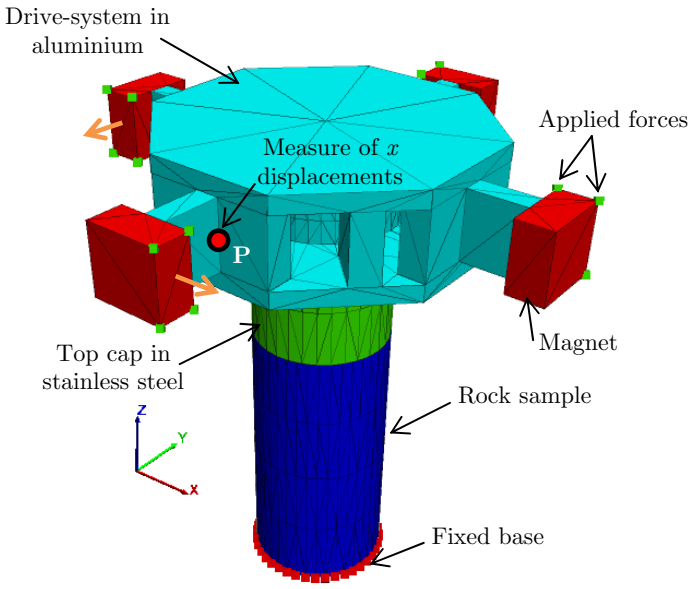

Figure 9.13 – 3DEC model of the resonant column apparatus

The fractures in the DEM model were given a linear elastic behaviour. Normal and shear joint stiffness were suitably computed. The shear stiffness of the joints was determined firstly by considering the deformational response of a crack in an elastic solid (Brady at al., 1985). This was done by assuming the RCA as a single-degree-of-freedom (SDOF) system. In this preliminary computation, we have considered the shear stiffness and not the torsional one because in 3DEC the joint is modelled with the shear stiffness.

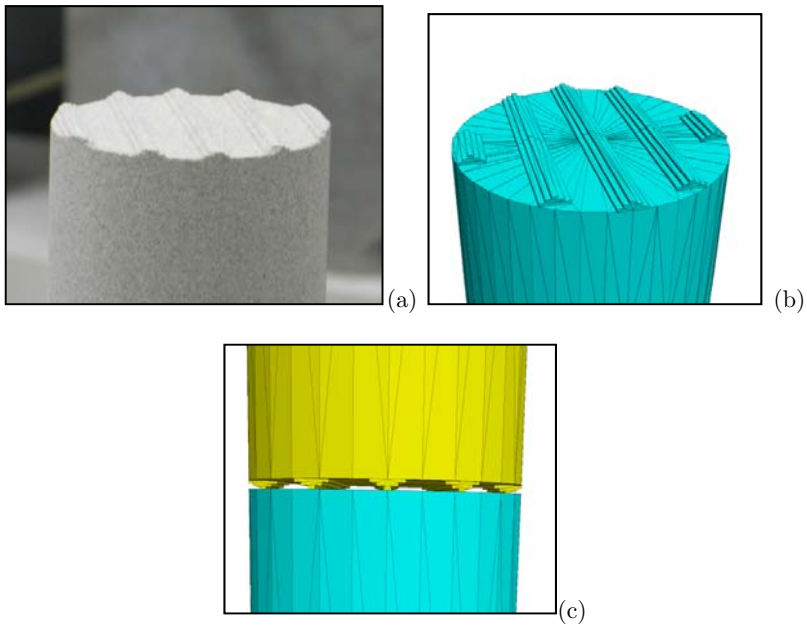

Figure 9.14 – Details of the fracture modelling: (a) real specimen, (b), (c) DEM model

The stiffness of the intact sample (k_A) can be computed from the resonant frequency of the intact specimen (A), obtained from the laboratory tests, as follows:

$$k_A = \left(2\pi f_n\right)^2 m \tag{9.1}$$

where m is the mass of the drive-system and f_n is the measured resonant frequency of the intact specimen = 374 *Hz*.

The shear joint stiffness k_{ss} of the specimen B1 was estimated as:

$$\frac{1}{k_{B1}} = \frac{1}{k_A} - \frac{1}{k_{ss}S_c} = \frac{h}{GS} - \frac{1}{k_{ss}S_c} \rightarrow k_{ss} \tag{9.2}$$

where:
k_{B1} was computed assuming the ensemble specimen B1 + drive-system as a SDOF system, substituting k_A with k_{B1} in Equation (9.1) and using the resonant frequency measured for the specimen B1;
S is the cross-section area of the cylindrical specimen while S_c is the contact area of the joint.

With Equation (9.2) we have obtained a first attempt value of k_{ss} for all the fractures of the specimens tested. To evaluate the correct value of k_{ss}, gravity was applied to the resonant column model in the horizontal direction to compute the natural frequency of the system. This frequency must be more or less equal to the resonant frequency computed experimentally.

The values of natural frequency of oscillation of the model were calculated by recording the horizontal displacements at the top of the numerical model versus the dynamic time. The recorded time history at the top of the model for the intact specimen A is shown in Figure 9.15. We can see that the period of oscillation is 2.69E-3s and the natural frequency of the model is 372Hz. In this analysis the material damping is assumed to be zero.

In this way we have computed the correct values of the shear stiffness by performing for all the specimens the analysis previously described for the specimen A. The values of the joint shear stiffness are $k_{ss} = 6N/mm^3$ for smooth fractures and $k_{ss} = 1500N/mm^3$ for tooth fractures. As will be shown in the paragraph below, these values of joint stiffness allow one to obtain satisfactory results if compared with those measured in laboratory tests.

In the DEM model, the response of the system is measured in terms of the displacements at the point P indicated in Figure 9.13. The measured response of the system was compared with that obtained with the DEM analysis. This comparison was possible with the unit conversion of the accelerometer recorded amplitudes. This conversion can be performed through the computation of the rotation of the head of the specimen:

$$\vartheta = \frac{\Delta a}{r_a} = \frac{\sqrt{2} \cdot a\left[mv - rms\right] \cdot g}{\left(2\pi f\right)^2 \cdot ACF \cdot r_a} \tag{9.3}$$

where:
Δa is the displacement of the accelerometer;
a is the rms acceleration amplitude obtained from the acceleration measurements of the accelerometer;
ACF is the calibration factor of the accelerometer = 2500 *pk-mv/pk-g*;
r_a is the radial distance between the axis of rotation and the point in which is located the accelerometer in the laboratory apparatus (= 50mm).

Finally, the displacements measured in the laboratory tests were computed as follows:

$$\Delta x = r \cdot \vartheta^{rad} \tag{9.4}$$

where $r = 55mm$ is the distance between the axis of rotation and the point P (Figure 9.13).

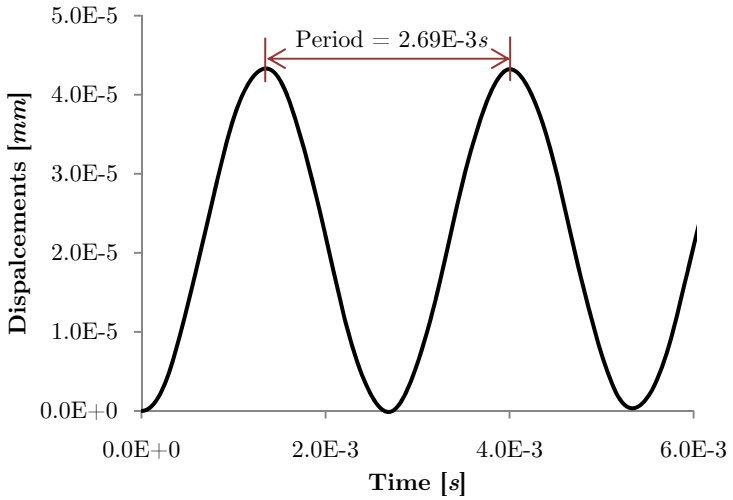

Figure 9.15 – Plot of horizontal displacements versus time recorded at the top of the 3DEC model for the intact specimen A

9.6 Comparison of experimental results with DEM modelling

The results obtained with the RCA tests and DEM can now be summarized and compared. Figure 9.16 shows the measured transfer function for the intact and fractured specimens (smooth joint type). The amplitudes of the measured spectra were transformed in displacements to compare them with the DEM modelling results.

We can note in Figure 9.16 that the resonant frequency decreases with the number of fractures increasing. This reduction of the resonant frequency is probably due to the reduction of the stiffness of the specimen. In fact, the resonant frequency of a specimen in the resonant column device subjected to torsional excitation can be also computed analytically (SDOF system) as follows:

$$f_n = \frac{1}{2\pi}\sqrt{\frac{k_i}{I_T}} \tag{9.5}$$

where:
k_i is the torsional stiffness of the specimen i;
I_T is the mass polar moment of inertia of the top cap and the drive-system ($39.25 g{\cdot}cm{\cdot}s^2$).

As an example the stiffness of the specimen A is:

$$k_A = \frac{GJ}{h} = \frac{G\left(\pi\phi^4/32\right)}{h} = 222.46Nm \tag{9.6}$$

and with the Equation (9.5) we can obtain a resonant frequency $f_n = 375.28Hz$ (the resonant frequency measured experimentally was $374Hz$). J is the area polar moment of inertia of the cross-section of the specimen, ϕ is the diameter and h is its height. In this case, we have assimilated the resonant column as a SDOF system and the results prove that this assumption is quite accurate.

The quantity that changes in the Equation (9.5) if we generate a fracture in the specimen is the stiffness. Instead, the inertia of the system remains essentially constant.

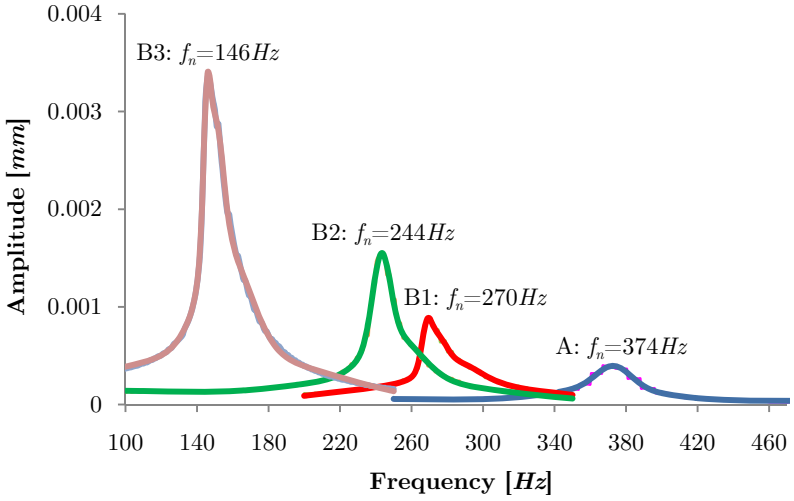

Figure 9.16 – Measured transfer functions for intact and fractured specimens

Moreover, the amplitude of the response increases with increasing the number of fractures. Probably, the amplitude recorded at the head of the specimen increases because increasing the number of fractures also increases the rotations of the head of the specimen.

For each specimen the resonant frequencies and the shear wave propagation velocities are summarized in Table 9.3. We have used for the fractured specimens the classical procedure to compute the shear wave velocity in the RCA tests. The results obtained for the specimens with tooth fractures (C1-C2) are shown in Table 9.3. As discussed below, the specimen C2 with two parallel tooth fractures does not give correct results. The RC tests were repeated three-four times for each specimen.

Table 9.3 – Shear wave velocities from RCA tests

Specimen	Resonant frequency f_n $[Hz]$	Shear wave velocity V_S $[m/s]$
A	374	1268.24
B1	270	913.15
B2	244	825.22
B3	146	490.06
C1	194	656.12
C2	388	-

The comparison between the measured transfer function and that obtained numerically with 3DEC is shown in Figure 9.17 to 9.21. The DEM results reproduce quite well the experimental results. Small differences in the resonant frequency values can be found. The amplitudes obtained numerically are smaller than those measured.

The experimental results, obtained with all the specimens, were found to be repeatable. Difficulties were found during testing of specimen C2. These difficulties are due essentially to the irregularities of the contact between the surfaces of the fractures because they produce small movements that affect the results. Moreover, the measured resonant frequency for specimen C2 is greater than the resonant frequency of the intact specimen. This is not possible and can be motivated from the fact that the specimen is not completely subjected to torque because the fractures very likely do not allow the transmission of the motion to all parts of the specimen. In fact, the upper parts of the sample C2 (Figure 9.4b) can be rotated on the part fixed on the base of the resonant column apparatus and do not transmit the torsional wave. This generates an increase of the resonant frequency and then of the stiffness of the system. This increase is only possible if the height of the equivalent SDOF system decreases and this proves that probably the fixed part of the specimen on the base of the resonant column is not mobilized.

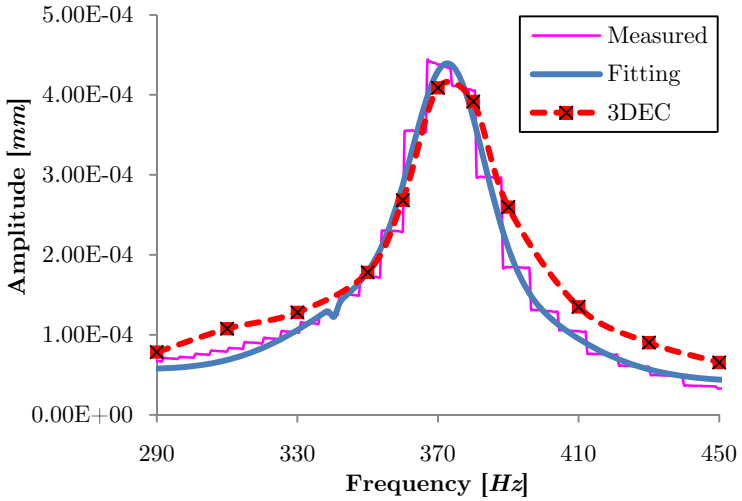

Figure 9.17 – Measured and numerical transfer function for intact specimen A

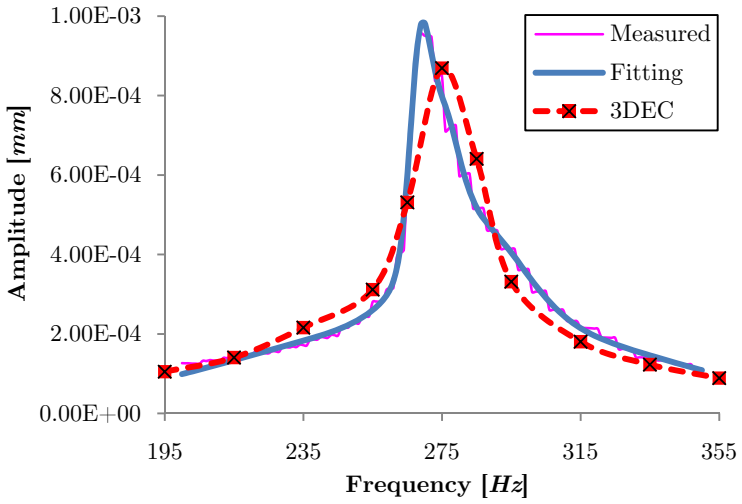

Figure 9.18 – Measured and numerical transfer function for fractured specimen B1

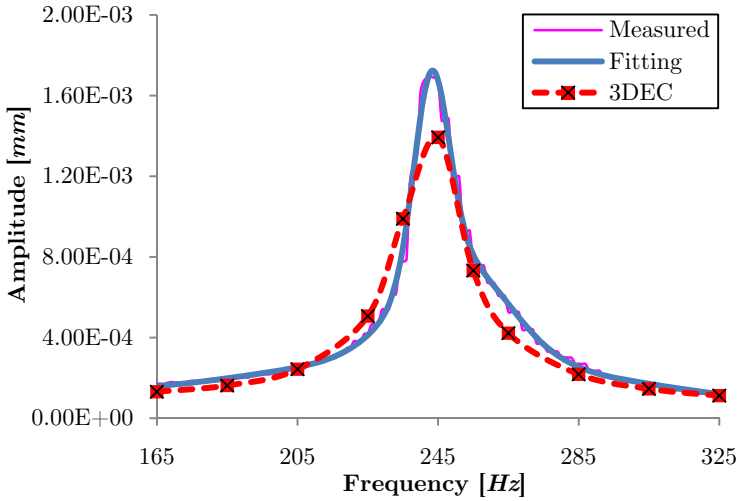

Figure 9.19 – Measured and numerical transfer function for fractured specimen B2

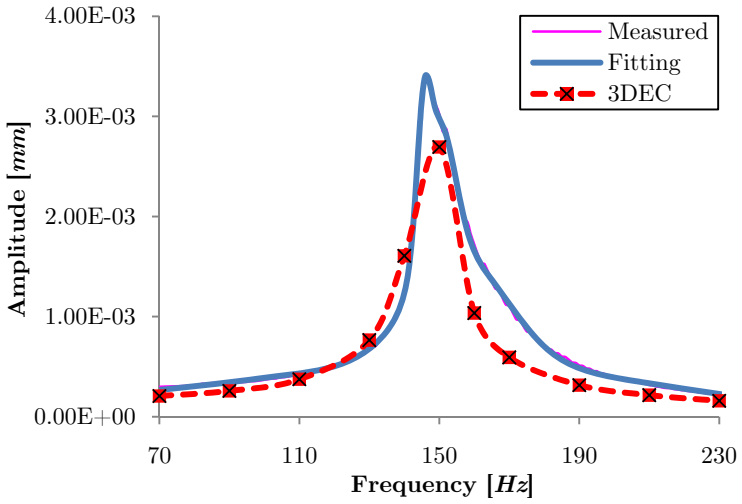

Figure 9.20 – Measured and numerical transfer function for fractured specimen B3

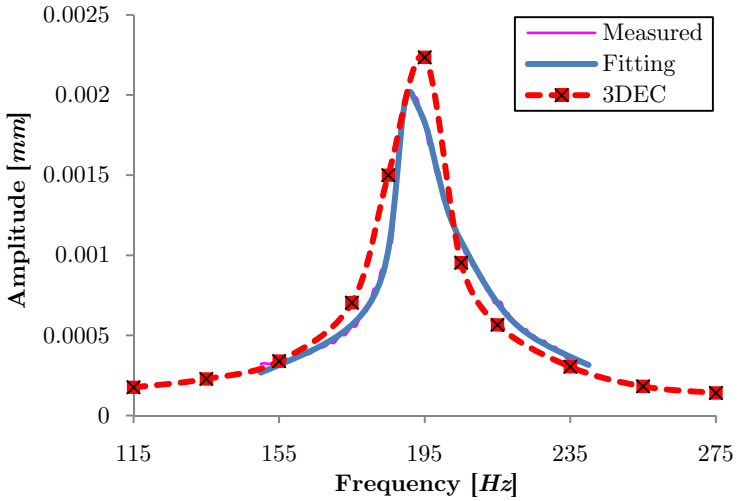

Figure 9.21 – Measured and numerical transfer function for fractured specimen C1

Therefore, with the DEM analyses, we have proven that in the specimens all parts of the specimen are mobilized with the exception of the specimen C2. As an example, the distribution of the horizontal displacements in the specimen B2 (specimen with two parallel smooth fractures, Figure 9.3b), evaluated at an instant of time during the RCA analysis, is shown in Figure 9.22. We can see clearly the discontinuity of displacements along the fractures in the same as we have assumed with the analytical methods (typically with the SMM). Figure 9.22 only shows the specimen while the drive-system and the top cap have been hidden.

Then, we have compared the decay of the response, recorded at the top of the specimen, obtained experimentally and numerically. This comparison is shown in Figure 9.23 where we can see that the DEM results reproduce very well the experimental ones and the decay of the response curve is essentially the same. This can be also noted in Figures 9.17 to 9.21, where the width of the spectra, at $1/\sqrt{2}$ of the maximum amplitude, obtained experimentally is quite similar to that obtained with DEM analyses.

To evaluate the attenuation of energy due to the fractures we have computed the damping ratio for both the fractured specimens and the intact one. Hence, the damping ratio computed for specimens with smooth fractures is 3.96% for B1, 4.03% for B2 and 3.62% for B3. On the other hand, the damping ratio for the specimen C2 is about 2.76%. By comparing the damping ratio of the intact specimen A (2.48%) we have found the part of energy attenuation due to fractures. However, it is not easy to evaluate, from these experimental results, the influence of a single fracture on the attenuation of energy but it is quite evident that the

damping ratio increases from intact specimen to fractured ones. Hence we can state that probably the greatest part of energy attenuation due to the fractures is produced by the first fracture (see frictional joints in chapter 8 paragraph 5).

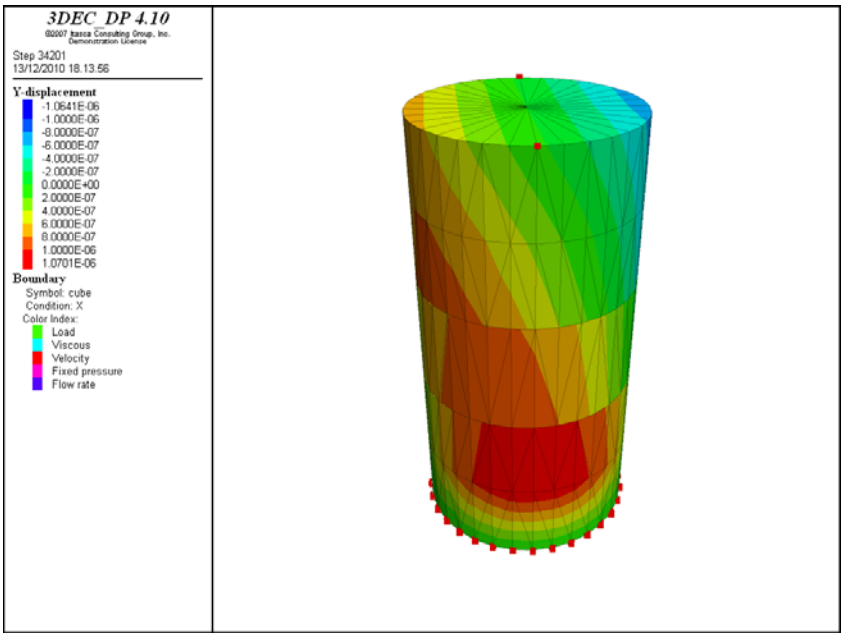

Figure 9.22 – Discontinuity of horizontal displacements in the specimen B2 evaluated in an instant of time of DEM resonant column analysis

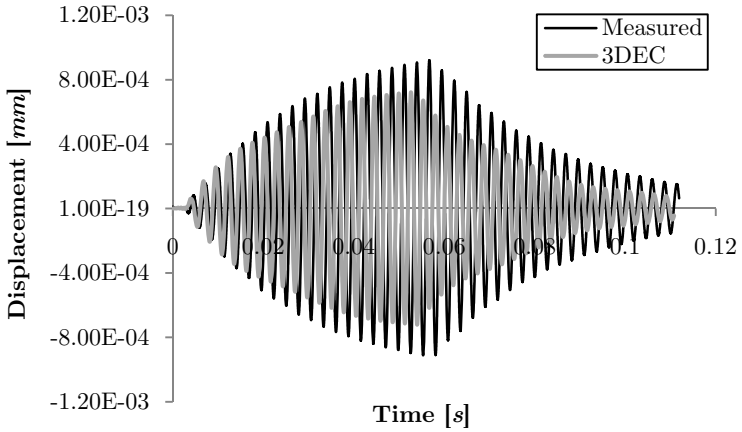

Figure 9.23 – Measured and DEM responses at the resonant frequency for the specimen A

9.7 Correction of the results

The RCA is generally suitable for soils. The use of this apparatus to test stiff materials such as rocks can be generate errors.

Xiaoming et al. (2006) showed that in the resonant column tests the shear modulus on stiff specimens can be underestimated. In fact, they found that when the specimen stiffness is compatible with that of the testing system, the tested resonant frequency of the stiff specimen is lowered and the Equation (9.7), normally used in the interpretation of the resonant column tests, underestimates the shear modulus:

$$G = \rho \cdot \left(\frac{2\pi \cdot f_n \cdot h}{\beta} \right)^2 \tag{9.7}$$

where β is a parameter that satisfy Equation (9.8):

$$\frac{I_S}{I_T} = \left(\frac{\omega_n h}{V_S} \right) \cdot \tan\left(\frac{\omega_n h}{V_S} \right) = \beta \cdot \tan \beta \tag{9.8}$$

where I_S is the mass polar moment of inertia of the specimen.

Therefore, Xiaoming et al. (2006) modified the Equation (9.7) as follows:

$$G = \rho \cdot \left(\frac{2\pi \cdot f_n \cdot h}{\beta} \right)^2 \cdot Q \tag{9.9}$$

where Q is the correction factor of the shear modulus of the stiff material.

Xiaoming et al. (2006) evaluated the correction factor by testing six cylindrical steel specimens with the same height but different diameter. These computations are dependent from the factor β that is function of the inertia of the drive-system of the resonant column apparatus used. For this reason, the correction factor, obtained by Xiaoming et al. (2006) versus the resonant frequency, cannot be applied in our tests.

In our case the correction factor was computed by performing numerical DEM analyses with the model of the resonant column apparatus on 8 aluminium cylindrical hollow specimens. The geometrical characteristics of the specimens are shown in Table 9.4. The mechanical properties of the aluminium material are given in Table 9.5. The calibration of these numerical analyses was done by comparing

the results with those obtained experimentally with the aluminium specimen P1 shown in Figure 9.24. The DEM model implemented to compare the experimental results is illustrated in Figure 9.25. The measured transfer functions are reported in Figure 9.26.

The numerical DEM analysis performed on the specimen P1 has allowed to obtain a resonant frequency very near to the $34Hz$ deduced experimentally.

Table 9.4 – Geometrical properties of the aluminium cylindrical hollow specimens

Specimen	Height $[mm]$	External diameter $[mm]$	Internal diameter $[mm]$
P1	165	12.2	10.5
P2	165	20.0	10.5
P3	165	25.0	10.5
P4	165	30.0	10.5
P5	165	33.5	10.5
P6	165	40.0	10.5
P7	165	45.0	10.5
P8	165	50.0	10.5

Table 9.5 – Mechanical properties of the aluminium material

Mass density	2727.0 kg/m^3
Young modulus	74.2 GPa
Poisson ratio	0.33
Shear modulus	27.9 GPa

Following this initial calibration, the DEM analyses were continued by computing the resonant frequency of the other seven specimens. Table 9.6 summarizes the shear moduli and the correction factors obtained for each specimen from the numerical simulation. The correction factors were computed by the ratio between the correct shear modulus of the aluminium (Table 9.5) and the shear moduli obtained from RCA tests (Table 9.6).

The numerical DEM models were fixed at the base and the maximum size of the element edge of the mesh was assumed $17mm$. The procedure used for simulation of the numerical resonant column test is the same as described above.

The inertia of the drive-system I_T is computed by considering that the top cap in stainless steel used in the test on rock specimens is substituted with another one in aluminium as shown in Figure 9.24.

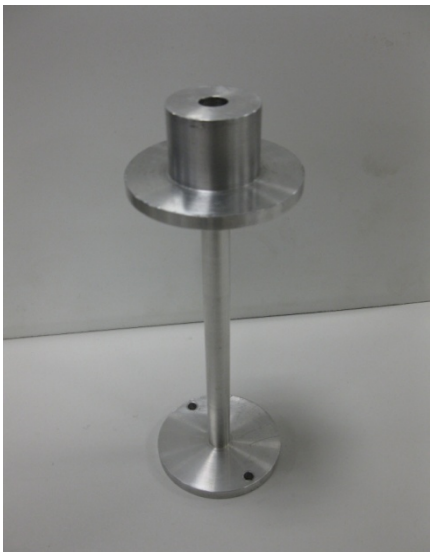

Figure 9.24 – Aluminium specimen P1

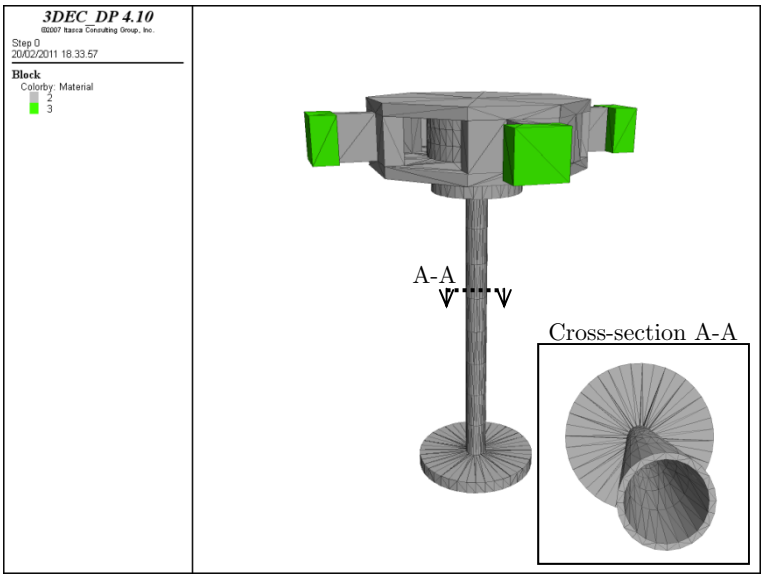

Figure 9.25 – 3DEC model of the resonant column with the aluminium specimen P1

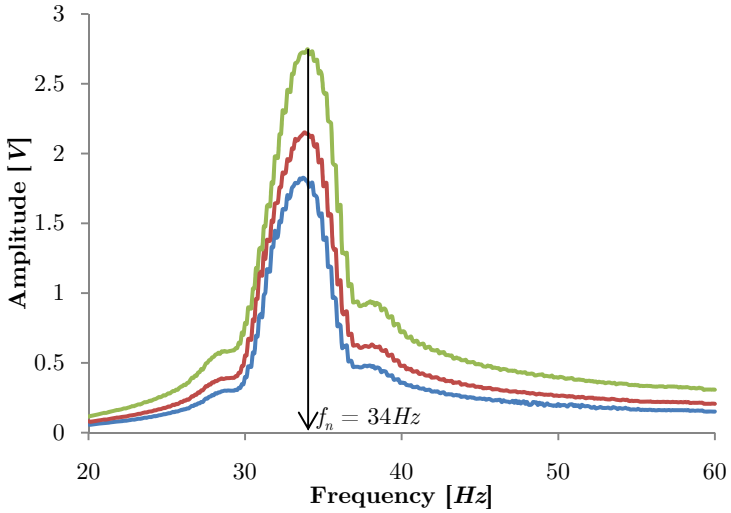

Figure 9.26 – Measured transfer functions of the aluminium specimen P1

Table 9.6 – Shear moduli and correction factors of the aluminium specimens obtained numerically by DEM analyses

Specimen	Inertia sample I_S $[g{\cdot}cm{\cdot}s^2]$	Inertia RCA I_T $[g{\cdot}cm{\cdot}s^2]$	β [-]	Resonant frequency f_n $[Hz]$	Shear modulus G $[MPa]$	Correction factor Q [-]
P1	0.005	37.737	0.0110	34.75	29439.33	0.95
P2	0.067	37.737	0.0420	127.01	26824.87	1.04
P3	0.170	37.737	0.0672	192.10	23990.32	1.16
P4	0.359	37.737	0.0974	253.09	19781.23	1.41
P5	0.562	37.737	0.1217	307.35	18696.06	1.78
P6	1.148	37.737	0.1735	369.30	13281.70	2.10
P7	1.842	37.737	0.2191	449.55	12339.74	2.26
P8	2.810	37.737	0.2695	514.98	10703.60	2.61

The correction factor Q versus the resonant frequency is plotted in Figure 9.27.

We can state that when the stiffness of the specimen increases the error in computation of the shear modulus increases and then the shear modulus obtained with the resonant column test is underestimated. It is clear that for frequencies less than about $120Hz$ the correction factor is essentially equal to 1. This proves that

for soil specimens the classical procedure for computing the shear modulus is applicable with accuracy.

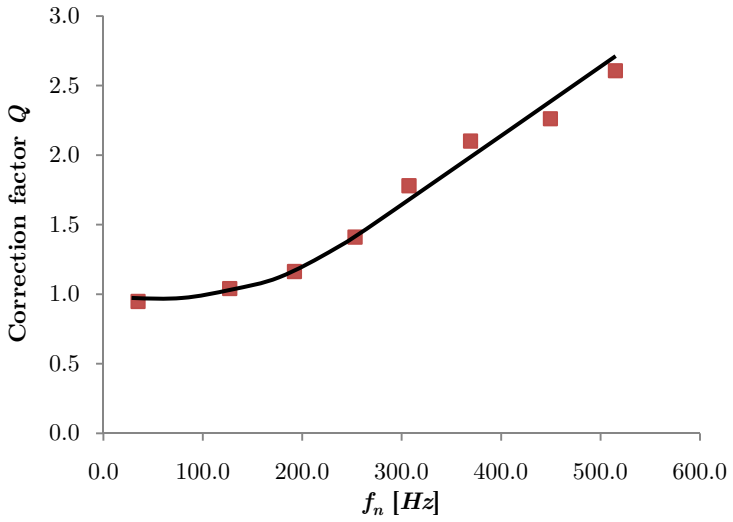

Figure 9.27 – Correction factor versus the resonant frequency

It might be noted that the trend of the plot in Figure 9.27 is similar to that proposed by Xiaoming et al. (2006) although the numerical values are not equal because the experimental apparatus used is different.

9.8 Discussion

The shear modulus and the shear wave velocity of the biocalcarenite obtained from resonant column tests have to be corrected. The resonant frequency is $374Hz$ for the intact rock specimen and then from Figure 9.27 we obtain a correction factor of about 2.1. This correction is necessary to reduce the underestimation of the shear modulus due to the high stiffness of the specimen.

Table 9.7 gives the corrected values of the shear wave velocity shown before in Table 9.3. The corrected shear wave velocity can be obtained directly by multiplying the incorrect one for $\sqrt{Q}$ as derived by Equation (9.9).

Table 9.7 – Corrected shear moduli and shear wave velocities

Specimen	Resonant frequency f_n $[Hz]$	Correction factor Q [-]	S-wave velocity $V_{S\text{-}COR}$ $[m/s]$
A	374	2.10	1837.86
B1	270	1.52	1125.81
B2	244	1.45	993.70
B3	146	1.07	506.92
C1	194	1.20	718.74

Hence, we have computed from the RCA tests a corrected shear modulus G of the biocalcarenite rock to be $7326.89MPa$ and a corrected shear wave velocity of $1837.86m/s$.

It is known that the modulus of deformation for rock is not constant but depends on the load and on the strain level. Hence, static and dynamic elastic constants were computed respectively from the results obtained from uniaxial compression tests, ultrasonic tests and resonant column tests.

The dynamic constants of the intact rock can be calculated by using the theory of elasticity as follows:

$$\nu_d = \frac{\left(V_P/V_S\right)^2 - 2}{2\left[\left(V_P/V_S\right)^2 - 1\right]} \tag{9.10}$$

$$E_d = \rho {V_P}^2 \frac{\left(1-2\nu\right)\left(1+\nu\right)}{\left(1-\nu\right)} \tag{9.11}$$

The dynamic Poisson's ratio was assumed to be equal to the static one obtained with the uniaxial compression tests. With ν_d= 0.244 and P-wave velocity deduced from ultrasonic tests, equal to $3416.8m/s$, we can use Equation (9.10) to compute the shear wave velocity of the biocalcarenite to be $1989.0m/s$. This can be assumed as the reference value of the shear wave velocity to evaluate the accuracy of the RCA results. The errors in the determination of the V_S are:

- 36.24% for V_S computed without correction factor Q;
- 7.60% for V_S computed with correction factor Q.

Hence, we can state that the correction procedure of the results of the RCA tests allow to reduce drastically the underestimation of the shear modulus and then of the shear wave velocity.

From Equation (9.11), the dynamic modulus of deformation E_d is $21340 MPa$ that is obviously greater that the static one of $15316 MPa$ (see Table 9.2).

To prove the reliability of the correction procedure we have rerun the 3DEC analyses with the corrected rock parameters (E_d= $21340 MPa$ and ν_d= 0.244). Obviously, these analyses provide resonant frequencies that are greater (of a factor $\sqrt{Q}$) than those showed previously in Figures 9.17 to 9.21 deduced from the uncorrected rock parameters. In Figures 9.28 and 9.29 are plotted the simulated transfer function obtained with 3DEC for the sample A and B1. In Table 9.8 are summarized the results obtained for all specimens. Hence, we have proven that the resonant frequencies, provided from 3DEC analyses with the corrected mechanical parameters, agree very well with the resonant frequencies estimated with the correction procedure.

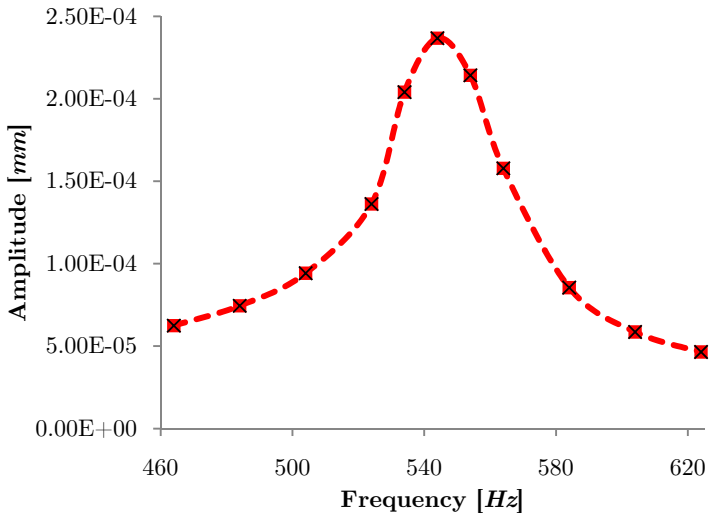

Figure 9.28 – Numerical transfer function for intact specimen A obtained with the corrected mechanical parameters of the rock

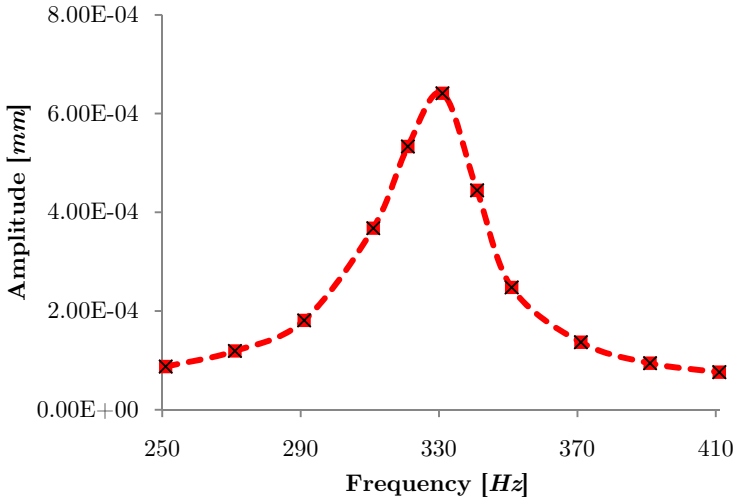

Figure 9.29 – Numerical transfer function for fractured specimen B1 obtained with the corrected mechanical parameters of the rock

Table 9.8 – Uncorrected and corrected resonant frequencies obtained from RCA laboratory tests and from 3DEC analyses

Specimen	Uncorrected resonant frequency from RCA [Hz]	Correction factor Q [-]	Corrected resonant frequency from RCA [Hz]	Corrected resonant frequency from 3DEC [Hz]
A	374	2.10	542	544
B1	270	1.52	333	331
B2	244	1.45	294	295
B3	146	1.07	151	152
C1	194	1.20	213	228

Finally, a comparison of the RCA results with the scattering matrix method will be executed.

As already described, the fractures generate an attenuation effect that increases with the increasing number of fractures (see Figure 9.16 and Table 9.7).

Moreover, each fracture generates a group time delay that causes a velocity dispersion phenomenon. The phase and the group velocities are equivalent in an elastic half-space and then we can compute the velocity dispersion from the ratio between the effective velocities and the intact group velocity (V_S). Hence, the

effective shear wave velocity for the sample B1 is smaller of 38%, for B2 of 46% and for B3 of 72% than the intact group velocity (V_S). The dispersion of the shear wave velocity can be also estimated with the analytical approach proposed by Pyrak-Nolte et al. (1987) or with the Scattering Matrix Method (Perino & Barla, 2010a). Unlike of the procedure proposed by Pyrak-Nolte et al. (1987), the SMM considers all multiple reflections in the evaluation of the time delay due to the fractures. The first step, of this approach, is the computation of the phase shift Θ_T of the transmission coefficient T_N obtained for a set of N fractures or joints.

$$\Theta_T\left(\omega,\vartheta\right) = angle(T_N) \tag{9.12}$$

where:
ω is the angular wave frequency;
ϑ is the angle of incidence of the elastic wave;

The second step is the evaluation of the group time delay due by the fractures (t_{frac}) for the transmitted wave with Equation (9.13):

$$t_{frac}\left(\omega,\vartheta\right) = \frac{d\Theta_T}{d\omega} \tag{9.13}$$

The effective shear wave velocity ($V_{S,eff}$) is obtained from the effective group travel time (t_{eff}):

$$t_{eff}\left(\omega,\vartheta\right) = \frac{l_i \;/\; \cos\vartheta}{V_g} + t_{frac}\left(\omega,\vartheta\right) \rightarrow V_{S,eff}\left(\omega,\vartheta\right) = \frac{L \;/\; \cos\vartheta}{t_{eff}} \tag{9.14}$$

where:
l_i is the travelled distance normal to the fractures before the first and after the last fracture from the ends of the specimen of length L;
V_g is the group velocity of the intact homogeneous isotropic rock ($= V_S$).

Here, $V_{S,eff}$ is computed for a rock with fractures with the assumption that no dispersion in the intact part of rock is developed.

The results computed from Equation (9.14) are obtained by assuming the joint shear stiffness used in 3DEC analyses and L equal to the height of the specimens (100mm). The frequencies are assumed equal to the resonant frequencies obtained experimentally for various types of specimens. In fact, the effective wave velocity is frequency and joint stiffness dependent. The results obtained with SMM and RCA tests are summarized in Table 9.9.

Table 9.9 – Rate of decrease of the shear wave velocity

Specimen	RCA [%]	SMM [%]
B1	38.7	41.8
B2	45.9	58.5
B3	72.4	68.0

9.9 Summary

With the resonant column tests on intact and fractured specimens described in this chapter we have attempted to understand if this apparatus is applicable on rock specimens and if one is in position to find the effects of fractures on wave propagation. The implementation of the DEM model has been also a way for understanding if the experimental results obtained are acceptable or not.

In conclusion, we can state that the RCA allows one to:

- compute, with a correction procedure, the shear modulus and the shear wave velocity for materials with stiffness comparable with that of the resonant column apparatus and then with high values of resonant frequency;
- evaluate the effects of fractures on wave propagation.

Chapter 10

Distinct Element Modelling of the Tel Beer Sheva cavern in static conditions

10.1 Introduction

This chapter is intended to study the stability of the underground water storage cavern at the archaeological site of Tel Beer Sheva, excavated in a highly jointed chalk in the Negev Desert, in Israel.

By using the distinct element method (DEM) and the UDEC and 3DEC codes, the failure of the roof of the cavern is back analysed in both two and three dimensional conditions.

Attention is given to the evidences of the archaeological researches that have shown that the roof of this cavern had collapsed during the time of construction and that a massive support pillar was erected in the centre of the cavity to support the remaining roof.

The analyses performed are intended as preliminary to the seismic analyses of the same cavern discussed in the subsequent Chapter 11. The interest stems from the fact that the same cavern with the pillar in place has remained stable through the centuries notwithstanding a number of seismic events that did take place in the area.

10.2 Location and description of the cavern

The underground water storage cavern is part of the water system of Tel Beer Sheva, an archaeological site (Iron age 1200-700 bc) located approximately $3km$ East of the modern city of Beer Sheva, near the communities of Tel Sheva and Omer, in Israel. The mound represents an urban ruling centre from the biblical period in the southern part of the country, where excavation in modern times revealed a system of walls and gates along with public and residential buildings, a storehouse and a water system.

Figure 10.1 shows the present archaeological site. Some authors suggest that a well at the gate of the city is associated with that mentioned in the Bible, in the book of Genesis. The oath sworn at the well gave the city its name: in Hebrew "sheva" means both seven and oath, "beer" means well.

Figure 10.1 – Photograph of Tel Beer Sheva archaeological site

Situated on a hilltop at an elevation of $307m$ asl, the site is in the centre of a wide valley on the northern bank of Beer Sheva streambed (south), near its confluence with the Hebron streambed (north). Tel Beer Sheva was declared a national park in 1986, covering a total area of approximately 44.5 acres. In 2005, UNESCO listed the biblical tels, including Tel Beer Sheva, as a World Heritage Site. A schematic layout of the archaeological site and the under-lying water reservoir are shown in Figure 10.2.

Together with the Arad Valley, the Beer Sheva Valley, identified with the biblical region of "Negev of Judah", is a wide plain covered with loess. The two valleys divide the Judean Mountains in the north from the Negev Highlands and the Sinai in the south. In the past, streambeds served as main passageways through the region, because they were both easy to traverse on foot and represented an under-ground water source readily available (by digging wells).

The moderate topography of the Beer Sheva Valley made it a convenient throughway, from the Arava and the Dead Sea to the Mediterranean Sea, and from the Sinai and the Negev towards the central and northern parts of the country. The history of Tel Beer Sheva and of the other settlements in the valley reflects periods in which settlement was possible either due to a more comfortable climate or through the initiative of the central government.

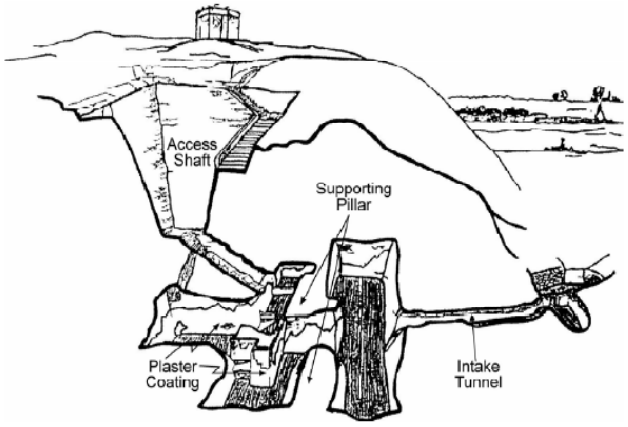

Figure 10.2 – Schematic representation of Tel Beer Sheva archaeological site

Excavations at Tel Beer Sheva were carried out from 1969 to 1976 by the Tel Aviv University Institute of Archaeology. In 1990, extensive restoration works were carried out by the National Park Authority, with the assistance of the Negev Tourism Development Administration. Excavation on the mound was undertaken from 1993 to 1995 under the direction of Professor Ze'ev Herzog to complete the uncovering of the water systems.

During the first stage, the well near the city gate was excavated. The water level was found to be $69m$ below the surface. During the second stage, the water system in the northeastern part of the city was revealed in its entirety: a stepped shaft some $17m$ deep was uncovered almost to the top, and a plastered water system was found out as it was abandoned over 2,000 years ago. Following the completion of extensive conservation works by the Israel Antiquities Authority, the Israel Nature and Park Authority opened the water system to the public in 2003.

The water system, dated to 1000 BC, was established as part of the city's fortifications. It consists of three components: a shaft $17m$ deep, lined with stones with a flight of steps along its sides; a reservoir divided into five spaces, with a total capacity of about $700m^3$; and a winding feeder channel that led flood waters from the spring into the reservoir.

Whilst the water system was built to serve the inhabitants of the city mainly during the time of siege, the well excavated near the city gate met their daily needs. Today, it is possible to descend the stairways and enter the underground storage cavern, being amazed by its size, the thick plaster that prevented the water from seeping out and the ancient support walls built to hold up the ceiling after the collapse. The exit from the water system is through a secondary cavity, which was excavated during the work on the system in the olden times and blocked after its completion. It was reopened during excavation and now serves as an exit from the mound.

The real excavation sequence of the water storage cavern is unknown. However, modern excavation of the underground water system revealed that the roof had collapsed, probably during the time of construction, and at that time the engineers had erected a massive support pillar in the centre of the opening to support the remaining roof. Also, the plaster coating that was explored on the sidewalls at ground level was discovered to be above the original roof, indicating the proximity of the failure episode to the original time of excavation.

The large storage cavern beneath the city was fed by seasonal run-offs from the Hebron streambed through a tunnel running beneath the city walls. From within the city, the access to the water reservoir was through a large vertical shaft. The intake capacity, without considering the support elements, is approximately $250m^3$. The water reservoir layout is shown in Figure 10.3.

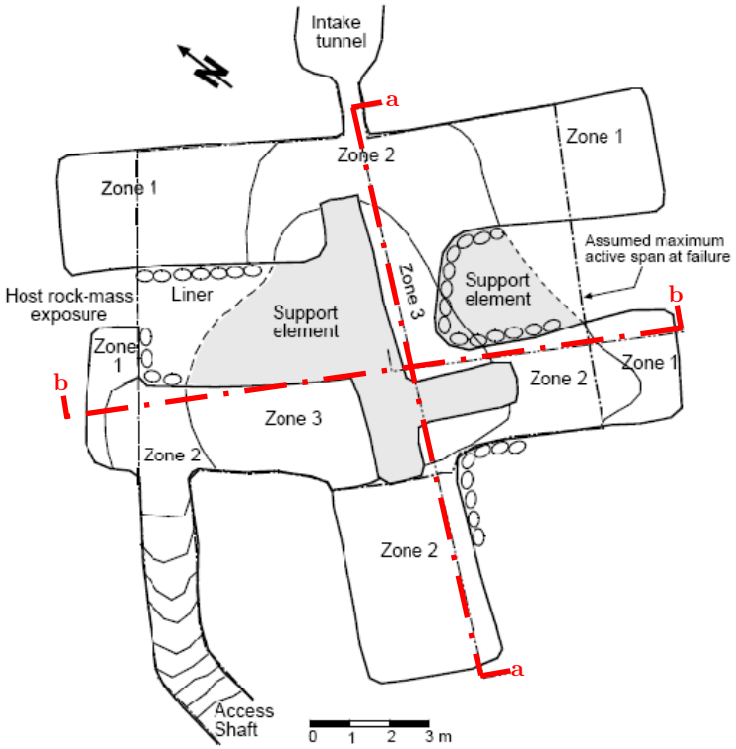

Figure 10.3 – Schematic layout of the water storage cavern after Hatzor & Benary (1998)

10.3 Geological and rock mass conditions at the Tel Beer Sheva site

The geological engineering of Tel Beer Sheva was previously studied by Hatzor and Benary (1998). The water storage cavern is shown to have been excavated in the sedimentary Gareb formation (Upper Cretaceous), which comprises horizontal layers of chalk, 0.3-0.8m thick, alternating with some thinner (up to 0.1m) layers of marly chalk of low plasticity and swelling potential.

A detailed geological mapping of the rock mass was performed both within the underground water storage cavern and in nearby outcrops. Four joint sets were mapped: the bedding planes, which are horizontal with a mean spacing of 0.50m, and the J1, J2 and J3 sets having a mean spacing of 0.20m, 0.25m and 0.60m, respectively (Table 10.1 and Figure 10.4). The strike of joint set J1 is nearly parallel to the axis of the intake tunnel, whilst J2 is perpendicular to J1 and co-linear with the reservoir walls. The strike direction of the joint set J3 is similar to that of the joint set J2. The intersection of the closely spaced joints with the bedding planes forms a network of nearly equidimensional cubic blocks.

Table 10.1 – Principal joint sets in the water storage cavern (Hatzor and Benary, 1998)

Set	Dip [°]	Strike Direction [°]	Room (see Figure 10.4)	Mean spacing [cm]
J1	90	39-61	1, 2, 3, 4	20
J2	90	124-127	1, 2	25
J3	90	107-112	3, 4	60

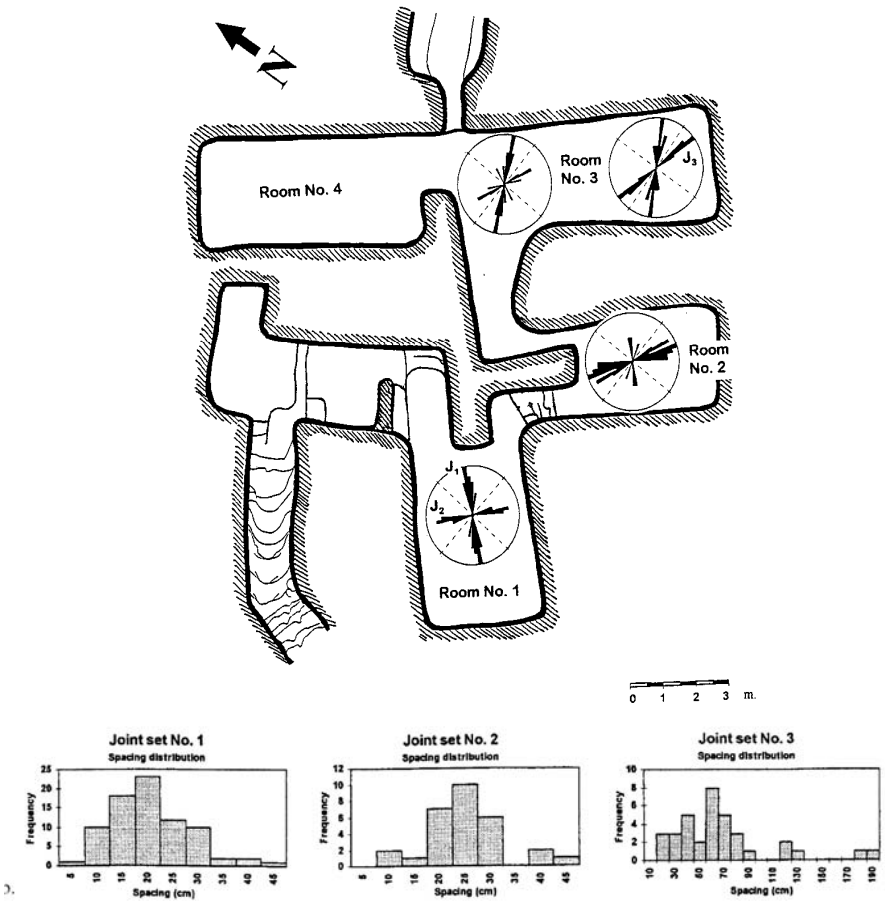

Figure 10.4 – A map of the underground water storage system with the strike of the joints as mapped underground and joint spacing distribution (Hatzor & Benary, 1998)

As depicted in the cross section of Figure 10.5, the roof of the water storage cavern is known to have collapsed by leaving the shape of a dome. Three distinct levels were mapped:

- Zone 1: the original excavation level at $286m$ elevation.
- Zone 2: the intermediate failure level at $287m$ elevation.
- Zone 3: the upper failure level at $288m$ elevation.

All the zones are developed along natural bedding planes. The transition between the different levels ranges from vertical to step like, running along block boundaries, defined by the intersections of joints and bedding planes.

Both the bedding planes and the joints in chalk are very persistent with trace line length greater than the cavern size. The joints are clean and tight with planar surfaces. The roughness of the joint planes was evaluated and the mean JRC value is estimated at 8-10. The mean residual friction angle is between 35 and 36°. Tilt tests performed on mating natural joints as found in the field yielded values between 49-71°.

In order to assess the peak friction angle which was available at the time of deformation the empirical criterion of Barton (1973) is used by Hatzor and Benary (1998): $\tau = \sigma_n \tan[JRC \log10(JCS/\sigma_n)+\phi_r]$ with the following input parameters: JRC = 8-10; $JCS = 7MPa$; σ_n= 0.5-2.5MPa; $\phi_r = 35°$ where σ_n is the maximum normal stress active on the joints that is a function of beam thickness. Hatzor and Benary (1998) estimated σ_n from output of Voussoir beam analysis (Beer & Meek, 1982) for a beam with span of $7m$ and thickness between 0.5 and 2.5m. Hatzor and Benary (1998), using the criterion of Barton, the dilation angle was estimated to vary between 3.6 and 11.4° and, therefore, the peak friction angle was assumed to vary between 38.6 and 46.4°.

The input data for rock mass classification methods yields are evaluated from Hatzor and Benary (1998) and they obtained a Q value between 0.4 and 4.0 and RMR value of 43. These values indicate a fair to poor rock with an expected stand up time of 1 to several days. The estimated rock mass classification values help explain the historic failure; with the given lithological conditions and considering modern experience we do not expect the rock mass to have been able to sustain the loads which were induced by the attempted excavation for a significant period of time (Hatzor and Benary, 1998).

Hence, to distinguish the different nature of the horizontal bedding planes and of the joint sets, the discontinuity parameters (according to the Mohr-Coulomb yield surface) cohesion c_j and friction angle φ_j may be assumed to be different as shown in Table 10.2, where also given are the normal stiffness k_{nn} and shear stiffness k_{ss}.

The intact rock properties are as follows: elastic modulus E = $2GPa$, Poisson's ratio $\nu = 0.1$ and unit weight $\gamma = 19kN/m^3$.

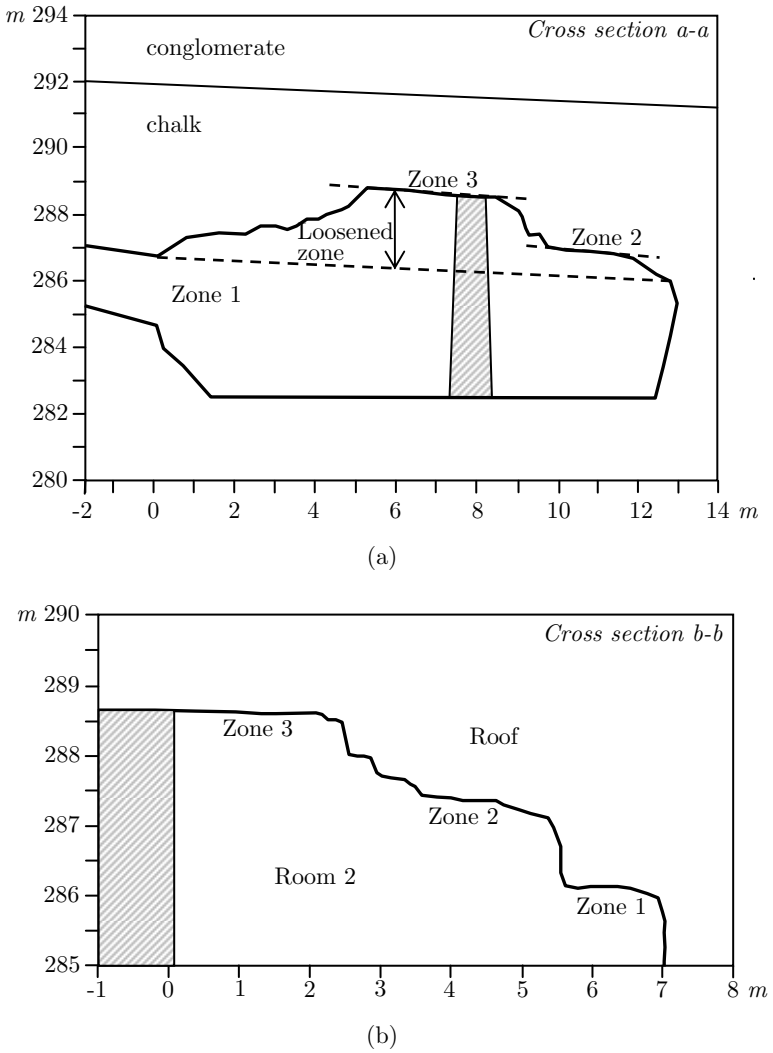

Figure 10.5 – Cross sections of the water storage cavern: (a) longitudinal section showing the ancient support pillar and (b) transversal cross section b-b as shown in Figure 10.3, after Hatzor & Benary (1998)

Table 10.2 - Mechanical parameters of bedding planes and vertical joints

	φ [°]	k_{nn} $[GPa/m]$	k_{ss} $[GPa/m]$	c $[MPa]$	σ_t $[kPa]$
Bedding planes	38	3.0	1.5	2.0	1.0
Vertical joints	42	3.0	1.5	0.1	0.001

10.4 DEM analyses of a laminated Voussoir beam

The roof failure of the water storage cavern was previously analysed by Hatzor and Benary (1998) using the classical Voussoir beam theory and discontinuous deformation analysis (DDA). The study was focused on the shear failure along the vertical abutments due to developed vertical shear stresses, rather than on failure by crushing at the hinge zones due to induced axial compressive stresses.

The DDA model used was finalised to reproduce the geometry of a beam representing the cavern roof, with a given span and overall height, however accounting for the presence of the individual horizontal layers, each with a given thickness (t) and vertical joint spacing (s). With the intention to model the water storage cavern in static conditions, similar analyses as with DDA were carried out with DEM.

Modelling was undertaken in plane strain conditions by using the UDEC code. As for the DDA analyses, the geometry of the failed roof in the cavern was used assuming the active span to be $7m$. The overall beam thickness was taken to be about $2.5m$, which is the height of the loosened zone shown in Figure 10.5. The individual layer thickness (t) was assumed to be equal to the average bedding thickness, about $0.5m$. Therefore, the geometric parameter used as variable was the mean joint spacing (s). The mechanical parameter was the joint friction angle (φ).

Figure 10.6 shows the DEM two-dimensional model adopted for the case of vertical joint spacing equal to $25cm$ and individual beam thickness of $0.5m$. It is noted that, as for DDA analyses, the model comprises a beam, which is subdivided into blocks (each block with a block dimension ratio s/t) and is free to move under gravity loading. The abutments in the model are represented by two vertical blocks, each $1.0m$ wide and $7.0m$ high. These blocks together with a top block, of length $9.0m$ and height $1.0m$, form a fixed frame for the beam.

As for the DDA analyses, the joints were assumed to be elastoplastic, with a Mohr-Coulomb yield criterion. The rock blocks were given a linearly elastic behaviour. With the joints considered to be planar with zero cohesion and tensile strength, the friction angle of the horizontal bedding planes and vertical joints was assumed to be equal. The input material parameters for the blocks were the same as reported above for the intact rock. Seven mean joint spacing values (s) were

analysed: 25, 50, 87.5, 116, 175, 350 and 700cm. The friction angle was taken to range between 20° and 90°.

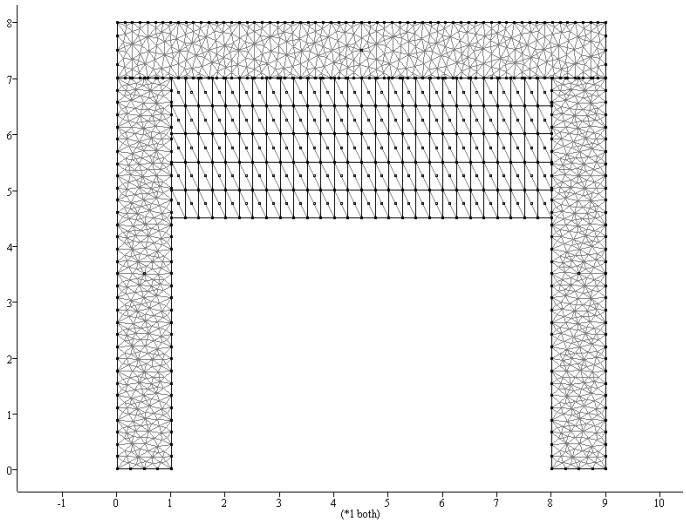

Figure 10.6 – Details of the DEM model of the cavern roof with span 7.0m. Individual beam thickness 0.5m; vertical joint spacing 0.25m

The DEM analyses were performed for each model having a given block dimension ratio s/t, by keeping the side vertical boundaries fixed and by changing the joint friction angle until the system showed stability. As for DDA analyses, the stability of the roof was defined by a specific value of maximum deflection at the mid-section of the beam, the magnitude of which would not change, regardless of the number of computation steps. The roof was considered to achieve stability with a maximum deflection at the mid-section of the beam of up to 5.5cm.

A comparison of the present DEM and DDA results is shown in Figure 10.7, where the required friction angle for stability is plotted versus the block length or joint spacing. It is noted that for the DEM analyses, the results are plotted depending on the degree of discretization adopted for the grid in the model, ranging from 0.0625m minimum to the maximum equal to the block size as side length of each triangle used. Inspection of this figure indicates that the DEM results agree well with the DDA results.

Note that with coarse discretization (element size in UDEC equal to grid edge), UDEC and DDA results agree very well for the large blocks (joint spacing $>$350cm) because modelling accurate stress and strain distribution in large blocks is limited in DDA due to the ''simply deformable blocks'' assumption, and in UDEC here due to the choice of coarse discretization. When higher discretization is introduced into UDEC, the demand for higher friction for the static stability of larger blocks is

relaxed, most probably due to the added stability gained by individual beam bending that can better be modelled in UDEC with high discretization. For smaller blocks, however (joint spacing smaller than $100cm$), the DDA "simply deformable blocks" assumption is less restricting, because the relatively high number of individual blocks in the mesh allows more accurate stress and strain distribution and thus a better agreement with UDEC when run with high discretization of elements.

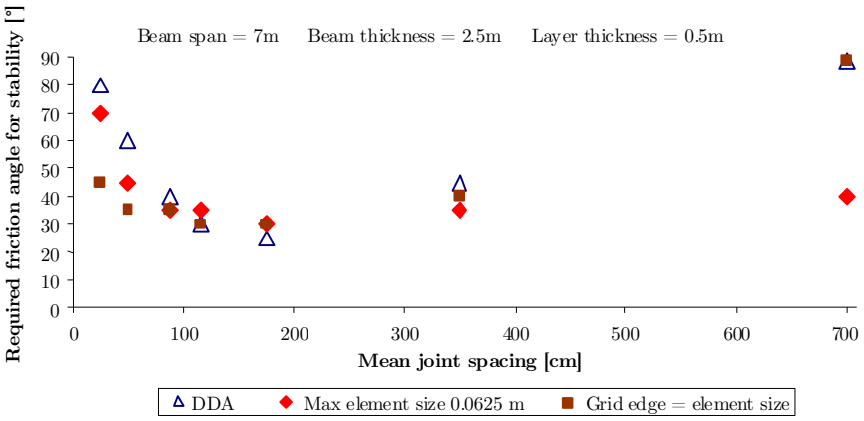

Figure 10.7 – Comparison of present DEM results and DDA results by Hatzor & Benary (1998). Plot of required friction angle for stable roof versus joint spacing for a layer thickness of $50cm$

The comparison between UDEC and DDA clearly indicates that the required friction angle for stability presents a minimum for 30°–35°: it decreases with increasing joint spacing, i.e., with decreasing the number of blocks in each individual layer, and increases again with the decreasing number of blocks. DEM appears not to agree with DDA for the maximum joint spacing, when ultimately each individual layer consists of a single block.

10.5 Back analysis of roof failure by DEM

As shown in Figure 10.3 and Figure 10.5, the cavern during construction was characterised, in the cross-section a-a, by a maximum total span of $12.8m$ and, in the cross-section b-b, by a total span of $15.0m$. After failure and construction of the massive supporting pillar in the centre of the cavern (see description of inferred sequence above), the roof was divided in two parts to stabilise it. As shown in the cross section a-a (Figure 10.5a), the beam with span $12.8m$ was divided into two

shorter beams: one on the left side spanning $7.2m$ and one on the right side spanning $4.6m$, which have remained stable until the present time. The same holds true for section b-b (Figure 10.5b) where the support pillar erected has divided the roof in two shorter parts with the same span of $7m$.

The stability of the water storage cavern has been analysed firstly in two dimensions and then in three-dimensions by modelling the entire cavern.

10.5.1 2D static analyses

The 2D analyses were carried out to study the stability of the cavern along cross sections a-a and b-b using the UDEC code. As shown in Figure 10.8 and 11.9, the cavern roof was assumed to be $13m$ below the ground surface. A superficial soil layer of $3m$ of thickness and below a conglomerate layer of $5m$ were assumed. Their mechanical properties are shown in Table 10.3.

Table 10.3 - Mechanical properties of the superficial layers

Layers	ρ $[kg/m^3]$	E $[MPa]$	ν
Soil	1800	20	0.2
Conglomerate	1800	100	0.2

The first static analysis was intended to evaluate the stability conditions of the cross-sections a-a (Figure 10.8) and b-b of the cavern with span respectively $12.8m$ and $15.0m$, whereas the second one was to analyse the present conditions, with the supporting pillar in the centre (Figure 10.9a-b). These analyses were performed as follows:

- Initialisation of the DEM model.
- Simulation of the cavity as in the past: excavation in a single step.
- Simulation of the cavity at present: activation of supporting pillar (about $1m$ thick and $7m$ high).

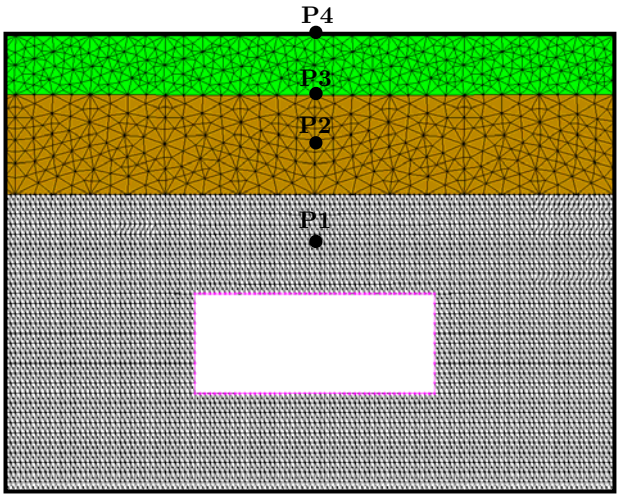

Figure 10.8 – Details of the DEM model of the cavern before collapse (cross-section a-a)

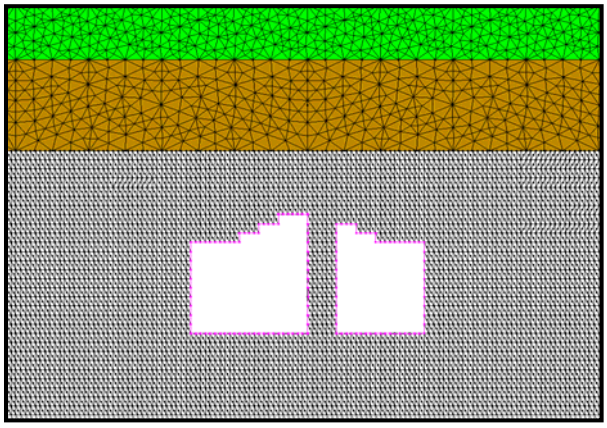

(a)

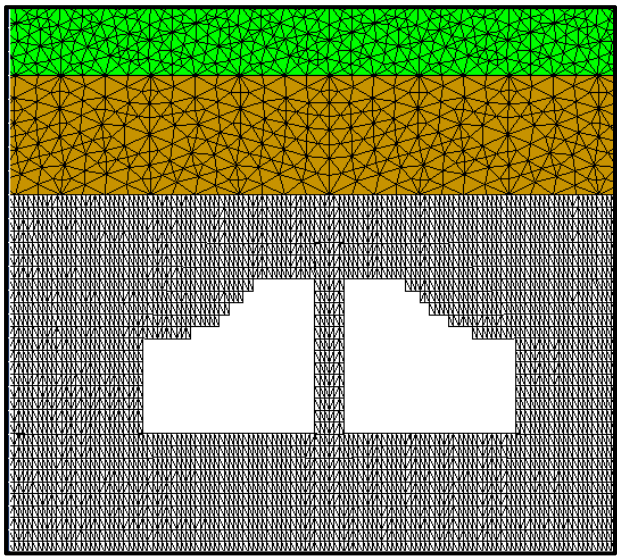

(b)

Figure 10.9 – Details of the DEM model of the cavern following collapse: (a) cross-sections a-a and (b) b-b

As for the analysis above, the joints were assumed to be elastoplastic, with a Mohr-Coulomb yield criterion. The rock blocks were given an elastic behaviour. The assumed mechanical properties are given in Table 10.2. The stress ratio K_0, i.e., the ratio between the horizontal and vertical initial stress, was taken to be equal to 0.5.

As shown in Figure 10.10, points P1, P2, P3 and P4 in the rock mass above the cavern, in cross-section a-a, undergo a vertical displacement of different magnitude as excavation takes place (i.e., as time steps increase). It is noted that a stable condition is reached, meaning that all the rock layers above point P1 and up to the surface undergo progressive deformations without falling down.

The roof deformation process and the initiation of the arching mechanism in the roof are depicted in Figure 10.11a-d, where the rock blocks in the immediate roof collapse while the overlying layers have already ended the downward movement and arching takes place. The lower rock layer inflects first like a beam and starts to detach from the upper one. The arch-forming mechanism is well reproduced and all the rock blocks falling down can be singled out.

As shown in Figure 10.12, with equilibrium being reached gradually, the roof configuration, in the cross-section a-a, obtained with the model reproduces that of the cavern, as visible nowadays. While the central section of the roof collapses, the sidewalls remain stable. In a similar manner, when the analysis is performed with the present configuration of the cavern roof supported by the pillar in the centre

(Figure 10.3), with the reservoir being subdivided in two openings (with $7.2m$ span, the left one, and $4.6m$ span, the right one), a new stable condition is reached.

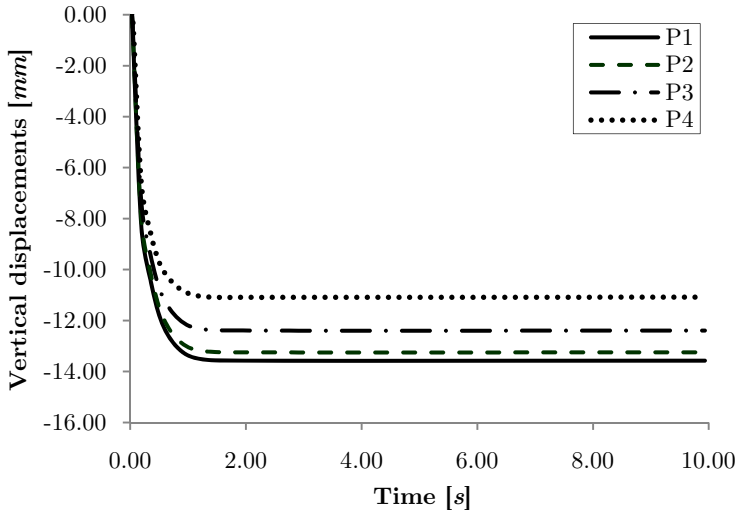

Figure 10.10 – Plot of the vertical displacement monitored at points P1-P4 above the cavern – Cross-section a-a

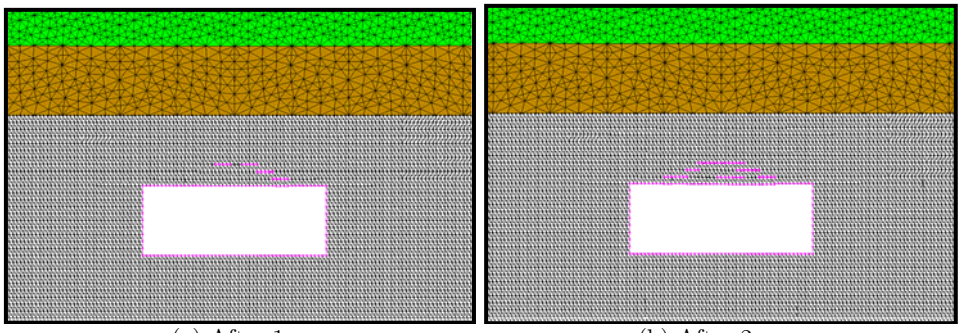

(a) After $1s$ (b) After $2s$

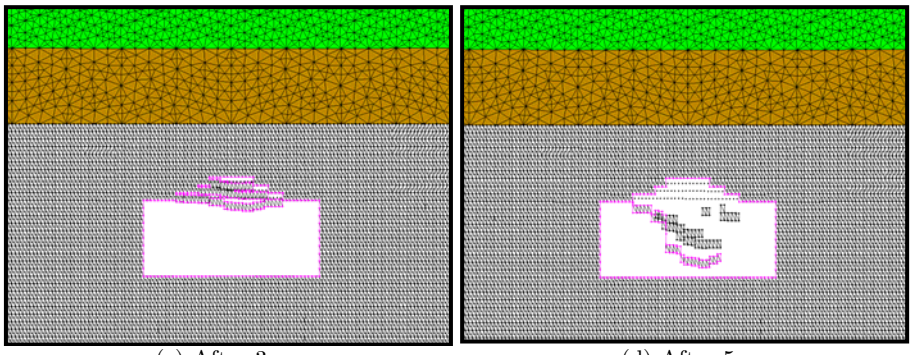

(c) After $3s$ (d) After $5s$

Figure 10.11 – Plots showing progressive instability of the cavern roof – cross-section a-a

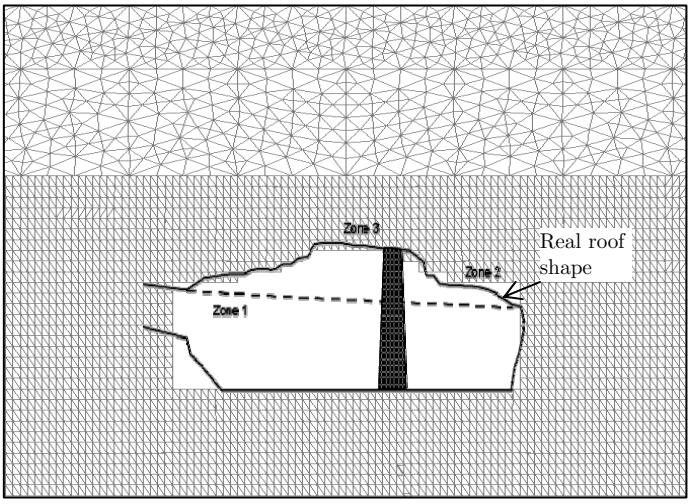

Figure 10.12 – Roof configuration of the cross-section a-a resulting from DEM modelling compared with the present configuration following collapse

The same analyses, performed above for the cross-section a-a, were performed for the cross-section b-b. In this section the vertical joint set J2 is not considered as the vertical joint set J1 with mean spacing $0.20m$ is introduced. The horizontal bedding planes are assumed with spacing $0.50m$ as in the previous analyses. The back-analysis of the cavern was performed leading the cavern roof to collapse as well illustrated in Figure 10.13.

For this cross-section the roof deformation process and the initiation of the arching mechanism (Figure 10.13) are very similar to those described for the cross-section a-a. Also in this cross section, the rock blocks in the immediate roof collapse

while the overlying layers have already ended the downward movement and arching has taken place.

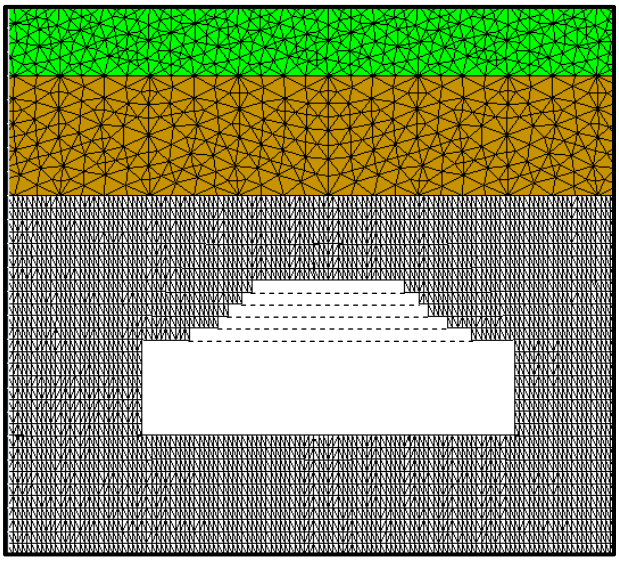

Figure 10.13 – Roof configuration of the cross-section b-b resulting from DEM modelling

The vertical deflections of the beams, identified by the bedding planes, are shown in Figure 10.14a. We can see that the first five beams collapse and then the vertical displacements increase without reaching stability. In the stable beams, the maximum vertical displacements, evaluated in the mid span, decrease to reach the stability condition with the deflections remaining constant during the computational time. On the other hand, the horizontal compressive stresses decrease approaching the immediate roof (Figure 10.14b).

The distribution of the principal stress immediately after the excavation in a single step ($0.7s$ of gravitational loading) is plotted in Figure 10.15a, whereas Figure 10.15b illustrates the principal stress trajectories during the collapse ($8s$). We can see the compressive arch that is generated as the equilibrium configuration is being reached. Below the compressive arch, a stress-free zone is evidenced which is undergoing collapse.

The extension of the collapsed area in the cross-section b-b and the values of the vertical displacements are greater than those in the cross-section a-a. This is due to larger span and the smaller spacing of the vertical joints.

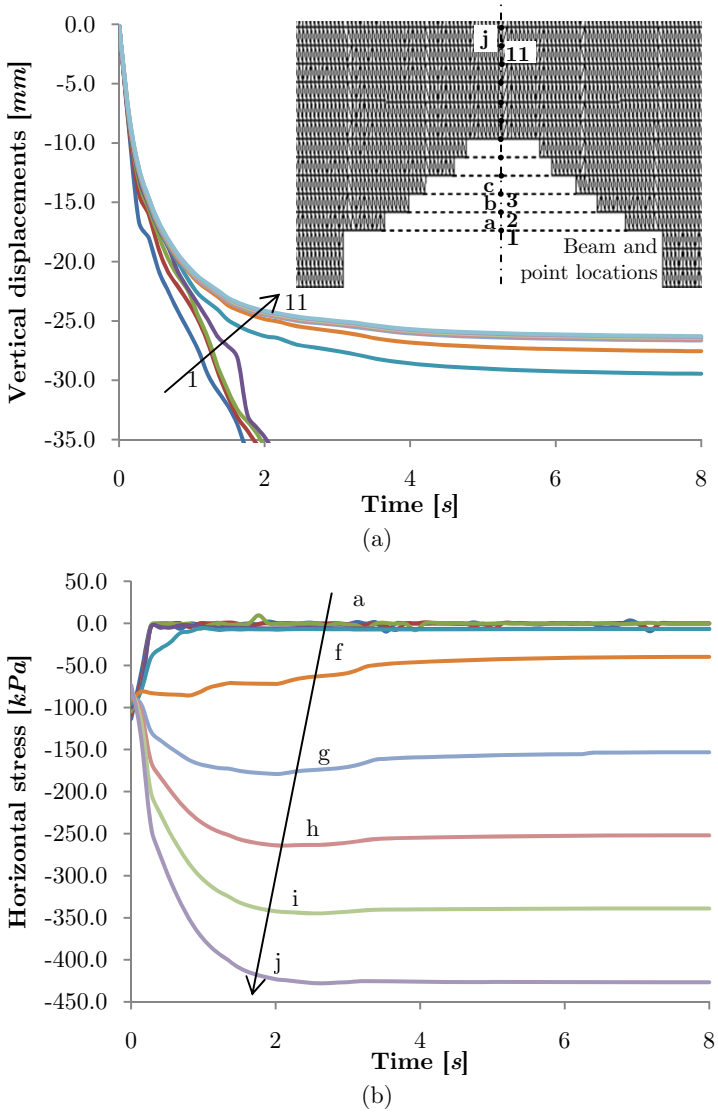

Figure 10.14 – Development of vertical deflections (a) and of horizontal compressive stresses (b) of the bedding layers during the numerical computation in the cross-section b-b (numbers indicate the location of points in which we have measured the vertical displacements while letters identify the beams)

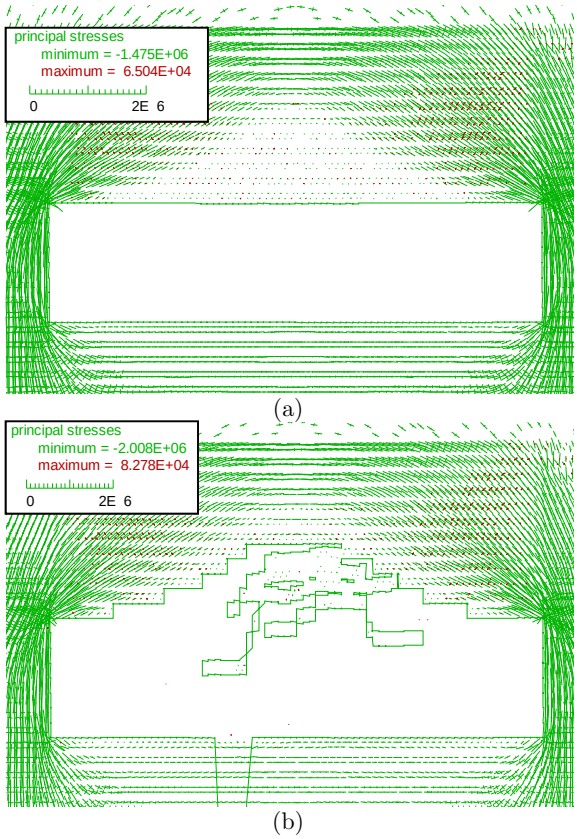

Figure 10.15 – Phases of instabilization of the section b-b**.** Principal stresses (Pa) trajectories configuration after (a) $0.7s$ and (b) $8s$ of gravitational loading

As shown in Figure 10.16, as equilibrium is being gradually reached, the stable roof configuration obtained with the model reproduces well the real one, as presently observed. Only the central part of section b-b collapses while the other parts remain stable. To guarantee stability a support pillar is activated in the centre of the cavern, as actually done in the past (Figure 10.9).

The support pillar consists of chalk blocks. The analyses performed for both the cross-sections a-a and b-b with the pillar activated show that this configuration is stable (Figure 10.17). It is of interest to plot in Figure 11.18 the new principal stress distribution which is attained, showing that the column generates compressive arches at two side of the pillar in the centre.

Opening of the vertical joints in the column is recorded (see Figure 10.19). These joint openings are well visible due to the modelling of the pillar with rock blocks not arranged with staggered joints. Some small joint openings in the roof

and along the abutments were detected in the numerical analyses. The same considerations made for cross-section b-b are also true for cross-section a-a.

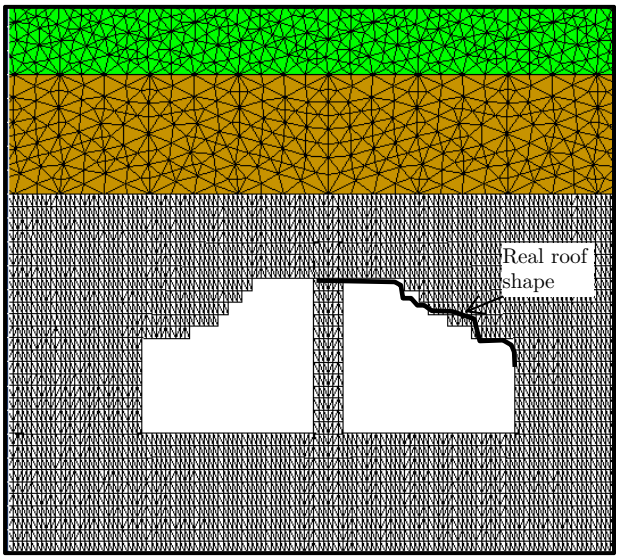

Figure 10.16 – Roof configuration of the cross-section b-b resulting from DEM modelling compared with the present configuration following collapse

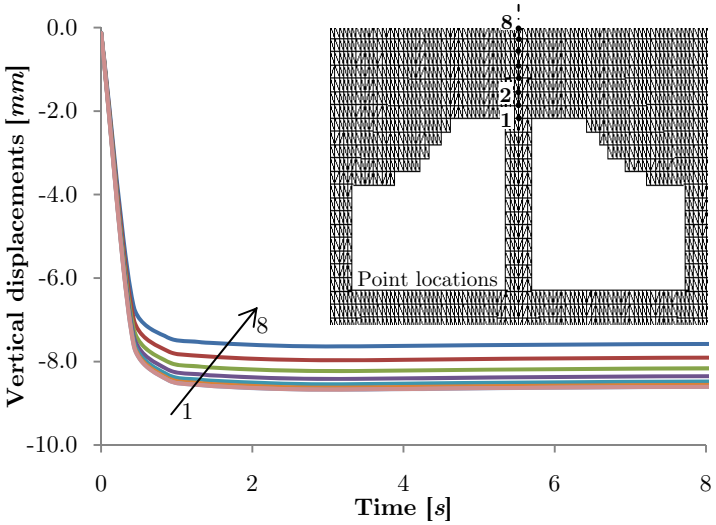

(a)

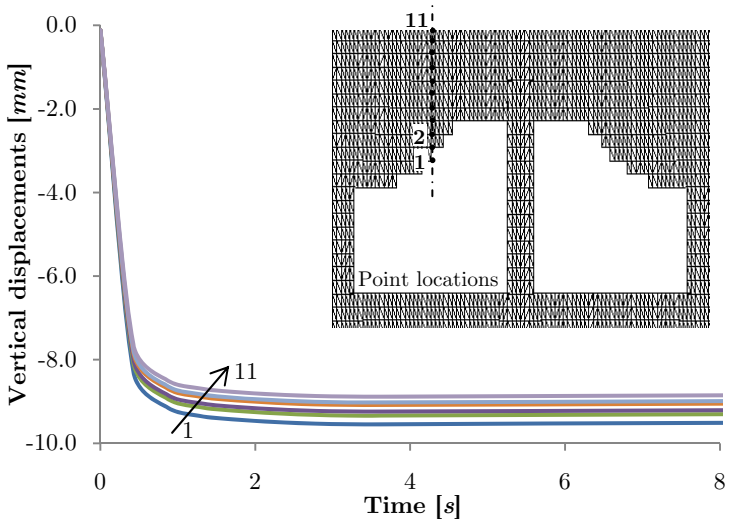

(b)

Figure 10.17 – Vertical deflections of the bedding layers during the numerical computation in the cross-section b-b

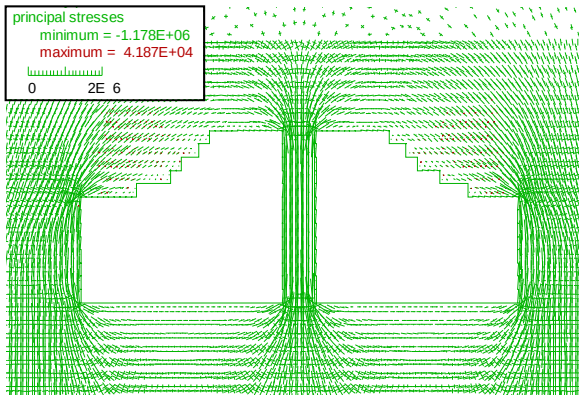

Figure 10.18 – Final principal stress (Pa) trajectories in the cavern with the support pillar. Cross-section b-b

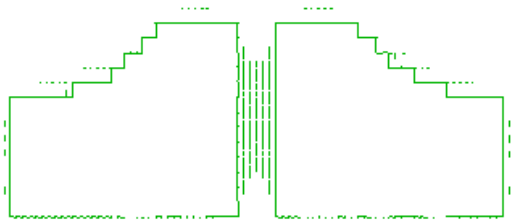

Figure 10.19 – Model of the cavern with the massive pillar in its centre following gravitational loading. Opening of the vertical and horizontal joints is shown. Cross - section b-b

10.5.2 3D static analyses

In order to represent more accurately the collapse and the actual configuration of the cavern, DEM analyses were also performed in three dimensional conditions. The stability of the entire water storage cavern was investigated. The steps of the analyses performed by using the 3DEC code are the same as for the 2D analyses with UDEC.

The simulation of the cavern excavation takes place in a single step according to the model shown in Figure 10.20. Figure 10.21 underlines the shape of the cavern with the blocks created to reproduce it in detail. It is noted that these blocks first were joined together to create a continuum and then they were cut to create a discontinuum.

The yz planes of the boundaries of the model (Figure 10.20) are fixed in x direction, the xz planes in y direction and the bottom in the z direction.

The first step was intended to evaluate the stability of the cavern without the support pillars being present as shown in Figure 10.3. The stability problem was analysed in the following stages:

1. equilibrium stage and in-situ stress initialization;
2. excavation of the cavern in a single step;
3. stability analysis under gravitational loading.

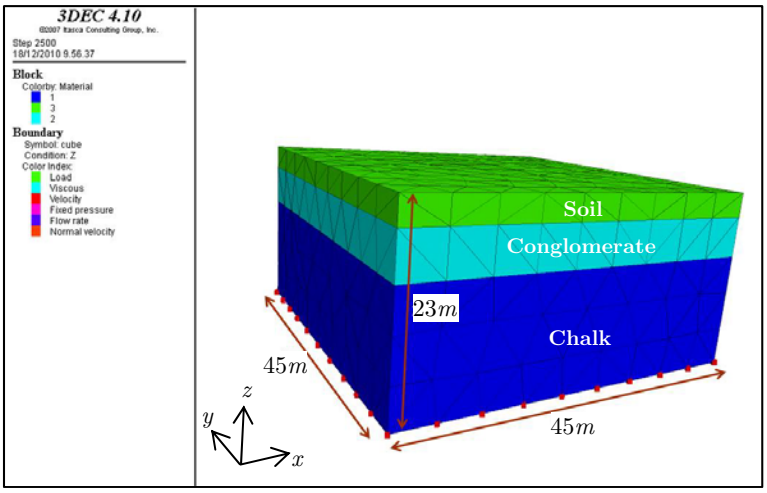

Figure 10.20 – 3D DEM model of the cavern

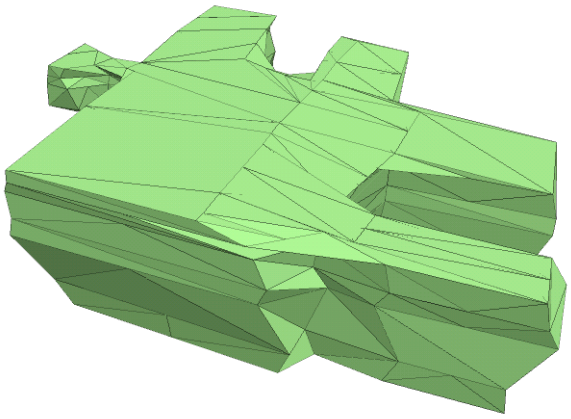

Figure 10.21 – View of the excavation of the 3D model of the cavern

The analyses were performed firstly with the large size model shown in Figures 10.20 and 10.21. It is noted that the presence of the discontinuities is introduced at the roof of the cavern only, while the other parts of the model are assumed as continuous. This assumption was needed to reduce the number of blocks in the model and then the computation time. The first analysis was performed with a spacing of $0.50m$ for the bedding planes and a spacing of 0.40 and $0.50m$ for the vertical joints sets J1 and J2 respectively.

Another model was also created as shown in Figure 10.22 by considering only the roof which was discretized according to its real shape in blocks with size 0.50x0.20x0.25m. The size of the blocks was defined based on the in situ average spacing of the joints sets. It is noted that in the model the joint sets were implemented with correct strike and dip directions. The extension and the characteristics of this model were evaluated from the results obtained with the first model previously described.

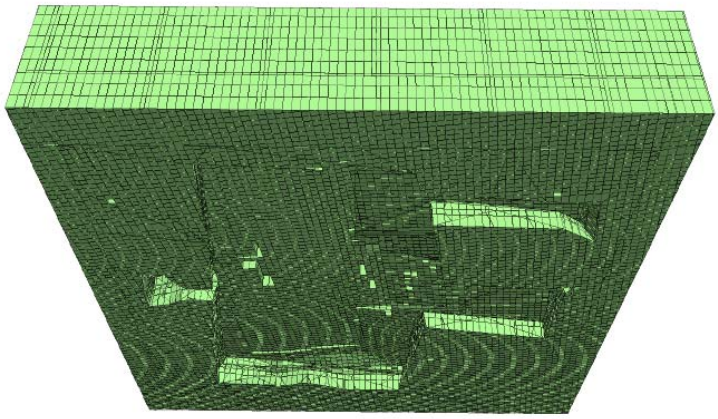

Figure 10.22 –View of the 3D model limited to the roof of the cavern

In the 3D analyses, the cavern is shown to be stable for a stress ratio K_0 equal to 0.5, in contrast with the 2D stability analyses. This may be motivated by the fact that the two-dimensional analyses are performed in plane strain conditions as the 3D analyses allow one to account for the confinement and the arching effect in all the horizontal directions.

Moreover, it is of interest to say that we have verified that the roof does not collapse by reducing the friction angle of the vertical joints down to 38.6° (minimum friction angle evaluated by Hatzor & Benary, 1998) and by maintaining K_0 equal to 0.5. In fact, by decreasing the friction angle from 42° to 38.6° the maximum vertical displacement at the mid-section of the cavern increases from 8.0 to 8.6cm.

Hence, in the 3D analyses, with the purpose to induce the collapse of the cavern roof, the value of K_0 was reduced down to 0.3. This produced an increase of the vertical displacements of about two times.

By comparing the results obtained with the two 3D models with blocks size of 0.50x0.40x0.50m and 0.50x0.20x0.25m respectively, the influence of the vertical joint spacing is clear. In fact, the vertical displacements at the mid-section of the

cavern increase of about 2 to 2.5 times, if the vertical joint spacing is reduced from 0.40 to 0.20m for joint set J1 and from 0.50 to 0.25m for J2.

The collapsed area obtained with 3D numerical analyses is depicted in Figure 10.23, where this is compared with the structural map of the roof as shown in Figure 10.3. Two cross sections a-a and b-b of the collapsed roof are plotted in Figure 10.24.

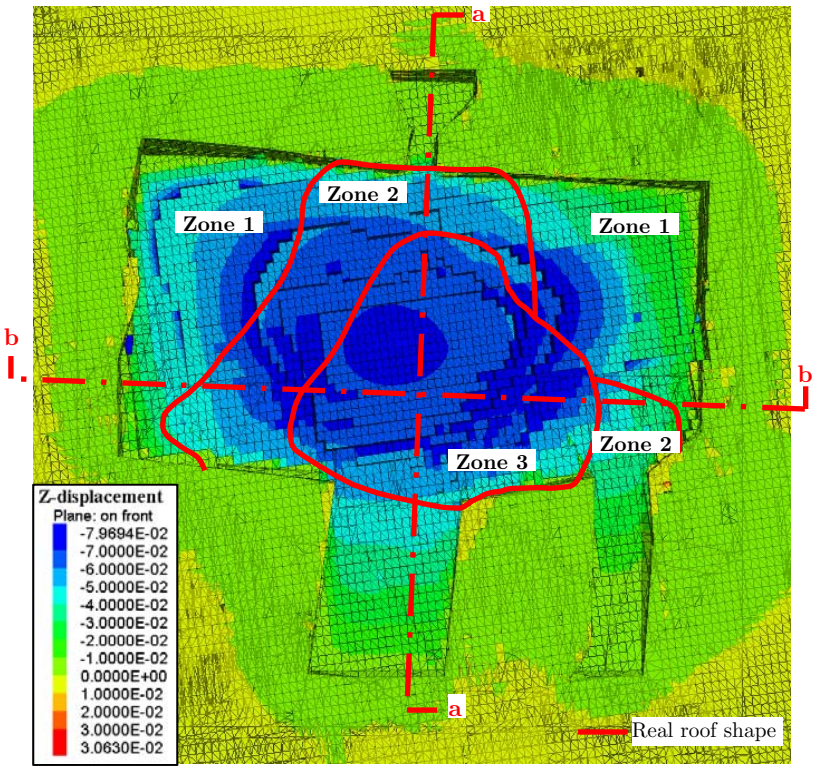

Figure 10.23 – View of the roof of the cavern with support system activated – Plot of vertical displacements magnitude and comparison of the collapsed area with the measured structural map of the roof showed in Figure 10.3

It is shown that the 3D model reproduces very well the three-dimensional dome formed in the cavern after the collapse. As in the 2D analyses, a compressive arch develops in three dimensions, i.e. a compressive dome is originated as well shown in Figure 10.25. This sustains the upper rock mass and identifies the stress-free zone where the collapse will develop.

The histories of the vertical displacements along the vertical in the middle of the cavern are shown in Figure 10.26. It is observed that the first three “beams”,

identified by the bedding planes, undergo collapse while stability is attained for the upper beams. The induced vertical displacements decrease with increasing of the vertical distance from the intrados of the roof.

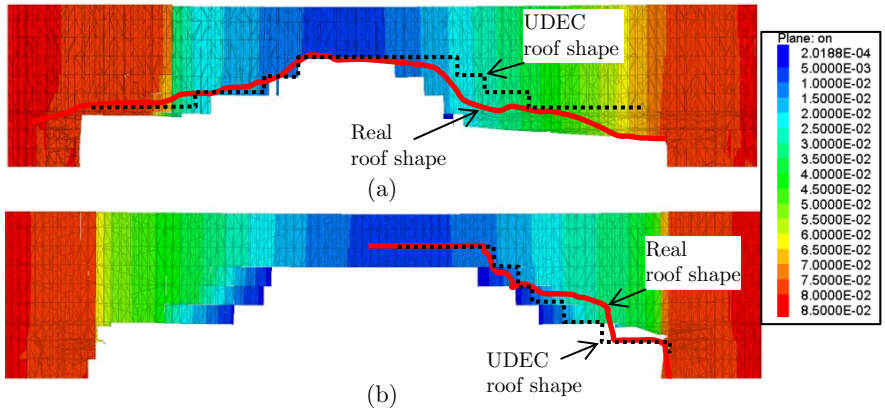

Figure 10.24 – Plots of vertical displacements magnitude and comparison of the collapsed zone, obtained with 3D analyses, with the measured structural roof showed in Figure 10.5 and with UDEC roof shape for the cross-section a-a (a) and cross-section b-b (b)

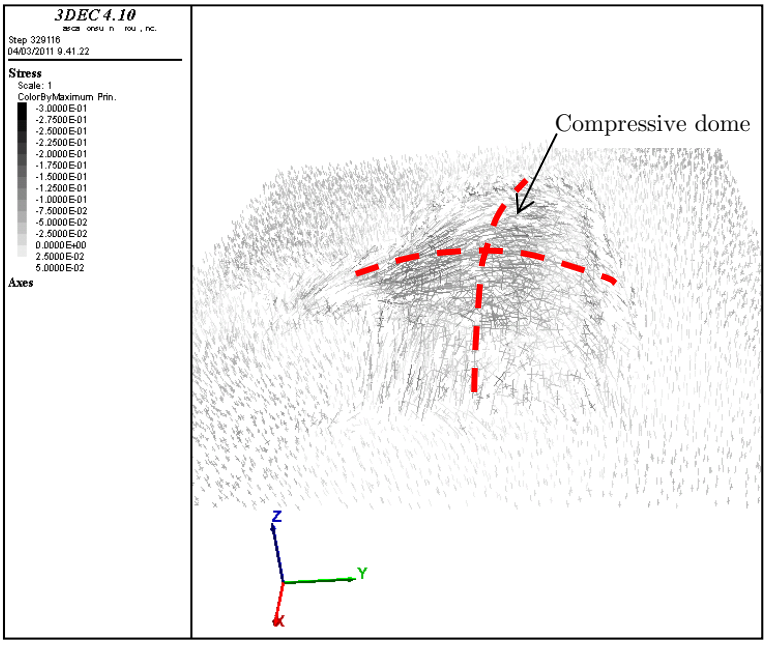

Figure 10.25 – 3D view of the principal stress (MPa) trajectories (dome effect)

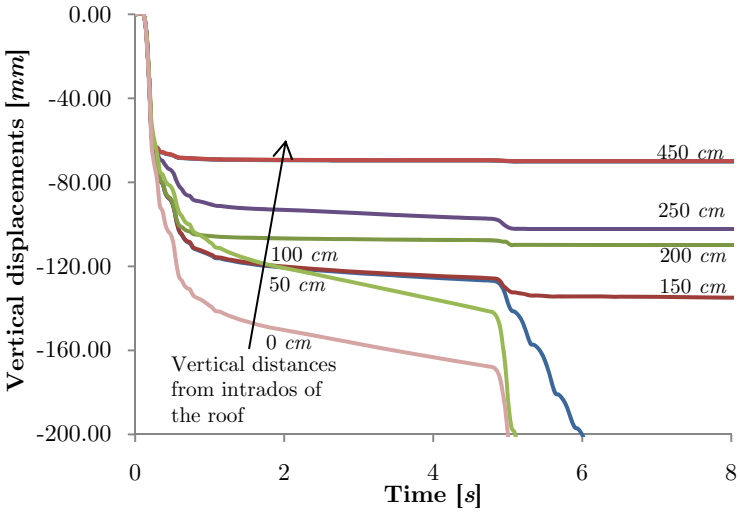

Figure 10.26 – Vertical displacements along the vertical passing through the point located at the middle of the cavern versus the computational time

As for the 2D analyses, 3D analyses of the cavern were also performed with the supporting pillars in place. Figure 10.27 shows the view of the excavation of the 3D model implemented in 3DEC. The support system is composed by one big pillar in the centre of the cavern and other lateral pillars constructed for reducing the cavern spans, thus reproducing in detail the in situ conditions.

The computed vertical displacements are shown in Figures 10.28 to 10.30. The maximum vertical displacements are about 2-3*mm* and then the cavern can be considered stable. A stability condition is achieved as illustrated in Figure 10.31 where the vertical displacements, at points located along the vertical directions passing through the six locations shown in Figure 10.28 at the roof, were monitored during the computational time.

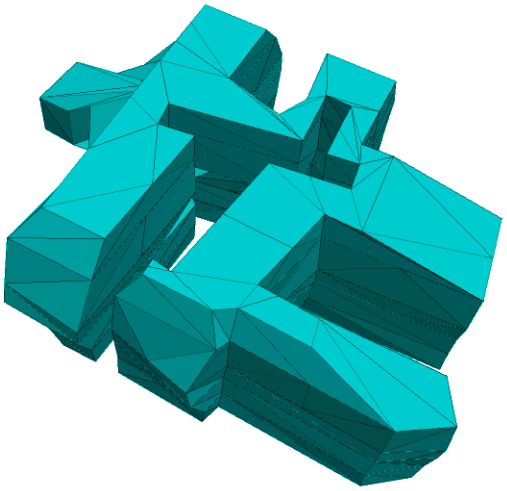

Figure 10.27 – View of the excavation of the 3D model of the cavern with support system

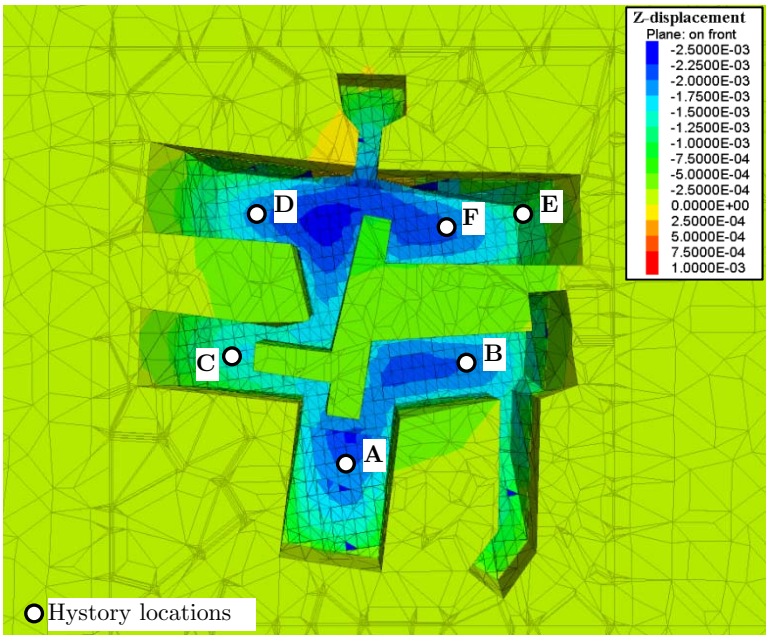

Figure 10.28 – View of the roof of the cavern with support system activated – Plot of vertical displacements (m)

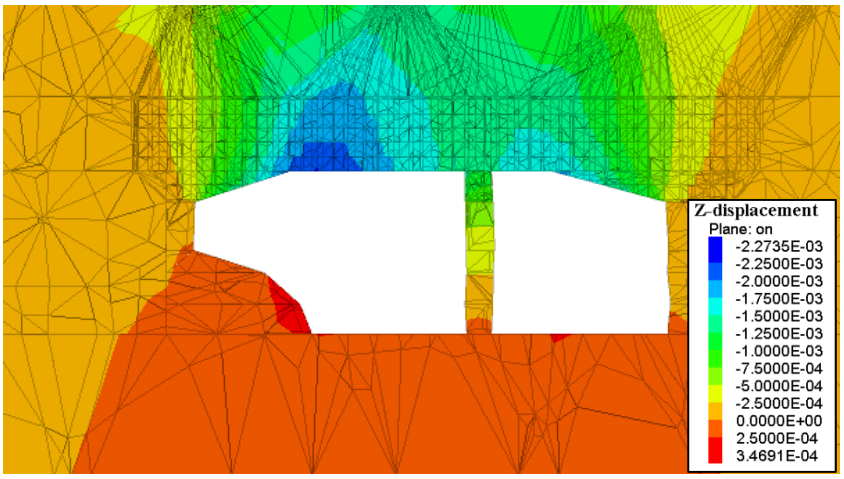

Figure 10.29 – Cross-section a-a of the cavern with support system activated – Plot of vertical displacements (m)

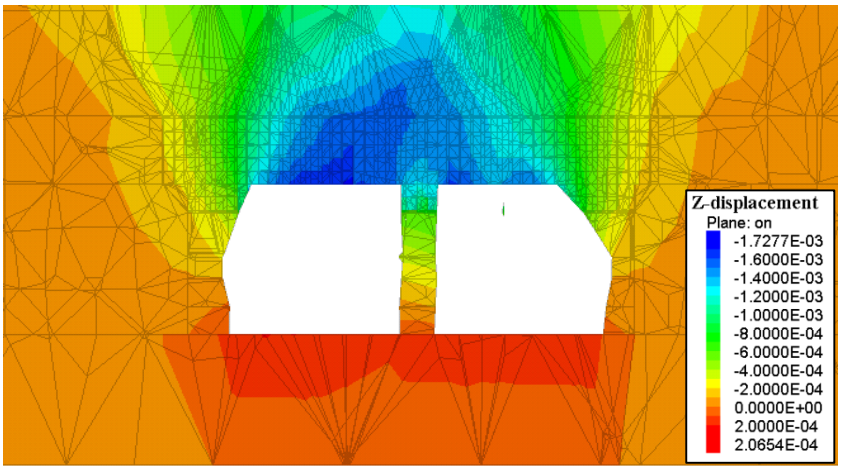

Figure 10.30 – Cross-section b-b of the cavern with support system activated – Plot of vertical displacements (m)

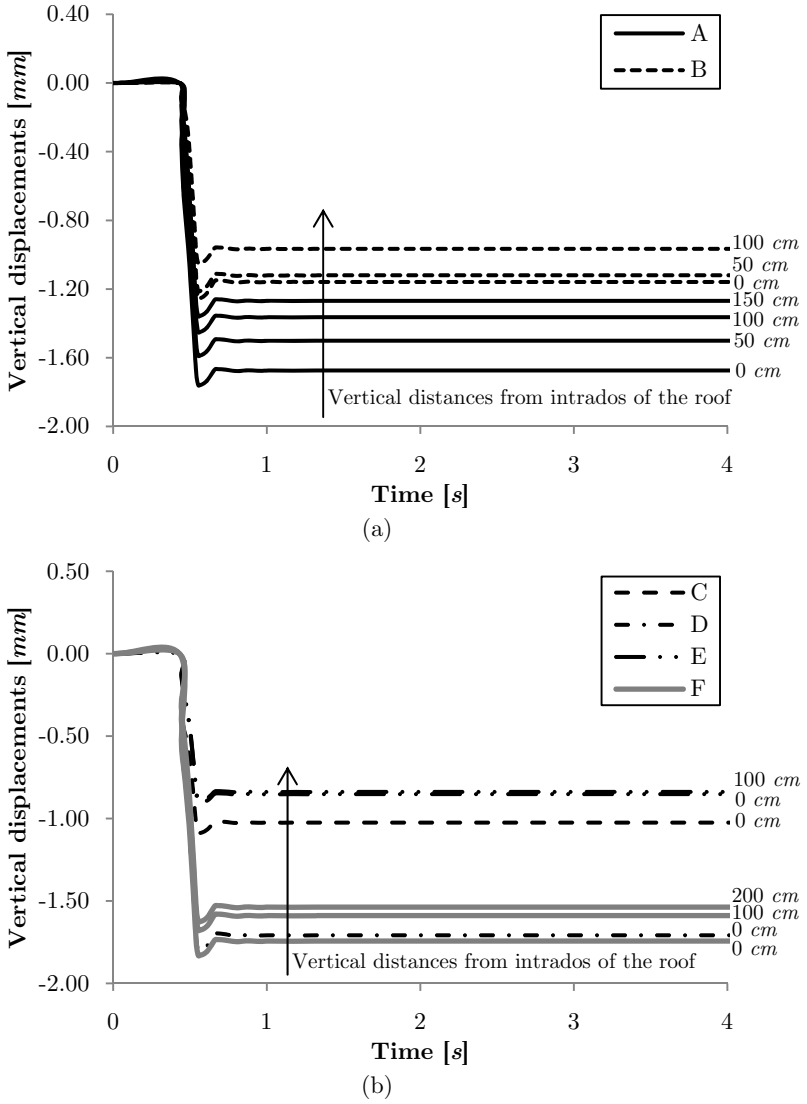

Figure 10.31 – Vertical displacements at the locations of the roof indicated in Figure 10.28 versus the computational time after the construction of the support system

10.6 Summary

By comparing 2D and 3D analyses carried out with DEM and by using the UDEC and 3DEC codes, the shape of the collapsed roof in the cavern is shown to be quite similar. 2D analyses provide however, as expected, a more cautious estimate than 3D analyses. In UDEC the roof collapse occurs with a stress ratio $K_0 = 0.5$ while in 3DEC this does not takes place, with the strength properties along the joints being the same. It is shown that greater vertical displacements are necessary to develop the collapse in the 3D analyses due the likely stabilizing effect which develops in the out-of-plane direction.

The role of K_0 appears to be very important in relation to the degree of lateral confinement which is provided, as is the case reported by Barton et al. (1994) with a thorough stability analysis of the Olympic Ice Hockey cavern at Gjøvik, Norway. This underground opening has a span of $62m$ and a cover of about $25m$ and is located in a rock mass with high horizontal stresses (K_0 of 1-4) that restrain horizontal movements. Barton et al. (1994) underlined that the key properties favourable to large cavern construction are the high horizontal stresses, the roughness or waviness of foliation planes and the more continuous joints.

Hence, we have verified that the fundamental parameter to evaluate correctly the stability of a near surface cavern is the level of the horizontal stress, although the size of blocks identified from the joint sets plays a very significant role in determining the stability condition in a good rock mass environment.

Chapter 11

Distinct Element Modelling of the Tel Beer Sheva cavern in dynamic conditions

11.1 Introduction

As a follow-up of the previous chapter, DEM dynamic analyses were performed for the Beer-Sheva water storage cavern in both two-dimensional and three-dimensional conditions. The results obtained are described in the following.

With the understanding that wave propagation in a discontinuous medium is well simulated if the size, degree of subdivision and boundary conditions of the DEM models are optimized, comparative analyses with the SMM are performed.

The seismic analyses are intended to study the stability conditions of the cavern in its present configuration with the supporting pillar in its centre as discussed in Chapter 11, The recorded accelerations of the Nuweiba earthquake, occurred in 1995, are taken as representative for the site.

11.2 Stability of underground openings during earthquakes

Underground structures are generally considered resistant to earthquakes. Nevertheless, some underground structures have undergone relevant damages in recent large earthquakes, including the 1995 Kobe, 1999 Chi-Chi, 1999 Kocaeli, 2004 Chuetsu, 2005 Kashmir and 2008 Wenchuan earthquakes.

Several studies have documented earthquake damage to underground structures (Duke and Leeds (1959), Stevens (1977), Dowding and Rozen (1978), Owen and Scholl (1981), Sharma and Judd (1991), Power et al. (1998), Kaneshiro et al. (2000) and Hashash et al. (2001)).

Sharma & Judd (1991) generated a database of seismic damage to underground structures using 192 case histories. We have extended this database to include 348 case histories (Perino, 2007 and Corigliano, 2007) and updated the illustrative diagrams proposed by Sharma & Judd (1991) as given in Appendix B.

The entity of the damage was classified in four levels: none, slight, moderate and heavy. For each case history, the effects on the damage level of the overburden depth, surrounding rock type, type of internal support, earthquake magnitude, epicentral distance and surface PGA (peak ground acceleration) were identified. In

addition we have analysed the effects on the damage of the surface PGV (peak ground velocity) and of the distance between the underground structure and the fault.

This extensive work has shown that the greater part of underground structures was heavily damaged when:

1. surface PGA is greater than $0.35g$;
2. Richter magnitude is between 7-8;
3. Epicentral distance is less than $50km$;
4. Distance between underground structure and fault is less than $30km$;
5. Surface PGV is larger than $15cm/s$;
6. Overburden depth is less than $50m$.

Hence, from this study and the previous ones, the following considerations about the underground structures subjected by seismic excitation can be made:

- underground structures are less vulnerable than surface structures.
- Damage level decreases with increasing overburden depth. Deep structures are more earthquake resistant than the shallow ones.
- Underground structures in weak rock masses can be more damaged than those in competent rock.
- A concrete support is not sufficient to resist to high underground shaking and fault slip. However, lined and grouted structures suffer less damage than unlined ones.
- Damage of the tunnel due to shaking can be reduced by stabilizing the ground around it and by improving the contact between the lining and the surrounding ground through grouting.
- Damage level depends on the PGA, PGV, magnitude, epicentral distance and tunnel-fault distance.
- Underground structures are more efficient if subjected to symmetric loading. Improving the stiffness of the lining without stabilizing the surrounding poor ground can generate an excess of seismic forces in the lining.
- Damage at and near tunnel portals may be significant due to slope instability.
- Fatigue failure and then large deformations are strongly related to the duration of strong-motion shaking during the earthquake.
- Local spalling of rock or concrete along planes of weakness can be due to high frequency motion. These frequencies attenuate rapidly with distance and may be expected mainly at small distances from the fault.

- Amplification of the ground motion can be generated if wavelengths are between one and four times the tunnel diameter or the main dimension of the underground structure.

11.3 Seismic event

The Tel Beer Sheva archaeological site is located in the zone shown in Figure 11.1. Many seismic events were observed in Israel and neighbouring countries, especially along the Dead Sea Fault, near the Arava Rift Valley. The seismic event considered in the following is the Nuweiba earthquake, from the name of an Egyptian city near the Red Sea. This earthquake occurred on 22 November 1995, about 90km south of Eilat, where the original data was recorded. The earthquake magnitude was Mw = 7.1 and its main rupture, at a depth of 12.5km, consisted of two sub-events, 4s apart (Shamir, 1996; Baer et al., 1999).

Figure 11.1 – Map of Israel showing the Dead Sea Fault

The fault plane solution suggests a nearly pure strike-slip earthquake, with a small normal component, on a steeply dipping fault, striking NNE (Shamir, 1996). The effects of the earthquake were observed throughout Israel and neighbouring countries, especially along the Dead Sea Fault, within and near the Arava Rift Valley. The most significant damages due to this earthquake included triggering of landslides and cracking of buildings (Wust, 1997). Changes in water levels near the Dead Sea itself (Zilberbrand et al., 1996) and farther north, near the Sea of Galilee, were also observed.

Accelerations were recorded throughout a period of $60s$ in three directions (vertical, N-S and W-E) as shown in Figure 11.2. The Eilat seismological station is situated on a thick fill layer of Pleistocene alluvial fan deposits. The recorded accelerogram therefore represents the response of a site situated on deep fill layer rather than on sound bedrock. For this reason, direct application of the original Eilat record to the case of the Tel Beer Sheva rock site would be inappropriate.

Therefore, a deconvolution of the signal recorded at Eilat during the Nuweiba earthquake was performed. To this end, the software EERA was used (Bardet et al., 2000), which implements the well-known concepts of equivalent linear earthquake site response analysis and requires as input the original accelerogram (in this case the deconvoluted one) and ground characteristics. The output is an accelerogram involving site effects at each point of the stratigraphic model being used.

The model comprises a conglomerate layer of $8m$ and a chalk layer of $32m$. The chalk parameters (Table 11.1), not being available for the site of interest, were based on the results of laboratory tests performed on a chalk from the Givat Shemen site, in the Negev desert, not far from Tel Beer Sheva (Barla et al., 1991). Accordingly, a linear change of these properties versus depth was assumed by subdividing the chalk layer in sub-layers.

Table 11.1 – Mechanical properties of the site

Layer	Layer thickness $[m]$	Mass density $[kg/m^3]$	Shear wave velocity $[m/s]$
Conglomerate	8	1800	220
Chalk 1	15	1900	692
Chalk 2	17	1900	1735
Chalk 3: "bedrock"	-	2000	2200

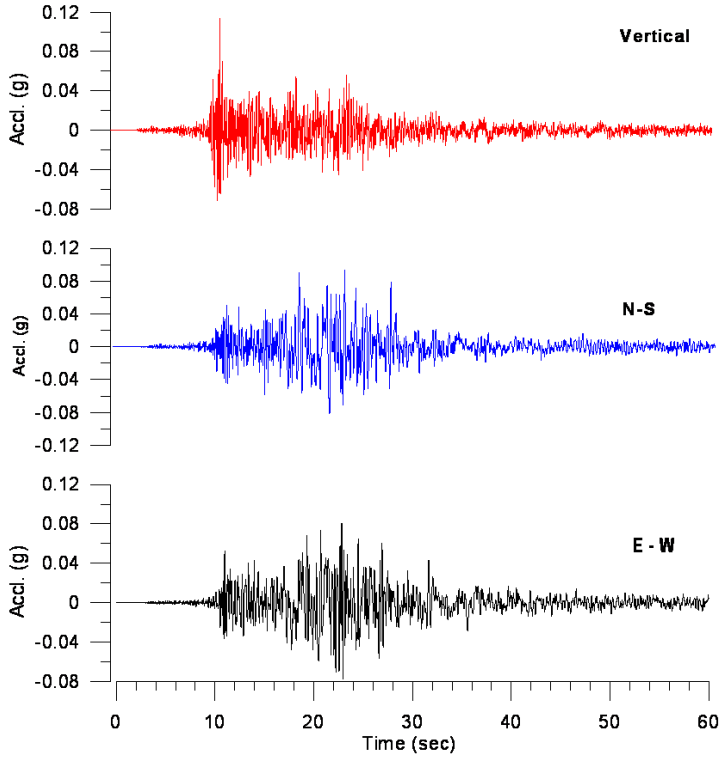

Figure 11.2 – Recorded accelerations in Eilat

EERA considers shear waves propagating vertically in a viscoelastic linear system, containing a certain number of layers extending to infinity in the horizontal direction. Each layer, homogeneous and isotropic, is characterised by the following parameters: thickness h, density ρ, shear modulus G and damping ratio D. G and D are assumed to change with shear strain as shown in Figure 11.3. As already noted, the magnitude of the seismic event (Nuweiba earthquake) is Mw = 7.1 (Yechieli et al. 2002).

EERA calculates the rock response to a seismic event and gives as output the highest absolute acceleration reached, the highest relative acceleration in each layer, the relative displacement, velocity, and absolute acceleration diagrams. It is noted that the absolute acceleration and relative velocity are used in the DEM model as dynamic input at the base boundary.

The trend for acceleration found gives values lower than $0.1g$, near the values expected in the area of Tel Beer Sheva, as shown in Figure 11.4, which illustrates a seismic hazard map of Israel. Tel Beer Sheva is located in the area where PGA is around $0.1g$.

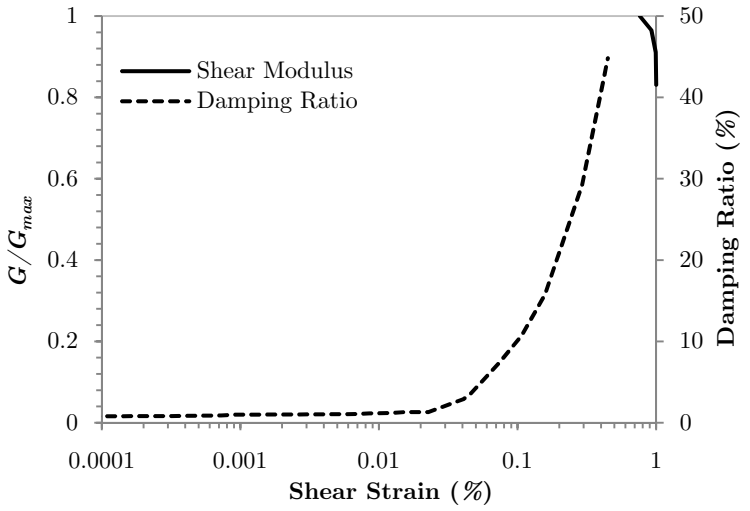

Figure 11.3 – Variation of G and D versus strain for chalk (Barla et al., 1991)

11.4 DEM modelling

Following the static analyses described in Chapter 11, dynamic analyses of the water storage cavern were performed in the present configuration with the support pillar system already described in the centre. To ensure that the most appropriate methods of modelling are used, the following main issues had to be addressed:

1. The DEM model is to satisfy the requirements for accurate wave transmission. The results of wave propagation through a DEM model without cavern are to be validated with SMM.
2. Appropriate mechanical damping, representative for the materials under study, and input frequency range, need be introduced. UDEC and 3DEC require two parameters to define the amount of Rayleigh damping: the minimum critical damping ratio ξ_{min} and the minimum frequency f_{min}. ξ_{min} is taken equal to 2%, according to the average value of natural material damping in dynamic conditions. f_{min} is taken equal to $7.5 Hz$.
3. Correct boundary conditions are to be applied in any analysis including the appropriate input for dynamic loading. In order to simulate an infinitely extended medium, viscous boundaries (Lysmer & Kuhlmeyer 1969) are introduced at both the vertical sides of the model. Dynamic loading has been applied at the bottom as horizontal and/or vertical wave velocity.

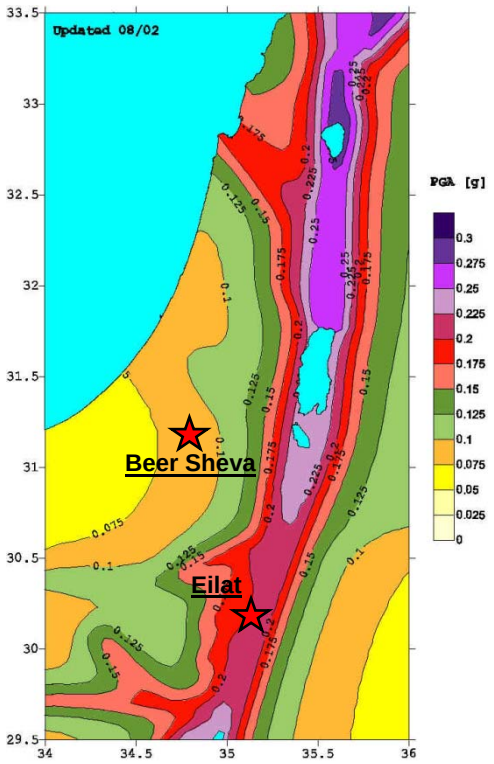

Figure 11.4 – Seismic hazard map of Israel. The Beer Sheva location is shown

Starting from the DEM models used in static analyses and following the previous suggestions, the DEM models for dynamic analyses were implemented. The UDEC model is $23m$ high and $60m$ wide as shown in Figure 11.5 while the 3DEC model is $23m$ high and $45m$ wide in two horizontal directions (Figure 11.20). In the 3DEC model, viscous boundaries were applied along the lateral boundaries and in x, y, z directions. The bottom was fixed in the vertical direction z.

The input motion was applied at the bottom of the models. It was filtered for a frequency corresponding to a wavelength (λ) 10 times the maximum length of a single element in the mesh (see Chapter 8) in order to allow correct wave propagation. A maximum size of the single element in the mesh less than $\lambda/10$ was assumed.

In the UDEC model the chalk is entirely discretized with blocks of 0.50x$0.25m$ for cross-section a-a and 0.50x$0.20m$ for cross-section b-b while two superficial layers are modelled as continuous. On the other hand, the 3DEC model is composed of an inner discontinuous zone and surrounded by a continuous one. The discontinuous zone is limited to the roof of the cavern while the other zones are

continuous (see Figure 11.6). The blocks are assumed of size 0.50x0.40x0.50m as smaller blocks would lead to an unacceptable exptension of the computational time.

11.5 Validation analysis of the free surface response

The accuracy of the DEM model used for dynamic analyses was verified using the DEM models without the cavern. The E-W component of Nuweiba earthquake was applied at the bottom of the models to evaluate the free surface response. These results are compared with the SMM developed in this thesis. As described in the previous paragraph the seismic input is obtained after an adequate deconvolution of the accelerogram recorded during the Nuweiba earthquake. The validation analyses are performed by considering only the bedding planes.

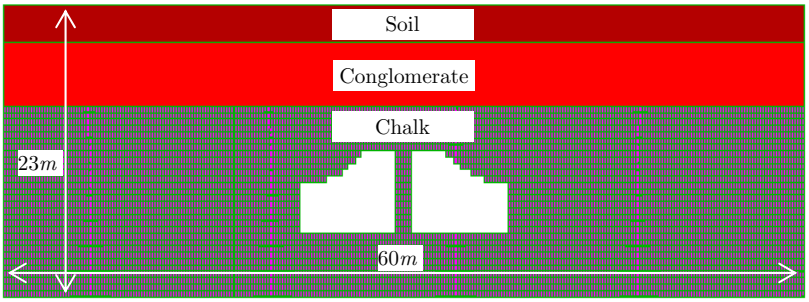

Figure 11.5 – 2D DEM model of the cross-section b-b

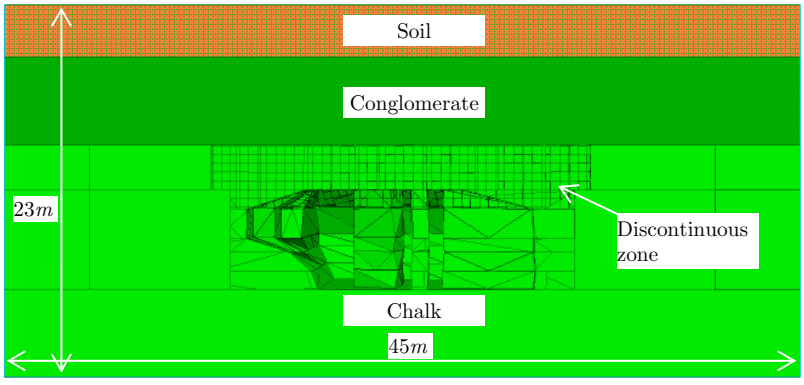

Figure 11.6 – 3D DEM model – View of the cross-section a-a

The UDEC model is $23m$ high and it is composed of 46 horizontal discontinuities with spacing $0.50m$. The deconvoluted signal was integrated to obtain the input in terms of velocities because UDEC does not allow the application of accelerations. The input can be assumed as a plane shear wave that impinges normally the set of horizontal bedding planes.

The free surface response obtained with the UDEC analyses was compared with that given by the SMM as illustrated in Figure 11.7. The SMM allows one to obtain results that are very near to those given by UDEC. Thus, the UDEC model can be considered adequate to represent the shear wave propagation problem.

On the other hand, the 3DEC model in this validation study was modified from that used in the following dynamic analyses (Figure 11.6). The model which is $13m$ height and $20m$ wide contain 26 parallel horizontal discontinuities. The comparison between the SMM and 3DEC results is not reported for brevity but the results are as good as those obtained in the SMM-UDEC comparison.

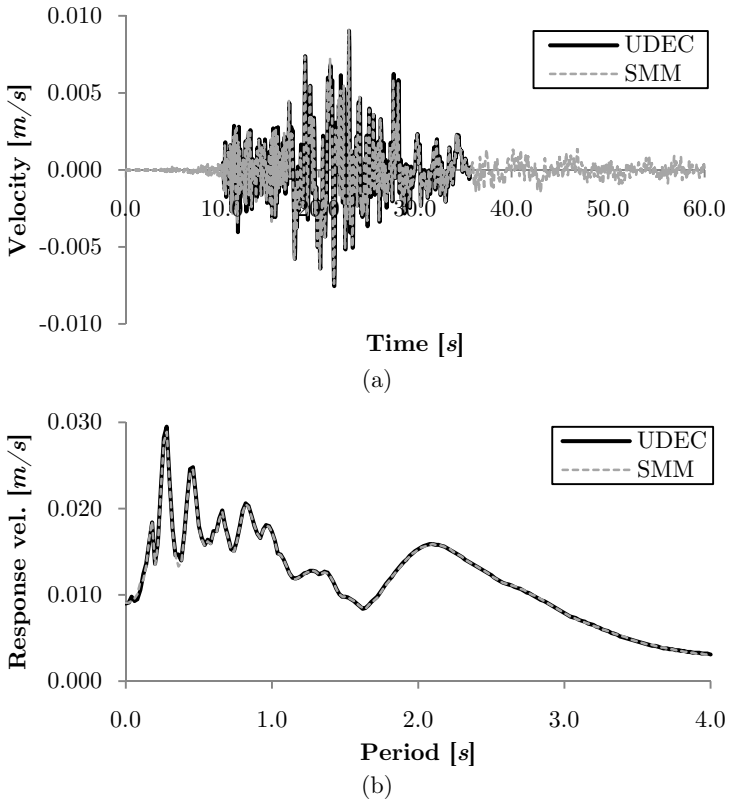

Figure 11.7 – Free surface response - Comparison of SMM and DEM modelling: (a) velocity time history and (b) response spectra with ratio of critical damping of 5%

As widely described in Chapters 4 and 5, the wave transmitted by a set of parallel joints depends on the joint spacing ratio ζ (= ratio between joint spacing d and wavelength λ). With the SMM the diagram of the transmission coefficient, for an incident sinusoidal shear wave pulse, versus the normalized joint spacing ratio can be obtained. This shows that in this case the transmission coefficient is essentially invariant with the increase of the number of parallel joints because $\zeta = 0.003$. In fact, a very small value of ζ means that the wavelength is much larger than the joint spacing and the transmission coefficient becomes independent of the number of joints.

The numerical models containing the horizontal bedding only can be considered adequate to simulate the problem to be studied in both two dimensional and three dimensional conditions. Considering that the rock mass containing the cavern is characterised by the presence of the vertical joint sets these were included in both the UDEC and 3DEC models. By performing the same analyses as described above with the horizontal joints only we have found that the free surface response when two joint sets are present in the model is reduced of about 15-20%.

11.6 2D analyses of the cavern

A series of dynamic analyses with the UDEC model shown in Figure 11.5 were performed first, with sinusoidal particle velocity inputs applied at the bottom of the same model. These analyses are performed by starting from the stable configuration of the cavern with the support pillar in its centre as shown in the cross-section b-b of Figure 10.16).

Sinusoidal P and S-waves with a frequency of $4Hz$ were applied. The amplitude of the acceleration waves was varied from $0.1g$ to $0.6g$. These acceleration waves are not applied directly to the UDEC model but were integrated to obtain the velocity waves because this code allows only the application of velocity or stress as input.

Figure 11.8 shows the deformed shapes of the cavern generated by an S-wave and a P-wave with vertical directions of propagation. These shapes are for an input amplitude of $0.60g$ but similar shape configurations could be obtained for other amplitudes.

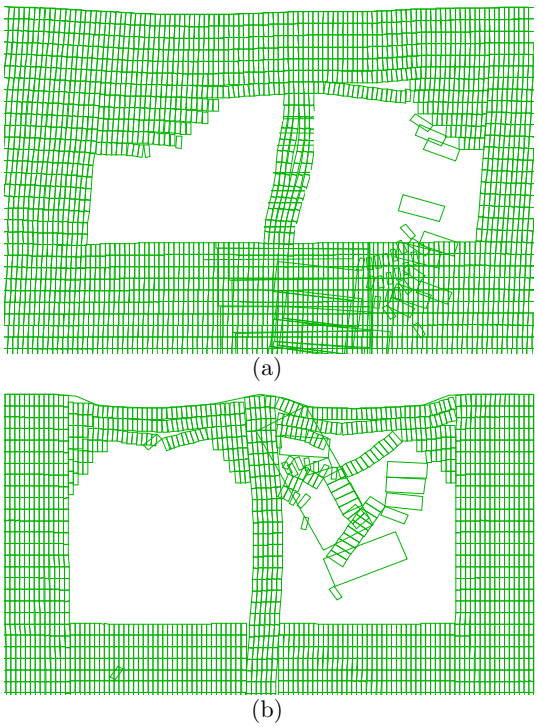

Figure 11.8 – Amplified deformed shapes of the cavern generated by an incident S-wave (a) and a P-wave (b) with vertical direction of propagation

The opening of the joints around the cavern is a good tool to evaluate the effects of the input waves. Figure 11.9 shows the extension of the joint openings and the falling down of blocks for incident S-waves obtained with different amplitudes. The extension of the joints opening zone and the collapsed area increases with the amplitude of the incident wave increasing. These analyses were performed with an input composed by 10 complete sinusoidal cycles.

As discussed in paragraph 11.2, the damage level is dependent on the duration of ground shaking. Figure 11.10 shows the comparison between the results obtained for a shear sinusoidal wave composed by 3 and 10 complete sinusoidal cycles and with amplitude of $0.40g$. The influence of the number of cycles of ground shaking on the stability of the cavern is evident.

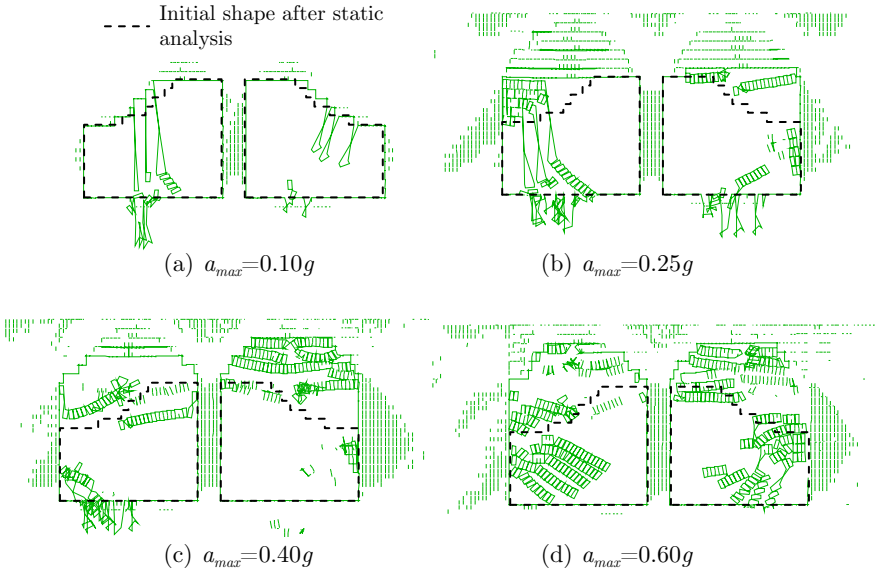

Figure 11.9 – Opening of the joints and falling down of blocks from the roof for an incident S-wave

Ground-shaking generated by the shear waves induces a redistribution of the stresses around the cavern. Figure 11.11 shows the principal stress trajectories following the end of shaking due to shear waves with amplitude 0.25 and 0.60g respectively. The collapse zone is located below the compressive arch which is generated in the static analyses when a stable configuration is attained. The shear wave with amplitude 0.60g induces a complete falling down of the blocks below this compressive arch (Figure 11.11b).

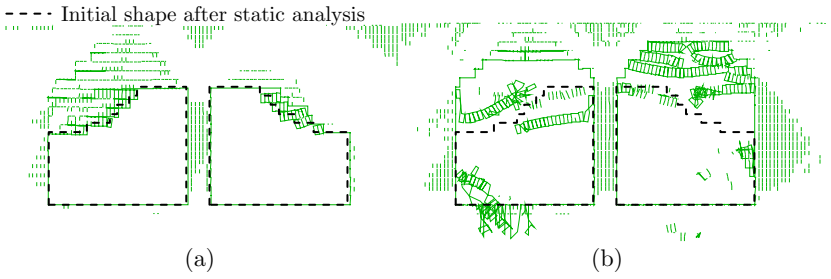

Figure 11.10 – Opening of the joints and falling down of blocks from the roof obtained by applying an incident vertical S-wave composed by 3 (a) and 10 (b) complete sinusoidal cycles and with amplitude of 0.40g

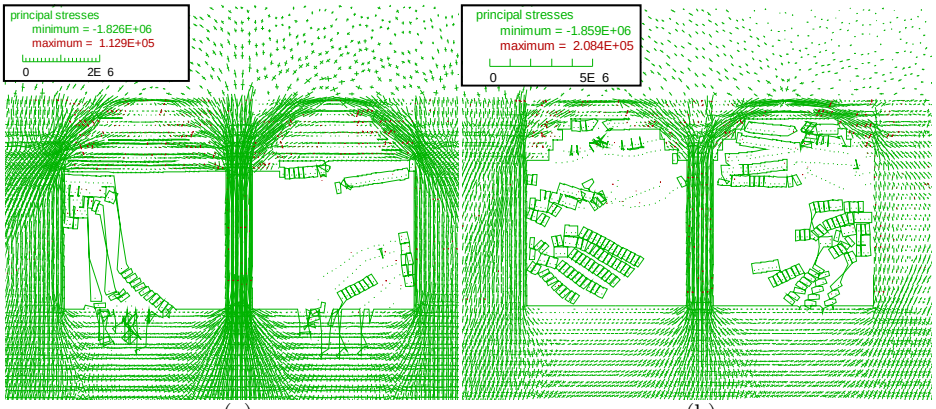

(a) (b)

Figure 11.11 – Principal stress (Pa) trajectories following the end of shaking due to S-waves with amplitudes $0.25g$ (a) and $0.60g$

The analyses performed with an incident plane P-wave with vertical direction of propagation are shown in Figure 11.12. The damage produced by the P-waves on the cavern is evident also for low values of amplitude of motion. When the collapse of the cavern occurs the vertical displacements measured at free surface are significant. Already for an input vertical acceleration of $0.25g$ the collapse of the roof is nearly complete.

By comparing the effects of the S and P-waves on the cavern we can observe that the P-waves produce a much greater damage than the S-waves.

Finally, we can state that the vertical or horizontal shaking produces the falling down of the blocks of the roof that are below the compressive arch. Indeed, the compressive stresses are low between these blocks.

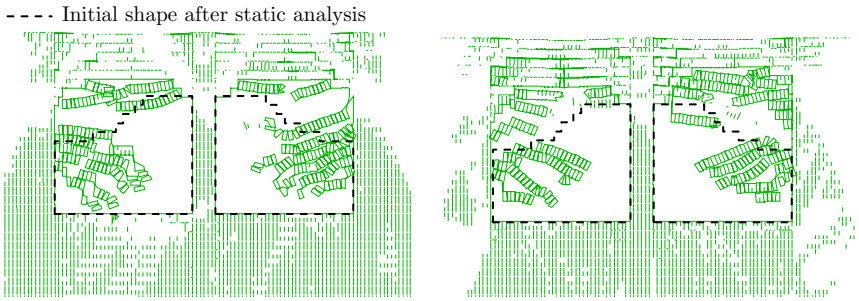

(a) a_{max}=0.10g (b) a_{max}=0.25g

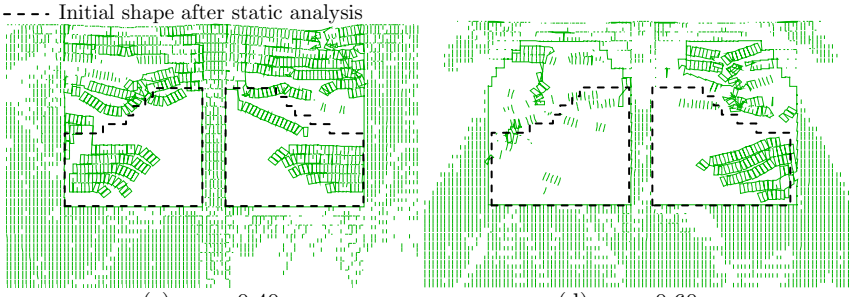

(c) a_{max}=0.40g (d) a_{max}=0.60g

Figure 11.12 – Opening of the joints and detachment of blocks from the roof for a vertical incident P-wave

Some parametrical analyses are conducted to evaluate the influence of the frequency of the applied wave on the damage. These analyses have shown that the damage decreases with the increasing of the frequency. As an example, low damage is evidenced if we apply a P-wave (composed by 10 sinusoidal cycles) with frequency of $50Hz$ and amplitude of $0.4g$ while if the frequency decreases the extension of collapsed zone on the roof of the cavern increases.

At this point we have run the same analyses, however by applying at the bottom of the model the deconvoluted accelerograms of the Nuweiba earthquake as shown in Figure 11.2. The deconvoluted E-W ($a_{max} = 0.048g$) and vertical ($a_{max} = 0.069g$) components were applied. The model used has the same size as in the previous analyses. Both the cross-section a-a and b-b were analysed. Given that the results obtained are very similar, only the results for cross-section b-b will be illustrated in the following.

The application of the horizontal component of motion generates the opening of joints and a change of the principal stress trajectories as shown in Figure 11.13. We can see that in this case only few blocks fall down from the roof of the cavern. The deformed shape is similar to that shown in Figure 11.8a. The distribution of horizontal and vertical displacements following the application of the maximum amplitude of the shear wave is depicted in Figure 11.14. It is observed that the vertical displacements due to the dynamic input motion are limited to 1-1.3mm.

With the vertical component of the deconvoluted accelerogram applied, the opening of the joints and the principal stress trajectories are as illustrated in Figure 11.15. In this case, a more significant falling down of blocks from the roof can be observed. The vertical displacement at free surface is about 3.3cm, much greater than the vertical displacements developed with the horizontal component of motion being applied.

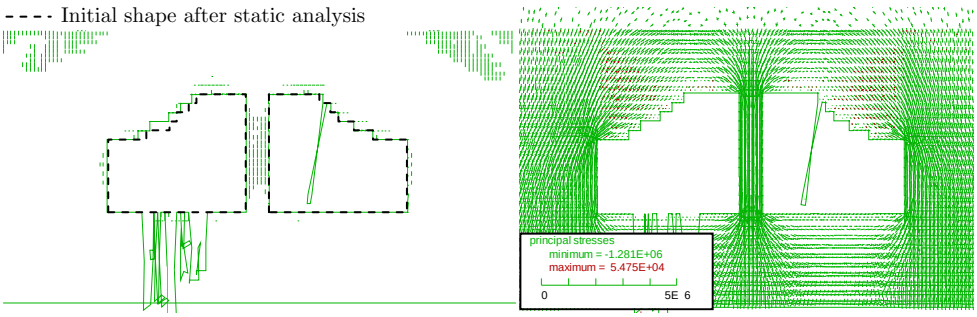

(a) (b)

Figure 11.13 – Opening of joints and principal stress (Pa) trajectories after the horizontal motion of the Nuweiba earthquake

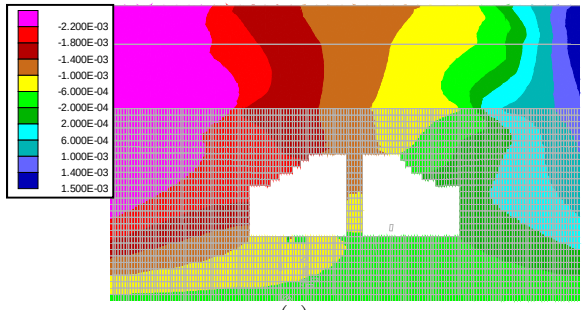

(a)

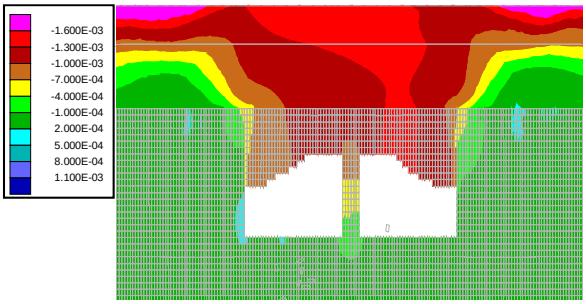

(b)

Figure 11.14 – Horizontal and vertical displacements (in m) distribution after the application of the maximum of the horizontal motion of the Nuweiba earthquake

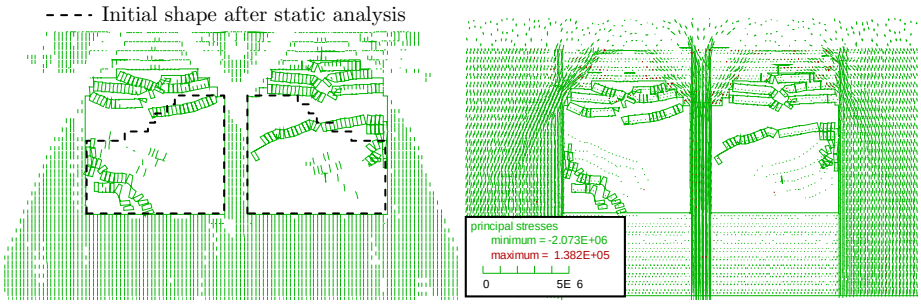

(a) (b)

Figure 11.15 – Opening of joints and principal stress (Pa) trajectories after the vertical motion of the Nuweiba earthquake

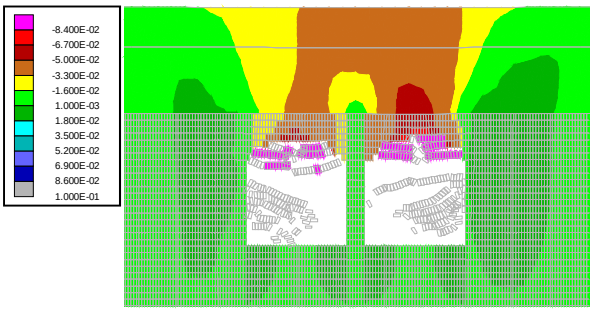

Figure 11.16 – Vertical displacements (in m) distribution after the application of the maximum vertical motion of the Nuweiba earthquake

An additional analysis with the horizontal and vertical components of the seismic motion simultaneously applied was also performed. It is shown that in such a case it is the vertical component that generates the greater damage. These analyses prove indeed that it is the vertical component of earthquake that needs more attention in the stability analyses and design analyses.

It is known that in reality the cavern did not experience any significant damage following the earthquake. The damage in the cavern as predicted by the numerical analyses performed with the seismic vertical component of motion applied, can be explained by the absence of any out-of-plane confinement. To verify this, three dimensional analyses were performed with the 3DEC code.

11.7 3D analyses of the cavern

The 3D analyses of the entire water storage system were performed with the three components of the Nuweiba earthquake being applied to the DEM model. We have assumed a horizontal stress ratio $K_0 = 0.3$ as in the static analyses. The dynamic analyses were performed by starting with the stable configuration of the cavern with the support system present. A vertical and two horizontal components of motion (Nuweiba earthquake) were applied at the bottom of the 3D model.

The main problem of the 3D dynamic analyses is the computer time needed. Obviously, the size of the model cannot be reduced as in the static analyses. Therefore, the decision was to perform the 3D analyses with blocks size 0.50x0.40x0.50m. The 3D model implemented in 3DEC code is shown in Figure 11.6 and 10.27. The external dimensions are shown in Figure 10.20.

Figures 11.17 and 11.18 show the magnitude of the displacements at the roof in cross-sections a-a and b-b. The maximum vertical and horizontal displacements at the roof are computed to be about 2.5mm and 3.5mm. No rock blocks fall down from the roof and the final configuration of the 3D cavern is stable.

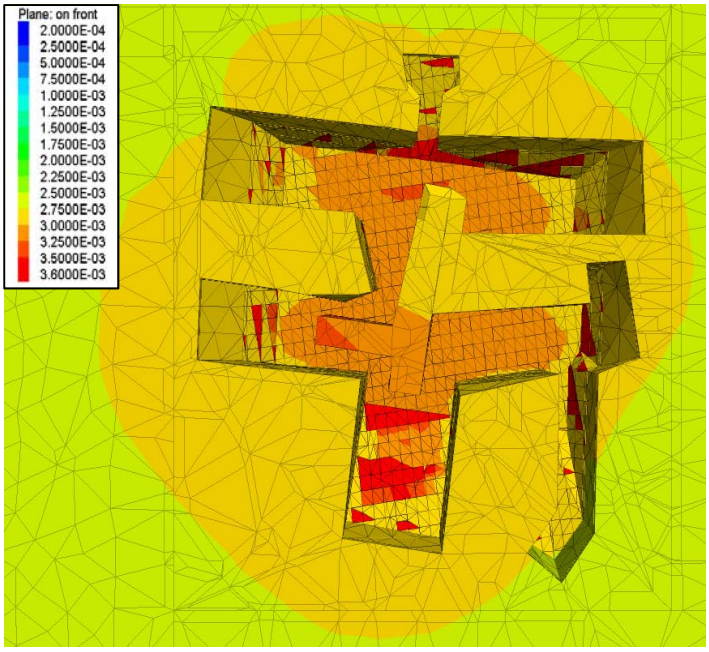

Figure 11.17 – Roof view: displacements magnitude (in m) distribution after the application of the Nuweiba earthquake

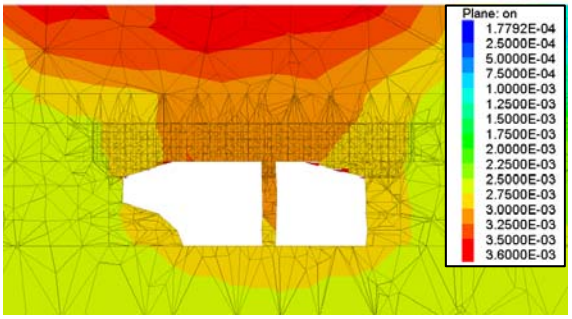

(a)

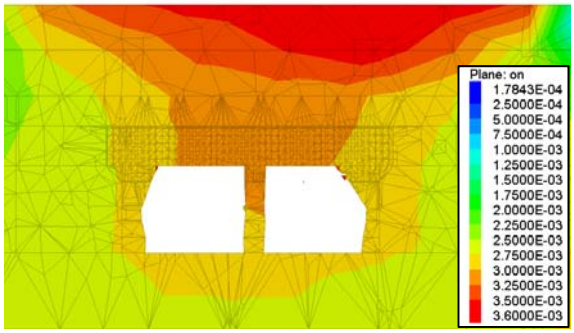

(b)

Figure 11.18 – Displacements magnitude (in m) distribution after the application of the Nuweiba earthquake: (a) cross-section a-a and (b) cross-section b-b

11.8 Summary

The stability of the underground water storage cavern of the archaeological site of Tel Beer Sheva, considered in the previous chapter in static conditions, has been analysed in this chapter with DEM and the UDEC and 3DEC codes in dynamic conditions.

The dynamic analyses have been carried out to study the present configuration of the cavern, with the stabilizing pillar in its centre, when subjected to shaking with the Nuweiba earthquake, a magnitude 7.1 event occurred in 1995, taken as representative for the site conditions.

Close attention has been given to the appropriate simulation of the rock mass conditions at the site, where the chalk formation comprises horizontal layers, $0.3m$ to $0.8m$ thick, alternating with some thinner (up to $0.1m$) layers of marly-chalk. Three joint sets are present including the bedding planes, which are horizontal with

mean spacing $0.50m$, and two vertical joint sets having as mean spacing $0.20m$ and $0.25m$ respectively.

The modelling of wave propagation has been shown to be well performed by appropriate comparative studies of SMM and DEM analyses. The effects of shear and compressional waves having different amplitude, frequency and duration on the stability of the cavern have been assessed with DEM analyses. The cavern has been shown to be more sensitive to vertical shaking than to horizontal one.

When the same analyses are performed in 2D conditions with the Nuweiba deconvoluted records applied, the vertical motion induces falling of blocks from the roof of the cavern, unlike it has been observed in situ. On the other hand, the results obtained with the corresponding 3D analyses demonstrate the overall stability of the cavern. This proves the existence of a three dimensional effect at the roof of the cavern which cannot be neglected.

Chapter 12

Summary and conclusions

12.1 Summary

The following main tasks have been accomplished in the present thesis:

- A detailed bibliographic study of wave propagation in rock masses was carried out. First, a description of the theories and the theoretical approaches used to solve wave propagation problems, with the main interest in discontinuous media, was given. Numerical methods used to model wave propagation phenomena were also described.

- The Scattering Matrix Method (SMM) was implemented and modified to allow one to simulate wave propagation through a single joint or a set of joints. All multiple reflections between the joints were considered. Dry, filled and frictional joints were modelled and parametric analyses were performed to evaluate the dependence of the quantities characterizing the joints on wave propagation.

- The validation of the SMM with other analytical, numerical and experimental methods was performed. The Discrete Element Method with the UDEC and 3DEC codes was also considered in detail with specific reference to the adequacy in modelling elastic wave propagation (single element size of the mesh, boundary conditions and model size).

- The Resonant Column Apparatus (RCA) was used to test intact and fractured rock specimens of a soft rock. Following a brief description of the equipment and of the interpretation procedures, the experimental results for intact or jointed rock specimens (containing up to three joints) were illustrated and compared with three-dimensional DEM modelling. Considerations about the dispersion of the shear wave velocity in fractured specimens were derived also in relation to the use of the SMM.

- The study of the influence of rock joints on the stability of the underground structures in static and dynamic conditions was carried out

by using the DEM in two and in three dimensional conditions. The UDEC and 3DEC codes were used to analyse the stability of the water storage cavern of the Tel Beer Sheva archaeological site in Israel.

- Static analyses were carried out to simulate the roof collapse undergone during construction and the stability of the present configuration of the cavern. Preliminary dynamic analyses were intended to study the dependence of the damage level on the amplitude, duration, frequency and direction of the dynamic motion in both horizontal and vertical directions. Finally, two and three-dimensional analyses were performed to evaluate the stability of the cavern in its present configuration with the application of the horizontal and vertical deconvoluted components of the Nuweiba earthquake (1995).

12.2 Conclusions

It is the purpose of the present chapter to draw some conclusions on the work presented. The following main aspects will be considered:

- Analytical approaches: the Scattering Matrix Method.
- Laboratory testing.
- Discrete Element Modelling of the Tel Beer Sheva cavern.

12.2.1 Analytical approaches: the Scattering Matrix Method

The Scattering Matrix Method (SMM) was developed with the intent to understand and to describe wave propagation through jointed rock masses. The following considerations can be made:

- The SMM is a simple tool which can be used effectively to analyse the influence of joints/discontinuities on wave propagation. The transmitted and reflected waves generated from an interface for an incident elastic wave can be analysed. All types of wave polarization (P, SV, SH) can be considered.

- SMM operates in frequency domain but can be also applied to transient waves (after FFT). This was proven to be true by comparing the SMM with numerical methods such as DEM and the Method of Characteristics.

- The Displacement Discontinuity Method (DDM) and the Thin Plate Layer Method (TPLM) were shown to model satisfactorily a joint only when its thickness d is much smaller than the wavelength λ (d / $\lambda < 0.1$).

- Linear elastic, viscoelastic and Coulomb slip models were implemented successfully with the SMM in order to simulate dry, filled and frictional joints. It was found that the admittance or compliance of the joint is the most significant parameter that influences the magnitude of the transmission and reflection coefficients.

- The Kelvin, Maxwell and Burger models, based on the modified split Hopkinson pressure bar (SHPB) tests and curve fitting, were found to describe satisfactorily the seismic response of viscoelastic joints filled with sand for P-wave incidence.

- When a periodic spatial distribution of joints is considered, the Bloch waves were found to be particularly appropriate for studying the wave propagation phenomenon. Simple expressions of the transmission and reflection coefficients for N joints were derived.

- Transmitted and reflected waves are significantly affected by the frequency content, angle of incidence, stiffness, viscosity, thickness, number and spacing of the joints. The filled joints response is also influenced by the impedance ratio between filling material and rock.

- The amplitude of the transmitted wave increases with the increasing of the joint stiffness and decreases with the increasing of the frequency and the number of joint. Moreover, $|T|$ decreases with the increasing of the joint thickness. The transmission coefficient becomes essentially independent from the number of joints when the ratio between the joint spacing and the wavelength is small.

- The effects of frictional joints on wave propagation were investigated. The Coulomb slip model was implemented to simulate the joint behaviour when non linear deformations are mobilised. The shear strength of the joint is the quantity that governs this problem. In fact, the transmission coefficient decreases with the increasing of the joint shear stress ratio. This is the ratio between the maximum of the incident shear stress wave and the shear strength.

- When slip occurs part of the incident energy is dissipated. This dissipation is evaluated with an absorption coefficient that increases rapidly for low

values of the shear stress ratio and tends to a constant value for large ones. Some considerations on the influence of the number of joints and the joint spacing on the transmission and reflection coefficients were given.

- The Maxwell analogy, that relates the electrical quantities with the mechanical quantities, allows one to prove analytically that the element size of $1/8\lambda$ of the mesh of the numerical model, prescribed by Kuhlemeyer & Lysmer (1973), can be used to model correctly the wave propagation across the mesh. In this case the error is assessed to be approximately 8%. Obviously lower values produce smaller errors in wave propagation modelling.

- With a comparative study with the SMM, the DEM codes such as UDEC and 3DEC are found to simulate accurately the wave propagation phenomena in rock masses. Some additional difficulties are experienced in the modelling of an oblique incident wave.

12.2.2 Laboratory testing

Laboratory tests, performed with the Resonant Column apparatus (RCA), have highlighted that:

- If the stiffness of the specimen becomes comparable with that of the RCA the shear modulus and then the shear wave velocity, obtainable from the interpretation of the experimental data, are underestimated. This problem does not occur with soil specimen where the stiffness of the specimen and then the resonant frequency are low. The correction factor depends on the inertia of the drive-system of the equipment. The RCA can be used without any correction if the resonant frequency measured for the specimen tested is lower than about $120 Hz$. When accounting for the correction factor, the error in the estimation of the shear wave velocity in intact specimens is reduced 4.8 times.

- The 3DEC code is able to model the RCA and to reproduce very well the experimental results. The RCA can be used for testing intact rock specimens and apparently can be also adopted for testing fractured specimens, as demonstrated by comparing the experimental results with the DEM results.

- The resonant frequency decreases with the increasing of the number of fractures. The entity of the effective velocity wave propagation is verified

with DEM and SMM analyses. Hence, the shear wave velocity decreases with increasing the number of fractures. A greater reduction of the shear wave propagation velocity occurs in the specimen with a single tooth fracture than that with a single smooth fracture. The maximum amplitude of the response increases with increasing the number of fractures.

- The free vibration decay of the response curves measured in laboratory tests is found to be very similar to that obtained with the DEM modelling of the RCA tests. Hence, the damping ratios of the material obtained experimentally and numerically are very similar.

- The attenuation of the wave energy due to the fractures is also observed in the damping ratio values. In fact, the damping ratios obtained for fractured specimens with the classical methods (half-power bandwidth method or amplitude decay method), are found to be greater than the damping ratio of the intact specimen. We think that part of the energy is likely to be attenuated by friction along the fractures.

- We have proven that the specimen is not completely loaded by torsional excitation when the resonant frequency of a fractured specimen becomes greater than that of an intact one. In these conditions the fractured specimen cannot be tested with the RCA.

12.2.3 DEM modelling of the Tel Beer Sheva cavern

A series of numerical analyses were carried out to study the stability of the water storage cavern of the Tel Beer Sheva archaeological site (Iron age 1200-700bc) located approximately near the modern city of Beer Sheva in Israel. The numerical DEM analyses were performed in two and in three dimensional conditions respectively with the DEM codes (UDEC and 3DEC) and were based on:

1. Back analyses of the cavern roof collapse as developed during the construction stages under gravitational loading.
2. Stability analyses of the cavern in the present configuration i.e. with the system of support pillars in place.
3. Seismic analyses of the cavern in the present configuration.

The analyses have highlighted that:

- The shape of the water storage cavern following failure can be simulated satisfactorily with DEM codes in two and three dimensional conditions.

- The analyses performed showed that the arching effect in the out-of-plane direction plays a very important role in the assessment of the cavern stability.

- The level of the in-situ horizontal stresses is the key parameter for the stability of large span caverns. The stability however is also influenced by the joint spacing and the joint orientation.

- The cavern in the present configuration with the supporting pillar system in place is stable under gravitational loading. The amplitude, the duration, the direction and the frequency of the applied dynamic motion have a large influence on the level of damage of the cavern.

- It is noted that the stability of the cavern is influenced by the vertical component of motion more than from the horizontal one. The horizontal motion produces shear deformations of the cavern while the vertical component generates compression and tension. Around the cavern, especially at the roof, the area where the joints are open increases with the increasing of the amplitude of the motion. The damage level increases with the increasing of the duration of the applied motion and decreases with the increasing of the frequency.

- As in the static analyses, also the dynamic analyses show that 2D modelling is more cautious than 3D modelling. In fact, with the cavern subjected to the Nuweiba earthquake (1995) the roof collapses in 2D conditions and with the vertical component of motion and does not develop any damage in 3D conditions.

- The dynamic analyses, performed in this thesis, show indeed that the vertical component of the earthquake motion needs more attention when performing design analyses for the assessment of stability of underground structures.

12.3 Recommendations for further developments

Further developments are needed as some open questions remain to be addressed for the study of wave propagation in rock masses and their effects on the stability of geotechnical structures. The following points are raised:

- Extension of the SMM to other more complex joint models. Evaluation of the effects on wave propagation of the presence of two joint sets mutually perpendicular or nearly perpendicular.

- Additional Resonant Column tests to be carried out for other geometries of fractures and for a greater number of fractures. Definition of the correction factors for the RCA by performing laboratory RCA tests on aluminium or steel specimens.

- Additional 3D dynamic analyses to evaluate the effects of the seismic motion on the Tel Beer Sheva cavern.

- Extension of 3D analyses to other case studies to better evaluate the effects of the earthquake especially on large underground openings. Hence, the definition of the link between the level of damage and the shape, the orientation of joints, the stress ratio, the frequency and the amplitude of the motion.

- The study of possible reinforcement systems to improve the stability of caverns or underground structures in general under dynamic loading.

Appendix A

Definition of the normalization coefficients

In this appendix, the normalization coefficients of plane wave polarization vectors will be defined. These coefficients guarantee that a unit amplitude wave carries a power density $P = 1\,W/m$.
The state vector in which are stored the velocity and the tractions can be defined as follows:

$$\begin{pmatrix} \mathbf{v} \\ -\mathbf{T}\cdot\hat{\mathbf{z}} \end{pmatrix} = \mathbf{c}^{+}\begin{pmatrix} \hat{\mathbf{v}}^{+} \\ -\mathbf{T}\cdot\hat{\mathbf{z}}^{+} \end{pmatrix} + \mathbf{c}^{-}\begin{pmatrix} \hat{\mathbf{v}}^{-} \\ -\mathbf{T}\cdot\hat{\mathbf{z}}^{-} \end{pmatrix} = \mathbf{c}^{+}\begin{pmatrix} \hat{\mathbf{v}}^{+} \\ \mathbf{Z}^{+}\cdot\hat{\mathbf{v}}^{+} \end{pmatrix} + \mathbf{c}^{-}\begin{pmatrix} \hat{\mathbf{v}}^{-} \\ \mathbf{Z}^{-}\cdot\hat{\mathbf{v}}^{-} \end{pmatrix} \tag{A.1}$$

where
$\mathbf{c}^{+}$ and $\mathbf{c}^{-}$ are the amplitudes of the incident and reflected waves.
The power density of a wave can be expressed as:

$$\begin{aligned} P &= -\frac{1}{2}\mathrm{Re}\left\{\mathbf{v}^{*}\cdot\mathbf{T}\cdot\hat{\mathbf{z}}\right\} = \\ &= \frac{1}{2}\mathrm{Re}\left\{\left(\mathbf{c}^{+*}\hat{\mathbf{v}}^{+*} + \mathbf{c}^{-*}\hat{\mathbf{v}}^{-*}\right)\left(\mathbf{c}^{+}\mathbf{Z}^{+}\hat{\mathbf{v}}^{+} + \mathbf{c}^{-}\mathbf{Z}^{-}\hat{\mathbf{v}}^{-}\right)\right\} = \\ &= \frac{1}{2}\mathrm{Re}\left\{\left|\mathbf{c}^{+}\right|^{2}\hat{\mathbf{v}}^{+*}\mathbf{Z}^{+}\hat{\mathbf{v}}^{+} + \left|\mathbf{c}^{-}\right|^{2}\hat{\mathbf{v}}^{-*}\mathbf{Z}^{-}\hat{\mathbf{v}}^{-} + \right. \\ &\quad \left. + \mathbf{c}^{+*}\mathbf{c}^{-}\hat{\mathbf{v}}^{+*}\mathbf{Z}^{-}\hat{\mathbf{v}}^{-} + \mathbf{c}^{+}\mathbf{c}^{-*}\hat{\mathbf{v}}^{-*}\mathbf{Z}^{+}\hat{\mathbf{v}}^{+}\right\} \end{aligned} \tag{A.2}$$

Obviously the components of the power depend on the wave polarization considered.

A.1 Computation of the normalization coefficients for a P wave:

The first step is the definition of the components of the power defined in the Equation (A.2)

$$\hat{\mathbf{v}}^{+*}\mathbf{Z}^{+}\hat{\mathbf{v}}^{+} = N^{P+*}\begin{pmatrix}\frac{\xi}{k_P} & 0 & \frac{k_{zp}^*}{k_p}\end{pmatrix}\frac{1}{\omega}\begin{bmatrix}C_{44}k_{zP} & 0 & C_{44}\xi\\ 0 & C_{44}k_{zP} & 0\\ C_{12}\xi & 0 & C_{11}k_{zP}\end{bmatrix}\begin{pmatrix}\frac{\xi}{k_P}\\ 0\\ \frac{k_{zP}}{k_P}\end{pmatrix}N^{P+} =$$

$$= \frac{\left|N^{P+}\right|^2}{\omega}\begin{pmatrix}\frac{\xi}{k_P} & 0 & \frac{k_{zP}^*}{k_P}\end{pmatrix}\begin{pmatrix}C_{44}2\frac{\xi k_{zP}}{k_P}\\ 0\\ C_{12}\frac{\xi^2}{k_P}+C_{11}\frac{k_{zP}^2}{k_P}\end{pmatrix} =$$

$$= \frac{\left|N^{P+}\right|^2}{\omega}\left[C_{44}2\frac{\xi^2 k_{zP}}{k_P^2}+C_{12}\frac{\xi^2 k_{zP}^*}{k_P^2}+C_{11}\frac{k_{zP}^2 k_{zP}^*}{k_P^2}\right] =$$

$$= \frac{\left|N^{P+}\right|^2}{\omega}\left[\frac{C_{44}2\xi^2 k_{zP}+\left(C_{11}-2C_{44}\right)\xi^2 k_{zP}^*+C_{11}k_{zP}^2 k_{zP}^*}{k_P^2}\right] =$$

$$= \frac{\left|N^{P+}\right|^2}{\omega}\left[\frac{C_{44}\left(k_{zP}-k_{zP}^*\right)2\xi^2+C_{11}k_{zP}^*\left(\xi^2+k_{zP}^2\right)}{k_P^2}\right] =$$

(with $\xi^2 + k_{zP}^2 = k_P^2$)

$$= \frac{\left|N^{P+}\right|^2}{\omega}\left[\frac{2C_{44}k_{zP}\xi^2-2C_{44}k_{zP}^*\xi^2+C_{11}k_{zP}^*}{k_P^2}\right] = \text{ if } k_{zP} \text{ is real}$$

$$= \frac{\left|N^{P+}\right|^2}{\omega}C_{44}k_{zP}$$

And then the other terms are the following:

$$\hat{\mathbf{v}}^{-*}\mathbf{Z}^{-}\hat{\mathbf{v}}^{-} = N^{P-*}\begin{pmatrix}\frac{\xi}{k_P} & 0 & -\frac{k_{zp}^*}{k_p}\end{pmatrix}\frac{1}{\omega}\begin{bmatrix}-C_{44}k_{zP} & 0 & C_{44}\xi\\ 0 & -C_{44}k_{zP} & 0\\ C_{12}\xi & 0 & -C_{11}k_{zP}\end{bmatrix}\begin{pmatrix}\frac{\xi}{k_P}\\ 0\\ -\frac{k_{zp}}{k_p}\end{pmatrix}N^{P-} =$$

$$= -\frac{\left|N^{P-}\right|^2}{\omega}C_{11}k_{zP}$$

if k_{zP} is real

$$\hat{\mathbf{v}}^{+*}\mathbf{Z}^{-}\hat{\mathbf{v}}^{-} = N^{P+*}\begin{pmatrix}\frac{\xi}{k_P} & 0 & \frac{k_{zp}^*}{k_p}\end{pmatrix}\frac{1}{\omega}\begin{bmatrix}-C_{44}k_{zP} & 0 & C_{44}\xi\\ 0 & -C_{44}k_{zP} & 0\\ C_{12}\xi & 0 & -C_{11}k_{zP}\end{bmatrix}\begin{pmatrix}\frac{\xi}{k_P}\\ 0\\ -\frac{k_{zp}}{k_p}\end{pmatrix}N^{P-} =$$

$$= \frac{N^{P+*}N^{P-}}{\omega}\left(-2\frac{\xi^2}{k_P^2}C_{44}\left(k_{zP}+k_{zP}^*\right)+C_{11}k_{zP}^*\right)$$

$$\hat{\mathbf{v}}^{-*}\mathbf{Z}^{+}\hat{\mathbf{v}}^{+} = N^{P-*}\begin{pmatrix}\frac{\xi}{k_P} & 0 & -\frac{k_{zp}^*}{k_p}\end{pmatrix}\frac{1}{\omega}\begin{bmatrix}C_{44}k_{zP} & 0 & C_{44}\xi\\ 0 & C_{44}k_{zP} & 0\\ C_{12}\xi & 0 & C_{11}k_{zP}\end{bmatrix}\begin{pmatrix}\frac{\xi}{k_P}\\ 0\\ \frac{k_{zp}}{k_p}\end{pmatrix}N^{P+} =$$

$$= -\frac{N^{P+}N^{P-*}}{\omega}\left(-2\frac{\xi^2}{k_P^2}C_{44}\left(k_{zP}+k_{zP}^*\right)+C_{11}k_{zP}^*\right)$$

The normalization coefficients can be defined:

$$N^{P+} = N^{P-} = \sqrt{\frac{\omega}{C_{11}k_{zP}}} \text{ if } k_{zP} \text{ is real}$$

$$N^{P+} = N^{P-} = \sqrt{\frac{\omega}{C_{11}k_{zP}}} \text{ if } k_{zP} = -j\alpha \text{ is imaginary } \left(\alpha > 0\right)$$

A.2 Computation of the normalization coefficients for a SV wave:

By following the previous procedure used for P-waves we obtain:

$$\hat{\mathbf{v}}^{+*}\mathbf{Z}^{+}\hat{\mathbf{v}}^{+} = N^{SV+*}\begin{pmatrix} \frac{k_{zS}^{*}}{k_S} & 0 & -\frac{\xi}{k_S}\end{pmatrix}\frac{1}{\omega}\begin{bmatrix} C_{44}k_{zS} & 0 & C_{44}\xi \\ 0 & C_{44}k_{zS} & 0 \\ C_{12}\xi & 0 & C_{11}k_{zS}\end{bmatrix}\begin{pmatrix} \frac{k_{zS}}{k_S} \\ 0 \\ -\frac{\xi}{k_S}\end{pmatrix}N^{SV+} =$$

$$= \frac{\left|N^{SV+}\right|^2}{\omega}C_{44}k_{zS}$$

if k_{zS} is real

$$\hat{\mathbf{v}}^{-*}\mathbf{Z}^{-}\hat{\mathbf{v}}^{-} = N^{SV-*}\begin{pmatrix} \frac{k_{zS}^{*}}{k_S} & 0 & \frac{\xi}{k_S}\end{pmatrix}\frac{1}{\omega}\begin{bmatrix} C_{44}k_{zS} & 0 & C_{44}\xi \\ 0 & C_{44}k_{zS} & 0 \\ C_{12}\xi & 0 & C_{11}k_{zS}\end{bmatrix}\begin{pmatrix} \frac{k_{zS}}{k_S} \\ 0 \\ \frac{\xi}{k_S}\end{pmatrix}N^{SV+} =$$

$$= -\frac{\left|N^{SV-}\right|^2}{\omega}C_{44}k_{zS}$$

if k_{zS} is real

$$\hat{\mathbf{v}}^{+*}\mathbf{Z}^{-}\hat{\mathbf{v}}^{-} = N^{SV+*}\begin{pmatrix} \frac{k_{zS}^{*}}{k_S} & 0 & -\frac{\xi}{k_S}\end{pmatrix}\frac{1}{\omega}\begin{bmatrix} -C_{44}k_{zS} & 0 & C_{44}\xi \\ 0 & -C_{44}k_{zS} & 0 \\ C_{12}\xi & 0 & -C_{11}k_{zS}\end{bmatrix}\begin{pmatrix} \frac{k_{zS}}{k_S} \\ 0 \\ \frac{\xi}{k_S}\end{pmatrix}N^{SV-} =$$

$$= \frac{N^{SV+*}N^{SV-}}{\omega}\begin{pmatrix}\frac{k_{zS}^*}{k_S} & 0 & -\frac{\xi}{k_S}\end{pmatrix}\begin{bmatrix}-C_{44}k_{zS} & 0 & C_{44}\xi \\ 0 & -C_{44}k_{zS} & 0 \\ C_{12}\xi & 0 & -C_{11}k_{zS}\end{bmatrix}\begin{pmatrix}-C_{44}\dfrac{k_{zS}^{*\,2}-\xi^2}{k_S} \\ 0 \\ C_{12}\dfrac{k_{zS}\xi}{k_S} - C_{11}\dfrac{k_{zS}\xi}{k_S}\end{pmatrix} =$$

$$= \frac{N^{SV+*}N^{SV-}}{\omega}C_{44}\left\{\frac{-k_{zS}^*\left(k_S^2-2\xi^2\right)+2k_{zS}\xi^2}{k_S^2}\right\}$$

$$\hat{\mathbf{v}}^{-*}\mathbf{Z}^{+}\hat{\mathbf{v}}^{+} = N^{SV-*}\begin{pmatrix}\frac{k_{zS}^*}{k_S} & 0 & \frac{\xi}{k_S}\end{pmatrix}\frac{1}{\omega}\begin{bmatrix}C_{44}k_{zS} & 0 & C_{44}\xi \\ 0 & C_{44}k_{zS} & 0 \\ C_{12}\xi & 0 & C_{11}k_{zS}\end{bmatrix}\begin{pmatrix}\frac{k_{zS}}{k_S} \\ 0 \\ -\frac{\xi}{k_S}\end{pmatrix}N^{SV+} =$$

$$= \frac{N^{SV+}N^{SV-*}}{\omega}C_{44}\left\{\frac{k_{zS}^*\left(k_S^2-2\xi^2\right)-2k_{zS}\xi^2}{k_S^2}\right\}$$

After the definition of the terms of the power of the wave, we can compute the normalization coefficients for having a unit power.
By assuming $N^{SV+} = N^{SV-}$ we obtain the final expression of the normalization coefficients for the forward and the backward waves:

$$\left|N^{SV+}\right|^2 = \left|N^{SV-}\right|^2 = \frac{\omega}{C_{44}\beta} \rightarrow \left|N^{SV+}\right| = \left|N^{SV-}\right| = \sqrt{\frac{\omega}{C_{44}\beta}} \text{ with } k_{zS} \text{ real}$$

$$\left|N^{SV+}\right|^2 = \left|N^{SV-}\right|^2 = \frac{\omega}{C_{44}\alpha} \rightarrow \left|N^{SV+}\right| = \left|N^{SV-}\right| = \sqrt{\frac{\omega}{C_{44}\alpha}} \text{ with } k_{zS} = -j\alpha$$

$\alpha > 0$ imaginary

A.3 Computation of the normalization coefficients for a SH wave:

The terms of the wave power can be defined for a SH wave with the same procedure used before for a SV wave:

$$\hat{\mathbf{v}}^{+*}\mathbf{Z}^{+}\hat{\mathbf{v}}^{+} = \begin{pmatrix} 0 & N^{SH+*} & 0 \end{pmatrix} \frac{1}{\omega} \begin{bmatrix} C_{44}k_{zS} & 0 & C_{44}\xi \\ 0 & C_{44}k_{zS} & 0 \\ C_{12}\xi & 0 & C_{11}k_{zS} \end{bmatrix} \begin{pmatrix} 0 \\ N^{SH+} \\ 0 \end{pmatrix} = \frac{\left| N^{SH+} \right|^2}{\omega} C_{44}k_{zS}$$

if k_{zS} is real

$$\hat{\mathbf{v}}^{-*}\mathbf{Z}^{-}\hat{\mathbf{v}}^{-} = \begin{pmatrix} 0 & N^{SH-*} & 0 \end{pmatrix} \frac{1}{\omega} \begin{bmatrix} -C_{44}k_{zS} & 0 & C_{44}\xi \\ 0 & -C_{44}k_{zS} & 0 \\ C_{12}\xi & 0 & -C_{11}k_{zS} \end{bmatrix} \begin{pmatrix} 0 \\ N^{SH-} \\ 0 \end{pmatrix} =$$

$$= -\frac{\left| N^{SH-} \right|^2}{\omega} C_{44}k_{zS}$$

if k_{zS} is real

$$\hat{\mathbf{v}}^{+*}\mathbf{Z}^{-}\hat{\mathbf{v}}^{-} = \begin{pmatrix} 0 & N^{SH+*} & 0 \end{pmatrix} \frac{1}{\omega} \begin{bmatrix} -C_{44}k_{zS} & 0 & C_{44}\xi \\ 0 & -C_{44}k_{zS} & 0 \\ C_{12}\xi & 0 & -C_{11}k_{zS} \end{bmatrix} \begin{pmatrix} 0 \\ N^{SH-} \\ 0 \end{pmatrix} =$$

$$= -\frac{N^{SH+*}N^{SH-}}{\omega} C_{44}k_{zS}$$

if k_{zS} is real

$$\hat{\mathbf{v}}^{-*}\mathbf{Z}^{+}\hat{\mathbf{v}}^{+} = \begin{pmatrix} 0 & N^{SH-*} & 0 \end{pmatrix} \frac{1}{\omega} \begin{bmatrix} C_{44}k_{zS} & 0 & C_{44}\xi \\ 0 & C_{44}k_{zS} & 0 \\ C_{12}\xi & 0 & C_{11}k_{zS} \end{bmatrix} \begin{pmatrix} 0 \\ N^{SH+} \\ 0 \end{pmatrix} =$$

$$= \frac{N^{SH+}N^{SH-*}}{\omega} C_{44}k_{zS}$$

if k_{zS} is real

Finally the normalization coefficients are the following:

$$N^{SH+} = N^{SH-} = \sqrt{\frac{\omega}{C_{44} k_{zS}}} \quad \text{if } k_{zS} \text{ is real}$$

$$N^{SH+} = N^{SH-} = \sqrt{\frac{\omega}{C_{44} \alpha}} \quad \text{if } k_{zS} = -j\alpha \text{ is imaginary } \left(\alpha > 0\right)$$

Appendix B

Database of seismic damage to underground structures

The database of seismic damage to underground structures (see Table B.1-B.2-B.3), obtained through a research of documented case histories, is reported in the following.

In Figure B.1-B.8 we can see respectively the graphs showing the effects of the overburden depth, of the surrounding rock type, of the type of internal support, of the earthquake magnitude, of the epicentral distance, of the surface PGA, of the surface PGV and of the distance between the underground structure and the fault on the damage level. The number of case histories analysed in the Figures B.1-B.6 is 348 while for Figures B.7-B.8 is only 129 because we did not find all the data about the fault necessary to compute the distance underground structure – fault and the surface PGV.

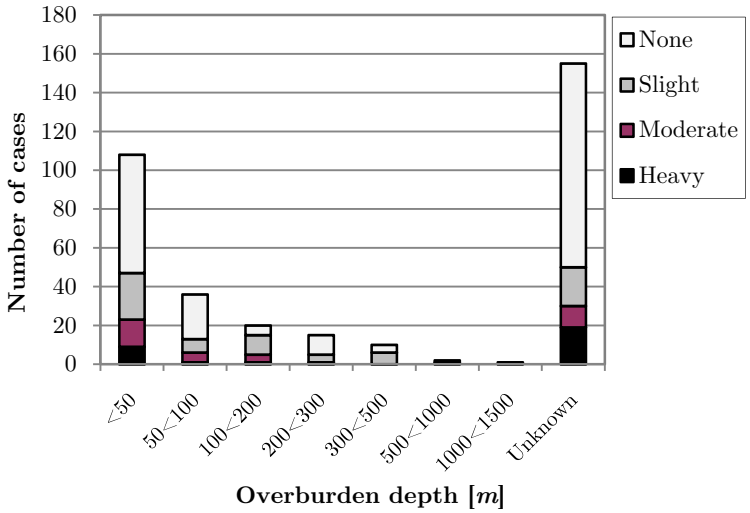

Figure B.1 - Effects of overburden depth on damage level

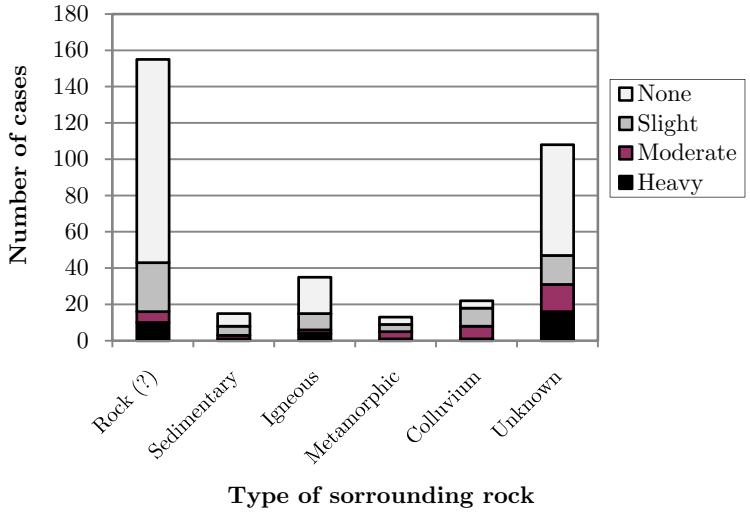

Figure B.2 - Effects of surrounding rock type on damage level

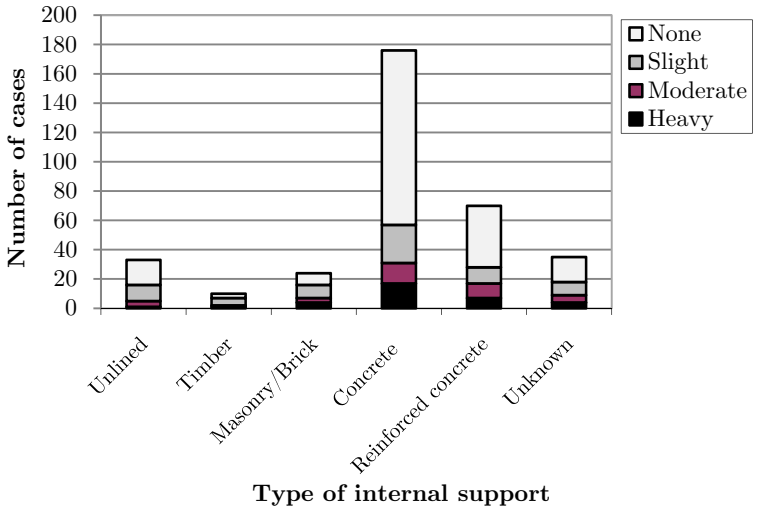

Figure B.3 - Effects of type of internal support on damage level

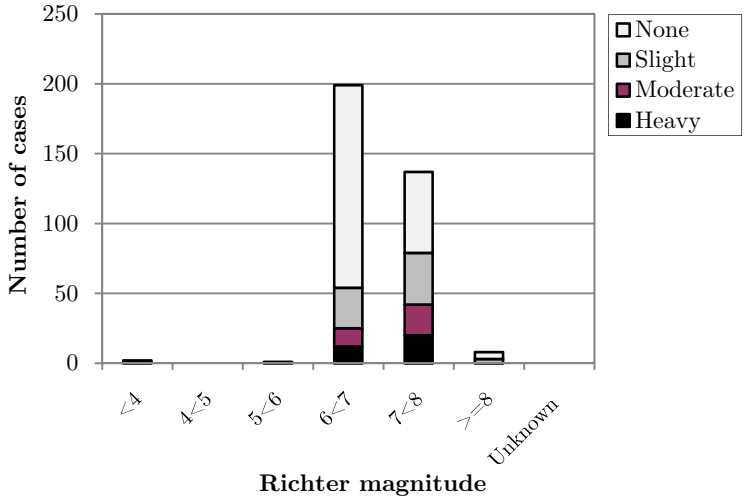

Figure B.4 - Effects of Richter magnitude on damage level

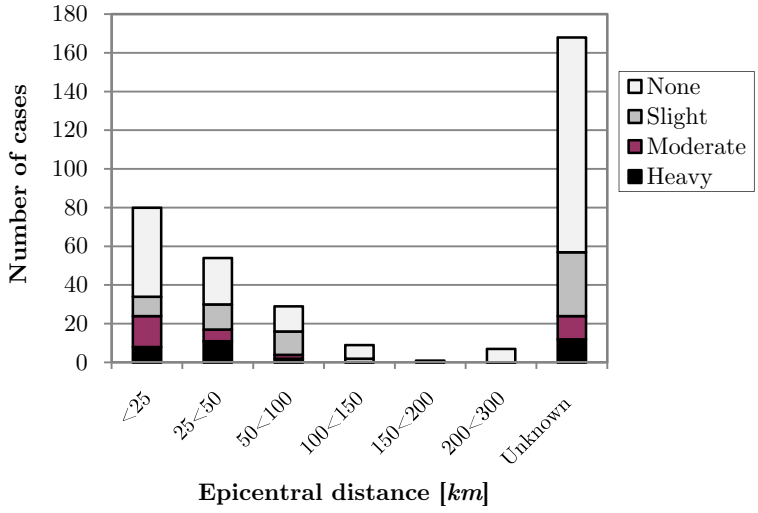

Figure B.5 - Effects of epicentral distance on damage level

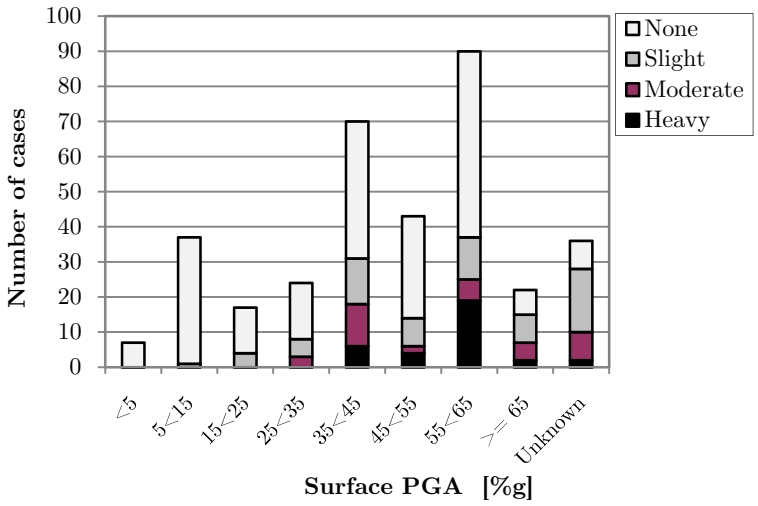

Figure B6 - Effects of surface PGA on damage level

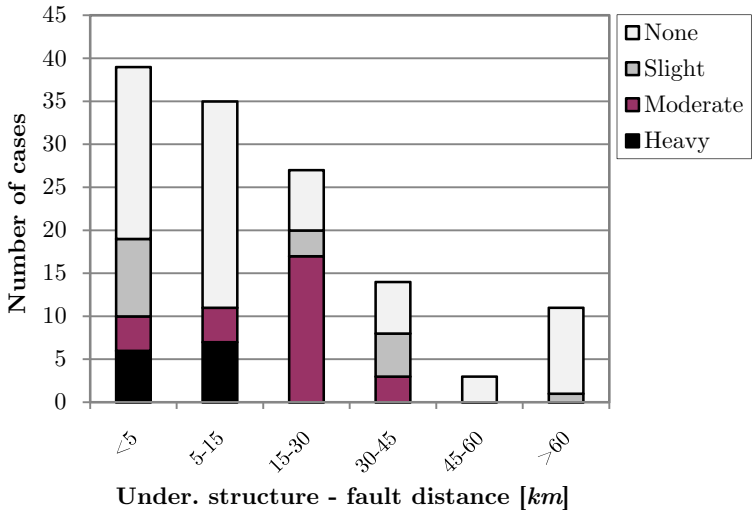

Figure B.7 - Effects of underground structure – fault distance on damage level

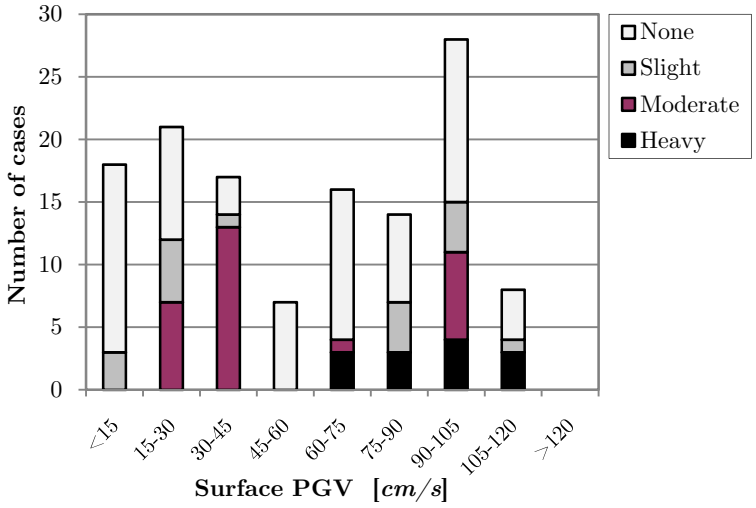

Figure B.8 - Effects of surface PGV on damage level

Table B.1 – Legend for the database summarized in Table B.2

Damage level		**Characteristics**
1	None	Damage not detected
2	Slight	Formation of cracks, displacement, strain small-scale
3	Moderate	Formation of significant cracks, detachment of the lining and strong deformations of the roof and rupture of the tunnel invert
4	Heavy	Collapse of the underground structure

Rock type	
Rock (?)	R
Sedimentary	S
Igneous	I
Metamorphic	M
Colluvium	C
Unknown	N

Rock support type	
Unlined	1
Timber	3
Masonry/Brick	4
Concrete	5
Reinforced concrete	6
Unknown	9

Table B.2 – Database of seismic damage to underground structures

N°	Earth-quake	Date	Name tunnel	Dama-ge level	Cover [m]	Rock type	Rock sup. type	Mom. Magni-tude	PGA [g]	Epic. dist. [km]
1	Sonoka, Mexico	03/05/ 1887	Tombstone Mine, Arizona, USA	2	46	R	1.00	7.4	N	130.00
2	Sonoka, Mexico	03/05/ 1887	Tombstone Mine, Arizona, USA	2	152	R	1.00	7.4	N	N
3	Sonoka, Mexico	03/05/ 1887	Tombstone Mine, Arizona, USA	2	152	R	1.00	7.4	N	N
4	San Francisco, CA	18/04/ 06	Wrigth Tunnel #2 near Los Gatos	1	206	R	4	7.8	0.13	135.80
5	San Francisco, CA	18/04/ 06	Wrigth Tunnel #1 near Los Gatos	1	214	R	4	7.8	0.13	135.00
6	San Francisco, CA	18/04/ 06	SF #1	1	24	R	4	7.8	0.41	45.00
7	San Francisco, CA	18/04/ 06	SF#3	2	46	R	4	7.8	0.41	46.00
8	San Francisco, CA	18/04/ 06	SF#4	1	24	R	1	7.8	0.43	47.00
9	San Francisco, CA	18/04/ 06	SF#5	2	24	R	4	7.8	0.45	50.00
10	San Francisco, CA	18/04/ 06	CorteM.T,	2	60	R	4	7.8	0.38	52.00
11	San Francisco, CA	18/04/ 06	PilarcitosRes #1	2	68	R	4	7.8	0.65	55.00
12	San Francisco	18/04/ 06	PilarcitosRes #2	2	152	R	3.00	7.8	0.65	60.00
13	San Francisco, CA	18/04/ 06	PilarcitosRes #3	2	137	R	3.00	7.8	0.69	135.00
14	Kanto, Japan	01/10/ 23	Terao Tunnel	2	N	N	1	7.9	0.47	31.60
15	Kanto, Japan	01/10/ 23	Hichigama Tunnel	1	N	R	4	7.9	0.42	36.40

N°	Earth-quake	Date	Name tunnel	Dama-ge level	Cover [m]	Rock type	Rock sup. type	Mom. Magni-tude	PGA [g]	Epic. dist. [km]
16	Kanto, Japan	01/10/23	Taura Tunnel	1	15	N	4	7.9	0.47	31.60
17	Kanto, Japan	01/10/23	Numana Tunnel	2	N	N	4	7.9	0.35	46.00
18	Kanto, Japan	01/10/23	Nokogiri-Yama Tunnel	2	N	S	1	7.9	0.24	70.70
19	Kanto, Japan	01/10/23	Kanome-Yama Tunnel	2	N	N	5	7.9	0.52	26.90
20	Kanto, Japan	01/10/23	Ajo Tunnel	2	N	N	1	7.9	0.55	25.00
21	Kanto, Japan	01/10/23	Ippamatzu Tunnel	3	N	N	1	7.9	0.55	25.00
22	Kanto, Japan	01/10/23	Nagoye	2	30	N	9.00	7.9	0.4	30.00
23	Kanto, Japan	01/10/23	Meno-Kamiana	3	17	R	4.00	7.9	0.6	16.50
24	Kanto, Japan	01/10/23	Yonegami Yama	2	50	R	4.00	7.9	0.66	50.00
25	Kanto, Japan	01/10/23	ShimomakiMatsu	3	29	S	4.00	7.9	0.69	29.00
26	Kanto, Japan	01/10/23	Happon-Matzu	3	20	N	9.00	7.9	0.73	20.00
27	Kanto, Japan	01/10/23	Nagasha-Yama	3	90	N	4.00	7.9	0.73	90.00
28	Kanto, Japan	01/10/23	Hakone#1	2	61	N	5.00	7.9	0.72	61.00
29	Kanto, Japan	01/10/23	Hakone#2	3	61	N	9.00	7.9	0.72	15.60
30	Kanto, Japan	01/10/23	Komine	2	6	R	6.00	7.9	0.52	26.90
31	Kanto, Japan	01/10/23	Fudu San	3	18	R	6.00	7.9	0.5	24.00

N°	Earth-quake	Date	Name tunnel	Dama-ge level	Cover [m]	Rock type	Rock sup. type	Mom. Magni-tude	PGA [g]	Epic. dist. [km]
32	Kanto, Japan	01/10/23	Hakone#3	4	46	R	9.00	7.9	0.56	17.20
33	Kanto, Japan	01/10/23	Hakone#4	4	46	S	9.00	7.9	0.54	19.70
34	Kanto, Japan	01/10/23	Hakone#7	4	31	R	9.00	7.9	0.63	22.40
35	Kanto, Japan	01/10/23	Yose	2	20	S	9.00	7.9	0.33	26.90
36	Kanto, Japan	01/10/23	Doki	3	N	S	9.00	7.9	0.25	61.00
37	Kanto, Japan	01/10/23	Namuya	2	75	N	9.00	7.9	0.52	63.00
38	Kanto, Japan	01/10/23	Mineoka-Yama	2	150	M	9.00	7.9	0.26	65.00
39	Kita-Tango, Japan	1927	railway tunnel	4	N	M	9.00	7.3	N	N
40	Kita-Izu, Japan	26/11/30	Tanna Tunnel, Japan	2	150	I	6.00	7	N	N
41	N. Idaho, USA	09/05/44	Morning Mine, Idaho, USA	3	1350	R	1.00	5	N	N
42	Fukui, Japan	1948	Kumasaka	2	N	N	4.00	7.2	0.3	25.00
43	Tokachi-oki, Japan	1952	railway tunnel	2	N	N	4.00	8	N	N
44	Kern County, CA	21/07/52	Saugus	1	40	R	1	7.3	0.06	N
45	Kern County, CA	21/07/52	SanFrancisquito	1	160	R	1	7.3	0.08	N
46	Kern County, CA	21/07/52	Elizabeth	1	250	R	1	7.3	0.1	55.15
47	Kern County, CA	21/07/52	Antelope	1	30	R	1	7.3	0.16	136.67

N°	Earth-quake	Date	Name tunnel	Dama-ge level	Cover [m]	Rock type	Rock sup. type	Mom. Magni-tude	PGA [g]	Epic. dist. [km]
48	Kern County, CA	21/07/ 52	S.P.R.R. Tunnel #3	1	46	M	1	7.3	0.24	25.81
49	Kern County, CA	21/07/ 52	S.P.R.R. Tunnel #4	1	38	M	5.00	7.3	0.24	36.88
50	Kern County, CA	21/07/ 52	S.P.R.R. Tunnel #5	1	76	M	5.00	7.3	0.24	59.77
51	Kern County, CA	21/07/ 52	S.P.R.R. Tunnel #6	1	15	M	5.00	7.3	0.24	77.10
52	Kita-Mino, Japan	1961	Aqueduct tunnel	1	N	C	9.00	7	N	N
53	Kita-Mino, Japan	1962	Powerhouse	2	N	C	9.00	7	0.25	32.00
54	Niigata, Japan	1964	Nezugaseki	2	N	C	9.00	7.5	N	N
55	Niigata, Japan	1964	Terasaka	2	N	C	9.00	7.5	N	N
56	Great Alaskan, USA	27/03/ 64	Whittier RR Tunnel #1, Alaska, USA	2	400	R	3	8.4	0.22	75.00
57	Great Alaskan, USA	27/03/ 64	Whittier RR Tunnel #2, Alaska, USA	2	350	R	3	8.4	0.21	75.00
58	Great Alaskan, USA	27/03/ 64	Seward#1	2	20	R	1	8.4	0.25	85.00
59	Great Alaskan, USA	27/03/ 64	Seward#2	1	20	R	1	8.4	0.25	85.00
60	Great Alaskan, USA	27/03/ 64	Seward#3	1	20	R	1	8.4	0.25	100.00
61	Great Alaskan, USA	27/03/ 64	Seward#4	1	20	R	1	8.4	0.25	100.00
62	Great Alaskan, USA	27/03/ 64	Seward#5	1	20	R	1	8.4	0.25	110.00
63	Great Alaskan, USA	27/03/ 64	Seward#6	1	20	R	3.00	8.4	0.25	115.00

N°	Earth-quake	Date	Name tunnel	Dama-ge level	Cover [m]	Rock type	Rock sup. type	Mom. Magni-tude	PGA [g]	Epic. dist. [km]
64	Koyna, India	10/12/67	Koyna Power Station, India	2	150	I	9.00	7	N	N
65	Tokachi-Oki, Japan	1968	railway tunnel	2	N	C	9.00	7.9	N	N
66	Tennessee, USA	13/07/69	Zinc Mine, Tennessee, Usa	2	305	M	1.00	3.5	N	N
67	San Fernando, CA	09/03/75	SanFernando	2	45	S	6.00	6.6	0.69	N
68	San Fernando, CA	09/03/75	Tehachapi#1	1	30	R	1	6.6	0.04	70.00
69	San Fernando, CA	09/03/75	Tehachapi#2	1	30	R	1	6.6	0.04	73.00
70	San Fernando, CA	09/03/75	Tehachapi#3	1	30	R	1	6.6	0.04	73.00
71	San Fernando, CA	09/03/75	Saugus	1	40	R	1	6.6	0.3	23.00
72	San Fernando, CA	09/03/75	SanFrancisquito	1	160	R	1	6.6	0.24	24.50
73	San Fernando, CA	09/03/75	Elizabeth	1	250	R	1	6.6	0.15	51.82
74	San Fernando, CA	09/03/75	Antelope	1	30	R	1	6.6	0.1	240.45
75	San Fernando, CA	09/03/75	Balboa	2	5	R	1	6.6	N	N
76	San Fernando, CA	09/03/75	PacoimaDamSpillway Tunnels,CA	2	43	S	1.00	6.6	0.69	N
77	Izu-Oshima-Kinkai, Japan	14/01/78	Inatori railway tunnel	3	100	M	6.00	7	N	N
78	Izu-Oshima-Kinkai, Japan	14/01/78	Tomoro Tunnel	3	100	M	6.00	7	N	N

N°	Earth-quake	Date	Name tunnel	Dama-ge level	Cover [m]	Rock type	Rock sup. type	Mom. Magni-tude	PGA [g]	Epic. dist. [km]
79	Izu-Oshima-Kinkai, Japan	14/01/78	Izu-Atagawa Tunnel	3	100	M	6.00	7	N	N
80	Izu-Oshima-Kinkai, Japan	14/01/78	Kawazu	2	100	M	6.00	7	N	N
81	Izu-Oshima-Kinkai, Japan	14/01/78	Izu-Kitagawa Tunnel	2	100	M	6.00	7	N	N
82	Izu-Oshima-Kinkai, Japan	14/01/78	Shirata Tunnel	3	100	M	5.00	7	N	N
83	EPRM, South Africa	21/04/78	ERP Gold Mine, South Africa	4	3000	I	1.00	3.7	N	N
84	Tangshan, China	28/07/78	Tangshan Coal Mine	3	40.5	R	1.00	7.8	N	N
85	Tangsham, China	28/07/78	Lai Luan Coal Mines, China	3	700	R	1.00	7.8	N	N
86	Fresno, California	25/05/80	Helms Project Tunnel, California, USA	2	250	I	1.00	6.1	N	N
87	Irpinia, Italy	23/11/80	Helms Project Tunnel ag=0,3g	2	400	R	4.00	6.9	N	N
88	Loma Prieta, CA	17/10/89	FortBaker-Berry	1	61	R	5	6.9	0.04	293.35
89	Loma Prieta, CA	17/10/89	PresidioPark	1	22	R	6	6.9	0.04	N
90	Loma Prieta, CA	17/10/89	AlamedaCreek Div	1	300	N	9	6.9	0.12	49.90
91	Loma Prieta, CA	17/10/89	CoastRange	1	240	R	5	6.9	0.09	N
92	Loma Prieta, CA	17/10/89	Pulgas	1	92	R	5	6.9	0.09	60.64

N°	Earth-quake	Date	Name tunnel	Dama-ge level	Cover [m]	Rock type	Rock sup. type	Mom. Magni-tude	PGA [g]	Epic. dist. [km]
93	Loma Prieta, CA	17/10/89	Irvington	1	122	R	5	6.9	0.1	N
94	Loma Prieta, CA	17/10/89	CrystalSprBaypass	1	76	R	6	6.9	0.09	N
95	Loma Prieta, CA	17/10/89	DowntownS.F.	1	N	R	9	6.9	0.05	N
96	Loma Prieta, CA	17/10/89	StanfordLinearCollider	1	N	R	5	6.9	0.25	N
97	Loma Prieta, CA	17/10/89	LomitaMall	1	N	S	5	6.9	0.14	N
98	Loma Prieta, CA	17/10/89	SantaTeresa	1	N	R	6	6.9	0.26	14.88
99	Loma Prieta, CA	17/10/89	Tunnel#5	1	N	R	3	6.9	0.4	N
100	Loma Prieta, CA	17/10/89	Tunnel#6	1	N	R	3	6.9	0.28	N
101	Loma Prieta, CA	17/10/89	Caldecott	1	243	R	6	6.9	0.04	94.42
102	Loma Prieta, CA	17/10/89	MacArthur	1	46	R	9	6.9	0.04	N
103	Loma Prieta, CA	17/10/89	Stanford	1	23	R	6	6.9	0.14	N
104	Loma Prieta, CA	17/10/89	Hillsborough	1	62	R	6	6.9	0.08	N
105	Loma Prieta, CA	17/10/89	SunolAqud.#1	1	N	R	5	6.9	0.09	N
106	Loma Prieta, CA	17/10/89	SunolAqud.#2	1	N	R	5	6.9	0.09	N
107	Loma Prieta, CA	17/10/89	SunolAqud.#3	1	N	R	5	6.9	0.09	N
108	Loma Prieta, CA	17/10/89	SunolAqud.#4	1	N	R	5	6.9	0.09	N

N°	Earth-quake	Date	Name tunnel	Dama-ge level	Cover [m]	Rock type	Rock sup. type	Mom. Magni-tude	PGA [g]	Epic. dist. [km]
109	Loma Prieta, CA	17/10/89	SunolAqud.#5	1	N	R	5.00	6.9	0.09	N
110	Urakawa-oki, Japan	1982	railway tunnel	1	N	N	9.00	7.1	N	N
111	Nihonkai-chubu, Japan	1983	railway tunnel	1	N	N	9.00	7.7	N	N
112	Kanto, Japan	1984	railway tunnel	2	N	R	5.00	6.8	N	N
113	Chibaken-toho-oki, Japan	1987	railway tunnel	1	N	N	9.00	6.7	N	N
114	Petrolia, CA	25/04/92	Tunnel#40	1	N	S	5	7	0.13	N
115	Petrolia, CA	25/04/92	Tunnel#39	1	N	R	5	7	0.25	N
116	Petrolia, CA	25/04/92	Tunnel#38	2	N	R	5	7	0.21	N
117	Petrolia, CA	25/04/92	Tunnel#37	1	N	R	5	7	0.15	N
118	Petrolia, CA	25/04/92	Tunnel#36	1	N	R	5	7	0.13	N
119	Petrolia, CA	25/04/92	Tunnel#35	1	N	R	5	7	0.12	N
120	Petrolia, CA	25/04/92	Tunnel#34	2	N	R	3	7	0.12	N
121	Petrolia, CA	25/04/92	Tunnel#31	1	N	R	3	7	0.08	246.23
122	Petrolia, CA	25/04/92	Tunnel#30	1	N	R	5	7	0.08	246.24
123	Petrolia, CA	25/04/92	Tunnel#29	1	N	R	5	7	0.06	271.70
124	Petrolia, CA	25/04/92	Tunnel#28	1	N	R	3	7	0.06	245.38

N°	Earth-quake	Date	Name tunnel	Dama-ge level	Cover [m]	Rock type	Rock sup. type	Mom. Magni-tude	PGA [g]	Epic. dist. [km]
125	Notohanto-oki, Japan	1993	road tunnel	1	N	N	9.00	6.6	N	N
126	Hokkaido-nansei-oki, Japan	1993	Seikan road tunnel	1	N	N	6.00	7.8	0.32	N
127	Northridge, CA	17/01/94	PershingSqSt.	1	N	R	6	6.7	0.27	N
128	Northridge, CA	17/01/94	McArthurSt.	1	N	R	6	6.7	0.27	N
129	Northridge, CA	17/01/94	CivicCenterSt.	1	N	R	6	6.7	0.27	N
130	Northridge, CA	17/01/94	Tun#25@I-5/14	2	92	R	5	6.7	0.67	N
131	Northridge, CA	17/01/94	SantaSusana	1	N	R	5	6.7	0.47	10.06
132	Northridge, CA	17/01/94	Chatworth	1	N	R	5	6.7	0.5	N
133	Northridge, CA	17/01/94	Chatworth	1	N	R	5	6.7	0.5	N
134	Northridge, CA	17/01/94	NearI15atCajonJunc	1	N	R	9	6.7	0.1	N
135	Northridge, CA	17/01/94	Balboainlet	1	N	R	6	6.7	0.67	N
136	Northridge, CA	17/01/94	Balboaoutlet	1	N	R	9	6.7	0.58	N
137	Northridge, CA	17/01/94	Castaic#1	1	N	R	6	6.7	0.29	31.58
138	Northridge, CA	17/01/94	Castaic#2	1	N	R	6	6.7	0.36	32.68
139	Northridge, CA	17/01/94	Saugus	1	N	S	6	6.7	0.54	N
140	Northridge, CA	17/01/94	Placerita	1	N	R	6	6.7	0.62	N

N°	Earth-quake	Date	Name tunnel	Dama-ge level	Cover [m]	Rock type	Rock sup. type	Mom. Magni-tude	PGA [g]	Epic. dist. [km]
141	Northridge, CA	17/01/94	Newhall	4	N	R	6	6.7	0.68	14.84
142	Northridge, CA	17/01/94	SanFernando	1	N	S	6	6.7	0.5	N
143	Northridge, CA	17/01/94	Sepulveda	1	N	R	6	6.7	0.27	N
144	Northridge, CA	17/01/94	Hollywood	1	N	R	9	6.7	0.22	N
145	Northridge, CA	17/01/94	SanRafael#1	1	N	R	6	6.7	0.16	N
146	Northridge, CA	17/01/94	SanRafael#2	1	N	R	6	6.7	0.18	N
147	Northridge, CA	17/01/94	Pasadena	1	N	S	6	6.7	0.15	298.05
148	Northridge, CA	17/01/94	SieraMadre	1	N	S	9	6.7	0.13	N
149	Northridge, CA	17/01/94	Monrovia#1, #2	1	N	R	6	6.7	0.09	N
150	Northridge, CA	17/01/94	Monrovia#3	1	N	R	6	6.7	0.1	N
151	Northridge, CA	17/01/94	Monrovia#4	1	N	R	6	6.7	0.1	N
152	Northridge, CA	17/01/94	Glendora	1	N	S	6	6.7	0.07	63.94
153	Northridge, CA	17/01/94	Oakhill	1	N	R	9	6.7	0.15	N
154	Northridge, CA	17/01/94	Ascat	1	N	R	9	6.7	0.14	N
155	Northridge, CA	17/01/94	Tonner#1	1	N	R	6	6.7	0.06	N
156	Northridge, CA	17/01/94	Tonner#2	1	N	R	6	6.7	0.06	N

N°	Earth-quake	Date	Name tunnel	Dama-ge level	Cover [m]	Rock type	Rock sup. type	Mom. Magni-tude	PGA [g]	Epic. dist. [km]
157	Northridge, CA	17/01/94	LAAqueduct	2	46	R	5	6.7	0.67	42.93
158	Kobe, Japan	17/01/95	Maico Road Tunnel	3	50	I	5	6.9	N	5.34
159	Kobe, Japan	17/01/95	Munobiki Road Tunnel	2	240	I	5	6.9	N	N
160	Kobe, Japan	17/01/95	Bantaki Road Tunnel	1	250	I	5	6.9	N	33.90
161	Kobe, Japan	17/01/95	Rokko Shinkansen Road Tunnel	1	400	I	5	6.9	N	31.56
162	Kobe, Japan	17/01/95	Shioya-Danigawa River Tunnel	1	80	R	5	6.9	N	N
163	Kobe, Japan	17/01/95	Rokkou(#1)	2	460	R	5	6.9	0.6	31.32
164	Kobe, Japan	17/01/95	Kobe(#2)	1	272	R	5	6.9	0.57	19.06
165	Kobe, Japan	17/01/95	Suma(#3)	1	45	N	5	6.9	0.53	N
166	Kobe, Japan	17/01/95	Okuhata(#4)	1	90	N	5	6.9	0.5	N
167	Kobe, Japan	17/01/95	Takatsukay(#5)	3	85	N	5	6.9	0.49	N
168	Kobe, Japan	17/01/95	Nagasaka(#6)	4	20	N	5	6.9	0.48	18.97
169	Kobe, Japan	17/01/95	Daiichinas(#7)	4	150	N	6	6.9	0.55	N
170	Kobe, Japan	17/01/95	Ikuse(#8)	4	250	N	5	6.9	0.57	N
171	Kobe, Japan	17/01/95	Daiichitaked(#9)	3	95	N	5	6.9	0.43	N
172	Kobe, Japan	17/01/95	Arima(#12)	2	25	N	5	6.9	0.46	N

N°	Earth-quake	Date	Name tunnel	Dama-ge level	Cover [m]	Rock type	Rock sup. type	Mom. Magni-tude	PGA [g]	Epic. dist. [km]
173	Kobe, Japan	17/01/95	Gosha(#13)	1	40	N	5	6.9	0.41	N
174	Kobe, Japan	17/01/95	Kitakami(#14)	1	350	N	5	6.9	0.51	N
175	Kobe, Japan	17/01/95	Iwataki(#15)	1	135	N	5	6.9	0.58	N
176	Kobe, Japan	17/01/95	Nunohiki(#18)	1	260	I	5	6.9	0.58	19.14
177	Kobe, Japan	17/01/95	DainiNun(#19)	2	240	I	5	6.9	0.58	N
178	Kobe, Japan	17/01/95	Hirano(#20)	2	85	I	5	6.9	0.58	17.81
179	Kobe, Japan	17/01/95	K.Daiichi(#21)	1	32	I	5	6.9	0.58	N
180	Kobe, Japan	17/01/95	K.Daini(#22)	4	25	N	5	6.9	0.58	N
181	Kobe, Japan	17/01/95	Kamoetsu1(#23)	4	29	N	5	6.9	0.55	N
182	Kobe, Japan	17/01/95	Kamoetsu2(#24)	3	40	N	5	6.9	0.55	N
183	Kobe, Japan	17/01/95	Kamoetsu3(#25)	1	47	N	5	6.9	0.55	N
184	Kobe, Japan	17/01/95	Hiyodori(#26)	1	40	R	5	6.9	0.54	16.45
185	Kobe, Japan	17/01/95	Shin-kobe1(#27)	2	330	R	5	6.9	0.49	20.89
186	Kobe, Japan	17/01/95	Shin-kobe2(#28)	1	330	R	5	6.9	0.49	21.25
187	Kobe, Japan	17/01/95	Karaki(#29)	2	145	R	5	6.9	0.42	N
188	Kobe, Japan	17/01/95	Arino1(#30)	1	25	I	5	6.9	0.39	28.24

N°	Earth-quake	Date	Name tunnel	Dama-ge level	Cover [m]	Rock type	Rock sup. type	Mom. Magni-tude	PGA [g]	Epic. dist. [km]
189	Kobe, Japan	17/01/95	Arino2(#31)	1	35	N	5	6.9	0.38	28.44
190	Kobe, Japan	17/01/95	Rokkousan(#32)	1	280	N	5	6.9	0.51	25.66
191	Kobe, Japan	17/01/95	Shinohara(#33)	1	15	N	5	6.9	0.55	8.68
192	Kobe, Japan	17/01/95	Hiyodori(#34)	1	67	N	5	6.9	0.59	16.24
193	Kobe, Japan	17/01/95	Suma(#36)	1	140	N	5	6.9	0.44	N
194	Kobe, Japan	17/01/95	Sumaext	1	N	I	5	6.9	0.58	N
195	Kobe, Japan	17/01/95	Ibuki(#38)	1	20	N	5	6.9	0.43	N
196	Kobe, Japan	17/01/95	Taizanji,1E(#39)	1	53	N	5	6.9	0.44	N
197	Kobe, Japan	17/01/95	Taizanji,1W(#40)	1	37	N	5	6.9	0.44	N
198	Kobe, Japan	17/01/95	Taizanji,2E(#41)	1	25	N	5	6.9	0.45	N
199	Kobe, Japan	17/01/95	Taizanji,2W(#42)	1	17	N	5	6.9	0.45	N
200	Kobe, Japan	17/01/95	Aina,E(#43)	1	68	I	5	6.9	0.46	17.18
201	Kobe, Japan	17/01/95	Aina,W(#44)	1	65	N	5	6.9	0.46	17.64
202	Kobe, Japan	17/01/95	Nagasaka.,E(#45)	1	68	N	5	6.9	0.42	N
203	Kobe, Japan	17/01/95	Nagasaka.,W(#46)	1	68	N	5	6.9	0.42	N
204	Kobe, Japan	17/01/95	T.Higa.,TOK(#47)	1	62	N	5	6.9	0.58	39.67

N°	Earth-quake	Date	Name tunnel	Dama-ge level	Cover [m]	Rock type	Rock sup. type	Mom. Magni-tude	PGA [g]	Epic. dist. [km]
205	Kobe, Japan	17/01/95	T.Higa.,KYU(#48)	1	59	N	5	6.9	0.58	39.76
206	Kobe, Japan	17/01/95	T.Nishi,TOK(#49)	1	42	N	5	6.9	0.57	38.87
207	Kobe, Japan	17/01/95	T.Nishi,KYU(#50)	1	42	N	5	6.9	0.57	38.72
208	Kobe, Japan	17/01/95	Takak.,1TOK(#51)	1	97	N	5	6.9	0.59	10.12
209	Kobe, Japan	17/01/95	Takak.,2TOK(#52)	1	86	R	5	6.9	0.59	9.77
210	Kobe, Japan	17/01/95	Takak.,KYU(#53)	1	87	R	5	6.9	0.59	10.39
211	Kobe, Japan	17/01/95	Tsuki.,TOK(#54)	1	43	R	5	6.9	0.6	11.66
212	Kobe, Japan	17/01/95	Takak.,KYU(#55)	1	34	R	5	6.9	0.6	10.11
213	Kobe, Japan	17/01/95	Omoteyama1(#61)	1	41	R	5	6.9	0.41	N
214	Kobe, Japan	17/01/95	Ochiai(#63)	1	N	R	5	6.9	0.56	N
215	Kobe, Japan	17/01/95	Yokoo,1(#64)	1	N	R	5	6.9	0.59	N
216	Kobe, Japan	17/01/95	Yokoo,2(#65)	1	N	N	5	6.9	0.6	N
217	Kobe, Japan	17/01/95	Shiroyama(#66)	1	N	N	5	6.9	0.58	N
218	Kobe, Japan	17/01/95	Nashio2(#67)	1	N	N	5	6.9	0.48	N
219	Kobe, Japan	17/01/95	Takedo2(#68)	1	N	N	5	6.9	0.4	N
220	Kobe, Japan	17/01/95	Douba1(#69)	1	N	N	5	6.9	0.4	N

N°	Earth-quake	Date	Name tunnel	Dama-ge level	Cover [m]	Rock type	Rock sup. type	Mom. Magni-tude	PGA [g]	Epic. dist. [km]
221	Kobe, Japan	17/01/95	Douba2(#70)	1	N	N	5	6.9	0.37	N
222	Kobe, Japan	17/01/95	Douba3(#71)	1	N	N	5	6.9	0.36	N
223	Kobe, Japan	17/01/95	Keietu(#76)	1	N	N	6	6.9	0.58	N
224	Kobe, Japan	17/01/95	Nakayama(#77)	1	N	N	9	6.9	0.58	N
225	Kobe, Japan	17/01/95	Kadoyama(#78)	1	N	N	9	6.9	0.58	N
226	Kobe, Japan	17/01/95	Kudari(#79)	1	N	N	5	6.9	0.54	N
227	Kobe, Japan	17/01/95	Kik,Nobori (#81)	1	N	N	5	6.9	0.54	17.42
228	Kobe, Japan	17/01/95	Tanigami(#82)	1	N	I	5	6.9	0.41	N
229	Kobe, Japan	17/01/95	Kobe(#84)	1	N	I	5	6.9	0.56	19.07
230	Kobe, Japan	17/01/95	Aina(#85)	1	N	I	5	6.9	0.48	16.71
231	Kobe, Japan	17/01/95	Tetsukaiy(#87)	1	20	N	5	6.9	0.6	N
232	Kobe, Japan	17/01/95	Taisanji(#88)	1	50	I	5	6.9	0.44	N
233	Kobe, Japan	17/01/95	Kaibara(#89)	1	20	N	5	6.9	0.36	N
234	Kobe, Japan	17/01/95	Shimohata(#91)	1	20	N	5	6.9	0.6	N
235	Kobe, Japan	17/01/95	Fukuchi(#92)	1	20	I	5	6.9	0.36	N
236	Kobe, Japan	17/01/95	Sumadera(#93)	1	15	N	5	6.9	0.6	N

N°	Earth-quake	Date	Name tunnel	Dama-ge level	Cover [m]	Rock type	Rock sup. type	Mom. Magni-tude	PGA [g]	Epic. dist. [km]
237	Kobe, Japan	17/01/95	ShinArima(#95)	1	20	I	5	6.9	0.48	N
238	Kobe, Japan	17/01/95	HigashiAina(#96)	1	10	I	5	6.9	0.43	N
239	Kobe, Japan	17/01/95	Fukuyama(#97)	1	15	I	5	6.9	0.59	N
240	Kobe, Japan	17/01/95	Minoya(#98)	1	20	N	5	6.9	0.4	N
241	Kobe, Japan	17/01/95	Iwayama(#99)	1	30	I	5	6.9	0.56	N
242	Kobe, Japan	17/01/95	Tamasaka (#100)	1	10	I	5	6.9	0.58	N
243	Kobe, Japan	17/01/95	Fukiage(#101)	4	30	N	4	6.9	0.44	N
244	Kobe, Japan	17/01/95	Maesaki(#102)	3	10	I	9	6.9	0.43	N
245	Kobe, Japan	17/01/95	Nishikou2(103)	1	20	N	6	6.9	0.39	N
246	Kobe, Japan	17/01/95	Fusehatagami (104)	1	30	N	5	6.9	0.47	N
247	Kobe, Japan	17/01/95	Fusehatashita (105)	1	30	I	6	6.9	0.47	N
248	Kobe, Japan	17/01/95	Enoshitayama (109)	1	37	N	5	6.9	0.6	N
249	Kobe, Japan	17/01/95	Motoyama(110)	4	96	I	5	6.9	0.59	N
250	Kobe, Japan	17/01/95	N.ofItayadaSt.	2	N	I	5	6.9	0.6	N
251	Kobe, Japan	17/01/95	NearNatani	1	N	I	5	6.9	0.6	N
252	Kobe, Japan	17/01/95	KoigawaRiver	4	N	N	6	6.9	0.6	N

N°	Earth-quake	Date	Name tunnel	Dama-ge level	Cover [m]	Rock type	Rock sup. type	Mom. Magni-tude	PGA [g]	Epic. dist. [km]
253	Kobe, Japan	17/01/95	Hosoyadani	2	6	N	6	6.9	0.59	N
254	Kobe, Japan	17/01/95	Sennomori	2	30	N	5	6.9	0.59	N
255	Kobe, Japan	17/01/95	Shioyadani	4	25	I	4	6.9	0.59	N
256	Kobe, Japan	17/01/95	Kabutoyama-Ashiya	4	25	N	4	6.9	0.58	N
257	Kobe, Japan	17/01/95	SannomiyaSt. St.3	2	25	I	5	6.9	0.59	N
258	Kobe, Japan	17/01/95	NTT@Chuo-ku@Chuo-ku	2	N	N	5	6.9	0.6	N
259	Kobe, Japan	17/01/95	KansaiElectric Electric	4	N	I	5	6.9	0.6	N
260	Kobe, Japan	17/01/95	HIGASHIYAMA(#10)(#10)	1	8	R	6	6.9	0.7	N
261	Kobe, Japan	17/01/95	EGEYAMA(#11)(#11)	1	13	N	6	6.9	0.68	N
262	Kobe, Japan	17/01/95	MAIKO(UP)(#16)(UP)(#16)	1	50	R	6	6.9	0.62	N
263	Kobe, Japan	17/01/95	MAIKO(DOWN)(#17)(DOWN)(#17)	1	50	R	6	6.9	0.62	N
264	Kobe, Japan	17/01/95	SHIOYA-DAN(#35)(#35)	1	80	N	5	6.9	0.7	N
265	Kobe, Japan	17/01/95	SEISHIN(2)(#58)(2)(#58)	1	7	R	5	6.9	0.36	N
266	Kobe, Japan	17/01/95	SEISHIN(1)(#59)(1)(#59)	1	3	R	5	6.9	0.37	N
267	Kobe, Japan	17/01/95	OMOTEYAMA (2)(#60)	3	N	N	5	6.9	0.41	N
268	Kobe, Japan	17/01/95	KODERA(#62)	1	7	N	6	6.9	0.47	N

N°	Earth-quake	Date	Name tunnel	Dama-ge level	Cover [m]	Rock type	Rock sup. type	Mom. Magni-tude	PGA [g]	Epic. dist. [km]
269	Kobe, Japan	17/01/95	OBU(#86)(#86)	1	50	I	5.00	6.9	0.55	N
270	Kobe, Japan	17/01/95	AINA(#90)(#90)	2	2	N	5.00	6.9	0.43	N
271	Kobe, Japan	17/01/95	FUTATABI(#94)(#94)	2	20	R	5.00	6.9	0.7	N
272	Kobe, Japan	17/01/95	SENGARI(#111)(#111)	2	25	I	5.00	6.9	0.6	N
273	Kocaeli, Turkey	17/08/99	Bolu tunnel	2	N	S	6.00	7.4	0.41	168.78
274	Chi-Chi, Taiwan	21/09/99	Shih-Gang Dam Water conveyance tunnel	4	N	R	5	7.6	0.6	54.05
275	Chi-Chi, Taiwan	21/09/99	Highway 8	1	N	R	5	7.6	0.58	35.10
276	Chi-Chi, Taiwan	21/09/99	Highway 8, Li-Lang Tunnel	1	N	R	5	7.6	0.48	38.60
277	Chi-Chi, Taiwan	21/09/99	Highway 8	3	N	N	5	7.6	0.4	44.00
278	Chi-Chi, Taiwan	21/09/99	Highway 8	3	N	N	5	7.6	0.4	44.00
279	Chi-Chi, Taiwan	21/09/99	Highway 8	3	N	N	5	7.6	0.37	44.80
280	Chi-Chi, Taiwan	21/09/99	Highway 8, old Ku-Kuan Tunnel	3	N	N	5	7.6	0.36	44.80
281	Chi-Chi, Taiwan	21/09/99	Highway 8, No.1 old Maa-Ling Tunnel	4	N	N	5	7.6	0.58	45.91
282	Chi-Chi, Taiwan	21/09/99	Highway 8, No.1 Maa-Ling Tunnel	4	N	R	5	7.6	0.58	45.88
283	Chi-Chi, Taiwan	21/09/99	Highway 8, No.2 Maa-Ling Tunnel	4	N	R	5	7.6	0.58	46.14
284	Chi-Chi, Taiwan	21/09/99	Highway 8, No.3 Maa-Ling Tunnel	4	N	R	4	7.6	0.54	46.38

N°	Earth-quake	Date	Name tunnel	Dama-ge level	Cover [m]	Rock type	Rock sup. type	Mom. Magni-tude	PGA [g]	Epic. dist. [km]
285	Chi-Chi, Taiwan	21/09/99	Highway 8, No.4 Maa-Ling Tunnel	1	N	R	9	7.6	0.54	47.81
286	Chi-Chi, Taiwan	21/09/99	Highway 8, No.4 old Maa-Ling Tunnel	4	N	R	6	7.6	0.41	47.75
287	Chi-Chi, Taiwan	21/09/99	Highway 8	4	N	R	5	7.6	0.56	48.30
288	Chi-Chi, Taiwan	21/09/99	Highway 8	2	N	R	6	7.6	0.48	48.26
289	Chi-Chi, Taiwan	21/09/99	Highway 8	4	N	N	5	7.6	0.6	48.44
290	Chi-Chi, Taiwan	21/09/99	Highway 14, Shuang-Fu Tunnel	1	N	N	5	7.6	0.44	19.71
291	Chi-Chi, Taiwan	21/09/99	Highway 14, Gang-Lin Tunnel	4	N	N	5	7.6	0.36	19.78
292	Chi-Chi, Taiwan	21/09/99	Highway 14, Gang-Lin Tunnel	1	N	R	5	7.6	0.6	19.77
293	Chi-Chi, Taiwan	21/09/99	Highway 14, Yu-Ler Tunnel	1	N	R	6	7.6	0.36	18.98
294	Chi-Chi, Taiwan	21/09/99	Highway 14, Yu-Ler Tunnel	1	N	R	6	7.6	0.6	18.97
295	Chi-Chi, Taiwan	21/09/99	Highway 14, Pei-Shan Tunnel	1	N	R	5	7.6	0.48	15.93
296	Chi-Chi, Taiwan	21/09/99	Highway 14, No.1 Kuan-Yin Tunnel	1	N	R	4	7.6	0.43	17.01
297	Chi-Chi, Taiwan	21/09/99	Highway 14, No.1 Kuan-Yin Tunnel	1	N	R	4	7.6	0.59	17.08
298	Chi-Chi, Taiwan	21/09/99	Highway 14, No. 2 Kuan-Yin Tunnel	1	N	R	5	7.6	0.4	17.45
299	Chi-Chi, Taiwan	21/09/99	Highway 14, No. 2 Kuan-Yin Tunnel	1	N	R	5	7.6	0.56	17.40
300	Chi-Chi, Taiwan	21/09/99	Highway 14, No. 3 Kuan-Yin Tunnel	3	N	R	5	7.6	0.58	17.65

N°	Earth-quake	Date	Name tunnel	Dama-ge level	Cover [m]	Rock type	Rock sup. type	Mom. Magni-tude	PGA [g]	Epic. dist. [km]
301	Chi-Chi, Taiwan	21/09/99	Highway 14, No. 3 Kuan-Yin Tunnel	1	N	R	6	7.6	0.44	17.58
302	Chi-Chi, Taiwan	21/09/99	Highway 16, Chi-Chi Tunnel	1	N	R	6	7.6	0.43	6.15
303	Chi-Chi, Taiwan	21/09/99	Highway 16, New Chi-Chi Tunnel L	1	N	R	6	7.6	0.39	6.42
304	Chi-Chi, Taiwan	21/09/99	Highway 16, New Chi-Chi Tunnel R	4	N	R	6	7.6	0.47	6.35
305	Chi-Chi, Taiwan	21/09/99	Highway 21, Da-Yuan Tunnel L	1	N	R	5	7.6	0.47	14.02
306	Chi-Chi, Taiwan	21/09/99	Highway 21, Da-Yuan Tunnel R	1	N	R	5	7.6	0.6	14.10
307	Chi-Chi, Taiwan	21/09/99	Highway 21, Shue-Sir Tunnel L	1	N	R	5	7.6	0.59	8.47
308	Chi-Chi, Taiwan	21/09/99	Highway 21, Shue-Sir Tunnel R	1	N	R	5	7.6	0.6	8.63
309	Chi-Chi, Taiwan	21/09/99	Highway 21A, No. 1 Huan-Hu Tunnel	1	N	R	6	7.6	0.6	9.26
310	Chi-Chi, Taiwan	21/09/99	Highway 21A, No. 2 Huan-Hu Tunnel	1	N	R	5	7.6	0.6	9.29
311	Chi-Chi, Taiwan	21/09/99	Highway 149, Tsao-Ling Tunnel	4	N	N	5	7.6	0.59	31.09
312	Chi-Chi, Taiwan	21/09/99	Highway 149, Ching-Shue Tunnel	4	N	N	5	7.6	0.59	32.06
313	Chi-Chi, Taiwan	21/09/99	Tou-6 highway, No. 1 Tu-Cheng Tunnel	1	N	N	5	7.6	0.59	15.46
314	Chi-Chi, Taiwan	21/09/99	Tou-6 highway, No. 2 Tu-Cheng Tunnel	2	N	N	5	7.6	0.58	15.24
315	Chi-Chi, Taiwan	21/09/99	Tou-6 highway, Shuang-Lung Tunnel E	2	N	N	5	7.6	0.59	15.10

N°	Earth-quake	Date	Name tunnel	Dama-ge level	Cover [m]	Rock type	Rock sup. type	Mom. Magni-tude	PGA [g]	Epic. dist. [km]
316	Chi-Chi, Taiwan	21/09/99	Tou-6 highway, Shuang-Lung Tunnel W	1	N	N	5	7.6	0.6	15.16
317	Chi-Chi, Taiwan	21/09/99	Tou-6 highway, No. 1 Shuang-Tung Tunnel	3	N	N	5	7.6	0.6	15.11
318	Chi-Chi, Taiwan	21/09/99	Tou-6 highway, No. 2 Shuang-Tung Tunnel	1	N	N	5	7.6	0.7	15.19
319	Chi-Chi, Taiwan	21/09/99	Chi-Chi line railway, No. 1 tunnel	1	N	N	5	7.6	0.68	6.14
320	Chi-Chi, Taiwan	21/09/99	Chi-Chi line railway, No. 2 tunnel	1	N	N	4	7.6	0.62	0.78
321	Chi-Chi, Taiwan	21/09/99	Chi-Chi line railway, No. 3 tunnel	3	N	N	9	7.6	0.62	4.50
322	Chi-Chi, Taiwan	21/09/99	Chi-Chi line railway, No. 5 tunnel	3	N	N	6	7.6	0.7	4.50
323	Chi-Chi, Taiwan	21/09/99	Da-Kuan power station, headrace tunnel	4	N	N	5	7.6	0.36	8.47
324	Chi-Chi, Taiwan	21/09/99	New Tien-Lun power station, headrace tunnel	4	N	N	6	7.6	0.37	39.78
325	Chi-Chi, Taiwan	21/09/99	Mountain line railway, No. 1 San-I Tunnel	4	N	N	5	7.6	0.41	55.10
326	Chi-Chi, Taiwan	21/09/99	Mountain line railway, No. 2 San-I Tunnel	1	N	R	5	7.6	0.47	49.71
327	Chi-Chi, Taiwan	21/09/99	Mountain line railway, No. 3 San-I Tunnel	1	N	R	5	7.6	0.55	49.38
328	Chi-Chi, Taiwan	21/09/99	Mountain line railway, No. 4 San-I Tunnel	1	N	N	5	7.6	0.43	48.87
329	Chi-Chi, Taiwan	21/09/99	Old mountain line, railway, No. 1 San-I Tunnel	1	N	R	6	7.6	0.7	58.94

N°	Earth-quake	Date	Name tunnel	Dama-ge level	Cover [m]	Rock type	Rock sup. type	Mom. Magni-tude	PGA [g]	Epic. dist. [km]
330	Chi-Chi, Taiwan	21/09/99	Old mountain line, railway, No. 2 San-I Tunnel	1	N	R	6	7.6	0.6	57.96
331	Duzce, Turkey	12/11/99	Bolu tunnel	4	600	C	6	7.2	0.8	49.76
332	Western Tottori	06/10/00	Tottori Head Race Tunnel	2	200	R	5	7.3	N	N
333	Niigata, Japan	23/10/04	Joetsu Shinkansen Tunnel	3	32	C	5	6.8	0.41	19.26
334	Niigata, Japan	23/10/04	Takitani Tunnel	2	30	C	5	6.8	0.38	7.02
335	Niigata, Japan	23/10/04	Myoken Tunnel	2	24	C	5	6.8	0.39	4.73
336	Niigata, Japan	23/10/04	Tsukayama Tunnel	1	12	C	5	6.8	0.42	18.36
337	Niigata, Japan	23/10/04	Uonuma Tunnel 1	3	15	C	6	6.8	0.41	3.34
338	Niigata, Japan	23/10/04	Uonuma Tunnel 2	2	26	C	6	6.8	0.41	2.16
339	Niigata, Japan	23/10/04	Tenno Tunnel	2	31	C	6	6.8	0.43	4.03
340	Niigata, Japan	23/10/04	Ushigashima Tunnel	2	12	C	6	6.8	0.41	4.22
341	Niigata, Japan	23/10/04	Uchigamachi Tunnel	3	16	C	5	6.8	0.44	6.96
342	Niigata, Japan	23/10/04	Myokozan Tunnel	1	17	C	5	6.8	0.41	9.07
343	Niigata, Japan	23/10/04	Takabayama Tunnel	1	19	C	5	6.8	0.41	7.47
344	Niigata, Japan	23/10/04	Wanazu Tunnel	2	22	C	5	6.8	0.40	5.19
345	Niigata, Japan	23/10/04	Horinouchi Tunnel	3	26	C	6	6.8	0.39	6.94

N°	Earth-quake	Date	Name tunnel	Dama -ge level	Cover [m]	Rock type	Rock sup. type	Mom. Magni -tude	PGA [g]	Epic. dist. [km]
346	Niigata, Japan	23/10/ 04	Shinhatsu Canal Tunnel	3	31	C	6	6.8	0.36	16.79
347	Niigata, Japan	23/10/ 04	Urasa Tunnel	3	33	C	6	6.8	0.31	13.21
348	Niigata, Japan	23/10/ 04	Fukuyama Tunnel	3	35	C	6	6.8	0.31	14.40

Table B.3 – Database for the computation of the PGV obtained from the attenuation relationship of Bray & Rodriguez-Marek (2004) (a= 4.51; b= 0.4; c= -0.57; d= 7)

N°	Earthquake	Date	Name tunnel	Name fault	R [km]	M_w	PGV [cm/s]
1	Kern County, CA	21/07/52	Elizabeth	White Wolf	55.24	7.4	11.51
2	Kern County, CA	21/07/52	Antelope	White Wolf	128.15	7.4	4.44
3	Kern County, CA	21/07/52	S.P.R.R. Tunnel #3	White Wolf	23.80	7.4	28.95
4	Kern County, CA	21/07/52	S.P.R.R. Tunnel #4	White Wolf	19.91	7.4	34.81
5	Kern County, CA	21/07/52	S.P.R.R. Tunnel #5	White Wolf	5.61	7.4	92.31
6	Kern County, CA	21/07/52	S.P.R.R. Tunnel #6	White Wolf	29.26	7.4	23.23
7	San Fernando, CA	09/03/71	Elizabeth	Cucamonga fault	105.55	6.6	4.22
8	San Fernando, CA	09/03/71	Antelope	Cucamonga fault	289.30	6.6	1.34
9	Loma Prieta, CA	17/10/89	FortBaker-Berry Tunnel 7		279.71	6.9	1.54
10	Loma Prieta, CA	17/10/89	AlamedaCreekDiv		39.39	6.9	14.16
11	Loma Prieta, CA	17/10/89	Pulgas		41.16	6.9	13.49
12	Loma Prieta, CA	17/10/89	SantaTeresa		9.19	6.9	58.36
13	Loma Prieta, CA	17/10/89	Caldecott		76.37	6.9	6.74
14	Petrolia, CA	25/04/92	Tunnel#31	Cascadia	242.97	7	1.87
15	Petrolia, CA	25/04/92	Tunnel#30	Cascadia	243.06	7	1.87

N°	Earthquake	Date	Name tunnel	Name fault	R [km]	M_w	PGV [cm/s]
16	Petrolia, CA	25/04/92	Tunnel#29	Cascadia	266.27	7	1.69
17	Petrolia, CA	25/04/92	Tunnel#28	Cascadia	242.26	7	1.88
18	Northridge, CA	17/01/94	SantaSusana		13.91	6.7	38.78
19	Northridge, CA	17/01/94	Castaic#1		10.39	6.7	49.72
20	Northridge, CA	17/01/94	Castaic#2		11.37	6.7	46.23
21	Northridge, CA	17/01/94	Newhall		5.53	6.7	73.20
22	Northridge, CA	17/01/94	Pasadena mine		277.33	6.7	1.45
23	Northridge, CA	17/01/94	Glendora mine		53.05	6.7	9.50
24	Northridge, CA	17/01/94	Los Angeles Aqueduct		24.41	6.7	22.21
25	Kobe, Japan	17/01/95	Maico Road Tunnel	Nojima Fault	0.70	6.9	102.71
26	Kobe, Japan	17/01/95	Bantaki Road Tunnel	Nojima Fault	0.43	6.9	103.08
27	Kobe, Japan	17/01/95	Rokko Shinkansen Road Tunnel	Nojima Fault	0.47	6.9	103.04
28	Kobe, Japan	17/01/95	Rokkou(#1)	Nojima Fault	1.23	6.9	101.53
29	Kobe, Japan	17/01/95	Kobe(#2)	Nojima Fault	1.00	6.9	102.12
30	Kobe, Japan	17/01/95	Nagasaka(#6)	Nojima Fault	4.76	6.9	83.18
31	Kobe, Japan	17/01/95	Nunohiki(#18)	Nojima Fault	1.28	6.9	101.39
32	Kobe, Japan	17/01/95	Hirano(#20)	Nojima Fault	1.04	6.9	102.03
33	Kobe, Japan	17/01/95	Hiyodori(#26)	Nojima Fault	0.27	6.9	103.22
34	Kobe, Japan	17/01/95	Shin-kobe1(#27)	Nojima Fault	0.25	6.9	103.23
35	Kobe, Japan	17/01/95	Shin-kobe2(#28)	Nojima Fault	0.58	6.9	102.90
36	Kobe, Japan	17/01/95	Arino1(#30)	Nojima Fault	5.43	6.9	79.01
37	Kobe, Japan	17/01/95	Arino2(#31)	Nojima Fault	5.79	6.9	76.73
38	Kobe, Japan	17/01/95	Rokkousan(#32)	Nojima Fault	0.77	6.9	102.61
39	Kobe, Japan	17/01/95	Shinohara(#33)	Nojima Fault	0.40	6.9	103.12
40	Kobe, Japan	17/01/95	Hiyodori(#34)	Nojima Fault	0.35	6.9	103.15
41	Kobe, Japan	17/01/95	Aina,E(#43)	Nojima Fault	3.82	6.9	89.03

N°	Earthquake	Date	Name tunnel	Name fault	R [km]	M_w	PGV [cm/s]
42	Kobe, Japan	17/01/95	Aina,W(#44)	Nojima Fault	3.81	6.9	89.09
43	Kobe, Japan	17/01/95	T.Higa.,TOK(#47)	Nojima Fault	4.82	6.9	82.79
44	Kobe, Japan	17/01/95	T.Higa.,KYU(#48)	Nojima Fault	4.96	6.9	81.93
45	Kobe, Japan	17/01/95	T.Nishi,TOK(#49)	Nojima Fault	3.89	6.9	88.62
46	Kobe, Japan	17/01/95	T.Nishi,KYU(#50)	Nojima Fault	3.72	6.9	89.62
47	Kobe, Japan	17/01/95	Takak.,1TOK(#51)	Nojima Fault	1.40	6.9	101.01
48	Kobe, Japan	17/01/95	Takak.,2TOK(#52)	Nojima Fault	1.56	6.9	100.50
49	Kobe, Japan	17/01/95	Takak.,KYU(#53)	Nojima Fault	1.75	6.9	99.80
50	Kobe, Japan	17/01/95	Tsuki.,TOK(#54)	Nojima Fault	1.88	6.9	99.29
51	Kobe, Japan	17/01/95	Takak.,KYU(#55)	Nojima Fault	1.84	6.9	99.43
52	Kobe, Japan	17/01/95	Kik,Nobori(#81)	Nojima Fault	0.76	6.9	102.61
53	Kobe, Japan	17/01/95	Kobe(#84)	Nojima Fault	0.99	6.9	102.14
54	Kobe, Japan	17/01/95	Aina(#85)	Nojima Fault	3.79	6.9	89.22
55	Kocaeli, Turkey	17/08/99	Bolu tunnel	North Anatolian Fault - Kocaeli Fault	70.86	7.4	8.70
56	Chi-Chi, Taiwan	21/09/99	Shih-Gang Dam Water conveyance tunnel	Che-Lung-Pu Fault	3.71	7.6	113.78
57	Chi-Chi, Taiwan	21/09/99	Highway 8	Che-Lung-Pu Fault	9.00	7.6	75.15
58	Chi-Chi, Taiwan	21/09/99	Highway 8, Li-Lang Tunnel	Che-Lung-Pu Fault	9.94	7.6	69.86
59	Chi-Chi, Taiwan	21/09/99	Highway 8	Che-Lung-Pu Fault	17.01	7.6	43.56
60	Chi-Chi, Taiwan	21/09/99	Highway 8	Che-Lung-Pu Fault	17.01	7.6	43.56
61	Chi-Chi, Taiwan	21/09/99	Highway 8	Che-Lung-Pu Fault	17.22	7.6	43.05
62	Chi-Chi, Taiwan	21/09/99	Highway 8, old Ku-Kuan Tunnel	Che-Lung-Pu Fault	17.22	7.6	43.05
63	Chi-Chi, Taiwan	21/09/99	Highway 8, No.1 old Maa-Ling Tunnel	Che-Lung-Pu Fault	17.00	7.6	43.59
64	Chi-Chi, Taiwan	21/09/99	Highway 8, No.1 Maa-Ling Tunnel	Che-Lung-Pu Fault	18.24	7.6	40.68
65	Chi-Chi, Taiwan	21/09/99	Highway 8, No.2 Maa-Ling Tunnel	Che-Lung-Pu Fault	18.20	7.6	40.77
66	Chi-Chi, Taiwan	21/09/99	Highway 8, No.3 Maa-Ling Tunnel	Che-Lung-Pu Fault	17.01	7.6	43.57

N°	Earthquake	Date	Name tunnel	Name fault	R [km]	M_w	PGV [cm/s]
67	Chi-Chi, Taiwan	21/09/99	Highway 8, No.4 Maa-Ling Tunnel	Che-Lung-Pu Fault	18.55	7.6	39.99
68	Chi-Chi, Taiwan	21/09/99	Highway 8, No.4 old Maa-Ling Tunnel	Che-Lung-Pu Fault	18.16	7.6	40.85
69	Chi-Chi, Taiwan	21/09/99	Highway 8	Che-Lung-Pu Fault	18.73	7.6	39.61
70	Chi-Chi, Taiwan	21/09/99	Highway 8	Che-Lung-Pu Fault	18.29	7.6	40.55
71	Chi-Chi, Taiwan	21/09/99	Highway 8	Che-Lung-Pu Fault	18.72	7.6	39.64
72	Chi-Chi, Taiwan	21/09/99	Highway 14, Shuang-Fu Tunnel	Che-Lung-Pu Fault	7.97	7.6	81.63
73	Chi-Chi, Taiwan	21/09/99	Highway 14, Gang-Lin Tunnel	Che-Lung-Pu Fault	8.57	7.6	77.77
74	Chi-Chi, Taiwan	21/09/99	Highway 14, Gang-Lin Tunnel	Che-Lung-Pu Fault	9.19	7.6	74.06
75	Chi-Chi, Taiwan	21/09/99	Highway 14, Yu-Ler Tunnel	Che-Lung-Pu Fault	9.05	7.6	74.87
76	Chi-Chi, Taiwan	21/09/99	Highway 14, Yu-Ler Tunnel	Che-Lung-Pu Fault	12.42	7.6	58.26
77	Chi-Chi, Taiwan	21/09/99	Highway 14, Pei-Shan Tunnel	Che-Lung-Pu Fault	10.39	7.6	67.51
78	Chi-Chi, Taiwan	21/09/99	Highway 14, No.1 Kuan-Yin Tunnel	Che-Lung-Pu Fault	11.68	7.6	61.40
79	Chi-Chi, Taiwan	21/09/99	Highway 14, No.1 Kuan-Yin Tunnel	Che-Lung-Pu Fault	10.45	7.6	67.19
80	Chi-Chi, Taiwan	21/09/99	Highway 14, No. 2 Kuan-Yin Tunnel	Che-Lung-Pu Fault	11.75	7.6	61.09
81	Chi-Chi, Taiwan	21/09/99	Highway 14, No. 2 Kuan-Yin Tunnel	Che-Lung-Pu Fault	10.41	7.6	67.40
82	Chi-Chi, Taiwan	21/09/99	Highway 14, No. 3 Kuan-Yin Tunnel	Che-Lung-Pu Fault	11.77	7.6	60.99
83	Chi-Chi, Taiwan	21/09/99	Highway 14, No. 3 Kuan-Yin Tunnel	Che-Lung-Pu Fault	12.22	7.6	59.07
84	Chi-Chi, Taiwan	21/09/99	Highway 16, Chi-Chi Tunnel	Che-Lung-Pu Fault	4.61	7.6	106.71
85	Chi-Chi, Taiwan	21/09/99	Highway 16, New Chi-Chi Tunnel L	Che-Lung-Pu Fault	4.55	7.6	107.23
86	Chi-Chi, Taiwan	21/09/99	Highway 16, New Chi-Chi Tunnel R	Che-Lung-Pu Fault	4.32	7.6	109.04
87	Chi-Chi, Taiwan	21/09/99	Highway 21, Da-Yuan Tunnel L	Che-Lung-Pu Fault	14.04	7.6	52.24
88	Chi-Chi, Taiwan	21/09/99	Highway 21, Da-Yuan Tunnel R	Che-Lung-Pu Fault	13.84	7.6	52.93
89	Chi-Chi, Taiwan	21/09/99	Highway 21, Shue-Sir Tunnel L	Che-Lung-Pu Fault	11.29	7.6	63.12
90	Chi-Chi, Taiwan	21/09/99	Highway 21, Shue-Sir Tunnel R	Che-Lung-Pu Fault	11.22	7.6	63.48

N°	Earthquake	Date	Name tunnel	Name fault	R [km]	M_w	PGV [cm/s]
91	Chi-Chi, Taiwan	21/09/99	Highway 21A, No. 1 Huan-Hu Tunnel	Che-Lung-Pu Fault	11.72	7.6	61.21
92	Chi-Chi, Taiwan	21/09/99	Highway 21A, No. 2 Huan-Hu Tunnel	Che-Lung-Pu Fault	11.39	7.6	62.69
93	Chi-Chi, Taiwan	21/09/99	Highway 149, Tsao-Ling Tunnel	Che-Lung-Pu Fault	3.43	7.6	115.91
94	Chi-Chi, Taiwan	21/09/99	Highway 149, Ching-Shue Tunnel	Che-Lung-Pu Fault	5.15	7.6	102.44
95	Chi-Chi, Taiwan	21/09/99	Tou-6 highway, No. 1 Tu-Cheng Tunnel	Che-Lung-Pu Fault	4.19	7.6	110.10
96	Chi-Chi, Taiwan	21/09/99	Tou-6 highway, No. 2 Tu-Cheng Tunnel	Che-Lung-Pu Fault	4.92	7.6	104.25
97	Chi-Chi, Taiwan	21/09/99	Tou-6 highway, Shuang-Lung Tunnel E	Che-Lung-Pu Fault	4.34	7.6	108.89
98	Chi-Chi, Taiwan	21/09/99	Tou-6 highway, Shuang-Lung Tunnel W	Che-Lung-Pu Fault	4.93	7.6	104.17
99	Chi-Chi, Taiwan	21/09/99	Tou-6 highway, No. 1 Shuang-Tung Tunnel	Che-Lung-Pu Fault	5.54	7.6	99.30
100	Chi-Chi, Taiwan	21/09/99	Tou-6 highway, No. 2 Shuang-Tung Tunnel	Che-Lung-Pu Fault	4.85	7.6	104.78
101	Chi-Chi, Taiwan	21/09/99	Chi-Chi line railway, No. 1 tunnel	Che-Lung-Pu Fault	4.64	7.6	106.47
102	Chi-Chi, Taiwan	21/09/99	Chi-Chi line railway, No. 2 tunnel	Che-Lung-Pu Fault	6.77	7.6	89.93
103	Chi-Chi, Taiwan	21/09/99	Chi-Chi line railway, No. 3 tunnel	Che-Lung-Pu Fault	5.48	7.6	99.82
104	Chi-Chi, Taiwan	21/09/99	Chi-Chi line railway, No. 5 tunnel	Che-Lung-Pu Fault	5.48	7.6	99.82
105	Chi-Chi, Taiwan	21/09/99	Da-Kuan power station, headrace tunnel	Che-Lung-Pu Fault	11.28	7.6	63.18
106	Chi-Chi, Taiwan	21/09/99	New Tien-Lun power station, headrace tunnel	Che-Lung-Pu Fault	10.13	7.6	68.84
107	Chi-Chi, Taiwan	21/09/99	Mountain line railway, No. 1 San-I Tunnel	Che-Lung-Pu Fault	37.46	7.6	18.99
108	Chi-Chi, Taiwan	21/09/99	Mountain line railway, No. 2 San-I Tunnel	Che-Lung-Pu Fault	33.29	7.6	21.61
109	Chi-Chi, Taiwan	21/09/99	Mountain line railway, No. 3 San-I Tunnel	Che-Lung-Pu Fault	32.74	7.6	22.01
110	Chi-Chi, Taiwan	21/09/99	Mountain line railway, No. 4 San-I Tunnel	Che-Lung-Pu Fault	32.05	7.6	22.53
111	Chi-Chi, Taiwan	21/09/99	Old mountain line, railway, No. 1 San-I Tunnel	Che-Lung-Pu Fault	26.81	7.6	27.31
112	Chi-Chi, Taiwan	21/09/99	Old mountain line, railway, No. 2 San-I Tunnel	Che-Lung-Pu Fault	25.36	7.6	28.97

N°	Earthquake	Date	Name tunnel	Name fault	R [km]	M_w	PGV [cm/s]
113	Duzce, Turkey	12/11/99	Bolu tunnel	North Anatolian Fault - Duzce Fault	21.25	7.2	30.41
114	Niigata, Japan	23/10/04	Joetsu Shinkansen Tunnel	Obiro Fault	17.84	6.8	31.67
115	Niigata, Japan	23/10/04	Takitani Tunnel	Obiro Fault	38.46	6.8	14.05
116	Niigata, Japan	23/10/04	Myoken Tunnel	Obiro Fault	36.32	6.8	14.97
117	Niigata, Japan	23/10/04	Tsukayama Tunnel	Obiro Fault	45.67	6.8	11.61
118	Niigata, Japan	23/10/04	Uonuma Tunnel 1	Obiro Fault	30.08	6.8	18.39
119	Niigata, Japan	23/10/04	Uonuma Tunnel 2	Obiro Fault	32.27	6.8	17.03
120	Niigata, Japan	23/10/04	Tenno Tunnel	Obiro Fault	32.01	6.8	17.19
121	Niigata, Japan	23/10/04	Ushigashima Tunnel	Obiro Fault	31.19	6.8	17.68
122	Niigata, Japan	23/10/04	Uchigamachi Tunnel	Obiro Fault	28.93	6.8	19.18
123	Niigata, Japan	23/10/04	Myokozan Tunnel	Obiro Fault	30.13	6.8	18.35
124	Niigata, Japan	23/10/04	Takabayama Tunnel	Obiro Fault	29.30	6.8	18.92
125	Niigata, Japan	23/10/04	Wanazu Tunnel	Obiro Fault	28.31	6.8	19.63
126	Niigata, Japan	23/10/04	Horinouchi Tunnel	Obiro Fault	26.80	6.8	20.82
127	Niigata, Japan	23/10/04	Shinhatsu Canal Tunnel	Obiro Fault	33.82	6.8	16.18
128	Niigata, Japan	23/10/04	Urasa Tunnel	Obiro Fault	21.43	6.8	26.32
129	Niigata, Japan	23/10/04	Fukuyama Tunnel	Obiro Fault	20.48	6.8	27.57

References

Abe, S., D. Place, et al. (2004). "A Parallel Implementation of the Lattice Solid Model for the Simulation of Rock Mechanics and Earthquake Dynamics". Pure and Applied Geophysics 161(11): 2265-2277.

Achenbach, J.D and Norris, A.N. (1982). "Loss of specular reflection due to nonlinear crack-face interaction", Journal of Nondestructive Evaluation, Vol. 3(4), pp. 229-239.

Achenbach, J.D. and Kitahara, M. (1986). "Reflection and transmission of an obliquely incident wave by an array of spherical cavities", Journal of the Acoustical Society of America, Vol. 80, pp. 1209.

Achenbach, J.D. and Li, Z.L. (1986a). "Reflection and transmission of scalar waves by a periodic array of screens", Wave Motion, Vol. 8, pp. 225-234.

Achenbach, J.D. and Li, Z.L. (1986b). "Propagation of horizontally polarized transverse waves in a solid with a periodic distribution of cracks", Wave Motion, Vol. 8, pp. 371-379.

Achenbach, J.D. and Zhang, Ch. (1990). "Reflection and transmission of ultrasound by a region of damaged material", Journal of Nondestructive Evaluation, Vol. 9(2/3), pp. 71-79.

Aki, K., Richards, P.G. (2002). "Quantitative seismology (2nd ed.)". University Science Books, California.

Al-Bender, F., Symens, W., Swevers, J. and Van Brussel, H., (2004). "Theoretical analysis of the dynamic behavior of hysteresis elements in mechanical system". International Journal of Non-Linear Mechanics, Vol. 39: pp. 1721-1735.

Anderson, E.M. (1985). "Electric Transmission Line Fundamentals", Reston Publication Company, VA.

Angel, Y.C. and Achenbach, J.D. (1985a). "Reflection and transmission of elastic waves by a periodic array of cracks", Journal of Applied Mechanics, Vol. 52, pp. 33-40.

Angel, Y.C. and Achenbach, J.D. (1985b). "Reflection and transmission of elastic waves by a periodic array of cracks: oblique incidence", Wave Motion, Vol. 9, pp. 375-382.

Angel, Y.C. and Achenbach, J.D. (1987). "Harmonic waves in an elastic solid containing a doubly periodic array of cracks", Wave Motion, Vol. 9, pp. 377-385.

Ass'ad, J. M., Tatham, R. H., Mcdonald, J. A., Kusky, T. M., and Jech, J. (1993). "A physical model study of scattering of waves by aligned cracks: comparison between experiment and theory", Geophysical Prospecting, Vol. 41, pp. 323-339.

Auld, J. M., Tatham, R. H., Mcdonald, J. A., Kusky, T. M., and Jech, J. (1993). "A physical model study of scattering of waves by aligned cracks: comparison between experiment and theory", Geophysical Prospecting, Vol. 41, pp. 323-339.

Auld, B. A. (1973). "Acoustic Fields and Waves in Solids". New York: John Wiley and Sons, Vol.1-2.

Baer G., D. Sandwell, S. Williams, Y. Bock, and G. Shamir, (1999). "Coseismic deformation associated with the November 1994," Mw-7.1 Nuweiba earthquake, Gulf of Elat (aqaba) detected by synthetic aperture radar interferometry, J. Geophys. Res., 104, 25, 221–25, 232.

Baik, J.M. and Thompson, P.B. (1984). "Ultrasonic scattering from imperfect interfaces", Journal of Nondestructive Evaluation, Vol. 4, pp. 177.

Banik, N.C., Lerche, I., and Shuey, R.T. (1985). "Stratigraphic filtering based on derivation of the O'Doherty-Anstery formula", Geophysics, Vol. 50(12), pp. 2768-2774.

Bardet J.P., Ichii K., Lin C.H., (2000). "EERA - A computer program for equivalent linear earthquake site response analyses of layered soils deposits". User Manual.

Barla G., J. Sharp, U. Rabagliati, (1991). "Excavation and support optimisation for a large underground storage facility in weak jointed chalk". International Congress on Rock Mechanics. Vol. 2, pp. 1067-1072.

Barton, N. (1995). "The influence of joint properties in modelling jointed rock masses". Keynote Lecture, 8th ISRM Congress, Tokyo, 3: 1023-1032, Balkema, Rotterdam.

Barton, N. R. (1973). "Review of a new shear strength criterion for rock joints". Eng. Geol., 8(4), pp: 287-332.

Barton, N. By, T.L. Chryssanthakis, P. Tunbridge, L. Kristiansen, J. Løset, F. Bhasin, R.K. Westerdahl, H. and Vik, G. (1994). "Predicted and measured performance of the 62 m span Norwegian olympic ice Hockey Cavern at Gjøvik". International Journal of Rock Mechanics and Mining Sciences & Geomechanics, Vol. 31, Issue 6, pp: 617-641.

Bedford, A., and Drumheller, D.S. (1994). Introduction to Elastic Wave Propagation, John Wiley & Sons, Chichester.

Beer G., Meek J.L. (1982). "Design curves for roofs and hanging-walls in bedded rock based on "voussoir" beam and plate solutions". Trans, Inst. Min. Metal, Vol. 91, pp. 18-22

Biot, M.A. (1956a). "Theory of propagation of elastic waves in a fluid saturated, porous solid: I. Low-frequency range", Journal of the Acoustical Society of America, Vol. 28, pp. 168-178.

Biot, M.A. (1956b). "Theory of propagation of elastic waves in a fluid saturated, porous solid: II. Higher-frequency range", Journal of the Acoustical Society of America, Vol. 28, pp. 179-191.

Boadu, F.K. (1997). "Fractured rock mass characterization parameters and seismic properties: Analytical studies", Journal of Applied Geophysics, 36: pp. 1-19.

Bostrom, A. and Eriksson, A.S. (1993). "Scattering by two penny-shaped cracks with spring boundary conditions", Proc. R. Soc. London, A 443, pp. 183-201.

Bourbié, T. Coussy, O. and Zinszner, B. (1987). "Acoustics of Porous Media", Gulf Publishing, Houston.

Brady, B.H.G. Cramer, M.L. and Hart, R.D. (1985). "Preliminary Analysis of a Loading Test on a Large Basalt Block," Int. J. Rock Mech., 22(5), 345-348.

Braja, M. D. and Ramana, C. V. (2011), "Principles of Soil Dynamics", Cengage Learning, Stamford.

Bray, J. D. and Rodriguez-Marek, A. (2004). "Characterization of forward-directivity ground motions in the near-fault region". Soil Dynamics and Earthquake Engineering, 24, 815-828.

Brekhovskikh, L.M. (1960). Waves in Layered Media, Academic Press, New York.

Budreck, D.E. and Achenbach, J.D. (1988). "Scattering from three-dimensional planar cracks by the boundary integral equation method", Journal of Applied Mechanics, Vol. 55, pp. 405.

Burstow, C.G., Corell, M.C. and Rogers, A.C. (1989). "Mechanisms of Dislocation Motion in 7075-T73 Aluminum Alloy at Strain Rates of 105 s-1", Materials at High Rates of Strain, Institute of Physics, Bristol, CT.

Cagniard, L. (1962). Reflection and Refraction of Progressive Seismic Waves, McGraw- Hill.

Campbell, C.S. and Brennen, C.E. (1985). "Computer simulation of granular shear flows", Journal of Fluid Mechanics, Vol. 151, pp. 167-188.

Cai, J.G. (2001). Phd thesis. "Effects of Parallel Fractures on Wave Attenuation in Rock". Advisor: Prof. Zhao Jian. School of Civil and Structural Engineering, Navyang Technological University, Singapore.

Cai, J.G., Zhao, J. (2000). "Effects of multiple parallel fractures on apparent wave attenuation in rock masses". Int J Rock Mech Min Sci 37:661–682.

Capuani, D. and Willis, J.R. (1997). "wave propagation in elastic media with cracks Part I: transient nonlinear response of a single crack", European Journal of Mechanics, A/Solids, Vol. 16(3), pp. 377-408.

Caughey, T. K. (1960). "Sinusoidal excitation of a system with bilinear hysteresis", Journal Applied Mechanics, Trans. ASME, Dec. 1960: 640-643.

Chatterjee, A.K. and Mal, A.K. (1978). "Elastic moduli of two-component systems", Journal of Geophysical Research, Vol. 83(B4), pp. 1785-1792.

Chatterjee, A.K., Mall, A.K., Knopoff, M.L. and Hudson, J.A. (1980). "Attenuation of elastic waves in a cracked, fluid-saturated solid", Math. Proc. Camb. Phil. Soc., Vol. 88, pp. 547-561.

Chen, W.Y., Lovell, C.W., Haley, G.M. and Pyrak-Nolte, L.J. (1993). "Variation of shear wave amplitude during frictional sliding", International Journal of Rock Mechanics and mining Science & Geomechanics Abstracts, Vol. 30(7), pp. 779-784.

Coates, R.T. and Schoenberg, M. (1995). "Finite-difference modelling of faults and fractures", Geophysics, Vol. 60(5), pp. 1514-1526.

Collin R (1992). Foundations for microwave engineering. McGraw-Hill, New York.

Cook, N. G. W. (1992). "Natural fractures in rock: mechanical, hydraulic and seismic behaviour and properties under normal stress", International Journal of Rock Mechanics and Mining Sciences & Geomechanics Abstracts. Vol. 29(3), pp. 198-223.

Corigliano, M. (2007). Phd thesis. "Seismic response of deep tunnels in near-fault conditions". Advisor: Prof. Barla Giovanni. Structural and Geotechnical Engineering Department, Politecnico di Torino, Italy.

Courant R. and Hilbert D. (1962). "Methods of mathematical physics II". Interscience, New York.

Coutant, O. (1989). "Numerical study of the diffraction of elastic waves by fluid-filled cracks", Journal of Geophysical Research, Vol. 94(B12), pp. 17,805-17,818.

Crampin, S. (1981). "A review of wave motion in anisotropic and cracked elastic-media", Wave Motion, Vol. 3, pp. 342-391.

Crampin, S. (1984). "Effective anisotropic elastic constants for wave propagation through cracked solids", Geophysical Journal of Royal Astronomical Society, Vol. 76, pp. 135-142.

Cundall, P.A. (1971). "A Computer Model for Simulating Progressive, Large-scale Movements in Block Rock System", Proceedings of Symposium International Society of Rock Mechanics, Nancy, France.

Cundall, P.A., Strack, O.D.L. (1979). "Discrete numerical model for granular assemblies". Geotechnique, Vol. 29, pp. 47–65.

Cundall, P.A. (1980). "A Generalized Distinct Element Program for Modelling Jointed Rock", Peter Cundall Associates, U.S. Army, European Research Office.

Cundall, P.A. and Hart, R.D. (1985). "Development of generalized 2-D and 3-D distinct element programs for modelling jointed rocks". Misc. Paper SL-85-1, U.S. Army Corp of Engineers, Itasca Consulting Group.

Cundall, P.A. (1988). "Formulation of a three-dimensional distinct element model – Part I, A scheme to detect and represent contacts in a system composed of

many polyhedral blocks", International Journal of Rock Mechanics and Mining Sciences, Vol. 25, pp 107-116.

Cundall, P.A. and Strack, O.D.L. (1979). "A discrete numerical model for granular assemblies", Geotechnique, No. 29, pp. 47-65.

Cundall, P. A., and Strack., O.D.L. (1983). "Modeling of Microscopic Mechanisms in Granular Material", Mechanics of Granular Materials: New Models and Constitutive Relations, J. T. Jenkins and M. Satake, Eds. Amsterdam: Elsevier Scientific, pp. 137-149.

Daehnke, A and Rossmanith, H.P. (1997a). "Reflection and transmission of plane stress waves at interfaces modelling various rock joints", The International Journal for Blasting and Fragmentation, Vol. 1(2): 111-231.

Daehnke, A and Rossmanith, H.P. (1997b). "Reflection and refraction of plane stress waves at dissipative interfaces", Proceedings of the 1st International Conference on Damage and Failure of Interfaces, Vienna, Austria, pp. 315-320.

Diederichs, M.S. and Kaiser, P.K. (1999). "Stability of large excavations in laminated hard rock masses: The Voussoir analogue revisited". International Journal of Rock Mechanics and Mining Science, Vol. 36, 97-117.

Donzé, F. V., J. Bouchez, et al. (1997). Modeling fractures in rock blasting. International Journal of Rock Mechanics and Mining Sciences 34(8): 1153-1163.

Donzé, F. V. and P. Bernasconi (2004). Simulation of blast patters in shaft sinking using Discrete Element Method. Electronic Journal of Geotechnical Engineering Geology 9(B): 22.

Dowding, C.H., Rozen, A., (1978). "Damage to rock tunnels from earthquake shaking". J. Geotech. Eng. Div., ASCE 104 GT2, 175-191.

Duke, C.M., Leeds, D.J., (1959). "Effects of Earthquakes on Tunnels", Paper Presented at the RAND Second Protective Construction Symposium, March 24-26.

Eriksson, L.I. Backlund, J. and Moller, P. (1995). "Design of multiple-row bolted composite joints under general in-plane loading". Composites Engineering, 5: pp. 1051-1068.

Eshelby, J.D. (1957). "The determination of the elastic field of an ellipsoidal inclusion, and related problems", Proc. R. Soc. London, A 241, pp. 376-397.

Evans, W.H. (1941). "The strength of undermined strata". Trans Inst Min Metal 1941, Vol. 50, pp. 475–500.

Ewing WM, Jardetzky WS, Press F (1957). "Elastic waves in layered media". McGraw-Hill, New York.

Fehler, M. (1982). "Interaction of seismic waves with a viscous liquid layer". Bulletin of Seismic Association of America 72: 55-72.

Fokkema, J.T. Ziolkowski, A. (1987). "The critical reflection theorem". Geophysics, 52: pp. 965-972.

Foldy, L.L. (1945). "Multiple scattering theory of waves", Physical Review, Vol. 67, pp. 107-119.

Fortsch, O. (1956). "Die ursachen der absorption elastischer wellen", Ann. Geof., Vol. 9, pp. 469-524.

Frazer, L.N. (1990). "Dynamic elasticity of microbedded and fractured rocks", Journal of Geophysical Research, Vol. 95(B4), pp. 4821-4831.

Frazer, L.N. (1995). "SH propagation in rocks with planar fractures - I. excess slowness", Geophysical Journal International, Vol. 122(1), pp. 33-62.

Garbin, H.D. and Knopoff, L. (1973). "The compressional modulus of a material permeated by a random distribution of circular cracks", Quart. Appl. Math, Vol. 30, pp. 453-464.

Garbin, H.D. and Knopoff, L. (1975a). "The shear modulus of a material permeated by a random distribution of free circular cracks", Quart. Appl. Math, Vol. 33, pp. 296-300.

Garbin, H.D. and Knopoff, L. (1975b). "Elastic moduli of a medium with liquid-filled cracks", Quart. Appl. Math, Vol. 33, pp. 301-303.

Goodman, R.E., Taylor, R.L. and Brekke, T.A. (1968). "Model for the Mechanics of Jointed Rock", Journal of the Soil Mechanics and Foundations Division, ASCE, Vol. 94(SM3), pp. 637-659.

Goodman, R.E. (1976). "Methods of Geological Engineering in Discontinuous Rocks", 1st edition, West, New York, 472p.

Green, G. (1939). "On the laws of reflexion and refraction of light". Transactions of the Cambridge Philosophical Society, vol. 7. (Reprinted in Mathematical Papers of George Green, pp. 245-269, London, 1871).

Gu, B. (1994). "Interface Waves on a Fracture in Rock", Ph.D. Thesis, University of California at Berkeley, USA.

Gu, B., Nihei, K.T., Myer, L.R. and Pyrak-Nolte, L.J. (1995). "Fracture interface waves", Journal of Geophysical Research, Vol. 101(B1), pp. 827-835.

Gu, B., Suarez-Rivera, R., Nihei, K. and Myer, L.R. (1996). "Incidence of plane waves upon a fracture", Journal of Geophysical Research, Vol. 101(B11): 25337-25346.

Gutierrez, M. & Barton, N. (1994). "Numerical modelling of the hydro-mechanical behaviour of single fractures". In Nelson and Laubach (eds.) Rock Mechanics: Models and Measurements, Challenges from Industry, pp. 165-172.

Han, S. (1995). "Equivalent mechanical effect of joint under wave loads", Fractured and Jointed Rock Masses (edited by Myer, L.R. et al.), pp. 335-340.

Han, S., Kyoya, T., Ichikawa, Y. and Kawamoto, T. (1986). "Dynamic analysis of jointed rock", Proceedings of International Symposium of Engineering in Complex Rock Formation, Beijing, pp. 338-344.

Harris, F.j. (1978). "On the use of Windows for Harmonic Analysis with the Discrete Fourier Transform". Proceedings of the IEEE 66 (1): 51–83.

Hart, R., Cundall, P.A. and Lemos , L. (1988). "Formulation of a three-dimensional distinct element model – Part II. Mechanical calculations for motion and interaction of a system composed of many polyhedral Blocks", International Journal of Rock Mechanics and Mining Sciences, vol. 25, pp 117-125.

Hashash, Y.M.A., Jeffrey, Hook, J.J., Schmidt, B., Yao, J. I-C., (2001). "Seismic design and analysis of underground structures". Tunnelling and Underground Space Technology 16: pp. 247-293.

Hatzor Y. H. & Benary R., (1998). "The Stability of a Laminated Voussoir Beam: Back Analysis of a Historic Roof Collapse Using DDA". Int. J. Rock Mech. Min. Sci. Vol. 35, No. 2, pp. 165-181.

Hazzard, J. F. and R. P. Young (2004). Numerical investigation of induced cracking and seismic velocity changes in brittle rock. Geophysical Research Letters 31: 4.

Hentz, S., F. V. Donzé, et al. (2004). Discrete element modelling of concrete submitted to dynamic loading at high strain rates. Computers & Structures 82(29-30): 2509-2524.

Hirose, S. and Achenbach, J.D. (1993). "Higher harmonics in the far field due to dynamic crack-face contacting", Journal of the Acoustical Society of America, Vol. 93(1), pp. 142147.

Hirose, S. and Kitahara, M. (1991). "Scattering of elastic waves by a crack with spring- mass contact" International Journal of Numerical Methods in Engineering, Vol. 31, pp. 789-801.

Hopkins, D.L., Myer, L.R., and Cook, N.G.W. (1988). "Seismic wave attenuation across parallel fractures as a function of fracture stiffness and spacing", EOS Transaction AGU, Vol. 68(44), pp. 1427.

Hudson, J.A. (1980). "Overall properties of a cracked solid", Math. Proc. Camb. Phil. Soc., Vol. 88, pp. 371-384.

Hudson, J.A. (1981). "Wave speeds and attenuation of elastic waves in material containing cracks", Geophysical Journal of the Royal Astronomic Society, Vol. 64, pp. 133-150.

Hudson, J.A. (1986). "A high order approximation to the wave propagation constants for a cracked solid", Geophysical Journal of the Royal Astronomical Society, Vol. 87, pp. 265274.

Hudson, J.A. (1988). "Seismic wave propagation through material containing partially saturated cracks", Geophysical Journal, Vol. 92, pp. 33-37.

Hudson, J.A. (1990). "Attenuation due to second-order scattering in material containing cracks", Geophysical Journal International, Vol. 102, pp. 485-490.

Hudson, J.A. and Knopoff, L. (1989). "Predicting the overall properties of composite materials with small-scale inclusions or cracks", Pageoph, Vol. 131(4), pp. 551-576.

Hudson, J.A., Liu, E. and Crampin, S. (1996). "The mechanical properties of materials with interconnected cracks and pores", Geophysical Journal International, Vol. 124(1), pp. 105112.

Iizuka, K. (2008). "Engineering Optics", 3rd ed., Springer.

Itasca Consulting Group, Inc. (2006). "UDEC Universal Distinct Element Code, Version 4.0: User's Guide", Minneapolis, Minnesota.

Itasca Consulting Group, Inc., (2007). "3DEC 3-Dimensional Distinct Element Code, Version 4.1: User's Guide", Minneapolis, Minnesota.

Iwan, W. D. (1973). "A generalization of the concept of equivalent linearization", Int. J. Non-Linear Mech. 8, 279-287

Jaeger J.C. Cook, N.G.W. and Zimmerman R.W. (2007). Fundamentals of Rock Mechanics, Fourth Edition, Blackwell Publishing.

Jennings, P. C. (1968). "Equivalent viscous damping for yielding structures", Journal the Engineering Mechanics Division, Proceedings ASCE, Vol. 94 (EM1): 103-116.

Johnston, D.H. (1978). "The Attenuation of Seismic Waves in Dry and Saturated Rocks", Ph.D. Thesis, Massachusetts Institute of Technology, Cambridge, Massachusetts, USA.

Johnston, D.H. and Toksoz, M.N. (1980). "Ultrasonic P- and S-wave attenuation in dry and saturated rocks under pressure", Journal of Geophysical Research, Vol. 85, pp. 925-936.

Johnston, D.H., Toksoz, M.N. and Timur, A. (1979). "Attenuation of seismic waves in dry and saturated rocks: II Mechanisms", Geophysics, Vol. 44, No. 4, pp. 691-711.

Jones, J.P. and Whitter, J.S. (1967). "Waves at a flexibly bonded interface", Journal of Applied Mechanics, Vol. 40, pp. 905-909.

Kaiser, M.A. (1998). "Advancements in the Split Bar Test", Virginia Polytechnic Institute & State University, Blacksburg, Virginia.

Kaneshiro, J.Y., Power, M., Rosidi, D., (2000). "Empirical correlations of tunnel performance during earthquakes and aseismic aspects of tunnel design".

Proceedings of the Conference on Lessons Learned From Recent Earthquakes - On Earthquakes in Turkey 1999, November 8-11.

Kendall, K., and Tabor, D. (1971). "An ultrasonic study of the area of contact between stationary and sliding surfaces", Proc. R. Soc. London, A 323, pp. 321-340.

Kennett, B.L.N. (1983). "Seismic Wave Propagation in Stratified Media", Cambridge University Press, Cambridge, London, 1983.

Kim, M. K., S. E. Kim, et al. (1997). A study on the behavior of rock mass subjected to blasting using modified distinct element method. International Journal of Rock Mechanics and Mining Sciences 34(3-4): 156.e1-156.e14.

Kim, S., W. Jeong, et al. (2006). Numerical simulation of blasting at tunnel contour hole in jointe rock mass. Tunnelling and Underground Space Technology 21(3-4): 306-307.

King, M.S. (1966). "wave velocities in rocks as a function of changes in overburden pressure and pore fluid saturants", Geophysics, Vol. 31, pp. 50-73.

King, M.S., Myer, L.R. and Rezowalli, J.J. (1986). "Experimental studies of elastic-wave propagation in a columnar-jointed rock mass", Geophysical Prospecting, Vol. 34(8), pp. 1185-1199.

King, M.S. and Xu, S (1989). "Shear-wave birefringence and directional permeability in fractured rock", Rock at Great Depth (edited by Maury, V. and Fourmaintraux, D.), Balkema, Rotterdam, pp. 262-272.

Kinoshita, N. and Mura, T. (1971). "Elastic fields of inclusions in anisotropic media", Physics Status Solidi, Serial A, Vol. 5, pp. 759-768.

Klerck, P.A., Sellers, E.J., Owen, D.R.J. (2004). "Discrete fracture in quasi-brittle materials under compressive and tensile stress states". Comp Meth Appl Mech 2004, Vol. 193, pp. 3035–56.

Knott, C. G. (1899). "Reflection and refraction of elastic waves with seismological applications". Philosophical Magazine, Series 5, 48, 64-97.

Kolsky, H. (1949). "An Investigation of the Mechanical Properties of Materials at Very high Rates of Strain", Proc. Roy. Phys. Soc., B 62, pp. 676-700.

Kolsky, H. (1952). "Stress Waves in Solids", Dover Publications, New York.

Krylov, N.M. and Bogolyubov, N.N. (1947). "Introduction to non-linear mechanics", Princeton Univ. Press.

Kuhlmeyer, R.L. and Lysmer, J. (1973). "Finite element method accuracy for wave propagation problems", Journal of Soil Mechanics and Foundation Division, ASCE, Vol. 99, pp. 421-427.

Kupradze, V.D. (1965). "Potential Methods in Theory of Elasticity", Proceedings of Israel Program for Scientific Translation, Jerusalem.

Kuster, G.T. and Toksoz, M.N. (1974a). "Velocity and attenuation of seismic waves in two- phase media: Part I Theoretical formulations", Geophysics, Vol. 39(5), pp. 587-606.

Kuster, G.T. and Toksoz, M.N. (1974b). "Velocity and attenuation of seismic waves in two-phase media: Part II experimental results", Geophysics, Vol. 39(5), pp. 607-617.

Lax, M. (1952). "Multiple scattering of waves II", Physical Review, Vol. 85, pp. 621-629.

Li, J.C., Ma, G.W., Zhao, J. (2010). "An equivalent viscoelastic model for rock mass with parallel joints". J Geophys Res 115. doi: 10.1029/2008JB006241.

Li, J. C. and Ma G. W. (2009). "Experimental study of stress wave propagation across a filled rock joint", Int. J. Rock Mech. Min. Sci., 46(3), 471-478.

Lin, W. and Keer, L.M. (1987). "Scattering by a planar three-dimensional crack", Journal of the Acoustical Society of America, Vol. 82, pp. 1442.

Loeb, J. (1961). "Attenuation des ondes sismiques dans les solids", Geophysical Prospecting, Vol. 9, pp. 370-381.

Lysmer J. & Kuhlmeyer R. L. (1969). "Finite Dynamic Model for Infinite Media". Journal of the Engineering Mechanics Division, Vol 95, pp 859-877

Macelwane, J.B. and Sohon, F.W. (1936). Introduction to Theoretical Seismology, Wiley, New York.

Mal, A.K. (1970). "Interaction of elastic waves with a penny-shaped crack", International Journal of Engineering Science, Vol. 8, pp. 381-388.

Martin, P.A. (1981). "Diffraction of elastic waves by a penny-shaped crack", Proc. R. Soc. London, A 378, pp. 263-285.

Martin, P.A. and Wickham (1983). "Diffraction of elastic waves by a penny-shaped crack: analytical and numerical results", Proc. R. Soc. London, A 390, pp. 91-129.

Matsuoka, T., H. Kusumi, et al. (2003). Simulation of Hopkinson effect by discrete element method. ISRM 2003 -- Technology Roadmap for Rock Mechanics, South Africa.

Mavko, G. and Nur, A. (1975). "Melt squirt in the atmosphere", Journal of Geophysical Research, Vol. 80, pp. 1444-1448.

Mavko, G. and Nur, A. (1979). "Wave attenuation in partially saturated rocks", Geophysics, Vol. 44, pp. 161-178.

Mavko, G., Mukerji, T. and Dvorkin, J. (1998). The Rock Physics Handbook, Cambridge University Press, Cambridge.

McCann, C. and McCann, D.M. (1985). "A theory of compressional wave attenuation in non-cohesive sediments", Geophysics, Vol. 52, pp. 1311-1317.

Mehtab, M.A. and Goodman, R.E. (1970). "Three-dimensional Finite Element Analysis of Jointed Rock Slopes", Proceedings of the 2nd International Congress on Rock Mechanics, Belgrad.

Mikata, Y. and Achenbach, J.D. (1988). "Interaction of harmonic waves with a periodic array of inclined cracks", Wave Motion, Vol. 10, pp. 59.

Miksis, M.J. (1988). "Effects of contact line movement on the dissipation of waves in partially saturated rocks", Journal of Geophysical Research, Vol. 93(B6), pp. 6624-6634.

Miller, R.K. (1977). "An approximate method of analysis of the transmission of elastic waves through a frictional boundary", Journal of Applied Mechanics, Vol. 44, pp. 652-656.

Miller, R.K. (1978). "The effects of boundary friction on the propagation of elastic waves", Bulletin of the Seismological Society of America, Vol. 68(4), pp. 987-998.

Mindlin, R. D. (1960) "Waves and vibrations in isotropic, elastic plates, in Structural Mechanics", edited by J. N. Goodier and J . J. Hoff, pp. 199-232, Pergamon, New York, 1960.

Mochizuki, S. (1982). "Attenuation in partially saturated rocks", Journal of Geophysical Research, Vol. 87, pp. 8,598-8,604.

Morris, W.L., Buck, O. and Inman, R.V. (1979). "Acoustic harmonic generation due to fatigue damage in high-strength aluminium", Journal of Applied Physics, Vol. 50, 67376741.

Murphy III, W.F. (1982a). "Effects of microstructure and pore fluids on the acoustic properties of granular sedimentary materials", Ph.D. Thesis, Stanford University, Stanford, USA.

Murphy III, W.F. (1982b). "Effects of partial water saturation on wave attenuation in Massilon sandstone and Vycor porous glass", Journal of the Acoustical Society of America, Vol. 71, pp. 1458-1468.

Murphy III, W.F. (1984). Acoustic measures of partial gas saturation in tight sandstones", Journal of Geophysical Research, Vol. 89, pp. 11,549-11,559.

Murty, G.S. (1975). "A theoretical model for the attenuation and dispersion of Stoneley waves at the loosely bonded interface of elastic half-space", Phys. Earth Planet Inter., Vol. 11, pp. 65-79.

Myer, L.R. (1998). "Seismic wave propagation in fractured rock", Proceedings of the 3rd International Conference on Mechanics of Jointed and Faulted Rock, (Edited by Rossmanith, H.P.), pp. 29-38.

Myer, L.R. Pyrak-Nolte, L.J., Cook, N.G.W. (1990), "Effects of single fractures on seismic wave propagation". Rock joints: 467-473. Barton, Stephansson. Balkema, Rotterdam.

Myer, L.R., Hopkins, D. and Cook, N.G.W. (1985). "Effects of contact area of an interface on acoustic wave transmission characteristics", Proceedings of the 26th U.S. Rock Mechanics Symposium, Boston, Vol. 1, pp. 565-572.

Myer L.R., Pyrak-Nolte L.J. & Cook N.G.W. (1990). "Effects of single fractures on seismic wave propagation". Rock joints: 467-473. Barton & Stephansson. Rotterdam: Balkema.

Myer, L.R., Hopkins, D., Peterson, J.E. and Cook, N.G.W. (1995). "Seismic wave propagation across multiple fractures", Fractured and Jointed Rock Masses (edited by Myer, L.R., Cook, N.G.W., Goodman, R.E. and Tsang, C.F.), Balkema Publishers, Rotterdam, pp. 105-109.

Myer, L.R., Nihei, K.T. and Nakagawa, S. (1997). "Dynamic properties of interfaces", Proceedings of the 1st International Conference on Damage and Failure of Interfaces, Vienna, Austria, pp. 47-56.

Nakagawa, S., Nihei, K.T. and Myer, L.R. (2000a). "Shear-induced conversion of seismic waves across single fractures", International Journal of Rock Mechanics and Mining Sciences, Vol. 37, pp. 203-218.

Nakagawa, S., Nihei, K.T. and Myer, L.R. (2000b). "Stop-pass behaviour of acoustic waves in a 1D fractured system", Journal of the Acoustical Society of America, Vol. 107(1), pp. 40-50.

Nihei, K.T., Yi, W., Myer, L.R. and Cook, N.G.W. (1999). "Fracture channel waves", Journal of Geophysical Research, Vol. 104(B3), pp. 4769-4781.

Ngo, D. and Scordelis, A.C. (1967). "Finite Element Analysis of Reinforcement Concrete", Jul. Am. Concrete Inst., No. 64-14, pp. 152-163.

Nishizawa, O. (1982). "Seismic velocity anisotropy in a medium containing oriented cracks - transversely isotropic case", Journal of Physics of the Earth, Vol. 30, pp. 331-347.

Nolte, D.D., Pyrak-Nolte, L.J., Beachy, J. and Ziegler, C. (2000). "Transition from the displacement discontinuity limit to the resonant scattering regime for fracture interface waves", International Journal of Rock Mechanics and Mining Sciences, Vol. 37, pp. 219230.

Nur, A. (1971). "Effects of stress on velocity anisotropy in rocks with cracks", Journal of Geophysical Research, Vol. 76, pp. 2022-2034.

Nur, A. and Simmons, G. (1969). "Stress-induced velocity anisotropy in rock: an experimental study", Journal of Geophysical Research, Vol. 74, pp. 6667-6674.

Obert, L., and Duvall, W.I. (1967), "Rock Mechanics and the Design of Structures in Rock", John Wiley & Sons, 650 pages.

O'Connell, R.J. Budianski, B. (1974). "Seismic velocities in dry and saturated cracked solids", Journal of Geophysical Research, Vol. 79, pp. 5412-5425.

O'Connell, R.J. Budianski, B. (1977). "Viscoelastic properties of fluid-saturated cracked solids", Journal of Geophysical Research, Vol. 82, pp. 5719-5730.

O'Doherty, R.F., and Anstey, N.A. (1971). "Reflections on amplitudes", Geophysical Prospecting, Vol. 19, pp. 430-458.

Owen, G.N., Scholl, R.E., (1981). "Earthquake engineering of large underground structures". Report no. FHWA_RD-80_195. Federal Highway Administration and National Science Foundation.

Peacock, S. and Hudson, J.A. (1990). "Seismic properties of rocks with distributions of small cracks", Geophysical Journal International, Vol. 102, pp. 471-484.

Perino, A. (2007). Master degree thesis. "Valutazioni empiriche ed analisi numeriche degli effetti sismici sul comportamento delle gallerie profonde". Advisor: Prof. Barla Giovanni. Structural and Geotechnical Engineering Department, Politecnico di Torino, Italy

Piau, M. (1979). "Attenuation of a plane compressional wave by a random distribution of circular cracks, International Journal of Engineering Science, Vo. 17, pp. 151-167.

Potyondy, D. O., P. A. Cundall, et al. (1996). Modelling rock using bonded assemblies of circular particles. Rock Mechanics US.

Potyondy, D. O. and P. A. Cundall (2004). A bonded-particle model for rock. International Journal of Rock Mechanics and Mining Sciences 41(8): 1329-1364.

Power, M., Rosidi, D., Kaneshiro, J., (1998). "Seismic vulnerability of tunnels-revisited". In: Ozedimir, L., ŽEd... Proceedings of the North American Tunneling Conference. Elsevier, Long Beach, CA, USA.

Pyrak-Nolte, L.J. (1988). "Seismic Visibility of Fractures", Ph.D. Thesis, University of California at Berkeley, USA.

Pyrak-Nolte, L.J. and Cook, N.G.W. (1987). "Elastic interface waves along a fracture", Geophysical Research Letters, Vol. 14(11), pp. 1107-1110.

Pyrak-Nolte, L.J, Myer, L.R., and Cook, N.G.W. (1987). "Seismic visibility of fractures", Proceedings of the 28th U.S. Symposium on Rock Mechanics, (edited by Farmer, I.W.), pp. 47-56.

Pyrak-Nolte, L.J, Myer, L.R. and Cook, N.G.W. (1990a). "Transmission of seismic waves across single natural fractures", Journal of Geophysical Research, Vol. 95(B6), pp. 86178638.

Pyrak-Nolte, L.J, Myer, L.R., and Cook, N.G.W. (1990b). "Anisotropy in seismic velocities and amplitudes from multiple parallel fractures", Journal of Geophysical Research, Vol. 95(B7), pp. 11345-11358.

Pyral-Nolte, L.J., Myer, L.R., Xu, J. and Haley, G.M. (1992). "Elastic interface waves propagating in a fracture", Physical Review Letters, Vol. 68(24), pp. 3650-3653.

Pyrak-Nolte, L.J., and Nolte, D.D. (1992). "Frequency dependence of fracture stiffness", Geophysical Research Letters, Vol. 19(3), pp. 325-328.

Pyrak-Nolte, L.J., and Nolte, D.D. (1995). "Wavelet analysis of velocity dispersion of elastic interface waves propagating along a fracture", Geophysical Research Letters, Vol. 22(11), pp. 1329-1332.

Pyrak-Nolte, L.J. (1996). "The seismic response of fractures and the interrelations among fracture properties", International Journal of Rock Mechanics and Mining Sciences, Vol. 33(8), pp. 787-802.

Pyrak-Nolte, L.J., Roy, S. and Mullenbach, B.L. (1996). "Interface waves propagated along a fracture", Journal of Applied Geophysics, Vol. 35(2/3), pp. 79-87.

Rezowalli, J.J., King, M.S. and Myer, L.R. (1984). "Cross-hole acoustic surveying in basalt", International Journal of Rock Mechanics and Mining Sciences & Geomechanics Abstracts, Vol. 21, pp. 213-216.

Rizzo, F.J. (1967). "An integral equation approach to boundary value problems of classical elastostatics". Quarterly of Applied Mathematics, 25: 83-95.

Rokhlin, S. I., and Y. G. Wang (1991). "Analysis of boundary conditions for elastic wave interaction with an interface between two solids", J. Acoust. Soc. Am., 89(2), 503-515.

Rossmanith, H.P., Xu, C., Knasnmillner, R.E. and Wegner, J.L. (1993). "Effect of stress waves on pre-damaged interfaces in rock mass", Proceedings of the 14th International Symposium on Rock Fragmentation by Blasting - Fragblast-4, Vienna, Austria, pp. 201210.

Roy, S., and Pyrak-Nolte, L.J. (1995). "Interface waves propagating along tensile fractures in dolomite", Geophysical Research Letters, Vol. 22(20), pp. 2773-2777.

Roy, S., and Pyrak-Nolte, L.J. (1997). "Observation of a distinct compressional-mode interface wave on a single fracture", Geophysical Research Letters, Vol. 24(2), pp. 173176.

Rytov, S.M. (1956). "Acoustical properties of a thinly laminated medium," Sov. Phys. Acount., Vol. 2, pp. 67-80.

Salganik, R.L. (1973). "Mechanics of bodies with many cracks", Mechanics of Solids, Vol. 8(4), pp. 135-143.

Sayers, C.M. and Kachanov, M (1991). "A simple technique for finding effective elastic constants of cracked solids for arbitrary crack orientation statistics", International Journal of Solid Structures, Vol. 27(6), pp. 671-680.

Schoenberg, M. (1980). "Elastic wave behaviour across linear slip interfaces", Journal of Acoustics Society of America, Vol. 68(5), pp. 1516-1521.

Schoenberg, M. (1983). "Reflection of elastic waves from periodically stratified media with interfacial slip", Geophysical Prospecting, Vol. 31, pp. 265-292.

Schoenberg, M. and Douma, J. (1988) "Elastic wave propagation in media with parallel fractures and aligned cracks", Geophysical Prospecting, Vol. 36, pp. 571-590.

Schoenberg, M. and Muir, F. (1989). "A calculus for finely layered anisotropic media", Geophysics, Vol. 54(5), pp. 581-589.

Schoenberg, M. and Sayers, C.M. (1995). "Seismic anisotropy of fractured rock", Geophysics, Vol. 60 (1), pp. 204-211.

Schoenberger, M. and Levin, F.K. (1974). "Apparent attenuation due to intrabed multiples", Geophysics, Vol. 39(3), pp. 278-291.

Shamir G., (1996). "The November 22, 1995, Nuweiba earthquake, Gulf of Elat (Aqaba): Mechanical analysis", Rep. 550/87/96 (114), Geophys. Inst. of Isr., Holon.

Sharma, S., Judd, W.R., (1991). "Underground opening damage from earthquakes". Eng. Geol. 30, 263-276.

Shi, G. (1988). "Discontinuous deformation analysis – a new numerical model for the statics and dynamics of block systems", Phd. Dissertation, Department of Civil Engineering, University of California at Berkeley, USA.

Shi, G. and Goodman R.E. (1985). "Two dimensional discontinuous deformation analysis", International Journal of Numerical and Analytical Method in Geomechanics, Vol. 9, pp. 541-556.

Shi, G. and Goodman R.E. (1988). "Discontinuous deformation analysis, a new method for computing stress, strain and sliding of block system", Proceedings of 29th U.S. Symposium Rock Mechanics, 381-393.

Shipley, S. A. Leistner, H. G. and Jones, R. E. (1968). "Elastic wave propagation a comparison between finite element predictions and exact solutions". Proceedings International Symposium on Wave Propagation and Dynamic Properties of Earth Materials, 23-25 Aug., University of New Mexico Press, pp. 509-519.

Sitar, N. and McLaughlin, M.M. (1997). "Kinematics and discontinuous deformation analysis of landslide movement". II Pan-American Symposium on Landslides, Rio de Janeiro, 10-14 November.

Smyshlyaev, V.P., Willis, J.R. and Sabina, F.J. (1993). "Self-consistent analysis of waves in a matrix-inclusion composite - III. A matrix containing cracks", Journal of Mechanics and Physics of Solids, Vol. 41, pp. 1809-1824.

Smyshlyaev, V.P. and Willis, J.R. (1994). "Linear and nonlinear scattering of elastic waves by microcracks", Journal of Mechanics and Physics of Solids, Vol. 42(4), pp. 585-610.

Sofianos, A.L. (1996), "Analysis and Design of an Underground Hard Rock Voussoir Beam Roof". Int. J. Rock Mech. Min. Sci., vol, 33, N° 2, pp.153 - 166.

Sotiropoulos, D.A. and Achenbach, J.D. (1988a). "Reflection of elastic waves by a distribution of coplanar cracks", Journal of the Acoustical Society of America, Vol. 84, pp. 752.

Sotiropoulos, D.A. and Achenbach, J.D. (1988b). "Ultrasonic reflection by a planar distribution of cracks", Journal of Nondestructive Evaluation, Vol. 7, pp. 123.

Spencer, J.W., Edwards, C.M., and Sonnad, J.R. (1977). "Seismic wave attenuation in nonresolvable cyclic stratification", Geophysics, Vol. 42(5), pp. 939-949.

Stephansson, O. Jing, L. and Tsang, C.F. (1996). "Coupled Thermo-Hydro-Mechanical Processes of Fractured Media Developments in Geotechnical Engineering", vol. 79, Elsevier Science B.V.

Stevens, P.R., (1977). "A review of the effects of earthquakes on underground mines". United States Geological Survey Open File Report 77-313. US Energy Research and Development Administration, Reston, VA.

Suarez-Rivera, R. (1992). "The Influence of Thin Clay Layers Containing Liquids on the Propagation of Shear Waves", Ph.D. Thesis, University of California at Berkeley, USA.

Swantek, S. D. (2000). "An Optical Method of Strain Measurement in the Split Hopkinson Pressure Bar", Virginia Polytechnic Institute & State University, Blacksburg, Virginia.

Toksoz, M.N., Johnston, D.H. and Timur, A. (1979). "Attenuation of seismic waves in dry and saturated rocks", I: laboratory measurements", Geophysics, Vol. 44, pp. 681-690.

Toomey, A. and C. Bean (2000). Numerical simulation of seismic waves using a discrete particle scheme Geophysical Journal International 141(3): 595-604.

Treitel, S. and Robinson, E.A. (1966). "Seismic wave propagation in layered media in terms of communication theory", Geophysics, Vol. 31, pp. 17-32.

Verruijt, A. (2010), "An Introduction to Soil Dynamics", Springer, Dordrecht.

Verweij, M.D. and Chapman, C.H. (1997). "Transmission and reflection of transient elastodynamic waves at a linear slip interface", Journal of the Acoustical Society of America, Vol. 101 (5), pp. 2473-2484.

Vestroni, F. and Noori, M. (2002). "Hysteresis in mechanical systems-modeling and dynamic response", Int. J. Non-Linear Mech. 37, 1261–1262 (Special Issue on Hysteresis).

Walsh, J.B. (1965a). "The effect of cracks on the compressibility of rocks", Journal of Geophysical Research, Vol. 70(2), pp. 381-389.

Walsh, J.B. (1965b). "The effect of cracks on the uniaxial elastic compression of rocks", Journal of Geophysical Research, Vol. 70(2), pp. 399-411.

Walsh, J.B. (1966). "Seismic wave attenuation in rock due to friction", Journal of Geophysical Research, Vol. 71(10), pp. 2593-2599.

Watanabe, T. and Sassa, K. (1989). "Effects of low velocity zone consisting of multiple thin layers on P-wave", Proceedings of International Symposium on Exploration Geophysics, Beijing, pp. 233-236.

Watanabe, T. and Sassa, K. (1995). "Velocity and amplitude of P-waves transmitted through fractured zones composed of multiple thin low-velocity layers", International Journal of Rock Mechanics and Mining Sciences & Geomechanics Abstracts, Vol. 32(4), pp. 313-324.

Waterman, P.C. (1976). "Matrix theory of elastic wave scattering", Journal of the Acoustical Society of America, Vol. 60, pp. 567-580.

Weidong, L. (2005). Phd thesis. "Numerical Studies on 2-D Compressional Wave Propagation in Jointed Rock Masses". Advisor: Prof. Hefny Ashraf Mohamed. School of Civil and Structural Engineering, Navyang Technological University, Singapore.

White, J.E. (1965). Seismic Waves: Radiation, Transmission and Attenuation, 1st edition, McGraw-Hill, New York.

White, J.E. (1983). Underground Sound, Elsevier, New York.

Williams, J.R. Hocking, G. and Mustoe, G.G.W. (1985). "The Theoretical Basis of the Discrete Element Method," NUMETA 1985, Numerical Methods of Engineering, Theory and Applications, A.A. Balkema, Rotterdam.

Wust H., (1997). "The November 22, 1995 Nuweiba earthquake, Gulf of Eilat (Aqaba): Post-seismic analysis of failure features and seismic hazard implications", Rep. GSI/3/97, 58 pp., Geol. Surv. of Isr., Jerusalem

Xiaoming, Y. Jing, S. & Rui, S. (2006). "A modified approach for calculating dynamic shear modulus of stiff specimens by resonant column tests". Earthquake Engineering and Engineering Vibration, vol.5, No.1, pp 143-150.

Xu, S. and King, M.S. (1990). "Attenuation of elastic waves in a cracked solid", Geophysical Journal International, Vol. 101, pp. 169-180.

Xu, S., King, M.S. and Worthington, M.H. (1990). "Elastic wave propagation and hydraulic properties of cracked rocks", Mechanics of Jointed and Faulted Rock (edited by Rossmanith, H.P.), Balkema, Rotterdam, pp. 651-658.

Yechieli Y. & Bein A. (2002). "Response of groundwater systems in the Dead Sea Rift Valley to the Nuweiba earthquake: Changes in head", water chemistry, and near-surface effects. Journal of Geophysical Research 107(B12): 2332.

Yi, W., Nihei, K.T., Rector, J.W., Nakagawa, S., Myer, L.R., and Cook, N.G.W. (1997). "Frequency-dependence seismic anisotropy in fractured rock", International Journal of Rock Mechanics and Mining Science & Geomechanics Abstract, Vol. 34(3/4), Paper No. 349.

Zhang, Ch. and Gross, D. (1993). "Wave attenuation and dispersion in randomly cracked solids- II. Penny-shaped cracks" International Journal of Engineering Science, Vol. 31, pp. 859-872.

Zhao, J., Cai, J.G. (2001). "Transmission of elastic P-waves across single fractures with a nonlinear normal deformational behavior". Rock Mech Rock Eng 34:3-22.

Zhao, J., Zhao, X.B., Cai, J.G., Hefny A.M. (2006). "A further study on P-wave attenuation across parallel fractures with linear deformational behavior". Int J Rock Mech Min Sci 43:776-788.

Zhao, X.B., Zhao, J., Cai, J.G. (2006a). "P-wave transmission across fractures with nonlinear deformational behavior". Int J. Numer Anal Methods Geomech 30:1097-1112.

Zhao, X.B., Zhao, J., Hefny, A.M., Cai, J.G. (2006b). "Normal transmission of S-wave across parallel fractures with coulomb slip behavior". J Eng Mech 132:641-650.

Zilberbrand M., Yechieli Y., & Hadad A., (1996). "Response of groundwater levels to changes in the Dead Sea in the past and the future (in Hebrew)", report submitted to the Minist. of Infrastruct. ES/9/96, Geol. Surv. of Isr., Jerusalem.

Zimmerman, R.W. (1984a). "Elastic moduli of a solid with spherical pores: new self-consistent method", International Journal of Rock Mechanics and Mining Sciences & Geomechanics Abstracts. Vol. 21, pp. 339-343.

Zimmerman, R.W. (1984b). "The Effects of Pore Structure on the Pore and Bulk Compressibilities of Consolidated Sandstones", Ph.D Thesis, University of California at Berkeley, USA.

Zimmerman, R.W. and King, M.S. (1985). "Propagation of acoustic waves through cracked rock", Proceedings of 26th US Symposium on Rock Mechanics, pp. 739-745.

Zoeppritz, K., Nach. D. K., Gesell., D. and Wissen, Z. G. (1919). Math.-phys., Berlin, pp. 66-84.

Zoeppritz, K. B. (1907). Über Erdbebenwellen II. Laufzeitkurven, Nachrichten der Königlichen Gesellschaft der Wissenschaften zu Göttingen, Mathematisch-Physikalische Klasse, 529-549.